RICE UNIVERSITY

Harnessing Data Structure for Health Monitoring and Assessment of Civil Structures: Sparse Representation and Low-rank Structure

by

Yongchao Yang

A Thesis Submitted
in Partial Fulfillment of the
Requirements for the Degree
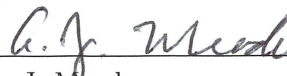
Doctor of Philosophy

Approved, Thesis Committee:

Satish Nagarajaiah, Chair
Professor of Civil and Environmental
Engineering and Mechanical Engineering

Jamie E. Padgett
Associate Professor of Civil and
Environmental Engineering

Andrew J. Meade
Professor of Mechanical Engineering

Houston, Texas

August, 2014

ProQuest Number: 10674120

ProQuest 10674120

RICE UNIVERSITY

Harnessing Data Structure for Health Monitoring and Assessment of Civil Structures: Sparse Representation and Low-rank Structure

by

Yongchao Yang

A Thesis Submitted
in Partial Fulfillment of the
Requirements for the Degree

Doctor of Philosophy

Approved, Thesis Committee:

_____

Satish Nagarajaiah, Chair
Professor of Civil and Environmental
Engineering and Mechanical Engineering

_____

Jamie E. Padgett
Associate Professor of Civil and
Environmental Engineering

_____

Andrew J. Meade
Professor of Mechanical Engineering

_____

Houston, Texas

August, 2014

ABSTRACT

Harnessing Data Structure for Health Monitoring and Assessment of Civil Structures: Sparse Representation and Low-rank Structure

by

Yongchao Yang

Civil structures are subjected to ambient loads, natural hazards, and man-made extreme events, which can cause deterioration, damage, and even catastrophic failure of structures. Dense networks of sensors embedded in structures, which continuously record structural data, make possible real-time health monitoring and diagnosis of structures. Effectively and efficiently sensing and processing the massive sensor data, potentially from hundreds of channels, is required to identify (update) structural information and detect damage as early as possible to inform immediate decision-making.

Different from traditional model-based and parametric methods that usually require intensive computation and expert attendance, this thesis explores a new data-driven methodology towards rapid, unsupervised, and automated system identification and damage detection of structures as well as data management by harnessing the data structure itself. Specifically, the sparse representation and low-rank structure inherent but implicit in the multi-channel structural response data are exploited for efficient data sensing, processing, and management in real-time health monitoring and non-destructive assessment of structures. Numerical simulations, laboratory experiments on bench-scale structures, and real-world structures examples, including

seismically excited buildings and a super high-rise TV tower, are investigated.

Acknowledgments

First of all, my most sincere and deepest gratefulness is to Professor Satish Nagarajaiah. I respect and look up to Professor Nagarajaiah from my heart not only because of his well-informed knowledge and well-recognized reputation, but also his big heart with most generous support, encouragement, and care to my research, career, and life. Thanks to Professor Nagarajaiah's guidance, I have always counted myself as one of the most fortunate students, to have the opportunity of challenging myself, improving myself, and growing mature not only as a researcher, but also as a human being. Working with Professor Nagarajaiah is such a great pleasure that I have truly enjoyed the joy of research, and have learned so many experience, inspirations, and wisdom, as well as immense encouragement and support from him, which, I believe, will continue to sustain me and prepare me for whatever difficulty ahead in the rest journey of my life.

I would also like to express many thanks to my dissertation committee members: Professor Jamie Padgett and Professor Andrew Meade. They have paid kind attention and support to my dissertation work and research career, for which I am genuinely thankful.

I am grateful to our collaborators Professor Hui Li, Dr. Shunlong Li, and Mr. Peng Zhou at Harbin Institute of Technology (HIT) for their assistance and help in our collaborations. Professor Li, who was my undergraduate mentor at HIT, has been very much supporting me, which has meant so much to me and for which I have been very thankful. I would also like to thank Professor Yiqing Ni and this co-workers at The Hong Kong Polytechnic University for sharing the Canton Tower field measurement data with our group.

Contents

9 Data Cleansing using Low-rank Representation   200

10 Conclusions and Future Research   216

Bibliography   225

Illustrations

Tables

Chapter 1

Introduction

1.1 Motivation

Detecting damage of civil structures as early as possible is essential to ensure structural safety and integrity during their service subjected to various natural disasters (e.g., earthquakes and hurricanes) and man-made extreme events (e.g., blasts and impacts). It allows prompt maintenance and thus reduces the repair cost; in addition, timely damage information makes possible for informed decisions and immediate actions before catastrophic failure of structures occurs. To achieve this goal, it has recently become a common practice to embed in structures a structural health monitoring (SHM) system with an array of networked sensors to continuously monitor and assess the structural performance. For example, the California Strong Motion Instrumentation Program (CSMIP) [37] has installed across California seismic monitoring sensor networks in more than 600 ground motion stations as well as 200 civil structures (e.g., buildings, bridges, dams, etc). Additionally, many landmark suspension bridges and high-rise buildings or towers have been equipped with dense networks of sensors: the Tsing Ma Bridge (1997) in Hong Kong, the Canton Tower (2010) in Guangzhou, the Stonecutters Bridge (2009) in Hong Kong, with more than 280, 800, 1500 sensors [108][107], respectively; other examples abound.

As such, the data-intensive issue has arisen. On the one hand, the continuously collected sensor data provides high-resolution and multi-dimensional information of

the structure, which is vital for identifying (updating) structural information, evaluating its health status, and detecting damage in real time. On the other, processing and managing the overwhelmingly voluminous data continuously collected from the SHM system requires the system identification and damage detection algorithms not only effective, but also efficient and automated, to extract useful structural information for on-line monitoring as well as off-line long-term performance assessment. In addition, real-time SHM and decision-making naturally requires sensing, transferring, and managing massive SHM data sets efficiently (especially during extreme events such as earthquakes and hurricanes), a subject which has received little attention in current literature and SHM practice. For example, the measured (or recorded) Canton Tower SHM data with many outliers (shown in Fig. 1.1) clearly needs to be cleansed before it can be used for further analysis.
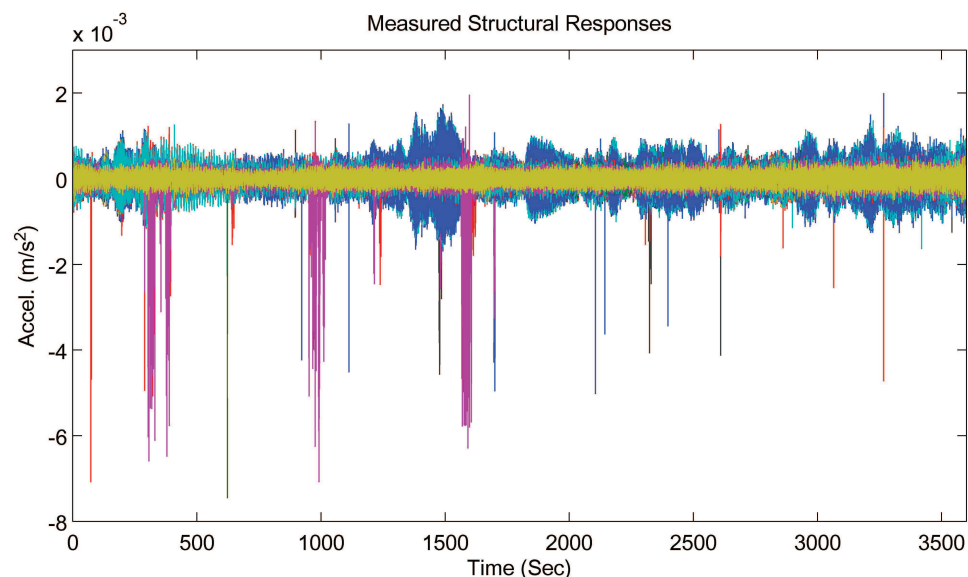
Figure 1.1 : The recorded ambient vibration accelerations of the Canton Tower from 12:00 am Jan. 20th, 2010 to 1:00 pm Jan. 20th, 2010. (20 channels data are shown with different colors, available in Ref. [1].) Chapter 9 proposes a solution to efficiently remove these outliers; compare to the denoised Fig. 9.4.

1.2 Traditional methods and their drawbacks

1.2.1 Parametric model based methods

Vibration-based techniques, such as modal analysis, have been widely studied for SHM. Traditional modal identification typically complies the wisdom of system identification which is based on the relationship of inputs and outputs [46][88][83]. This corresponds to an ideal situation where excitation to the system can be controlled or measured. For civil structures, typically large-scale, such as bridges, buildings, dams, etc., it is extremely difficult or expensive, if not impossible, to apply controllable excitation to conduct input-output modal identification; equally challenging is the measurement of the ambient excitation (e.g., wind, traffic, etc) to structures. Output-only modal identification methods using only the available structural response data [110][18] are therefore needed, especially for real-time SHM.

Existing output-only modal identification algorithms, such as Ibrahim time domain (ITD) method [66], eigensystem realization algorithm (ERA) [68], natural excitation technique (NExT) [67], stochastic subspace identification (SSI) [139], and frequency domain decomposition (FDD) [19], are widely used to perform modal identification of civil structures [22][121][18][97][95]. Most of these methods presume a parametric mathematical model, e.g., stochastic state-space model (with model state matrix $\mathbf{A} \in \mathbb{R}^{n \times n}$, output matrix $\mathbf{C} \in \mathbb{R}^{p \times n}$, state vector $\mathbf{x}(k) \in \mathbb{R}^n$ and output $\mathbf{y}(k) \in \mathbb{R}^p$, and process noise (excitation) $\mathbf{w}(k) \in \mathbb{R}^n$ and measurement noise $\mathbf{v}(k) \in \mathbb{R}^p$)

$$\mathbf{x}(k+1) = \mathbf{A}\mathbf{x}(k) + \mathbf{w}(k) \tag{1.1}$$

$$\mathbf{y}(k) = \mathbf{C}\mathbf{x}(k) + \mathbf{v}(k) \tag{1.2}$$

to characterize the structural dynamic behaviors and then fit the measured structural

responses to the model.

Many established damage detection methods also share similar strategy with the assumption that the structural behaviors follow a certain form of model (e.g., physical or modal model), where abnormal behavior indicates damage. Especially, modal-based damage identification methods, which assume that a change of modal parameters signifies damage, have been extensively studied (a summary review [41]). Other parameter-dependent methods are also developed, e.g., the observer-based methods [29], flexibility-based method [14][52], method using input error function [79].

These system identification and damage detection methods are mostly model based and parametric; as such, they are typically computationally demanding and require much expert attendance for parameter adjustments associated with the model fitting process. For example, the model order problem remains a challenge, for which using the stability chart demands exhaustive expert interference and time-consuming computation burden: although effective for offline applications, they are not suitable for real-time unsupervised processing of the large-scale data sets of civil structures. On the other hand, non-parametric data-driven algorithms, which extract structural features and performs structural assessment directly from the data, are computationally efficient and have high potential for real-time processing the massive SHM data.

1.2.2   Data-driven approaches

Unlike traditional parametric model based methods which are derived from the (mathematically) assumed physical processes, data-driven approaches aim to extract the desirable information directly from the available data, without explicit knowledge of the (assumed) physical or dynamic model of the underlying system.

Many signal processing based system identification and damage detection algorithms that have been developed in the literature fall into this category, featuring efficient computation and adaptive implementation, such as those based on wavelet transform [75][125][59][55][10][56], Hilbert-Huang transform (HHT) [61][141][142], and other time-frequency analysis techniques [96], to name a few. Successful implementations, however, require practitioners to wisely adjust the algorithm parameters; for example, the wavelet basis and the scales need to be carefully selected in the wavelet-based methods, and the prescription of the modal bandwidth as well as the sifting process also influence the abilities of the HHT methods. In addition, measurement noise also presents a challenge to their effectiveness; the popular wavelet transform is briefly reviewed in the following and its advantages and drawbacks are shown with an example.

The discrete wavelet transform (DWT) achieves a multi-resolution analysis of a signal $f(t)$ by [90][38]

$$v_k^l = \frac{1}{2^{l/2}} \int_{-\infty}^{\infty} f(t)\phi^*(\frac{t}{2^l} - k)dt \tag{1.3}$$

$$w_k^l = \frac{1}{2^{l/2}} \int_{-\infty}^{\infty} f(t)\psi^*(\frac{t}{2^l} - k)dt \tag{1.4}$$

where l and k are the scale and translation parameters, respectively, and $*$ denotes the complex conjugate operator. v and w are the resultant approximation and detail (wavelet) coefficients from the scaling function $\phi(t)$ and wavelet basis $\psi(t)$, respectively. Therefore, WT realizes a multi-resolution time-frequency analysis of $f(t)$ by decomposing it into low-frequency (approximation) and high-frequency (detail) band at each level. At the lth scale level, the approximated component f_a^l and detailed component f_d^l also retain the temporal information of $f(t)$ and are represented, re-

spectively, by

$$f_a^l = \sum_k v_k^l \phi(\frac{t}{2^l} - k) \tag{1.5}$$

$$f_d^l = \sum_k w_k^l \psi(\frac{t}{2^l} - k) \tag{1.6}$$

If $f(t)$ is decomposed into L levels, then it can be reconstructed by

$$f(t) = f_a^L(t) + \sum_{l=1}^{L} f_d^l(t) \tag{1.7}$$

The interesting property (e.g., pulse-like sparse feature, which is the salient signature of damage, as detailed in later Section 1.3.1 and Fig. 1.7) of $f(t)$ may be revealed on certain wavelet scales [90]. However, it is easily destroyed by noise; see Fig. 1.2 for example.

Many pattern recognition or classification based damage identification techniques [16][21] belong to the supervised family of data-driven approaches. The classification-based methods typically involve three steps: feature extraction (from data), training (the empirical model, typically parametric), and classification (Fig. 1.3). For damage identification, the extracted features from various predefined or *reference* damage classes, including different damage locations and damage extents, are used as inputs to train the classifiers, which can then identify the damage class of the *test* (unknown) feature (representing the current state of the structure). For example, the support vector machines (SVMs) classifier model is

$$f(\mathbf{x}_i) = \text{sign}(\mathbf{w}\mathbf{\Phi}(\mathbf{x}_i) + b) \tag{1.8}$$

where $\mathbf{x}_i \in \mathbb{R}^n$ is the input vector, and $\mathbf{w} \in \mathbb{R}^n$, $\mathbf{\Phi}$ (mapping function), and b are the parameters of the classifier, which are obtained by a training set of $\mathbf{x}_j \in \mathbb{R}^n (j =$
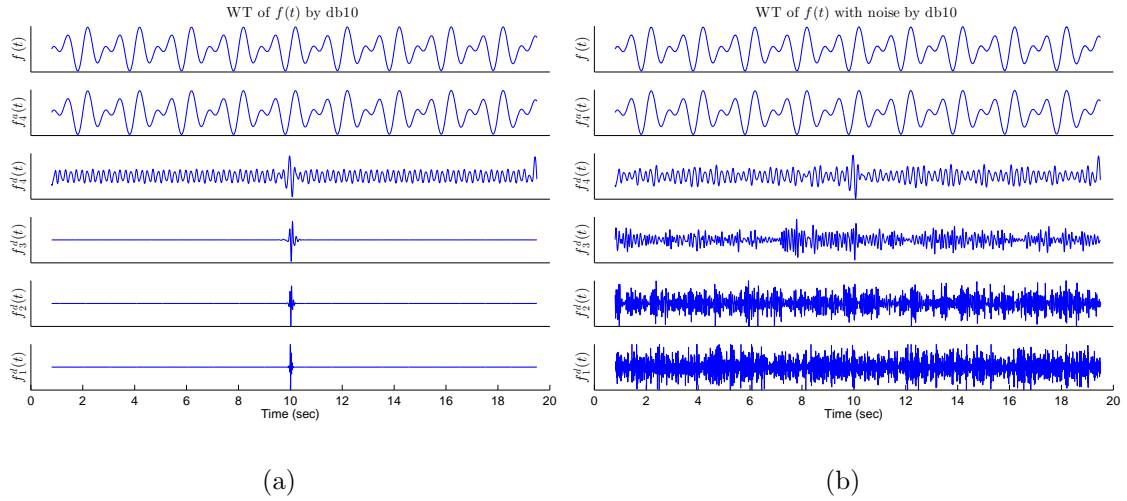
Figure 1.2 : The pulse-like feature hidden in a signal can be revealed in the wavelet domain and is also easily destroyed by noise. A signal with a sampling frequency of 100 Hz $f(t) = \sin(2\pi \cdot 1 \cdot t) + \sin(2\pi \cdot 1.5 \cdot t), t = 0 \sim 10; \sin(2\pi \cdot 1 \cdot t) + \sin(2\pi \cdot 1.499 \cdot t), t = 10 \sim 20$ experiences a slight frequency transition from 1.500 Hz to 1.499 Hz at the 10th second. Although no sign of such transition can be observed from its time history, pulse-like feature is distinguished in the wavelet-domain decomposed signal using the db10 wavelet basis [38]. **(a)** It is shown as a pulse-like feature at the 10th second in the detailed components $f_d(t)$ on all the four scales. **(b)** This pulse-like feature in the wavelet domain is completely buried when $f(t)$ is contaminated by Gaussian white noise with a level of SNR=40 dB. ICA is capable of extracting the buried pulse-like feature from the noisy wavelet-domain signals, as detailed in Section 1.3.4 and Fig. 1.13 and more in Chapter 4.

$1, ..., q)$ and their associated label; the decision function sign($\cdot$) assigns the class (label) of $\mathbf{x}_i \in \mathbb{R}^n$. Successful examples based on SVMs are seen in [137][135][136]; others also include those based on artificial neural networks (ANN) [154][124], nearest neighbor [134], and Markov observers [40].

Several factors, however, could influence the performance of these classification-based damage identification methods that are mostly dependent on the training process of the classifiers. In the ANN-based methods, for example, the number of input/output and hidden nodes in the network could affect its accuracy [154][124], and
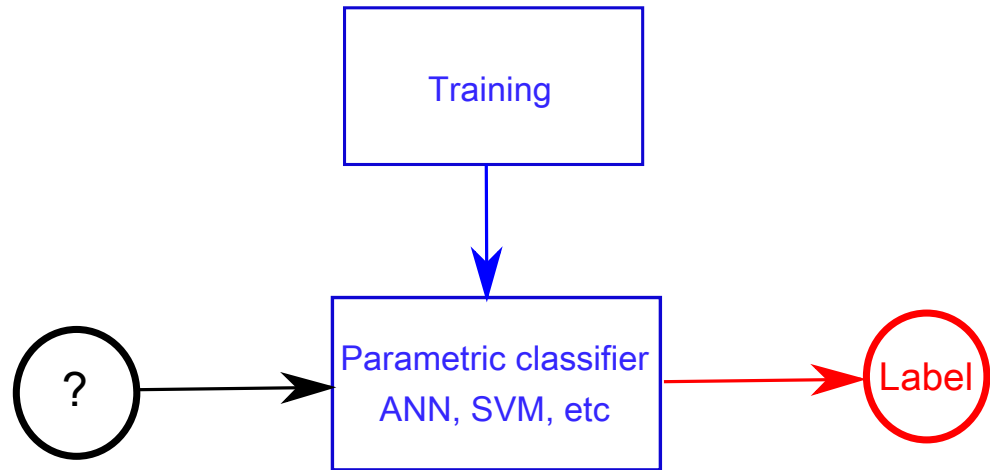
Figure 1.3 : The principle of traditional pattern recognition or classification. Reference information is used to train the parametric classifier (blue) such as artificial neural network (ANN) and support vector machines (SVMs), which then assigns the unknown object (black) a predefined label or class (red). The parametric training process can be time-consuming and user-involved. One may compare to the new sparse representation classification without a parametric classifier model or a training process (Fig. 1.8) and more explorations in Chapter 5).

the global convergence of the algorithm is not guaranteed in most cases [16]. Compared to ANN, the multi-class SVM-based methods have advantages when the sample numbers are small [21][135]; nevertheless, their success depends on the choice of the algorithm parameters, i.e., the kernel function selection and its associated parameters [21][137][136]. Although optimal choice may be obtained through trial and error or optimization algorithms, and such an approach increases computational burden and needs the skill of an experienced practitioner; hence is not preferable in many situations, e.g., in real-time monitoring, where rapid and unsupervised processing of the large-scale data set is required.

1.3   A new perspective

Traditional research on SHM relies on either the physical model or the use of different signal processing techniques; this thesis shifts the focus on to **harnessing the inherent data structure itself** of the structural response data to extract the desirable structural features and damage information, otherwise invisible, towards rapid (even real-time), unsupervised (automated), and effective system identification, damage detection, as well as massive SHM data management. Particularly, the structural features and damage information intrinsic within the structural response data, usually large-scale in SHM, possesses **sparsity nature** and **low-rank structure**, which, fortunately, are readily reachable by new mathematical tools.

In particular, the recent developments of sparse representation (SR) [20] and compressed sensing (CS) [26][43], as well as the unsupervised blind source separation (BSS) [34], have presented new opportunities to develop innovative data-driven approaches towards efficient and effective sensing, processing, managing large-scale SHM data sets. In each of the following sections, their fundamental theories are first reviewed, and then their implications in output-only modal identification, damage detection, and massive data management of civil structures, which are explored in this thesis, are briefly introduced with details in the ensuing chapters.

1.3.1   Sparse representation

In MRI [84], computer vision [138], digital camera/video [132], etc, SR and CS have provided a new solution to sensing and processing of large-scale data sets, with recent exploratory applications also in SHM [9][148][152][150][91][109].

To mathematically express sparsity of a signal $x \in \mathbb{R}^N$, it is useful to define the

ℓ_0-norm [20],

$$\|x\|_{\ell_0} = \#\{i : x_i \neq 0\} \tag{1.9}$$

simply counting the number of non-zeros in x. A signal x (vector) is k-sparse if it has at most k non-zeros, i.e., $\|x\|_{\ell_0} \leq k$. In a more general perspective, x is said to be k-sparse (transform sparse) in a domain $\boldsymbol{\Psi}$ with a representation $\alpha \in \mathbb{R}^N$

$$x = \boldsymbol{\Psi}\alpha = \sum_{j=1}^{N} \alpha_j \psi_j \tag{1.10}$$

if $\|x\|_{\ell_0} \leq k$. $\boldsymbol{\Psi} = [\psi_1, ..., \psi_N]^T \in \mathbb{R}^{N \times N}$ is an orthonormal basis (e.g., sinusoid, wavelet, etc), whose jth row is $\psi_j \in \mathbb{R}^N$ (or $\mathbb{C}^N$ on Fourier basis). $\boldsymbol{\alpha} \in \mathbb{R}^N$ is the coefficient sequence of $x \in \mathbb{R}^N$ on $\boldsymbol{\Psi}$, whose jth element $\alpha_j = \langle x, \psi_j \rangle$ (inner product). This generalization is particularly useful since, in practice, x is typically sparse in an appropriate domain instead of its original domain. A simple example is the sinusoid, which is sparsest $(k = 1)$ in the frequency domain. Another example concerning multivariate signals is shown Fig. 1.4.

It is seen that a sparse representation of signals reveals their hidden characteristics that are otherwise implicit. The recent breakthrough in signal sensing and processing, compressed sensing [26][43], further exploits the sparsity of signals in an appropriate representation domain and allows exact recovery of a sparse signal, enabled by ℓ_1-minimization ($\|x\|_{\ell_1} = \sum_{i=1}^{N} |x_i|$, the tightest convex relaxation of ℓ_0-minimization), from far fewer incoherent random measurements than what is suggested by the sampling theorem. A simple example shown in Fig. 1.5 illustrates that ℓ_1-minimization correctly recovers the sparse signal from few random measurements, while it is not the case for the conventional ℓ_2-minimization (least square estimation).

It turns out that the structural features and damage information of interest hidden in the structural response data are naturally sparse and can be readily revealed by
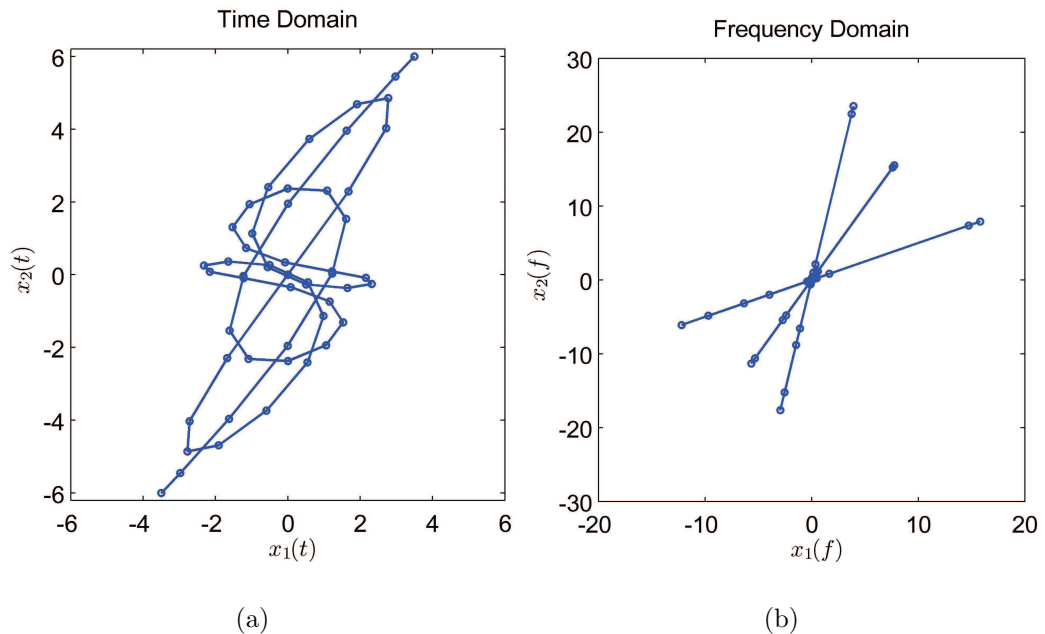
Figure 1.4 : Sparse representation reveals multivariate signal characteristics: three hidden source signals, $s_1(t) = \cos{(2\pi \cdot 0.3 \cdot t)}$, $s_2(t) = \cos{(2\pi \cdot 0.7 \cdot t)}$, and $s_3(t) = \cos{(2\pi \cdot 1.3 \cdot t)}$ are mixed by a rectangular matrix $\mathbf{A} = \begin{bmatrix} 1 & 0.5 & 2 \\ 2 & 3 & 1 \end{bmatrix}$ to yield two observable mixtures $x_1(t) = s_1(t) + 0.5s_2(t) + 2s_3(t)$, $x_2(t) = 2s_1(t) + 3s_2(t) + s_3(t)$. **(a)** In the original time domain, the scatter plot of $\mathbf{x}(t)$ reveals little information on the characteristics of source signals and the mixing process. **(b)** As opposed, notice that $\mathbf{x}(t)$ has sparse representations in frequency domain–its constituent sources are spectrally monotone; transform $\mathbf{x}(t)$ into the sparse frequency domain to yield $\mathbf{x}(f)$ (f is the frequency index), and the scatter plot of $\mathbf{x}(f)$ ($x_1(f)$ versus $x_2(f)$) shows that the points of $\mathbf{x}(f)$ (sparsely) cluster to three significant directions of the columns of $\mathbf{A}$, which can be captured by visual inspections. The interpretation of sparse component analysis (SCA) in output-only modal identification is covered on Chapter 3.

the mathematical tools of sparse representation. It has been the common thread to explicitly exploit such data structure towards developing innovative data-driven system identification and damage detection approaches in the thesis. For example, in output-only modal identification, express the available structural responses $\mathbf{x}(t)$ as
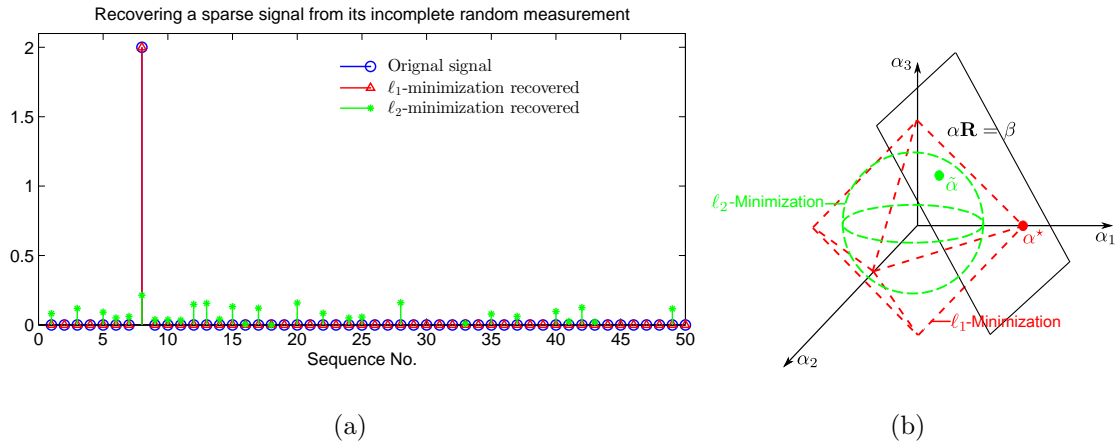
Figure 1.5 : **(a)** A sparse signal $\alpha \in \mathbb{R}^{50}$ (row vector) with only one non-zero entry is incompletely sensed by multiplying by a zero-mean and unit-variance normally distributed mixing matrix $\mathbf{R} \in \mathbb{R}^{50\times5}$, yielding an observation signal $\beta = \alpha\mathbf{R} \in \mathbb{R}^{5}$ (row vector). For recovery of the underlying α from the incomplete knowledge of $\mathbf{R}$ and β, ℓ_1-minimization correctly recovers the original sparse signal while the minimal least square estimation ℓ_2-minimization fails; **(b)** The geometric illustration of ℓ_1-minimization in 3-dimensional space. The ℓ_1-norm sphere (dashed red) expanding from the origin to the three coordinates α_1, α_2, and α_3, intersects for the first time the constraint subspace plane $\alpha\mathbf{R} = \beta$, yielding the solution $\alpha^\star$ with minimal ℓ_1-norm. $\alpha^\star$ is seen sparsest with only one non-zero element living on the α_1 axis. On the other hand, spreading the well-known ℓ_2-minimization (minimal square ℓ_2-norm solution) sphere (dashed green) unfortunately harvests a dense solution $\tilde{\alpha}$ whose energy disperses among all three axis. The rich implications of the ℓ_1-minimization sparse recovery technique are explored in Chapter 3 and Chapter 5.

modal expansion,

$$\mathbf{x}(t) = \mathbf{\Phi}\mathbf{q}(t) = \sum_{i=1}^{n} \boldsymbol{\varphi}_i q_i(t) \tag{1.11}$$

The underlying modal responses $\mathbf{q}(t)$ are monotone–active at only one distinct frequency– and are most sparsely and disjointly distributed in the frequency domain. Hence, transform the modal expansion Eq. (1.11) into the sparse frequency domain,

$$\mathbf{x}(f) = \mathbf{\Phi}\mathbf{q}(f) = \sum_{i=1}^{n} \boldsymbol{\varphi}_i q_i(f) \tag{1.12}$$

Then in the scatter plot of $\mathbf{x}(f)$, the points of $\mathbf{x}(f)$ that belong to $q_i(f)$ will

sparsely cluster to the direction of the ith modeshape $\boldsymbol{\varphi}_i$ $(i = 1, ..., n)$ (Fig. 1.6) , making the output-only modal identification problem fairly intuitive and efficient, even when the sensor number is far less than that of the active modes (see Chapter 3 for more details).
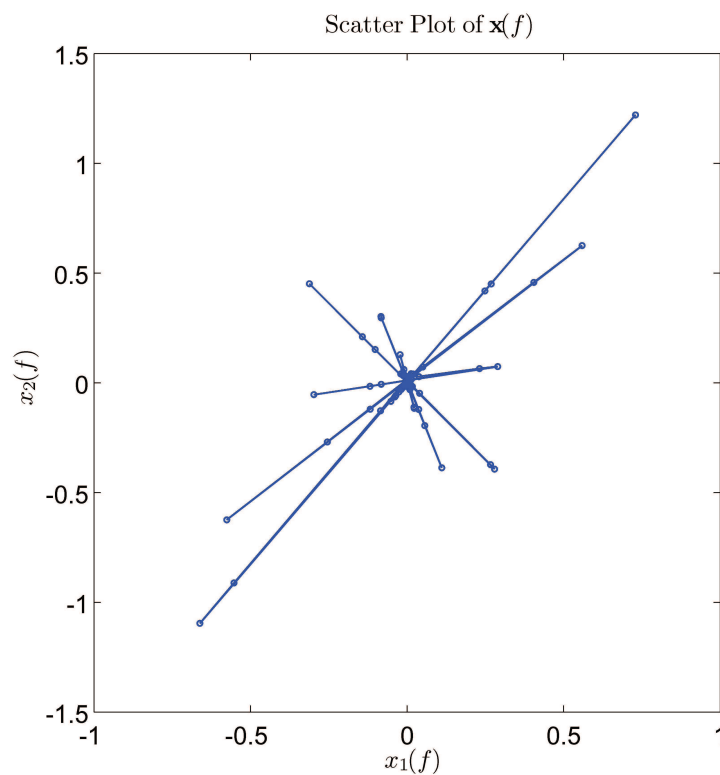
Figure 1.6 : The sparse clustering of the modal expansion in the scatter plot of the system responses in frequency domain using Sensor 1 and 2 of a 6-DOF system (more than Chapter 3).

As another example, sparsity is naturally the salient signature of damage (see Fig. 1.7) in the structural responses on some sparse signal representation domain, e.g., the popular wavelet domain, which, however, is easily affected by noise as seen in Fig. 1.2. Fortunately, the new mathematical tool, independent component analysis (ICA) [64] with a learning rule towards multivariate sparse components, enables

extraction of the hidden sparse signature from the noisy signals (see Section 1.3.4 for a brief introduction and more in Chapter 4).
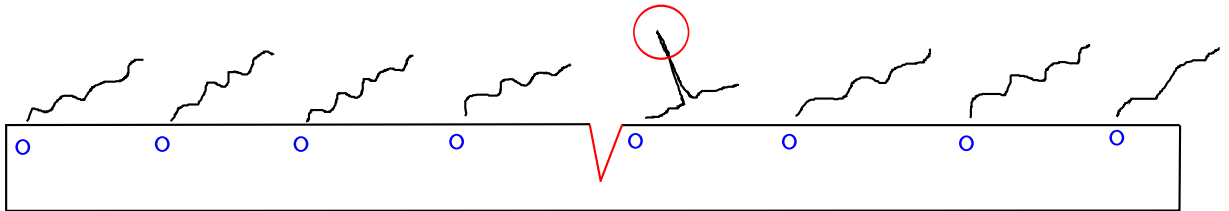
Figure 1.7 : Interpretation of structural damage as sparse signature in structural responses. The structure is embedded with a network of sensors (denoted as blue circles) which continuously measure structural responses. If damage (e.g., a crack, denoted as red) occurs, then the sensor data in the vicinity of damage will experience singular phonomenon, which behaves as implicit spike-like feature on some sparse domain such as wavelet domain. Its implication in structural damage identification is explored in Chapter 4.

Not only the structural dynamic and damage features have implicit sparse representation, the pattern recognition or classification framework for damage identification itself is also sparse in nature: the damage class of the test structure can only belong to *one* of the predefined reference damage classes, thus establishing a fairly straightforward sparse representation (SR) classification method for damage quantification, which alleviates the computationally-intensive parametric training process that is traditionally required. See Fig 1.8 for a brief introduction and Chapter 5 presents this new classification framework for damage identification.

1.3.2   Low-rank representation

Structural responses, from potentially hundreds of channels or sensors, can be represented as a data matrix. Analogous to the sparsity nature of single-channel data (vector), in this thesis, the intrinsic low-dimensional data structure of multi-channel
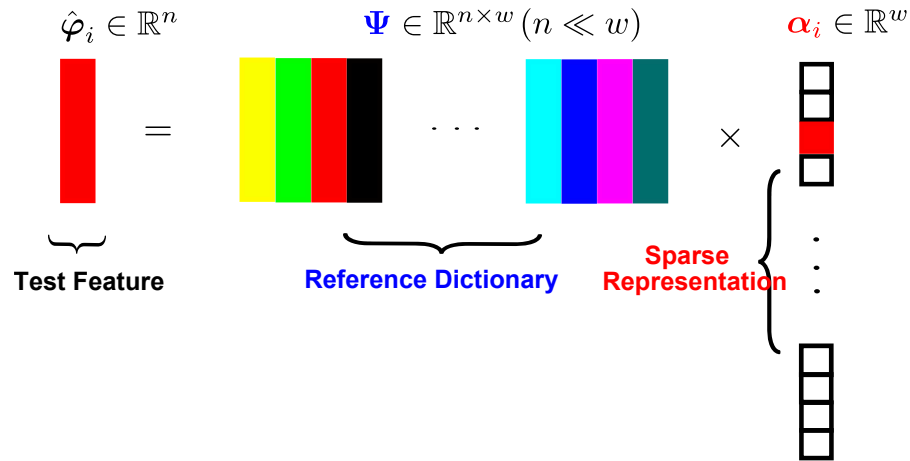
Figure 1.8 : The sparse representation classification framework. The test feature $\hat{\boldsymbol{\varphi}}_i \in \mathbb{R}^n$ (the red column, e.g., the modeshape column in structural damage identification) only activates itself via its sparse representation $\boldsymbol{\alpha}_i \in \mathbb{R}^w$ (red in its own location, white denotes inactivated zero) in terms of the large reference dictionary $\boldsymbol{\Psi} \in \mathbb{R}^{n \times w}$ ($n \ll w$) (by concatenating all feature columns of all candidate reference classes), expressed as a highly underdetermined linear system of equations $\hat{\boldsymbol{\varphi}}_i = \boldsymbol{\Psi}\boldsymbol{\alpha}_i$. The unique non-zero element (red) in $\boldsymbol{\alpha}_i$ (recovered by ℓ_1-minimization) directly dictates which class the test feature belongs to, within the predefined reference dictionary. Sparse representation classification does not assume a parametric classifier or training; its implication in structural damage identification is explored in Chapter 5.

data matrix is also explicitly exploited, e.g., by singular value decomposition (SVD) or principal component analysis (PCA).

The data matrix $\mathbf{X} \in \mathbb{R}^{m \times N}$ with m sensors and N time history sampling points ($m < N$) has an SVD representation (also see Fig. 1.9(a) for a brief illustration)

$$\mathbf{X} = \mathbf{U}\boldsymbol{\Sigma}\mathbf{V}^T = \sum_{i=1}^{r} \sigma_i \mathbf{u}_i \mathbf{v}_i^T \tag{1.13}$$

where $\mathbf{U} = [\mathbf{u}_1, ..., \mathbf{u}_m] \in \mathbb{R}^{m \times m}$ is an orthonormal matrix associated with the channel (variable) dimension, called left-singular vectors or principal component directions; $\boldsymbol{\Sigma} \in \mathbb{R}^{m \times N}$ has m diagonal elements σ_i as the ith singular value ($\sigma_1 > ... > \sigma_r > \sigma_{r+1} = ... = \sigma_m = 0$), and $\mathbf{V} = [\mathbf{v}_1, ..., \mathbf{v}_N] \in \mathbb{R}^{N \times N}$ is associated with the time history (measurement) dimension, called the right-singular vector matrix. SVD is

closely related to the eigenvalue decomposition (EVD): the left-singular vector matrix $\mathbf{U}$ is obtained by the EVD of its covariance matrix

$$\mathbf{X}\mathbf{X}^T = \mathbf{U}\hat{\mathbf{\Sigma}}^2\mathbf{U}^T \tag{1.14}$$

and similarly for the right-singular vector matrix $\mathbf{V}$,

$$\mathbf{X}^T\mathbf{X} = \mathbf{V}\tilde{\mathbf{\Sigma}}^2\mathbf{V}^T \tag{1.15}$$

where $\hat{\mathbf{\Sigma}} \in \mathbb{R}^{m \times m}$ and $\tilde{\mathbf{\Sigma}} \in \mathbb{R}^{N \times N}$ are zero-truncated and zero-padded version of $\mathbf{\Sigma} \in \mathbb{R}^{m \times N}$, respectively.

It is well understood that the ith singular value σ_i is related to the energy captured by the ith principal direction of $\mathbf{X}$. In structural dynamics, under some assumption, the principal directions would coincide with the mode directions [48] with the corresponding singular values indicating their participating energy in the structural responses $\mathbf{X}$, i.e., the structural active modes are captured by r principal components under broadband excitation.

An empirical, but frequently sound, observation is that there are typically only few active modes in the structural responses [149]; in other words, few of its singular values are active: r is typically quite small. If the sensor or channel number m is reasonably large, then $r \ll \min(m, N) = m$ and $\mathbf{X} \in \mathbb{R}^{m \times N}$ is said to be low-rank. However, this is seldom so for large civil structures, because the sensor number m is not so *much* more than (often times even less than) the involved r modes; as a result, $r \ll m$ can't be guaranteed for a low-rank representation.

In this thesis, a simple yet effective strategy–**rank-invariant matrix reshape** [150] (Fig. 1.9(a)) is proposed to guarantee a low-rank representation of structural response data matrix, regardless of the original dimension of $\mathbf{X} \in \mathbb{R}^{m \times N}$. Essentially, mode information (few are active; hence, the rank of the structural response data

matrix is small) remains invariant regardless of the reshape of the structural response data matrix; a brief example of the structural seismic response data is shown in Fig. 1.10, where in the original dimension of the structural response data matrix, the implicit low-rank structure is not impressive (Fig. 1.10(a)); after reshape of the data matrix, the low-rank representation stands out Fig. 1.10(b)). It is detailed in Chapter 6, Chapter 7, Chapter 8, and Chapter 9, where many examples indicate that such implicit (reshaped) low-rank structure inspires innovative and efficient solutions to process and manage the multi-channel, often very large-scale, structural response data.

1.3.3 Low-rank plus sparse representation

Inspired by the intrinsic low-dimensional structure of the multi-channel structural responses and the sparsity nature of the damage signature, this thesis explores an emerging high-dimension data analysis technique, principal component pursuit (PCP) or robust principal component analysis, and finds new applications in the proposed data-driven paradigm towards rapid and unsupervised SHM and damage detection.

PCP is able to decompose a matrix $\mathbf{X} \in \mathbb{R}^{m \times N}$ into a superposition of a low-rank matrix $\mathbf{L} \in \mathbb{R}^{m \times N}$ and a sparse matrix $\mathbf{S} \in \mathbb{R}^{m \times N}$ as

$$\mathbf{X} = \mathbf{L} + \mathbf{S} \tag{1.16}$$

$\mathbf{S} \in \mathbb{R}^{m \times N}$ is said to be sparse if it has only few non-zero entries, and $\mathbf{L} \in \mathbb{R}^{m \times N}$ is low-rank in the sense that its SVD has few active singular values.

The $\mathbf{L} + \mathbf{S}$ representation can intuitively represent the multi-channel structural vibration responses corrupted by gross outliers, which is not uncommon in real-recorded SHM data (see Fig. 1.1): the outliers or gross errors are sparse in nature, and the underlying clean multi-channel structural responses typically possess intrinsic (reshaped)

(a)
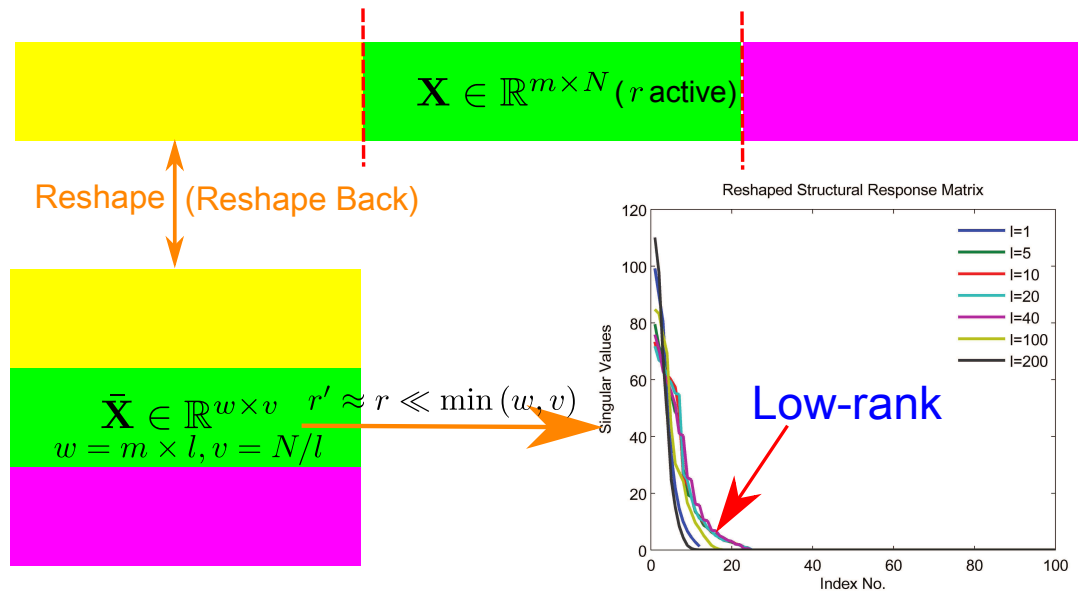
(b)

Figure 1.9 : **(a)** The singular value decomposition of the data matrix $\mathbf{X} \in \mathbb{R}^{m \times N}$ (e.g., m sensors and N time history points) as a linear combination of r active singular vector subspaces. If $r \ll \min(m, N) = m$, then explicitly $\mathbf{X}$ has a low-rank structure. **(b)** Matrix reshape is proposed to guarantee and enhance the low-rank representation of $\mathbf{X}$ if it does not have an explicit low-rank structure (i.e., if $r \ll \min(m, N) = m$ is not true, which is often the case for SHM data). Divide the fat $\mathbf{X} \in \mathbb{R}^{m \times N}$ into l segments and reshape it to a new more "square" matrix $\bar{\mathbf{X}} \in \mathbb{R}^{w \times v}$ ($w = m \times l, v = N/l$) with each segment as one "row". If $\mathbf{X}$ is structural vibration response data matrix, the rank of $\bar{\mathbf{X}}$ remains $r' \approx r$ (associated with the active modes) but $r' \approx r \ll \min(w, v)$ is significantly low hence a low-rank representation. The right plot shows that the singular values of the reshaped data matrices with different reshape factor l vanish radically (more in Chapter 8 and Chapter 9).

low-rank structure. Therefore, after decomposition of the corrupted $\mathbf{X} \in \mathbb{R}^{m \times N}$ into $\mathbf{L} \in \mathbb{R}^{m \times N}$ plus $\mathbf{S} \in \mathbb{R}^{m \times N}$, $\mathbf{L} \in \mathbb{R}^{m \times N}$ represents the underlying clean structural responses, removing the outliers represented by $\mathbf{S} \in \mathbb{R}^{m \times N}$ (see Chapter 9).
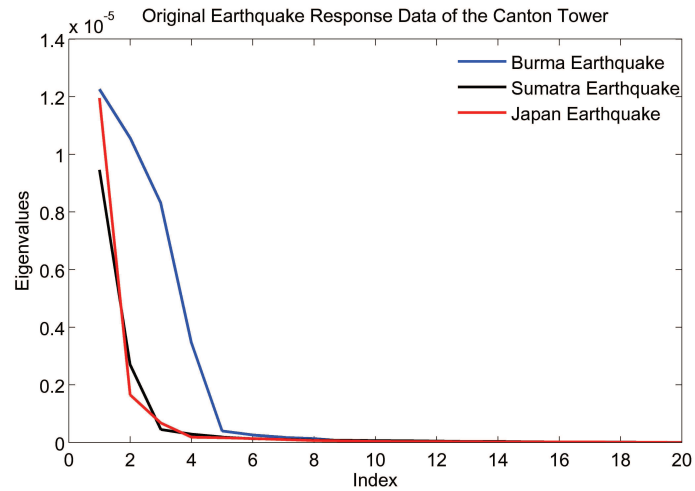
(a)
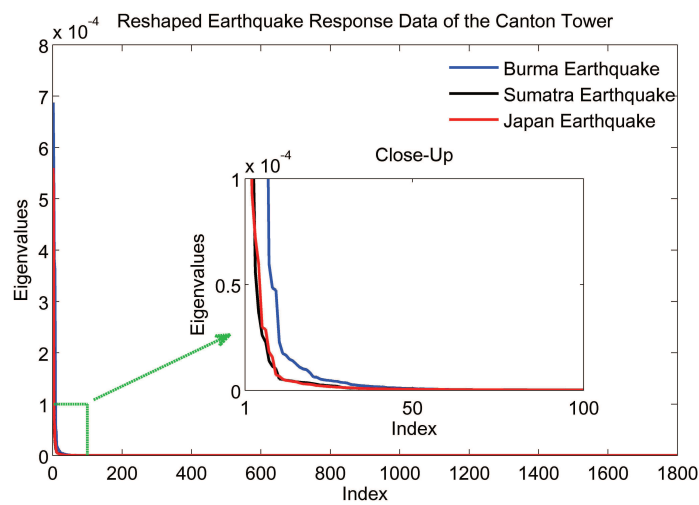
(b)

Figure 1.10 : After reshaping of the structural seismic response data matrix, its low-rank structure is dramatically outstanding with its singular values vanishing radically (more in Chapter 8). **(a)** The eigenvalues (square of the singular values) of the earthquake response data matrices of the Canton Tower in their original dimension: $\mathbf{X} \in \mathbb{R}^{20 \times 180000}$ for the Burma Earthquake, $\mathbf{X} \in \mathbb{R}^{17 \times 180000}$ for the Sumatra Earthquake, and $\mathbf{X} \in \mathbb{R}^{20 \times 180000}$ for the Japan Earthquake. **(b)** The eigenvalues (square of the singular values) of the earthquake response data matrices of the Canton Tower in *reshaped* dimension: $\bar{\mathbf{X}} \in \mathbb{R}^{2000 \times 1800}$ for the Burma Earthquake, $\bar{\mathbf{X}} \in \mathbb{R}^{1700 \times 1800}$ for the Sumatra Earthquake, and $\bar{\mathbf{X}} \in \mathbb{R}^{2000 \times 1800}$ for the Japan Earthquake.

In addition, the $\mathbf{L} + \mathbf{S}$ representation has an innovative insight into the data structure of the multiple temporal close-up frames of structures as a superposition of a background component and an innovation component: $\mathbf{L}$ represents the static or slowly-changing correlated background component among the temporal frames, which is naturally low-rank; $\mathbf{S}$ captures the innovation information in each frame induced by the evolutionary damage, which is naturally sparse standing out from the background. See the proposed dynamic imaging framework for local structural assessment in Fig. 1.11 and Chapter 6 for more details.

1.3.4   Blind source separation (BSS)

Real-time SHM requires continuous and efficient processing of the massive measured data with as little expert attendance as possible. BSS as a promising unsupervised multivariate machine learning technique is able to recover the hidden source signals and their characteristic factors using only the measured mixture signals, with high potential in unsupervised learning of the patterns and features hidden in the large-scale multi-channel SHM data set.

The linear instantaneous BSS model is expressed as

$$\mathbf{x}(t) = \mathbf{A}\mathbf{s}(t) = \sum_{i=1}^{n} \mathbf{a}_i s_i(t) \tag{1.17}$$

where $\mathbf{x}(t) = [x_1(t), ..., x_m(t)]^T$ is the observed mixture vector with m mixture signals, and $\mathbf{s}(t) = [s_1(t), ..., s_n(t)]^T$ is the latten source vector with n sources; $\mathbf{A} \in \mathbb{R}^{m \times n}$ is the unknown constant mixing matrix consisting of n columns with its ith column $\mathbf{a}_i \in \mathbb{R}^m$ associated with $s_i(t)$. The striking resemblance between the BSS model (Eq. (1.17)) and the modal expansion (Eq. (3.1)) of structural responses $\mathbf{x}(t)$ as linear mixtures of the modal responses $\mathbf{q}(t)$, proposed in Ref. [74], naturally incorporates

the output-only modal identification problem to the BSS problem (see Fig. 1.12 for illustrations).

With only $\mathbf{x}(t)$ known, Eq. (1.17) may not be mathematically solved. To alleviate the problem, most BSS techniques, such as independent component analysis (ICA) [65], second order blind identification (SOBI) [13], and complexity pursuit (CP) [129], exert a general assumption that the source signals $\mathbf{s}(t)$ are statistically independent (or as independent as possible) at each time instant t; surprisingly, it suffices to recover the sources and the mixing matrix in most practical applications [64]. However, for output-only modal identification, ICA method is restricted to undamped and very lightly-damped structures [74][145][146]; SOBI methods meet with difficulty in non-stationary excitation, closely-spaced modes, and non-diagonalizable damping cases [112][159][93][57][7][93].

This thesis explores another approach to solve the BSS problem (incorporating the output-only modal identification problem): to exploit the signal complexity (CP method) of the mixtures (structural responses) and sources (modal responses) itself [147] (Chapter 2); a simple example of signal complexity is shown in Fig. 1.14. Besides, the rich implications of the learning rule, independence of source signals measured by non-Gaussianity (ICA method), lead to sparse distribution (Fig. 1.13) which indicates the structural damage feature in data-driven damage detection [146] (Chapter 4) and inspires new applications in significantly compressing the multi-channel structural responses [149] (Chapter 7). The multivariate unsupervised BSS learning rule is exploited in Chapter 2, Chapter 3, Chapter 4, and Chapter 7.

1.4 Objective

The overall objective of the dissertation research is to systematically develop a new paradigm with effective and efficient data processing and management algorithms towards rapid, unsupervised, and automated health monitoring and assessment of civil infrastructure. It aims to address two bottlenecks which have hindered modern SHM systems from achieving real-time monitoring and assessment: rapid processing of continuously-streaming data sets and efficient large-scale data management (sensing, transfer, communication, etc) with dense networked sensors (Fig. 1.15). Opposed to the traditional model based and parametric methods that are usually computationally intensive and require extensive user-involvement, the proposed methodology is data-driven in nature–by harnessing the data structure itself of the (available) structural response data set. Specifically, the sparse representation and low-rank structure of the massive data set, which turn out to be the salient structural dynamic and damage features, are exploited to establish a novel data-driven paradigm, enabling rapid data sensing and transmission, efficient output-only modal identification, real-time damage detection and non-destructive assessment of civil structures. Numerical simulations, laboratory experiments, and field measurement data of a real-world large-scale cable-stayed bridge, the super high-rise Canton Tower, and seismically excited buildings are investigated.

1.5 Outline

This thesis centers around the methodology of harnessing the data structure itself (mostly, sparsity and low-rank structure) of the multi-channel structural responses towards rapid and unsupervised health monitoring and assessment of civil infrastruc-

ture. It is organized as follows:

Part 1 includes Chapter 2 and Chapter 3, which present new output-only non-parametric data-driven modal identification methods based on the unsupervised multivariate blind source separation techniques. Specifically, in a data-driven framework, the signal complexity of the (only available) structural responses and the underlying modal responses are exploited by the complexity pursuit (CP) learning rule, establishing a physical connection between the modal expansion and the BSS model (see a new modal identification CP algorithm in Chapter 2). Chapter 3 further harnesses the sparsity nature of the underlying modal coordinates and addresses the problem of performing data-driven output-only modal identification using limited sensors (less than the mode number). The proposed sparse component analysis (SCA) based method interprets the modal expansion in a new perspective of sparse representation and clustering, allowing fairly intuitive and efficient output-only modal identification.

Part 2 includes Chapter 4, Chapter 5, and Chapter 6, developing a data-driven multi-scale (global and local) damage detection framework. Explicitly, the sparse feature, which is proposed as the salient signature of damage hidden in the (often very noisy) structural data, either vibration responses in global SHM (see the proposed damage identification method via sparse representation in Chapter 4) or close-up images/videos of structures in local non-destructive assessment (see the proposed new local damage assessment framework dynamic imaging in Chapter 6), is intentionally targeted. Chapter 5 presents a novel sparse representation classification method for both locating damage and estimating damage severity; it exploits the underlying sparsity nature of the classification problem itself and establishes an extremely simple data-driven empirical sparse representation methodology, without the need of reference training and setting up parametric classifier model that is computationally

intensive and user-dependent.

Part 3 includes Chapter 7, Chapter 8, and Chapter 9, addressing the emerging large-scale SHM data management problems by harnessing the low-rank structure, intrinsic but implicit, in the multi-channel structural response data. Specifically, Chapter 7 presents a new unsupervised data compression method based on low-rank representation and optimal adaptive multivariate learning rule, removing both intra- and inter- redundancy of the multi-channel structural response data. Chapter 8 further proposes a matrix reshape strategy to guarantee a low-rank representation of any structural response data matrix to achieve most effective compression of very large-scale structural response data. Finally, Chapter 9 develops a new data cleansing algorithm for simultaneously removing both dense noise and gross outliers (naturally as sparse elements) which are ubiquitous in multi-channel structural health monitoring data sets (with an intrinsic low-rank structure).

Chapter 10 concludes the thesis and recommends future work.
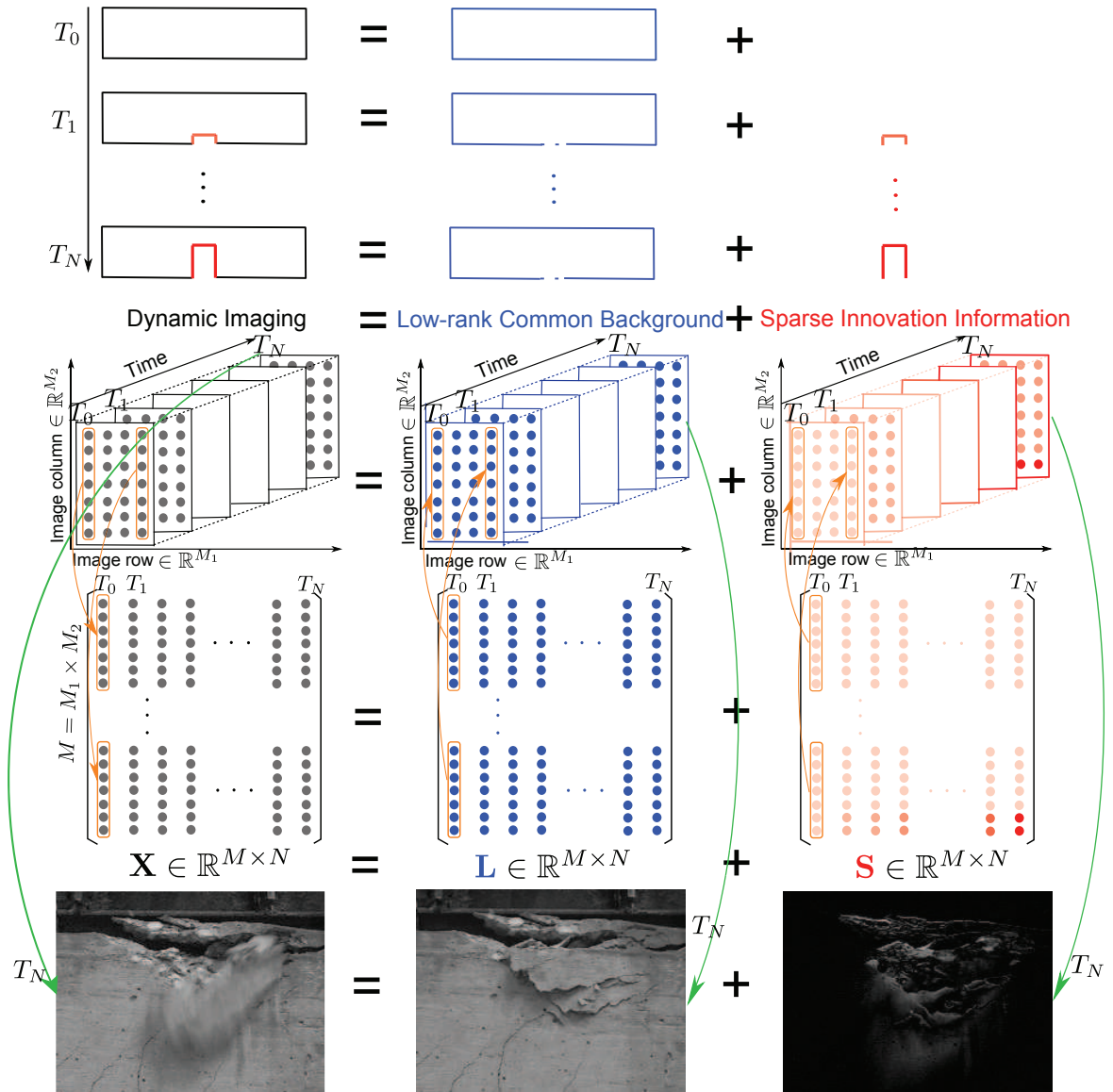
Figure 1.11 : The dynamic imaging of structures paradigm for real-time automated damage detection. The upper plot shows that the multiple frames (black) of the crack developing in the structure (from time T_0 to T_N) can be thought of as a static background (blue) plus the sparse innovation (red) induced by the cracking. The middle plot shows that each temporal frame of resolution $M_1 \times M_2$ is stacked into one column of the data matrix $\mathbf{X} \in \mathbb{R}^{M \times N}$ (each column is of dimension $M = M_1 \times M_2$ rows representing one temporal frame and there are N columns), which is decomposed into a superposition of a low-rank coherent background component $\mathbf{L} \in \mathbb{R}^{M \times N}$ and a sparse innovation component $\mathbf{S} \in \mathbb{R}^{M \times N}$ that indicates the time-evolutionary damage development. Each column of $\mathbf{L} \in \mathbb{R}^{M \times N}$ and $\mathbf{S} \in \mathbb{R}^{M \times N}$ is finally restacked back to the original image dimension, and the bottom plot shows the recovered background component and sparse component at time T_N.

(a)

(b)

Figure 1.12 : **(a)** Interpretation of the blind source separation (BSS) framework. Without knowing the original source signals and their mixing process, BSS techniques such as ICA, SOBI, and CP, assume the sources are independent and simultaneously recover both the source signals and their mixing characteristics using only the measured mixture signals. **(b)** Incorporating the output-only modal identification problem to the BSS model: the structural responses from the coupled structures are linear mixtures (modeshapes) of the independent modal responses, each from the de-coupled SDOF "system" on the modal coordinate (more in Chapter 2 and Chapter 3).

(a)

(b)
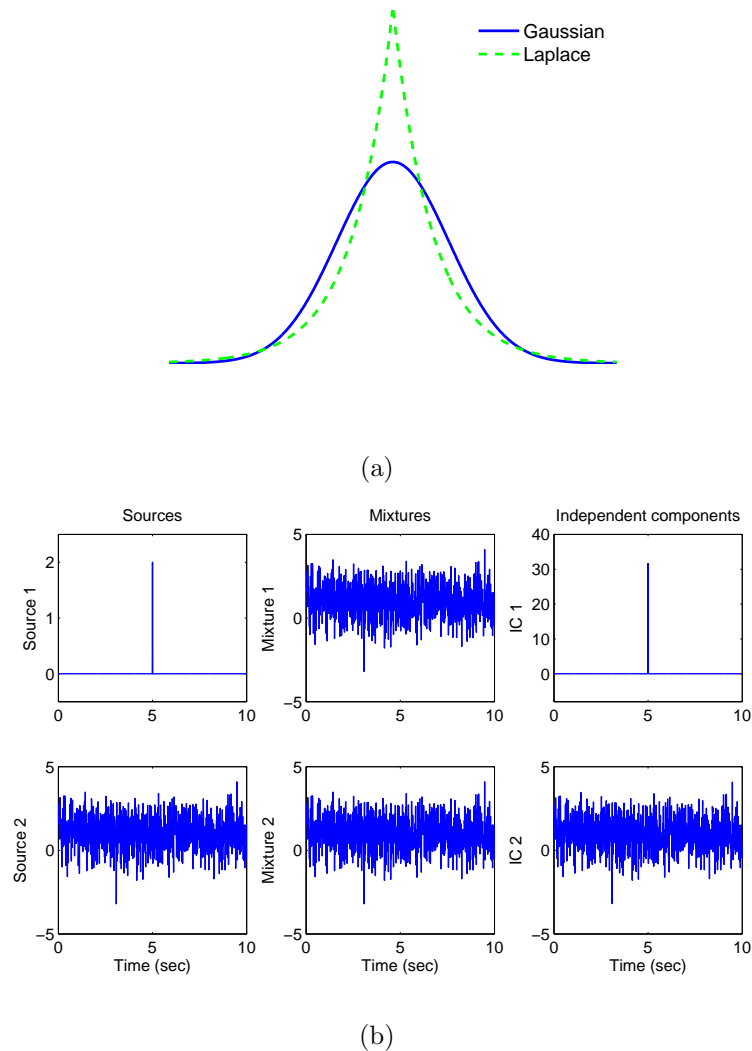
Figure 1.13 : **(a)** The BSS technique ICA seeking most independent (non-Gaussian) source signals leads to extracting signals with spiky distribution (such as Laplace distribution); the theoretical justification is in Chapter 4. **(b)** Two sources (left column), a pulse-like signal ($s_1(t) = 2$, $t = 5$ sec; $s_1(t) = 0$, otherwise) and a Gaussian white noise ($s_2(t) = 1 + randn(t)$), both with a sampling frequency of 100 Hz and a time history of 10 seconds, are mixed by a matrix $\mathbf{A} = \begin{bmatrix} 1 & 1 \\ 0.5 & 1 \end{bmatrix}$, yielding the mixtures (middle column) $x_1(t) = s_1(t) + s_2(t)$, $x_2(t) = 0.5s_1(t) + s_2(t)$. The pulse-like source signal of interest is buried in noisy observed mixtures; however, it is correctly extracted by ICA, with the first IC (IC1) approximating the pulse-like source. In the recovered IC1, the temporal location of the pulse-like feature indicates its spike occurrence instant at 5th second, which agrees with the original pulse-like source. In addition, the recovered mixing matrix also carries the spatial signature of the recovered component that can indicate damage location; More in Chapter 4 and Chapter 7.
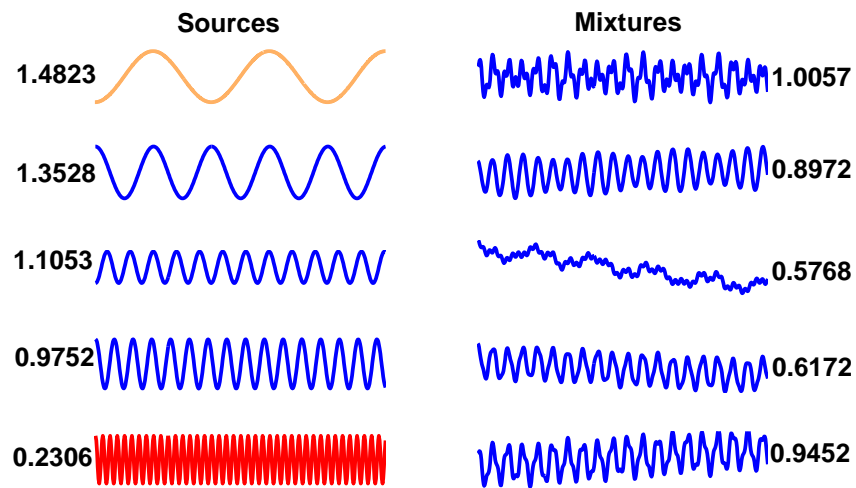
Figure 1.14 : The BSS technique CP extracts the simple components from the mixtures as the source signals. Signal complexity is approximated by temporal predictability: the simplest source signal (yellow line), corresponding to the 1st modal response, is most preditable and has highest predictability value, and so on. More in Chapter 2.
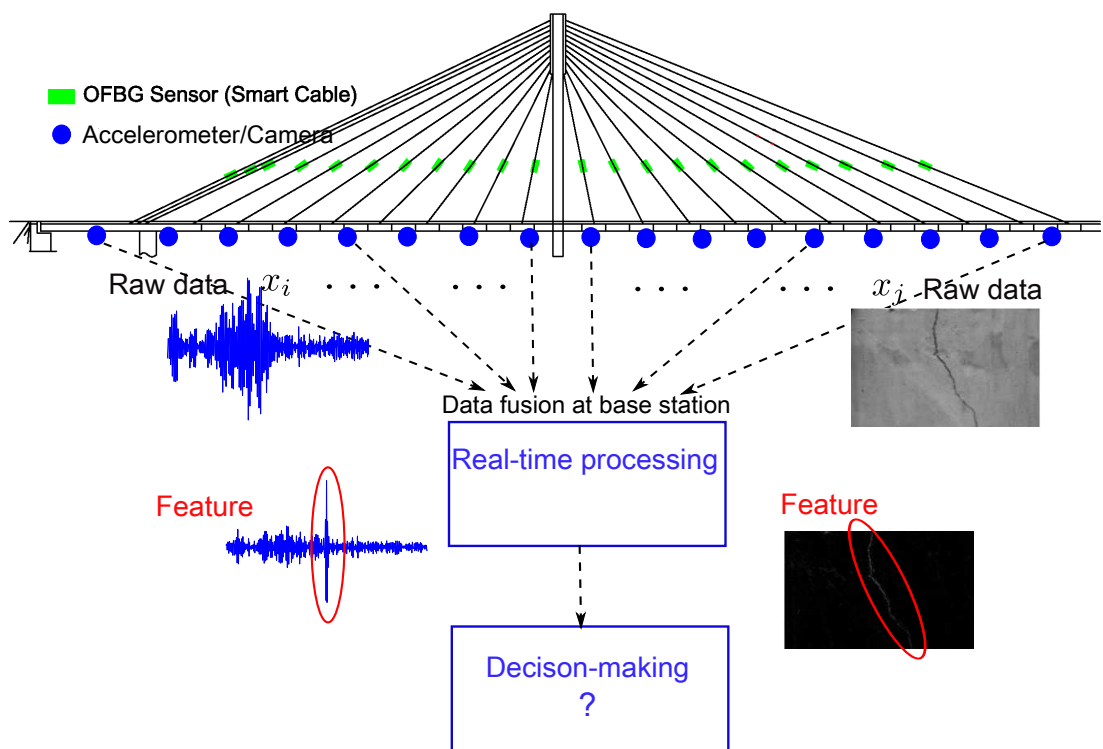
Figure 1.15 : A framework of multi-scale sensor network for health monitoring and assessment of civil structures (e.g., a cable-stayed bridge). The structural data measured from the optical fiber bragg grating (OFBG) sensors and accelerometers or the close-up images/videos from digital cameras are transferred to the base station of the SHM system and then processed to extract the structural and damage features (e.g., sparsity and low-rank structure, the thread of this thesis) for decision-making.

Chapter 2

Output-only Modal Identification by Complexity Pursuit

Rapid identification of structural modal parameters is essential for online model updating, semi-active structural control, and modal-based damage detection. The lack of input or excitation information presents the need to develop output-only modal identification methods, whereas existing output-only modal identification methods (parametric model based or signal processing based) suffer from intensive computation and user involvement burdens. This chapter exploits the signal property itself (complexity) of the available structural responses and the underlying modal responses, establishing a new data-driven non-parametric output-only modal identification method based on a novel blind source separation learning rule complexity pursuit, which can be implemented efficiently and *blindly*.

2.1 Introduction

In the recent years, blind source separation (BSS) has shown prominent capability as a new unsupervised signal processing tool [65], and has been introduced into structural dynamics [6]. Essentially, BSS techniques are able to recover the hidden source signals and their underlying factors using only the observed mixtures; it may thus be suitable to perform output-only modal identification.

Two BSS techniques, independent component analysis (ICA) [65] and second order blind identification (SOBI) [13], have been successfully applied to conduct output-

only modal identification of structures [74][145][146][112][159][93][57][7], where the modal responses are viewed as the targeted sources of the BSS model. Compared to conventional parameter-fitting methods, the BSS based methods are non-parametric with straightforward and efficient implementations, and may thus enjoy wider applications. Several issues on the BSS methods are noted, however. For example, ICA method is restricted to undamped and very lightly-damped structures [74][145][146]; SOBI methods make assumption of stationary sources [112][159][93][57][7] and meet with difficulty in the closely-spaced modes and non-diagonalizable damping cases [93], which are quite common in practical applications of structural dynamics. Besides, the modified SOBI method proposed in [93] only addresses the lightly-complex modes in the non-proportional damping case, where the time-frequency ICA method proposed by the authors [145], which is able to handle highly-damped structures, also shows degradation.

This chapter proposes a new output-only time-domain modal identification method using a novel BSS learning rule termed complexity pursuit (CP) [63][129][130], intending to handle the aforementioned issues in modal identification. The CP learning rule is cast into the modal identification framework using the proposed concept of independent "physical systems" living on the modal coordinates that connects the modal expansion and the BSS model targeted by the CP learning rule, such that when the system responses are fed as mixtures into the BSS model, the CP algorithm can blindly extract the mode matrix and time-domain modal responses, thereby readily estimating the modal parameters of the system.

Numerical simulations, experimental study, and real-world seismically exicted structures examples show that the CP method is able to accurately and efficiently extract modal information (frequency, modeshape, and damping ratio) directly from the

measured system responses, even in closely-spaced mode and highly-damped mode cases, as well as in the approximation of the non-diagonalizable highly-damped complex modes.

2.2 Blind source separation (BSS)

2.2.1 The BSS problem

The linear instantaneous BSS model [65] is expressed as

$$\mathbf{x}(t) = \mathbf{A}\mathbf{s}(t) = \sum_{i=1}^{n} \mathbf{a}_i s_i(t) \tag{2.1}$$

where $\mathbf{x}(t) = [x_1(t), ..., x_m(t)]^T$ is the observed mixture vector with m mixture signals, and $\mathbf{s}(t) = [s_1(t), ..., s_n(t)]^T$ is the latten source vector with n sources; $\mathbf{A}$ is the unknown constant mixing matrix consisting of n columns with its ith column $\mathbf{a}_i$ associated with $s_i(t)$. Assume $m = n$, i.e., $\mathbf{A}$ is square such that $\mathbf{A} \in \mathbb{R}^{n \times n}$ and $\mathbf{a}_i \in \mathbb{R}^n$. Note that the overdetermined case can always be cast into the square one using the preprocessing technique principle component analysis (PCA) to reduce the dimension; whereas the underdetermined case $m < n$, i.e., the available sensors are less than the sources, is not considered in this study. With only $\mathbf{x}(t)$ known, Eq. (2.1) may not be mathematically solved. To alleviate the problem, most BSS techniques exert little assumption that the sources $\mathbf{s}(t)$ are statistically independent at each time instant t; surprisingly, it suffices to recover the sources and the mixing matrix in most practical applications [65].

As the most popular technique to solve the BSS problem, ICA [65] treats the signals as random variables; it estimates the sources by the recovered components which are as non-gaussian as possible, i.e., the temporal structure of signals is ignored and only the information of their (high-order) statistical distribution are used. Although

such a learning rule by ICA is proven powerful and efficient in many applications, it has also been pointed out that ICA may fail when the sources possess significant temporal structures [63][129]. On the other hand, SOBI only uses the second-order statistics of signals and makes assumption of stationary sources and known noise distribution (stationary temporally white) [13], which may hinder its capability in practice.

2.2.2 Stone's theorem for BSS

A novel learning algorithm for the BSS problem, CP [63][129][130], has been proposed to address the drawback of ICA; it explicitly explores the significant temporal structure hidden in the signals and can recover even the Gaussian sources that ICA is incapable of handling. Stone [129] proposed an efficient CP scheme based on a conjecture that exploits the mechanism underwriting the generation of a source signal; that is, possible source in the physical system is generated by the motion of mass over time governed by certain physical law. As such, the observed mixtures must consist of simpler sources, each of which is generated by a different governing law.

Xie et al. [140] theoretically proved that the complexity of any mixture always lies between the simplest and the most complex constituent sources; it is currently termed as Stone's theorem. Based on this basis, the least complex signal extracted from a set of mixtures is guaranteed to be a source signal. Specifically, CP seeks a de-mixing (row) vector $\mathbf{w}_i$ such that the recovered component $y_i(t)$

$$y_i(t) = \mathbf{w}_i \mathbf{x}(t) \tag{2.2}$$

yields least complexity and thus approaches the (simplest) source signal.

2.2.3 Measuring signal complexity by temporal predictability

In statistics, the complexity of a signal, say, y_i (the temporal index t is made implicit), is rigorously measured by Kolmogorov complexity. Given that Kolmogorov complexity is not intuitive and difficult to approximate in practice, Stone [129] provided a simple yet robust complexity measure of a signal, temporal predictability, which is defined by

$$F(y_i) = \log \frac{V(y_i)}{U(y_i)} = \log \frac{\sum\limits_{t=1}^{N} (\overline{y}_i(t) - y_i(t))^2}{\sum\limits_{t=1}^{N} (\hat{y}_i(t) - y_i(t))^2} \tag{2.3}$$

where the long-term predictor $\overline{y}_i(t)$ and short-term predictor $\hat{y}_i(t)$ are given, respectively, by

$$\begin{aligned}
\overline{y}_i(t) &= \lambda_L \overline{y}_i(t-1) + (1 - \lambda_L) y_i(t-1) \quad 0 \le \lambda_L \le 1 \\
\hat{y}_i(t) &= \lambda_S \hat{y}_i(t-1) + (1 - \lambda_S) y_i(t-1) \quad 0 \le \lambda_S \le 1
\end{aligned} \tag{2.4}$$

The parameter λ is defined by the half-life parameter h as

$$\lambda = 2^{-1/h} \tag{2.5}$$

where $h_S = 1$ and h_L is arbitrarily set (say, 900000) as long as $h_L \gg h_S$ [129].

Note that $V(\cdot)$ measures the verall variability [129] of $y_i(t)$, described by the prediction error of a long-term moving average $\overline{y}_i(t)$; it generally characterizes the global statistical information of $y_i(t)$. On the other hand, $U(\cdot)$ measures the local smoothness [128] of $y_i(t)$, by exploiting the temporal structure of $y_i(t)$ using a predicting short-term moving average $\hat{y}_i(t)$. Thus, the temporal predictability operator $F(\cdot)$, which is used as the contrast function of CP, explicitly incorporates the statistical and temporal information of $y_i(t)$ by using the ratio of these two terms; it is constrained to search for the most predicted component which possesses small local

variance (smoothness) as compared to its global (long-term) variance. It turns out useful in extracting sources with proper temporal structure.

An example is presented here to illustrate Stone's theorem with the signal complexity measured by temporal predictability $F(\cdot)$. Five zero-mean sinusoids with random variance and different frequencies (Fig. 1.14 and Table 2.1) are used as source signals, which are mixed by a normal-distributed random mixing matrix, yielding five mixtures. The sampling frequency is set at 100 Hz and with a time history of 1000 seconds. The predictability of the sources and mixtures are computed using Eq. (2.3). Due to randomness of the signal variance and mixing matrix, the procedures are repeated 100 times. For illustrations, the result for one run is listed in Table 2.1. Obviously the predictability of all the five mixtures lies between the most predicted source 1 (simplest) and least predictable source 5 (most complex), which exactly follows Stone's theorem. The results from other 99 runs also indicate the validity of Stone's theorem, but they are not presented here.

Another interesting point noted is that lower frequency signal has higher predictability, regardless of signal variance. This result is quite straightforward to understand; for example, a signal with a constant value (zero frequency) is obviously most predictable among others. Also note that the conclusion holds for signals with arbitrary variance, since the predictability measure has naturally incorporated the (global) variance term.

2.2.4 Stone's algorithm performing CP

Incorporate Eq. (2.2) into Eq. (2.3),

$$F(y_i) = F(\mathbf{w}_i, \mathbf{x}) = \log \frac{V(\mathbf{w}_i, \mathbf{x})}{U(\mathbf{w}_i, \mathbf{x})} = \log \frac{\mathbf{w}_i \overline{\mathbf{R}} \mathbf{w}_i^T}{\mathbf{w}_i \hat{\mathbf{R}} \mathbf{w}_i^T} \tag{2.6}$$

Table 2.1 : Predictability of the sources and mixtures.

Source	Frequency	Predictability	Mixture	Predictability
1	0.1	1.4823	1	1.0057
2	1	1.3528	2	0.8972
3	π	1.1053	3	0.5768
4	$\sqrt{15}$	0.9752	4	0.6172
5	10	0.2306	5	0.9452

where $\overline{\mathbf{R}}$ and $\hat{\mathbf{R}}$ are the $n \times n$ long-term and short-term covariance matrix between the mixtures, respectively; their elements are defined as

$$
\begin{aligned}
\overline{r}_{ij} &= \sum_{t=1}^{N} (x_i(t) - \overline{x}_i(t))(x_j(t) - \overline{x}_j(t)) \\
\hat{r}_{ij} &= \sum_{t=1}^{N} (x_i(t) - \hat{x}_i(t))(x_j(t) - \hat{x}_j(t))
\end{aligned}
\tag{2.7}
$$

The covariance matrices can be computed by fast convolution operations [17][129]. Therefore, given a set of mixtures $\mathbf{x}(t)$, the CP learning rule is formulated to search for the de-mixing vector $\mathbf{w}_i$ which maximizes the temporal predictability contrast function $\mathrm{F}(\cdot)$; this can be solved by the classic gradient ascent technique as described in the following.

Following Eq. (2.6), the derivative of F with respect to $\mathbf{w}_i$ is

$$
\nabla_{\mathbf{w}_i} \mathrm{F} = \frac{2\mathbf{w}_i}{V_i}\overline{\mathbf{R}} - \frac{2\mathbf{w}_i}{U_i}\hat{\mathbf{R}}
\tag{2.8}
$$

By iteratively updating $\mathbf{w}_i$, a maximum of F is guaranteed to be found; the extracted component $y_i = \mathbf{w}_i \mathbf{x}$ with maximum temporal predictability is the least complex signal, and thus approaches the simplest source hidden in the mixtures, according to Stone's theorem in the CP learning rule.

Restricted to Stone's theorem, however, only the simplest source can be extracted by maximizing the temporal predictability using the gradient ascent technique. Fortunately, such ambiguity can be easily resolved by the deflation scheme. Thereby, the sources can be subsequently extracted: after one source (the currently simplest one) is extracted, it is "removed" from the mixtures using a Gram-Schmidt de-correlation technique [129]; the second simplest source then becomes the simplest one in the remaining mixtures and can thus be extracted by CP, and so on. Stone [129] proposed a more elegant algorithm that can efficiently extract all the hidden sources simultaneously, described as follows.

The gradient of F reaches zero in the solution, where

$$\nabla_{\mathbf{w}_i} F = \frac{2\mathbf{w}_i}{V_i}\overline{\mathbf{R}} - \frac{2\mathbf{w}_i}{U_i}\hat{\mathbf{R}} = 0 \tag{2.9}$$

Rewriting as

$$\mathbf{w}_i\overline{\mathbf{R}} = \frac{V_i}{U_i}\mathbf{w}_i\hat{\mathbf{R}} \tag{2.10}$$

yields a well-defined generalized eigenproblem [17][129]; the solution for $\mathbf{w}_i$ can thus be obtained as the eigenvector of the matrix $\hat{\mathbf{R}}^{-1}\overline{\mathbf{R}}$, with the eigenvalue $\gamma_i = V_i/U_i$. The sources can then be efficiently extracted simultaneously by

$$\mathbf{s}(t) = \mathbf{y}(t) = \mathbf{W}\mathbf{x}(t) \tag{2.11}$$

where the eigenvector matrix $\mathbf{W}$, with $\mathbf{w}_i$ as its ith row, is the target de-mixing matrix such that $\mathbf{A} = \mathbf{W}^{-1}$, and $\mathbf{y}(t) = [y_1(t), ..., y_n(t)]^T$ is the recovered component vector which approaches the source vector $\mathbf{s}(t)$.

It should be mentioned that $\mathbf{W}$ (also $\mathbf{A}$) is real-valued, since both $\overline{\mathbf{R}}$ and $\hat{\mathbf{R}}$ are symmetric. However, it does not undermine the capability of the CP algorithm, which provides excellent performance in identifying modal information of structures

even with complex modes, detailed in later sections. Also note that CP and other BSS methods are inherently incapable of identifying the order (sequence) and the variance of the sources and the mixing matrix [65]; yet this turns out trivial in modal identification, as will be discussed in section 2.3.2.

2.3   Complexity pursuit on modal coordinates

The CP learning rule lays its foundation on the observation that statistically independent sources hidden in the observed mixtures generally originate from the motion of mass over time, each is independently governed by some physical law. It is particularly suitable to describe system motions and can be cast into the modal identification framework.

2.3.1   "Physical systems" on modal coordinates

For a linear time-invariant system, its equation of motion (EOM) is

$$\mathbf{M}\ddot{\mathbf{x}}(t) + \mathbf{C}\dot{\mathbf{x}}(t) + \mathbf{K}\mathbf{x}(t) = \mathbf{f}(t) \tag{2.12}$$

where $\mathbf{M}$, $\mathbf{C}$, and $\mathbf{K}$ are constant mass, diagonalizable damping, and stiffness matrices, respectively, and are real-valued and symmetric; $\mathbf{x}(t) = [x_1(t), ..., x_n(t)]^T$ is the system response (displacement) vector and $\mathbf{f}(t)$ is the external force vector.

Feeding the observed system responses $\mathbf{x}(t)$ as mixtures into the BSS model with the CP learning rule, $\mathbf{x}(t)$ must (linearly) consist of simple source signals independently driven by some physical law. Such a viewpoint coincides with the modal identification issue, which expands the coupled system responses $\mathbf{x}(t)$ as linear combinations of the decoupled modal responses, similar to the BSS model Eq. (2.1),

$$\mathbf{x}(t) = \mathbf{\Phi}\mathbf{q}(t) = \sum_{i=1}^{n} \boldsymbol{\varphi}_i q_i(t) \tag{2.13}$$

where $\mathbf{\Phi} \in \mathbb{R}^{n \times n}$ is the normal vibration mode basis matrix with its ith column (modeshape) associated with the ith modal response $q_i(t)$ in the modal response vector $\mathbf{q}(t) = [q_1(t), ..., q_n(t)]^T$, which can be recovered by

$$\mathbf{q}(t) = \mathbf{\Phi}^{-1}\mathbf{x}(t) \tag{2.14}$$

The main virtue of using modal expansion to characterize the motion of system (2.12) is that the vibration mode matrix provides a complete basis set for the space spanned by the linear system Eq. (2.12) and is thus able to decouple the system Eq. (2.12). Substituting Eq. (2.13) into Eq. (2.12) and pre-multiplying both sides of Eq. (2.12) by $\mathbf{\Phi}^T$,

$$\mathbf{\Phi}^T\mathbf{M}\mathbf{\Phi}\ddot{\mathbf{q}}(t) + \mathbf{\Phi}^T\mathbf{C}\mathbf{\Phi}\dot{\mathbf{q}}(t) + \mathbf{\Phi}^T\mathbf{K}\mathbf{\Phi}\mathbf{q}(t) = \mathbf{\Phi}^T\mathbf{f}(t) \tag{2.15}$$

yielding

$$\mathbf{\Phi}^T\mathbf{M}\mathbf{\Phi}\ddot{\mathbf{q}}(t) + \mathbf{\Phi}^T\mathbf{C}\mathbf{\Phi}\dot{\mathbf{q}}(t) + \mathbf{\Phi}^T\mathbf{K}\mathbf{\Phi}\mathbf{q}(t) = \mathbf{\Phi}^T\mathbf{f}(t) \tag{2.16}$$

where $\mathbf{M}^*$, $\mathbf{C}^*$, and $\mathbf{K}^*$ are, respectively, the diagonal real-valued modal mass, damping, and stiffness matrices; $\mathbf{f}^*(t)$ is the modal force vector. The n-DOF system (12) is thus decoupled into n single-degree-of-freedom (SDOF) systems, each motion $q_i(t)$ (at the ith mode, $i = 1, ..., n$) is governed by

$$m_i^*\ddot{q}_i(t) + c_i^*\dot{q}_i(t) + k_i^*q_i(t) = f_i^*(t) \tag{2.17}$$

whose damping ratio and resonant (damped) frequency are $\zeta_i = c_i^*/2\sqrt{m_i^*k_i^*}$ and $\omega_{di} = \omega_i\sqrt{1 - \zeta_i^2} = \sqrt{(1 - \zeta_i^2)k_i^*/m_i^*}$ (ω_i is the natural frequency of the ith mode), respectively. The fundamental idea of the proposed CP method lies in the observation that the "physical system" Eq. (2.17) underwrites the motion of the ith modal mass over time (i.e., the decoupled SDOF system motion on the ith modal coordinate $q_i(t)$);

the generation mechanism of this modal response well matches Stone's theorem such that it can be viewed as the constituent source targeted by the CP learning rule, and the mode matrix $\boldsymbol{\Phi}$ combining n modal responses corresponds to the mixing matrix of the CP based BSS model.

2.3.2 CP for modal identification

With the connection established between the modal responses (and the mode matrix) and constituent sources (and the mixing matrix) in the CP learning rule through the "physical systems" living on the modal coordinates, the only requirement is that modal responses be statistically independent, which corresponds to the general assumption by most BSS techniques (e.g., ICA, SOBI, CP, etc).

It has been shown in Ref. [74] that modal responses can be viewed as statistically independent sources if their oscillating frequencies are incommensurable (e.g., the ratio between two frequencies is irrational). A generalization of this conclusion is proposed in the CP framework that, if the "physical systems" on modal coordinates have incommensurable inherent resonant frequencies (i.e., ω_i and ω_j are incommensurable for any $i, j = 1, ..., n, i \neq j$), they then function as statistically independent systems, generating independent modal responses that dominate the system responses in respond to the initial conditions (e.g., impact force in free vibration) or random excitation (in ambient vibration), or others provided that they are not monotone (or narrow-band) harmonic force. Such assumptions are naturally satisfied in the modal identification issue in practice. On the one hand, most systems in practice have incommensurable resonant frequencies. On the other hand, two fundamental excitation types, namely impact excitation (free vibration) and random excitation (e.g., white noise), are expected to induce the modal responses (i.e., those vibrating at the res-

onant frequencies) that dominate the system responses, which may additionally be accompanied, though, by other non-resonant vibrations and measurement noise in practice. Therefore, in most practical applications, the CP method guarantees to extract modal responses directly from the system responses in both free and ambient vibrations, regardless of the level of damping and the topology of the modes (e.g., whether separated or close-spaced).

In free vibration $\mathbf{f}(t) = \mathbf{0}$, modal responses are exponentially decaying sinusoids, and the motion of the ith modal mass governed by Eq. (2.18) can be written as

$$q_i(t) = u_i \mathrm{e}^{-\zeta_i \omega_i t} \cos(\omega_{di} t + \theta_i) \tag{2.18}$$

and the system responses are linear combinations of these modal responses, expressed as

$$\mathbf{x}(t) = \sum_{i=1}^{n} \boldsymbol{\varphi}_i q_i(t) = \sum_{i=1}^{n} \boldsymbol{\varphi}_i u_i \mathrm{e}^{-\zeta_i \omega_i t} \cos(\omega_{di} t + \theta_i) \tag{2.19}$$

where u_i and θ_i are some constants determined by initial conditions.

In random excitation, the resonant vibrations (modal responses) dominate the system responses [74]. Compared to the free vibration of the decoupled SDOF in form of exponentially decaying sinusoid, the random vibration at the ith mode is characterized by an envelope function $e_i(t)$, randomly modulating the exponentially decaying sinusoid,

$$q_i(t) \cong e_i(t) u_i \mathrm{e}^{-\zeta_i \omega_i t} \cos(\omega_{di} t + \theta_i) \tag{2.20}$$

and the system responses are written as

$$\mathbf{x}(t) = \sum_{i=1}^{n} \boldsymbol{\varphi}_i q_i(t) \cong \sum_{i=1}^{n} \boldsymbol{\varphi}_i e_i(t) u_i \mathrm{e}^{-\zeta_i \omega_i t} \cos(\omega_{di} t + \theta_i) \tag{2.21}$$

Note that the random excitation need not to be white-noise type (although this is one of the ideal situations) as assumed by a few traditional modal identification

methods (e.g., NExT); the CP method holds validity as long as the excited modal responses dominate the system responses, since the formulations of the output-only CP method as per Eq. (2.12) to (2.21) assumes no knowledge with respect to the explicit distribution of the excitation. Also, the formulations use the displacement as the system responses, yet they can also apply to other types of system responses (e.g., velocity, acceleration, or strain).

In the case of non-diagonalizable damping (damping matrix may not be diagonalized by the normal mode matrix), Eq. (2.12) may not be directly decoupled by $\mathbf{\Phi}$. Still, the system (2.12) can be decoupled into (2.17) in the state-space by the vibration mode matrix $\mathbf{\Phi}_c$ which is complex-valued in such a case, as well as the modal responses $\mathbf{q}_c(t)$. Besides, the inherent resonant frequency and damping property of the "physical system" on the modal coordinate remain invariant, such that the validity of the proposed CP algorithm for modal identification holds. The formulations of modal responses and system responses in this case are analogous to those of proportional damping as per Eq. (2.18) to (2.21)), and not presented herein.

Therefore, using Stone's CP algorithm based on temporal predictability as detailed above, the time-domain modal responses $\mathbf{q}(t)$, which are the constituent sources hidden in the system motion mixtures $\mathbf{x}(t)$, can be efficiently extracted by CP simultaneously,

$$\tilde{\mathbf{q}}(t) = \mathbf{s}(t) = \mathbf{W}\mathbf{x}(t) \tag{2.22}$$

and the vibration mode matrix can be estimated by

$$\tilde{\mathbf{\Phi}} = \mathbf{W}^{-1} \tag{2.23}$$

The frequency and damping ratio can be readily computed from the recovered time-domain modal response $\tilde{\mathbf{q}}(t)$ using Fourier transform (FT) and logarithm-decrement

technique (LT), respectively.

As mentioned at the end of Section 2.2.2, CP and other BSS methods may not recover the exact order and variance of the modal responses and their associated modeshapes (the columns of the mixing matrix). This is easily resolved, however: the mode order can be rearranged according the frequency values, e.g., the recovered modal response (as well as its associated modeshape vector) with smallest frequency is recognized as the 1st mode, and so on. Also, the frequency and damping ratio are not dependent on the variance of the modal response, and only the directions of the recovered modeshape vectors are needed to decouple the system responses [145].

2.4   Numerical simulations

To validate the proposed CP modal identification method, numerical simulations are conducted on a three-DOF linear time-invariant spring-mass damped model (Fig. 2.1) (a 12-DOF system example is presented in Section 2.4.5).

Different system parameters are set to address several issues in modal identification, namely well-separated modes, closely-spaced modes, and complex modes, respectively, in both lightly- and highly- damped system. In each case, free vibration and random vibrations are studied, respectively. Both stationary and non-stationary random vibrations are considered. Stationary random excitation uses Gaussian white noise (GWN), whereas non-stationary random excitation is generated by modulating the GWN with an exponentially decaying function at a constant rate. Newmark-Beta algorithm is used to obtain the time histories of the system responses with a sampling frequency of 10 Hz.

In the following, the procedures of the CP method are carried out on the obtained system responses. The long-term and short-term half-life parameters are set to be
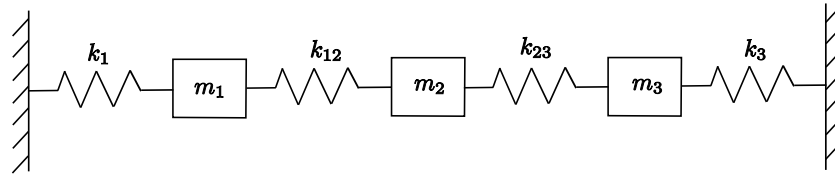
Figure 2.1 : The 3-DOF linear spring-mass damped system

$h_L = 900000$ and $h_S = 1$, respectively, where $h_S = 1$ is a fixed setting and $h_L = 900000$ is arbitrary as long as $h_L \gg h_S$ [129] (these parameters remain unchanged for all the examples). In the following, the long-term and short-term covariance matrices are computed using the fast convolution filter. Eigen-decomposition is then conducted on the obtained covariance matrices, yielding the eigenvector matrix as the de-mixing matrix. The vibration mode matrix is estimated by Eq. (2.23), and the time-domain modal responses are recovered by Eq. (2.22) such that the frequency and damping ratio can be calculated in a straightforward way by FT and LT [96], respectively. The correlation between the estimated mode $\tilde{\varphi}_i$ and the theoretical mode φ_i is evaluated by the modal assurance criterion (MAC), defined as

$$\text{MAC}(\tilde{\varphi}_i, \varphi_i) = \frac{(\tilde{\varphi}_i^T \cdot \varphi_i)^2}{(\tilde{\varphi}_i^T \cdot \tilde{\varphi}_i)(\varphi_i^T \cdot \varphi_i)} \tag{2.24}$$

ranging from 0 to 1, where 0 means no correlation and 1 indicates perfect correlation. Note that estimation of the damping ratio in random vibration needs additional information with respect to the system or preprocessing technique (e.g., random decrement or NExT), and this is not conducted in this study.

2.4.1 Proportional damping

For convenient comparison, the following parameters are borrowed from Kerschen et al. [74] and set to the system (Fig. 2.1) for the proportional damping case,

$$\mathbf{M} = \begin{bmatrix} 2 & 0 & 0 \\ 0 & 1 & 0 \\ 0 & 0 & 3 \end{bmatrix} \qquad \mathbf{K} = \begin{bmatrix} 2 & -1 & 0 \\ -1 & 2 & -1 \\ 0 & -1 & 2 \end{bmatrix} \qquad \mathbf{C} = \alpha\mathbf{M} = \alpha \begin{bmatrix} 2 & 0 & 0 \\ 0 & 1 & 0 \\ 0 & 0 & 3 \end{bmatrix} \quad (2.25)$$

Three values $\alpha = 0.01$, 0.05 , and 0.13 are considered corresponding to different damping levels. In free vibration, $\mathbf{f}(t) = \mathbf{0}$, with initial condition $\mathbf{x}(0) = \begin{bmatrix} 0 & 1 & 0 \end{bmatrix}^T$ and $\dot{\mathbf{x}}(0) = \begin{bmatrix} 0 & 0 & 1 \end{bmatrix}^T$. For random vibration, stationary GWN and non-stationary WN are used to excite the system at the 2nd and 3rd DOFs, respectively.

The identified results by the CP method are compared with the theoretical results as shown in Table 2.2 and 2.3. Clearly the identified frequency, damping ratio, and vibration modes are in excellent agreement with those theoretical results, regardless of the levels of damping and excitation types. As shown in Fig. 2.2, the MAC values of the identification ($\alpha = 0.01$) remain very high with different sample (window) lengths of the time histories of the system responses: all are above 0.99 (except when the sample length reduces to 10 seconds, but it has been less than the period of the 1st mode $1/0.0895 = 11.1732$ seconds); it indicates that the accuracy of the CP method is insensitive to the sample length.

Also presented in Fig. 2.3 to Fig. 2.5 are the case of $\alpha = 0.05$ with system responses in free vibration, and the recovered modal responses in free vibration, stationary random vibration, and non-stationary vibration, respectively, as well as their power spectral density (PSD). To show the original results by CP, the sequence of the recovered modal responses depicted within each case is not rearranged (e.g., in

Fig. 2.4, Modal Response 1 merely means the first recovered one by CP, not implying Mode #1), but this trivial issue can be easily solved by what is mentioned at the end of Section 2.3.2. It is observed that the multi-component system responses are well separated into monotone modal responses. In free vibration, the recovered modal responses match the desired exponentially decaying sinusoids. Note that ICA fails when $\alpha > 0.01$, as shown in Ref. [74].

2.4.2   Noise effects

To investigate the robustness of the CP method, zero-mean GWN is added to the system responses (Section 2.4.1) with a 10% (with respect to the original signal) RMS (root-mean-square operator of a signal) noise level. The procedures of the CP method are then performed on the noise-contaminated system responses. For conciseness, only the identification results of $\alpha = 0.05$ in free vibration is given in Table 2.4. It is seen that the identification results are rarely affected by the noisy data (other cases with different damping levels and excitation types also indicate similar accuracy), i.e., the CP method is robust in the noisy environment also.

2.4.3   Closely-spaced modes

This section considers the closely-spaced mode case. The model with diagonalizable damping matrix in McNeill et al. [93] is modified to yield a similar form of the model in proportional damping matrix, as

$$
\mathbf{M} = \begin{bmatrix} 1 & 0 & 0 \\ 0 & 2 & 0 \\ 0 & 0 & 1 \end{bmatrix} \qquad \mathbf{K} = \begin{bmatrix} 5 & -1 & 0 \\ -1 & 4 & -3 \\ 0 & -3 & 3.5 \end{bmatrix} \qquad \mathbf{C} = \alpha \mathbf{M} = \alpha \begin{bmatrix} 1 & 0 & 0 \\ 0 & 2 & 0 \\ 0 & 0 & 1 \end{bmatrix} \tag{2.26}
$$

All the parameters are set the same as the above sections, except that the initial

Table 2.2 : Results of free vibration (proportional damping well-separated modes)

		Frequency (Hz)			Damping ratio (%)		
Mode		1	2	3	1	2	3
$\alpha = 0.01$	Exact	0.0895	0.1458	0.2522	0.8887	0.5460	0.3155
	CP	0.0879	0.1465	0.2539	0.8822	0.5691	0.3116
$\alpha = 0.05$	Exact	0.0895	0.1458	0.2522	4.4437	2.7299	1.5775
	CP	0.0879	0.1465	0.2539	4.4493	2.8233	1.5248
$\alpha = 0.13$	Exact	0.0895	0.1458	0.2522	11.5537	7.0977	4.1015
	CP	0.0879	0.1465	0.2539	11.4167	7.3448	3.9240

Table 2.3 : MAC results in proportional damping cases (well-separated modes)

α	Free vibration			Stationary GWN			Non-Stat. GWN		
Mode	1	2	3	1	2	3	1	2	3
0.01	0.9999	0.9999	0.9998	1.0000	0.9998	0.9998	1.0000	0.9987	1.0000
0.05	0.9990	0.9993	0.9975	1.0000	0.9962	0.9998	0.9998	0.9977	0.9981
0.13	0.9929	0.9816	0.9876	0.9990	0.9916	0.9996	0.9996	0.9977	0.9873

Table 2.4 : CP Identification in noisy free-vibration (10% RMS noise, $\alpha = 0.05$)

	Frequency (Hz)		Damping ratio (%)		MAC
Mode	Theoretical	Identified	Theoretical	Identified	
1	0.0895	0.0879	4.4437	4.2058	0.9997
2	0.1458	0.1465	2.7299	2.8200	0.9516
3	0.2522	0.2539	1.5775	1.5454	0.9963
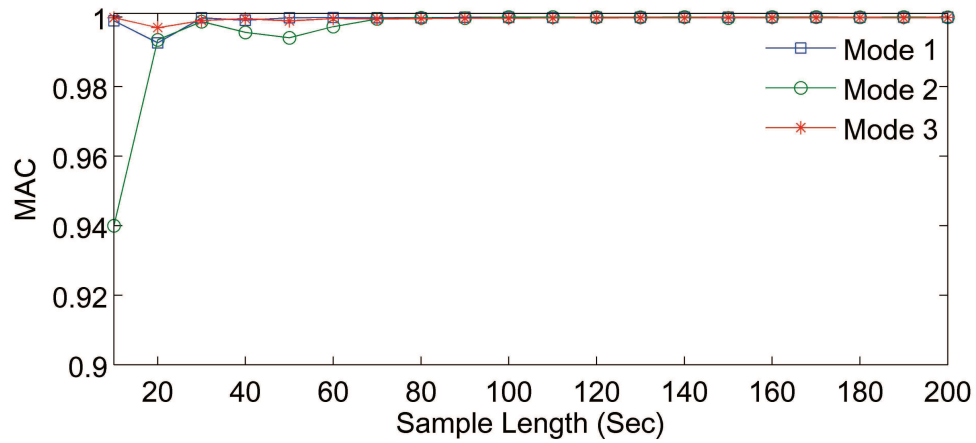
Figure 2.2 : The MAC values from the identification results by CP with different sample lengths of the system responses of the 3-DOF system (proportional damping with well-separated modes, $\alpha = 0.01$).
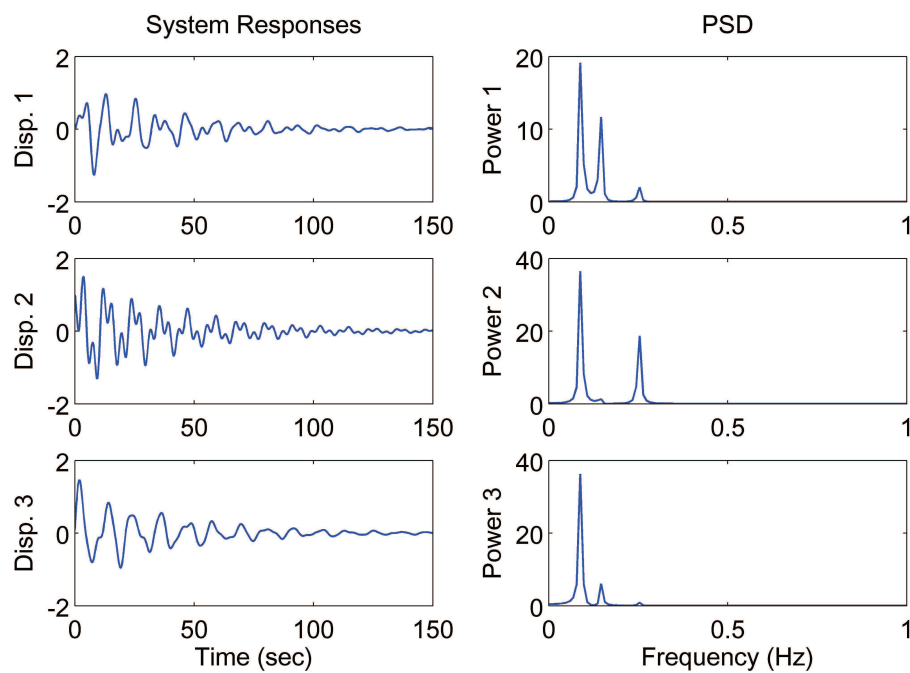
Figure 2.3 : The system responses in free vibration (proportional damping with well-separated modes, $\alpha = 0.05$).
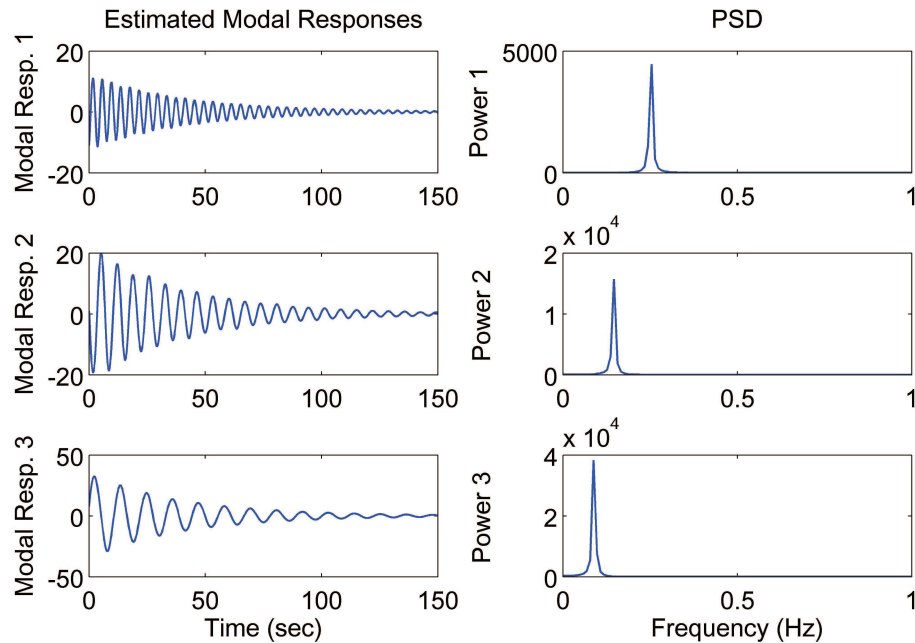
Figure 2.4 : The modal responses recovered by CP in free vibration (proportional damping with well-separated modes, $\alpha = 0.05$).

conditions used in free vibration are $\mathbf{x}(0) = \begin{bmatrix} 0 & 0 & 0 \end{bmatrix}^T$ and $\dot{\mathbf{x}}(0) = \begin{bmatrix} 0 & 0 & 1 \end{bmatrix}^T$. The identification results are shown in Table 2.5 and 2.6, which indicate that the CP method provides fairly accurate modal identification of structures with closely-spaced modes in all cases. Fig. 2.6 to Fig. 2.7 give an example of identifying highly-damped system ($\alpha = 0.13$) with close modes in free vibration. It is shown in Fig. 2.6 that the 2nd and 3rd modes are very closely-spaced and rarely distinguished in the PSD of the system responses; still, they are completely separated by the CP method as shown in Fig. 2.7. On the other hand, as shown in Ref. [93], SOBI is incapable of identifying the close modes of this similar model.
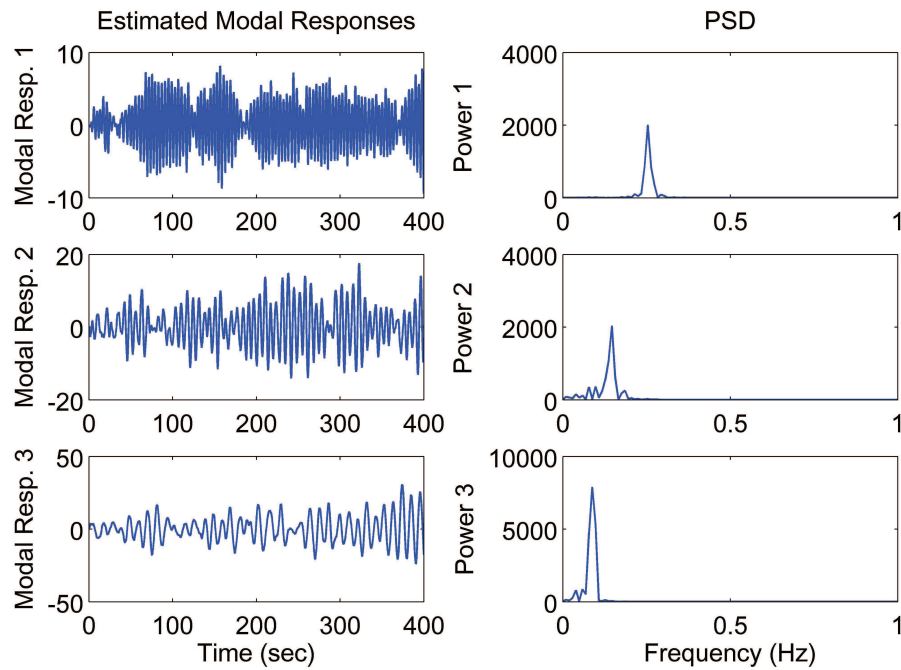
Figure 2.5 : The modal responses recovered by CP in stationary random vibration (proportional damping with well-separated modes, $\alpha = 0.05$).

Table 2.5 : Results of free vibration in closely-spaced modes cases

		Frequency (Hz)			Damping ratio (%)		
Mode		1	2	3	1	2	3
$\alpha = 0.01$	Exact	0.1039	0.3425	0.3713	0.7656	0.2324	0.2143
	CP	0.1074	0.3418	0.3711	0.7667	0.2314	0.2030
$\alpha = 0.05$	Exact	0.1039	0.3425	0.3713	3.8279	1.1618	1.0715
	CP	0.1074	0.3418	0.3711	3.8199	1.1434	1.0151
$\alpha = 0.13$	Exact	0.1039	0.3425	0.3713	9.9526	3.0208	2.7860
	CP	0.1074	0.3418	0.3711	9.9770	2.9906	2.7274

Table 2.6 : MAC results in closely-space mode cases

α	Free vibration			Stationary GWN			Non-Stat. GWN		
Mode	1	2	3	1	2	3	1	2	3
0.01	1.0000	0.9999	0.9998	0.9999	1.0000	0.9996	1.0000	1.0000	0.9990
0.05	1.0000	0.9971	0.9999	0.9999	1.0000	0.9991	1.0000	0.9973	0.9963
0.13	1.0000	0.9735	0.9759	0.9998	0.9999	1.0000	0.9999	0.9765	0.9914
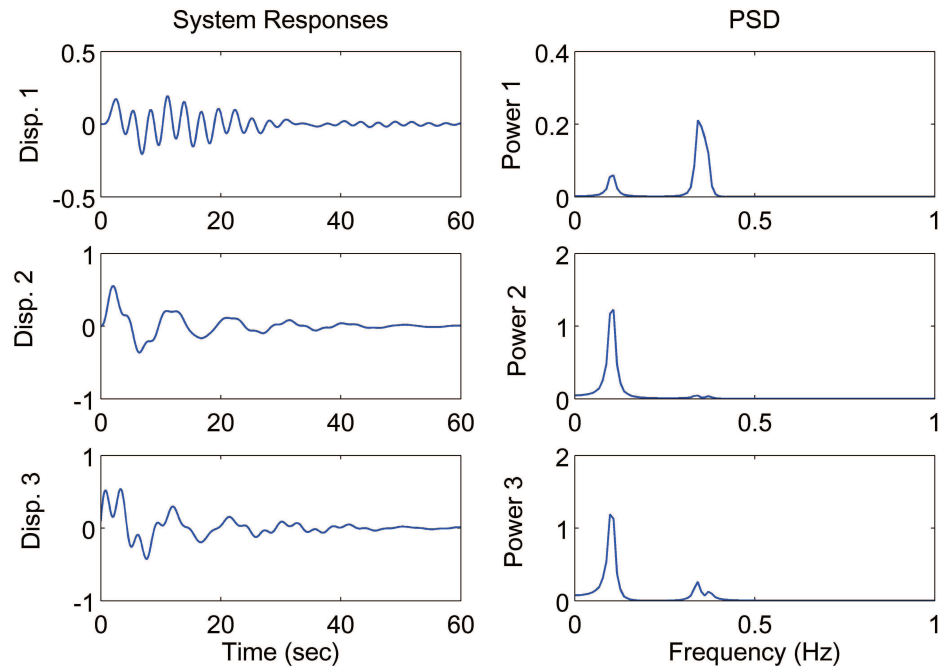
Figure 2.6 : The system responses in free vibration (closely-spaced modes, $\alpha = 0.13$).

2.4.4 Non-diagonalizable high damping

This section investigates a more general situation of non-proportional (non-diagonalizable) damping. The damping matrix of the model from McNeill et al. [93] is slightly mod-
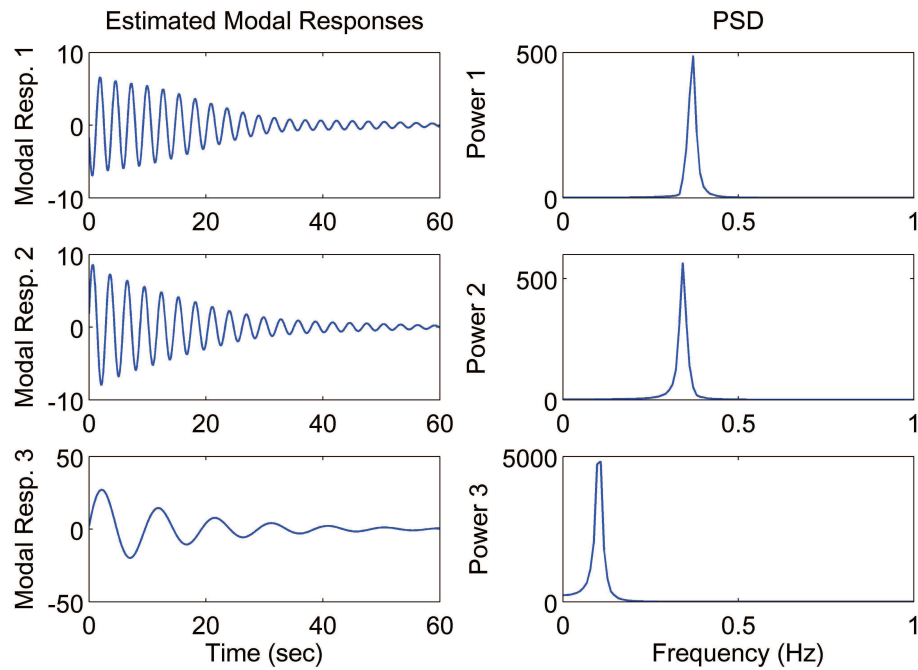
Figure 2.7 : The modal responses recovered by CP in free vibration (closely-spaced modes, $\alpha = 0.13$).

ified to obtain a non-diagonalizable high-damping example as follows.

$$
\mathbf{M} = \begin{bmatrix} 3 & 0 & 0 \\ 0 & 2 & 0 \\ 0 & 0 & 1 \end{bmatrix} \quad \mathbf{K} = \begin{bmatrix} 4 & -2 & 0 \\ -2 & 4 & -2 \\ 0 & -2 & 10 \end{bmatrix} \quad \mathbf{C} = \begin{bmatrix} 0.3856 & 0.2290 & -0.9702 \\ 0.2290 & 0.5080 & -0.0297 \\ -0.9702 & -0.0297 & 0.3241 \end{bmatrix}
$$
(2.27)

Complex modes result in this case. Since the CP method gives real-valued de-mixing matrix, the theoretical complex modes are transformed into real modes using the standard method described in Ref. [93], such that the accuracy of the identified vibration mode matrix (modeshapes) can be evaluated using Eq. (2.24). The identification results are listed on Table 2.7 and 2.8, also shown in Fig. 2.8. It is seen that the identified modal parameters agrees fairly well with those theoretical results, indicating that the CP method suffers little in the presence of the non-proportional

high damping and provides excellent approximation to the complex modes in both free and random vibration. On contrary, it is noticed in Ref. [93] that SOBI loses accuracy even in the light damping case of this non-diagonalizable damped model, and the modified SOBI method only addresses the lightly-complex modes.

Table 2.7 : Identified results of free vibration in non-proportional high damping

Mode	Frequency (Hz) Theoretical	Identified	Damping ratio (%) Theoretical	Identified	MAC
1	0.1343	0.1367	10.8998	10.9694	0.9843
2	0.2454	0.2441	6.8853	6.7217	0.9510
3	0.5094	0.4980	4.8827	4.6758	0.9823

Table 2.8 : MAC results in random vibration (non-proportional high damping)

	Stationary GWN			Non-stationary WN		
Mode	1	2	3	1	2	3
MAC	0.9974	0.9991	0.9894	0.9978	0.9916	0.9892

2.4.5 Identification of a 12-DOF system & comparing to SOBI

To show that the CP method is suitable for large-scale structures with more DOFs, a 12-DOF system (Fig. 2.9) is set up (larger system can also be built), i.e., $m_1 = 2, m_2 = ... = m_{11} = 1, m_{12} = 3, k_1 = k_2 = ... = k_{13} = 1$, and $\mathbf{C} = \alpha \mathbf{M}$ with $\alpha = 0.03$. The first four natural frequencies of the structure are 0.0378, 0.0716, 0.0990, 0.1250 Hz, respectively. Impact or Gaussian white noise excitation is induced at the 6th DOF (mass) and the 200-second system responses are used with a sampling frequency of 10
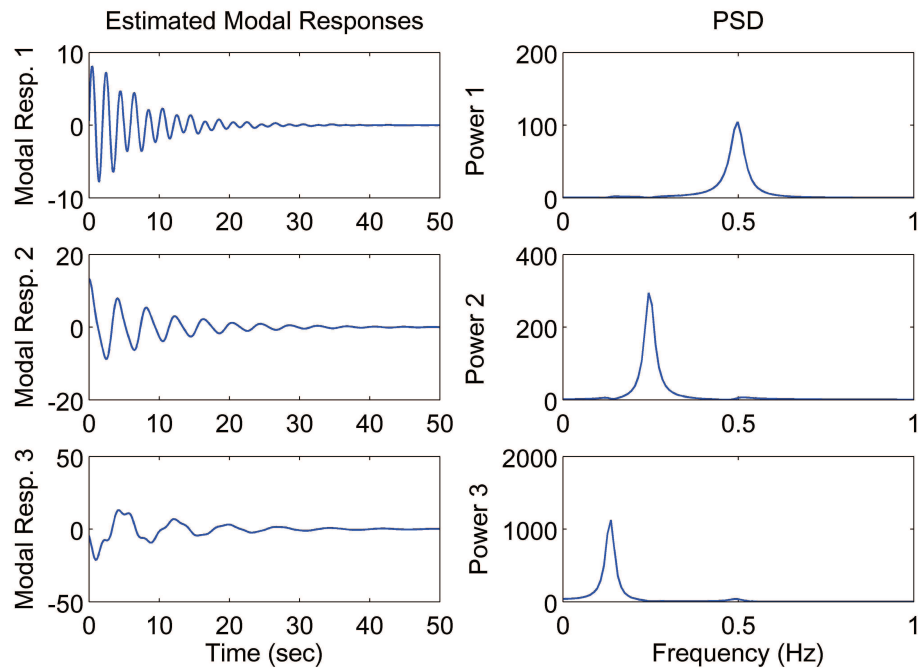
Figure 2.8 : The modal responses recovered by CP in free vibration (non-proportional high damping case).

Hz. Both the CP method and SOBI method are performed directly on the measured system responses.

For the CP method, $h_S = 1$ is a fixed setting, and $h_L \gg h_S$ is required. The MAC results using a wide range of values of h_L between 100 and $900,000$ are presented in Fig. 2.11, as well as the corresponding computational time. For random vibration, the results are averaged over 100 tests.

It is seen both for free or random vibration, the MAC values are very high and the computational time is quite little, both of which remain stable with varying h_L values, indicating that CP efficiently provides reliable modal parameters without adjusting the parameters. Note that the lower MAC of the 11th mode (shown as green star marker in Fig. 2.11) is because it is not well excited, as it is rarely present in the structural responses. The frequency and damping ratio can also be accurately

identified from the simultaneously recovered time-domain modal responses; they are not presented here, however.

Comparisons with SOBI are also conducted on the same set of structural responses, and its performance with different lag parameters is shown in Fig. 2.11. It is seen that SOBI's accuracy depends on the lags, and the computational time increases linearly with increasing lags. Table 2.9 lists some of the MAC results by CP and compared with SOBI method.
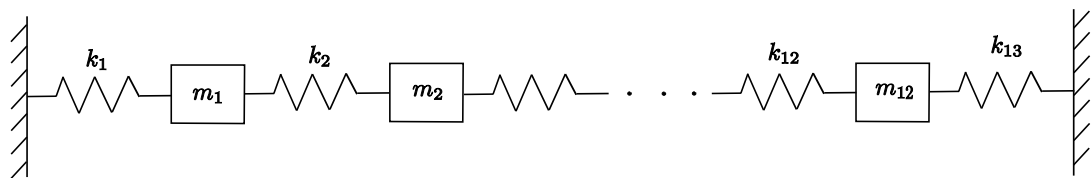
Figure 2.9 : The 12-DOF linear mass-spring damped model

2.4.6   Identification of a distributed-parameter beam

This section considers applying CP to identify a two-dimensional distributed-parameter fixed beam model (Fig. 2.12). The parameters of the beam are set similar with those presented in Kerschen et al. [74]: the Young's module is 200 GPa, the density is 7800 kg/m^2, the cross section dimension is 0.014×0.014 m, the length of the beam is 0.7 m, and the damping matrix is set $\mathbf{C} = 2 \cdot \mathbf{M} + 2 \times 10^{-6} \cdot \mathbf{K}$. The beam is modeled by finite element method, divided into seven elements, and each node has three DOFs: axial, vertical, and rotational, resulting in $n = 3 \times 6 = 18$ DOFs of the structure. The first four natural frequency of the structure are 148.74, 410.38, 806.85, and 1342.12 Hz. A vertical velocity is induced in the 2nd node and the structural responses are computed/recorded only at $m = 6$ (vertical) sensors with a sampling frequency of

Table 2.9 : Identification results of MAC by SOBI and CP of the 12-DOF structure ($h_L = 900,000$).

Mode	Free vibration				Random vibration	
	SOBI (20 lags)	SOBI (50 lags)	SOBI (200 lags)	CP	SOBI (200 lags)	CP
1	1.0000	0.9999	1.0000	1.0000	0.9995	1.0000
2	0.9900	0.9092	0.9935	0.9991	0.8641	0.9822
3	0.9965	0.9840	0.9987	0.9993	0.9718	0.9945
4	0.9926	0.9768	0.9981	0.9993	0.9699	0.9915
5	0.9897	0.9862	0.9982	0.9996	0.9776	0.9882
6	0.9865	0.9918	0.9992	0.9995	0.9843	0.9900
7	0.9708	0.9933	0.9982	0.9987	0.9671	0.9970
8	0.9822	0.9967	0.9993	0.9991	0.9843	0.9847
9	0.9150	0.9778	0.9939	0.9919	0.9098	0.9833
10	0.9891	0.9943	0.9985	0.9987	0.9780	0.9922
11	0.6541	0.6724	0.7988	0.6706	0.5322	0.4130
12	0.9970	0.9981	0.9990	0.9993	0.9839	0.9984
Computational time (sec)	0.0427	0.0731	0.1256	0.0047	0.1684	0.0028

10,000 Hz. The time history is recorded for one second.

CP extracts 6 modes from the structural responses. Table 2.10 shows that the CP modes match the theoretical modeshapes very well. It is seen that SOBI also provides reasonable identification, but the lag parameter affects the accuracy of SOBI. CP yields good accuracy and computational efficiency.

Table 2.10 : MAC results by SOBI and CP of the beam model in free vibration.

Mode	SOBI (20 lags)	SOBI (50 lags)	SOBI (200 lags)	SOBI (900 lags)	CP ($h_L = 900,000$)
1	1.0000	1.0000	1.0000	1.0000	1.0000
2	1.0000	1.0000	0.9999	1.0000	1.0000
3	1.0000	0.9996	0.9994	1.0000	1.0000
4	0.9607	0.7555	0.7836	0.9842	0.9980
5	0.9939	0.9881	0.9809	0.9985	0.9993
6	0.9828	0.9663	0.9160	0.9972	0.9992
Computational time (sec)	0.3891	0.9050	3.4754	15.1780	0.1607

2.5 Experimental verification

A three-story steel frame model (Fig. 2.13(a)) is built to experimentally investigate the capability of the CP modal identification method. The structural model is dominated by the masses on each floor, which are framed by two steel columns. The base of the model is fixed on the shaking table, which is controlled by a feedback control system. Accelerometers are attached on top of the masses to record the system responses. Band-limited white noise excitation is generated at the base by the shaking table, and the measured responses are recorded by the National Instrument data acquisition system. The original sampling frequency is set 5128 Hz.

For more efficient computation, the measured data are down-sampled by a factor of 128, and then the CP method is directly applied on the data without additional preprocessing. The measured system responses and recovered modal responses are de-

picted in Fig. 2.14 to Fig. 2.15, which clearly indicate that the coupled random system responses are completely separated into three mono-component modal responses.

The classic peak-picking (PP) method is also implemented to identify modal information of the system; it uses both the input excitation and output information. In this method, the chirp sinusoid wave is applied to excite the system at the base; besides, one additional accelerometer is attached on the surface of the shaking table to record the input signal.

The identification results are summarized in Table 2.11. The identified frequency in both methods matches fairly well, and the high MAC values in all the three modes indicate high correlation of the mode shapes identified by the two methods (Fig. 2.13(b)). While giving comparable accuracy with the input-output PP method, the CP method needs no input excitation information; such an advantage is attractive in applications when the excitation is not available or extremely difficult to obtain. Besides, the CP method is straightforward to implement with little interactions with the users.

Table 2.11 : Experimental results

Mode	Frequency (Hz)		MAC
	PP	CP	
1	2.550	2.600	1.0000
2	7.330	7.395	0.9993
3	10.460	10.720	0.9997

2.6   Seismic application

The proposed method is also applied on the seismic responses of the USC hospital building (Fig. 2.16(a)) from the Northridge earthquake in 1994. It is a highly-damped (the damping ratio of the 1st mode is as high as 14%) eight-story base-isolated nonlinear system [100][98]. The base and three stories (4th, 6th, and the roof) are embedded with sensors. A segment of the recorded seismic responses in the North-South direction from the latter three sensors (#12, 17, and 21 in Fig. 2.16(a)) are used, which is from 15-30 second, sampled at 100 Hz.

A preliminary observation of the PSD of the system responses in Fig. 2.17 shows that only the first three modes are visible (the 3rd mode is marginally present, though). This is quite common in the seismic responses of structures that the responses in low frequency (lower modes) are usually dominant. On the other hand, it implies that using few sensors may be sufficient to identify the active modes of structures subjected to the seismic excitation, such like this example.

The identified results by the CP method are listed in Table 2.12, as well as the recovered modal responses shown in Fig. 2.18. Note that a 3D analytical model has been previously developed [100] such that analytical results are available as reference for comparison. As can be seen, the results by the CP method satisfactorily match the analytical results in both the frequency and mode shape identification (Fig. 2.16(b)). Compared with the first two identified modeshapes with high MAC values, the lower MAC value in the 3rd mode is primarily because it is not reasonably excited out. This is seen from the PSD of the system responses (Fig. 2.17) that the 3rd mode is rarely present, while the first two modes are quite active. It is on the other hand a generic requirement for output-only methods (even input-output ones) that the modes be reasonably excited out. This is also discussed in the time-frequency ICA

method [145] proposed by the authors, where the identified 3rd modeshape does not quite match the analytical one.

Table 2.12 : Identification of the USC hospital building

	Frequency (Hz)		MAC
Mode	Analytical	CP	
1	0.746	0.768	0.9751
2	1.786	1.907	0.9054
3	3.704	3.941	0.7874

2.7 Summary

This chapter presents a new time-domain output-only modal identification method using the novel BSS learning rule CP by exploiting the signal property itself of the available system responses and the underlying modal responses. Stone's theorem for CP is investigated in detail and found to be particularly suitable for modal identification using the proposed concept of independent "physical systems" on modal coordinates.

The CP method is illustrated with numerical simulations to address modal identification for both proportional damped (well-separated and closely-spaced modes) and non-proportional highly-damped (complex modes) structures in free and random vibration. In all the studied cases, CP method holds accuracy, as well as robustness against noise contamination. In addition, the high-level damping has little influence on the CP method; this is expected as long as the independent "physical systems" on modal coordinates are valid.

The CP method is also applied to an experimental model and a real-world seismic-excited structure, which generally possess complex modes; it provides excellent estimation of the modal information of structures in practice.

Inheriting the virtues of BSS algorithms, the proposed CP method realizes blind identification of structural modal information; it is completely unsupervised, i.e., it needs no input excitation information or any information with respect to the structure. This advantage is evident from the experimental study where the CP method is able to perform reliable output-only identification, as compared to the traditional modal analysis technique which is based on input-output relationship.

The CP method has a straightforward and efficient implementation to perform completely blind identification of modal parameters of a wide range of structures, and it is therefore suitable for on-line identification as well as for off-line applications. As CP assumes a square BSS model, i.e., the sensor number equals that of the active mode number, a method addressing the problem with only limited sensors needs to be further developed, which is the topic of the next chapter.
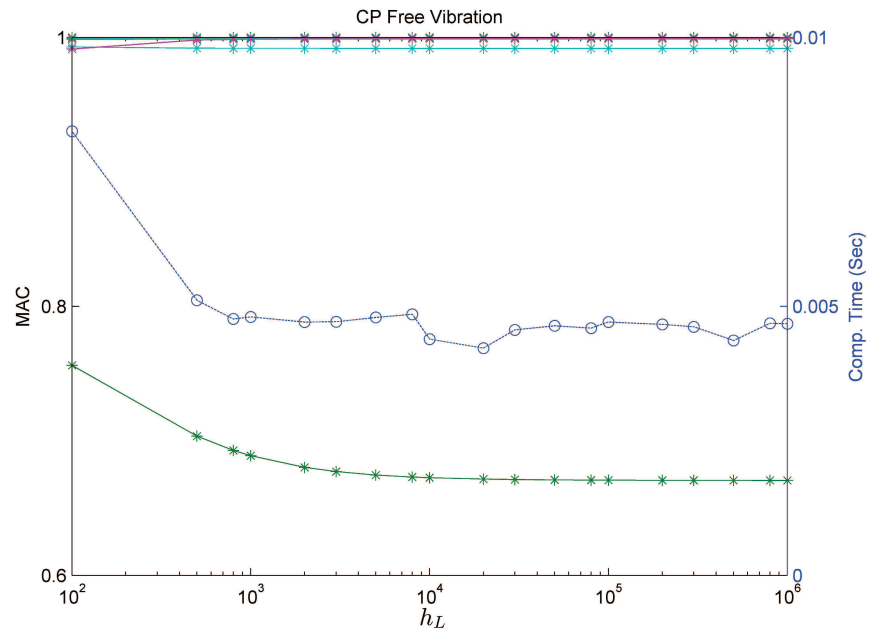
(a)
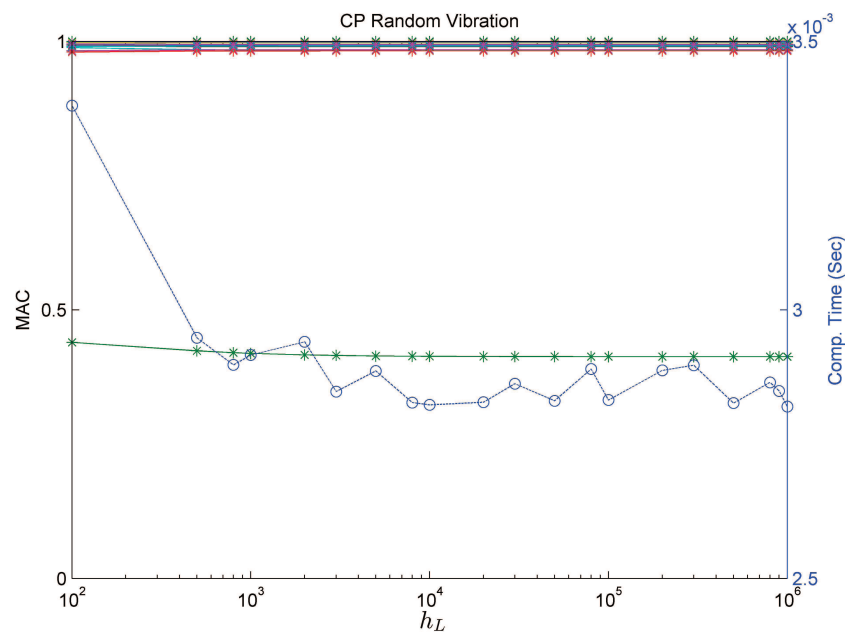
(b)

Figure 2.10 : The CP performance with varying long-term parameter h_L in (a) free vibration and (b) random vibration. (The star markers are the MAC values of 12 modes using the left y-axis and the circle markers are computational time using the right y-axis.)
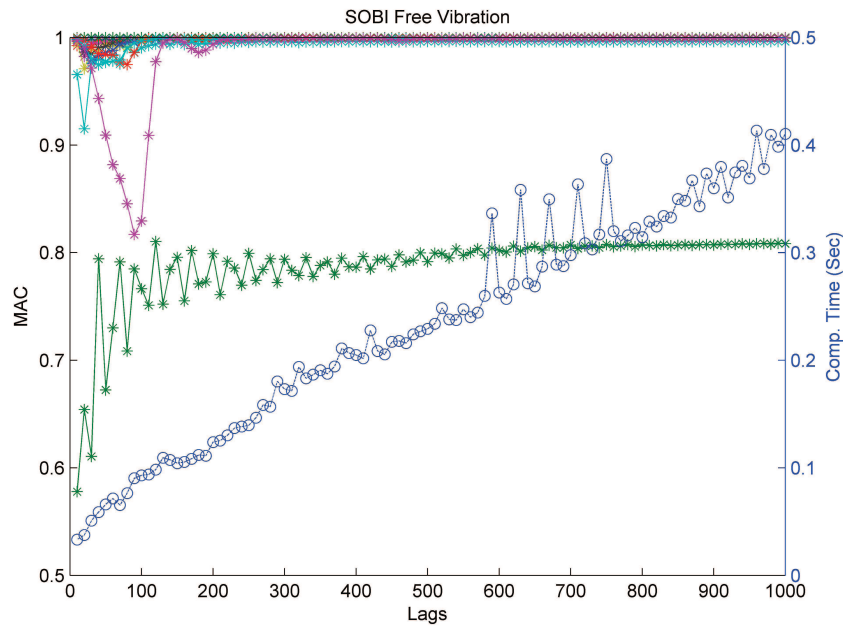
(a)
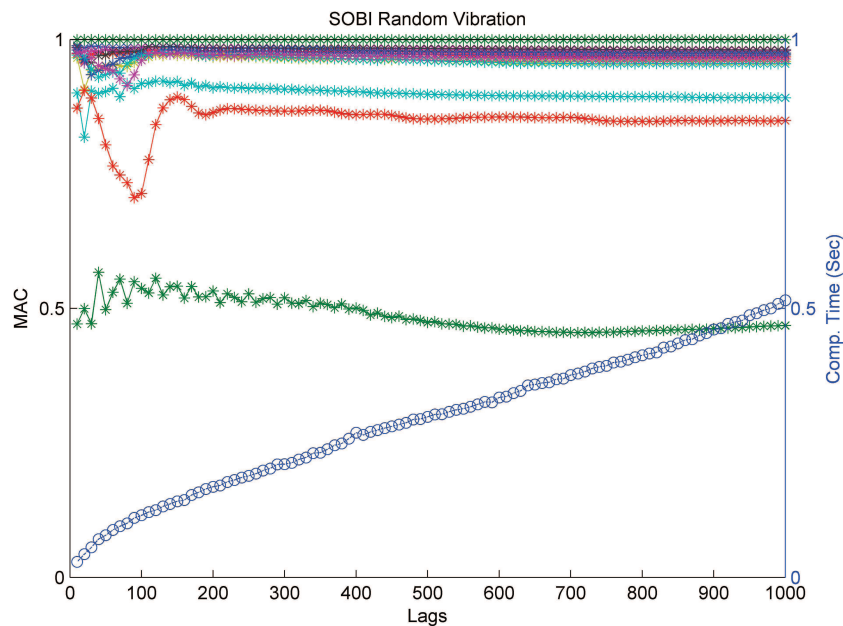
(b)

Figure 2.11 : The SOBI performance with varying lag parameters in (a) free vibration and (b) random vibration. (The star markers are the MAC values of 12 modes using the left y-axis and the circle markers are computational time using the right y-axis.)
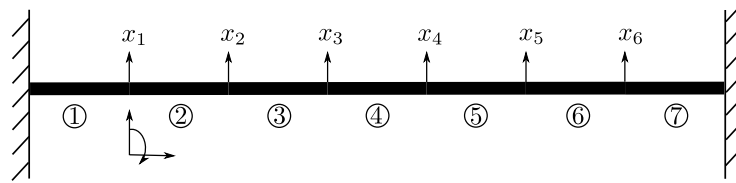
Figure 2.12 : The distributed-parameter fixed beam model with seven elements and six vertical sensors. Each node has three DOFs.
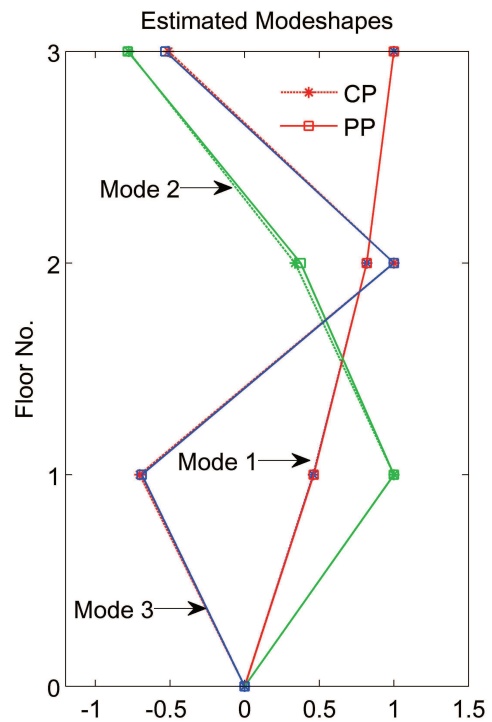
(a)   (b)

Figure 2.13 : (a) The experimental model; (b) the identified modeshapes by CP and PP.
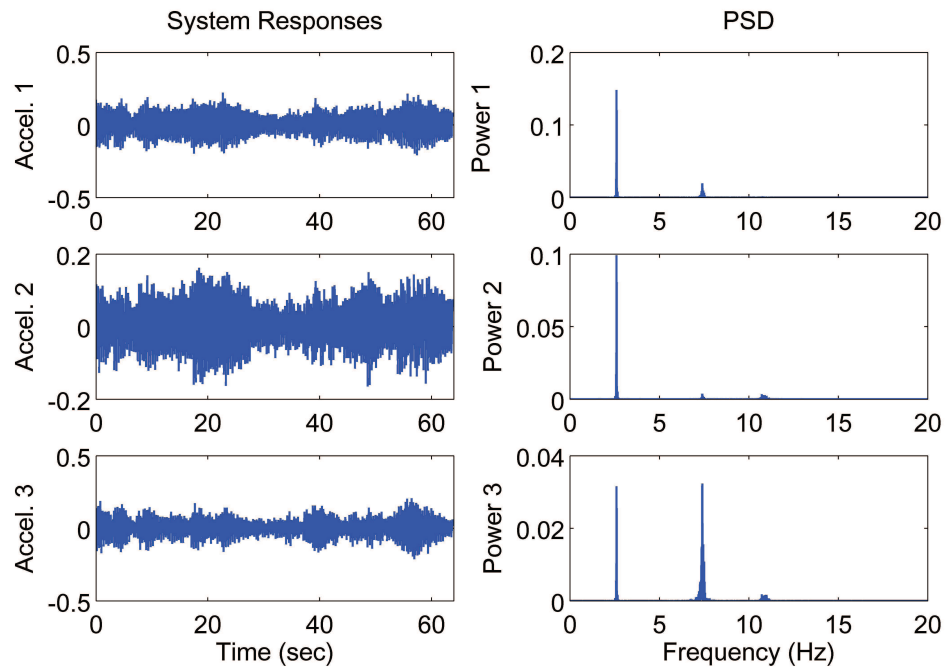
Figure 2.14 : The measured system responses of the experimental model subject to white noise excitation.
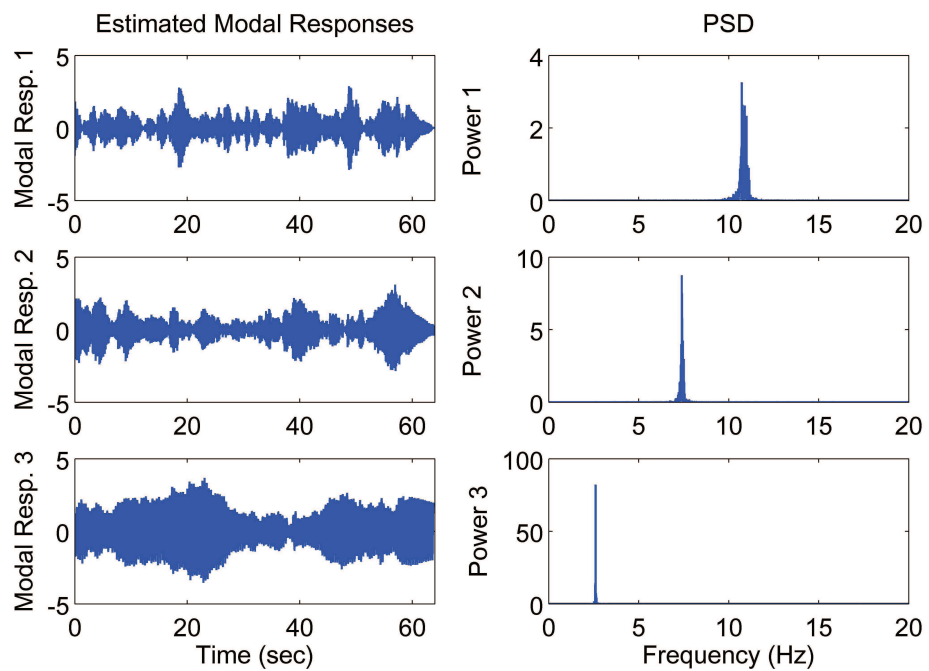
Figure 2.15 : The modal responses recovered by CP of the experimental model subject to white noise excitation.

(a)   (b)
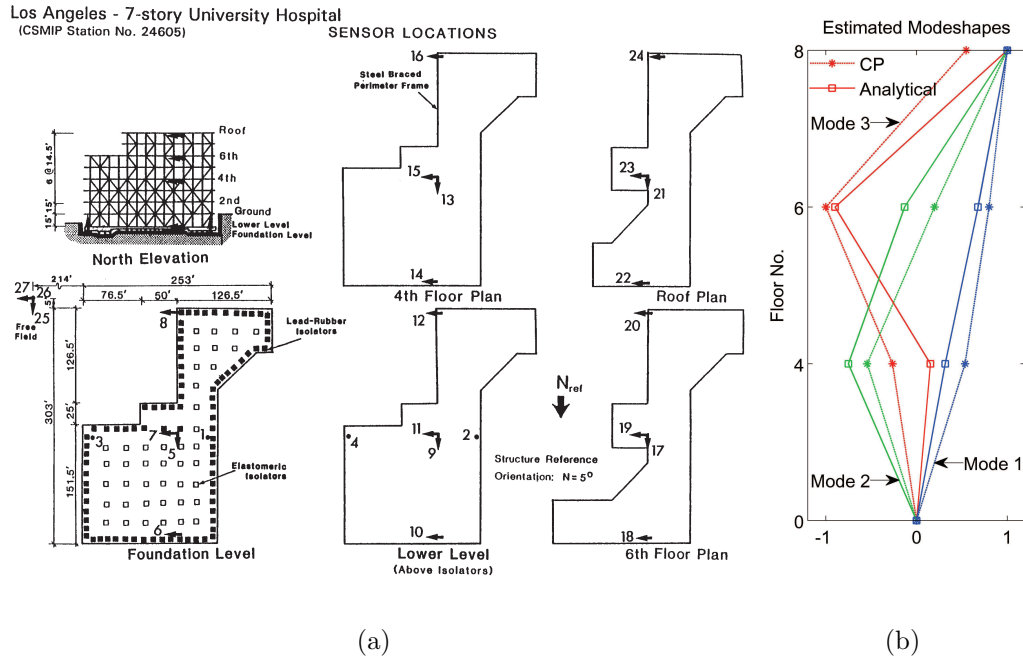
Figure 2.16 : (a) The USC hospital building and its sensor location; (b) the identified modeshapes compared with the analytical ones.
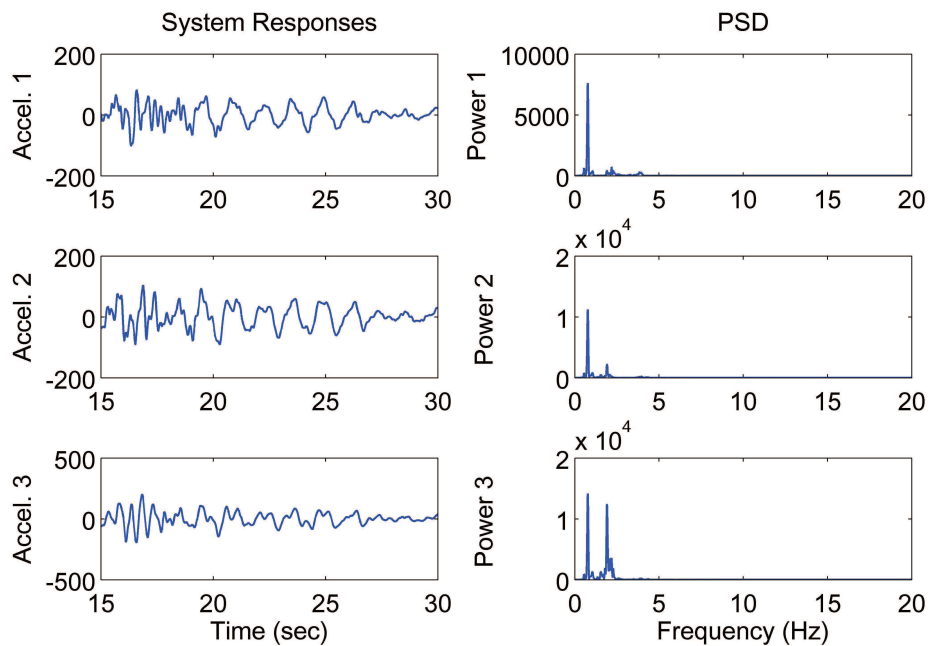
Figure 2.17 : The measured system responses of the USC hospital building in the Northridge earthquake 1994.
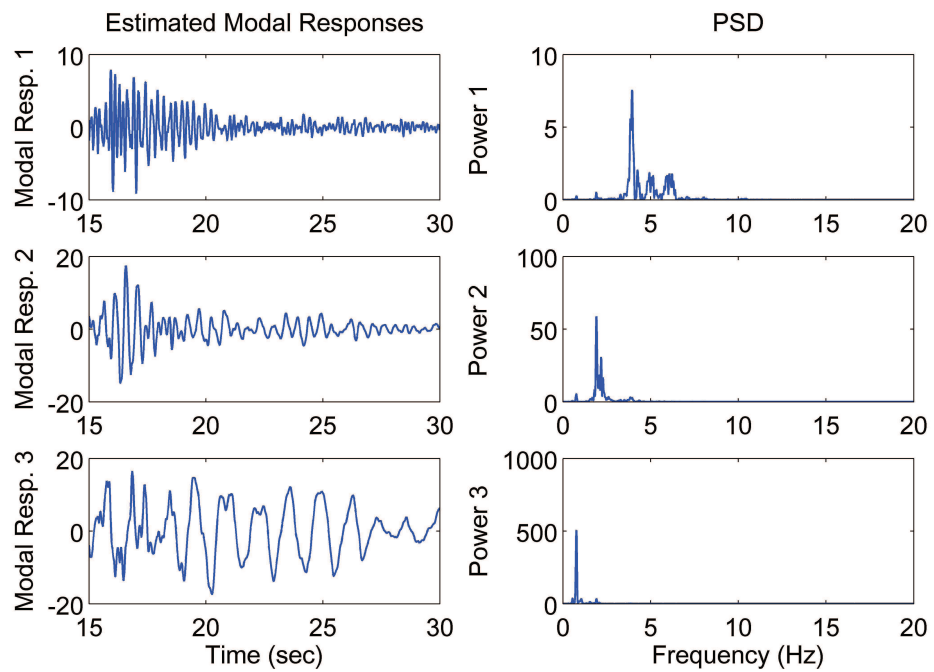
Figure 2.18 : The modal responses recovered by CP of the USC hospital building in the Northridge earthquake 1994.

Chapter 3

Sparse Clustering of Modal Expansion

Chapter 2 explores the signal complexity of the available structural responses and the underlying modal responses and presents a data-driven output-only modal identification method based on the complexity pursuit (CP) technique. CP (as well as other existing BSS based methods) assumes the number of sensors equal that of the active modes, which may not be satisfied in many applications with limited measurement sensors; e.g., for a large-scale or complex structure, sensors may be inadequate compared to the number of active modes. This chapter explicitly exploits the implicit sparse nature of the underlying modal responses and interprets the modal expansion in a sparse data-clustering perspective, thus developing a fairly straightforward and efficient output-only modal identification method based on sparse component analysis (SCA) [148], which is applicable for both determined and underdetermined output-only modal identification problems with limited sensors.

3.1 SCA for modal identification

The targeted modal responses, which are viewed as sources in the BSS framework, are monotone, implying that they are active at only one distinct frequency, respectively. Therefore, they are most sparsely and disjointly distributed in the frequency domain and naturally satisfy the source sparsity assumption of SCA [53][54]. Hence, transform the modal expansion Eq. (2.13) (with m sensors and n modes) into the

sparse frequency domain to incorporate modal identification to the SCA framework,

$$\mathbf{x}(f) = \mathbf{\Phi}\mathbf{q}(f) = \sum_{i=1}^{n} \boldsymbol{\varphi}_i q_i(f) \tag{3.1}$$

with

$$\begin{aligned} \mathbf{x}(f) &= \mathcal{F}(\mathbf{x}(t)) = \int_{-\infty}^{\infty} \mathbf{x}(t) e^{-\mathrm{j}2\pi ft}\mathrm{d}t \\ \mathbf{q}(f) &= \mathcal{F}(\mathbf{q}(t)) = \int_{-\infty}^{\infty} \mathbf{q}(t) e^{-\mathrm{j}2\pi ft}\mathrm{d}t \end{aligned} \tag{3.2}$$

where $\mathcal{F}$, f, and j denote the Fourier transform operator (on each $x_i(t)$ or $q_i(t)$ separately), frequency index, and the imaginary operator, respectively. Note that $\mathcal{F}$ is an invertible linear transform; it holds the form of the modal expansion such that Eq. (3.1) is valid and $\mathbf{\Phi}$ remains invariant.

To avoid complex elements in Eq. (3.1), it is more practical to use the cosine transform $\mathcal{F}^c$ (also linear) to yield real-valued $\mathbf{x}(f)$, simply replacing the Fourier basis $e^{-\mathrm{j}2\pi ft}$ with the cosine basis $\cos 2\pi ft$ in Eq. (3.2). The discrete cosine transform (DCT) is popularly used in data compression of audio (e.g., MP3) and image (e.g., JPEG) [117], where it outperforms the standard discrete Fourier transform (DFT). The DCT is adopted in the proposed SCA method, then $\mathbf{x}(f)$ and $\mathbf{q}(f)$ are understood as real-valued cosine transform coefficients.

Using the disjoint sparsity property of modal responses with distinct frequencies, at some f_k where only one modal response q_j $(j = 1, ..., n)$ is active and $q_i = 0$ for $i \neq j$, Eq. (3.1) becomes

$$\mathbf{x}(f_k) = \boldsymbol{\varphi}_j q_j(f_k) \tag{3.3}$$

Therefore, the points of $\mathbf{x}(f)$ will cluster to the direction of the jth modeshape $\boldsymbol{\varphi}_j$ $(j = 1, ..., n)$, such that the estimated vibration mode matrix $\tilde{\mathbf{\Phi}}$ can be extracted by the automatic FCM clustering algorithm [15].

For determined case $(m = n)$, $\tilde{\mathbf{\Phi}} \in \mathbb{R}^{m \times n}$ is square, and the time-domain modal

responses can be recovered directly by

$$\tilde{\mathbf{q}}(t) = \tilde{\boldsymbol{\Phi}}^{-1}\mathbf{x}(t) \tag{3.4}$$

From which the frequency and damping ratio can be estimated by straightforward Fourier transform and logarithm decrement, respectively. In underdetermined case $(m < n)$, $\tilde{\boldsymbol{\Phi}} \in \mathbb{R}^{m \times n}$ is rectangular. Therefore, the frequency-domain modal sources $\tilde{\mathbf{q}}(f)$ is first recovered using the sparsity-seeking ℓ_1-minimization (P_1), at *each* $f \in \Omega$,

$$(P_1): \quad \tilde{\mathbf{q}}(f) = \arg\min \|\mathbf{q}(f)\|_{\ell_1} \quad \text{subject to} \quad \tilde{\boldsymbol{\Phi}}\mathbf{q}(f) = \mathbf{x}(f) \tag{3.5}$$

where $\|\mathbf{q}(f)\|_{\ell_1} = \sum_{i=1}^{n} |q_i(f)|$. (P_1) is a well-defined convex optimization problem whose solution is guaranteed to be globally optimal, and can be efficiently solved by standard linear programming techniques [24].

The ℓ_1-minimization, as the tightest convex relaxation of the non-convex ℓ_0-minimization (simply counting the non-zeros of a vector, see Section 1.3.1 in Chapter 1), is able to find the sparsest solution with minimal ℓ_1-norm that explains the observations $\mathbf{x}(f)$ [42][20]. The validity of this strategy resides in the ability of the ℓ_1-minimization to recover the sparsest solution to Eq. (3.5), which is exactly the desired monotone frequency-domain modal responses since they are the sparsest solution among all feasible solutions to Eq. (3.5).

The advantages of using cosine transform in Eq. (3.1) are now evident: using Fourier transform would otherwise render complex entries of $\mathbf{x}(f)$ in both Eq. (3.3) and Eq. (3.5). In such a case, $\mathbf{x}(f)$ would cluster to both real and imaginary axis, and solving (P_1) would also require implementations on both real and imaginary axis to recover the sparse complex Fourier coefficients of the modal responses. The use of the cosine transform on the other hand results in real-valued $\mathbf{x}(f)$, upon which it's

simpler for the clustering algorithm and (P_1) to conduct and saves at least half of the computational burden.

Using the inverse cosine transform, the time-domain modal responses can be readily recovered by

$$\tilde{\mathbf{q}}(t) = \mathcal{F}^{c-1}(\tilde{\mathbf{q}}(f)) \tag{3.6}$$

thereby estimating the frequency and damping ratio.

Also note that the proposed SCA method is not applicable to identify highly non-diagonalizable damped structures, where both $\mathbf{\Phi}$ and $\mathbf{q}(f)$ would be highly complex. In this situation, $q_j(f_k)$ and the clustered direction $\boldsymbol{\varphi}_j$ would both be complex, which may not be extracted directly by the clustering algorithm of SCA, thus unable to obtain the mode matrix $\tilde{\mathbf{\Phi}}$. For those with weakly-complex modes, however, SCA may provide reasonable identification, since a real-valued constant scale difference $q_j(f_k)$ approximately holds between the weakly-complex $\boldsymbol{\varphi}_j$ and $\mathbf{x}(f_k)$. Refer to [148] for more details.

3.2 Numerical simulations

The developed SCA is performed for modal identification. The time-domain system responses are first windowed by the Hanning function and then transformed into the frequency domain using DCT with 1024 samples. The mode matrix (partial in the underdetermined case) is then obtained using the automatic clustering algorithm: the DCT coefficients are first normalized [77] and then fed as inputs to the FCM clustering algorithm.

With the estimated mode matrix, in the determined case, the time-domain modal responses are directly recovered using Eq. (3.4) to obtain the time-domain modal responses. For the underdetermined situation, the frequency-domain modal responses

are recovered by ℓ_1-minimization (P_1) solving 1024 underdetermined linear systems of equations (because of a 1024-point DCT), each of which is of scale 2×3 (in the 3-DOF system example) or 2×6 (in the 6-DOF system)-the computation is nevertheless fairly efficient, as will be discussed later. Inverse DCT and multiplication of the inverse Hanning window are then subsequently conducted on the frequency-domain modal responses to obtain the time-domain modal responses. Due to edge effects (mostly from windowing and its inverse operator), few samples (here 50 samples, but may be arbitrary as long as the envelop of the recovered modal response is clear for damping estimation) at two ends of the recovered time-domain modal responses are truncated. Frequency and damping ratio are estimated from the time-domain modal responses by Fourier transform and logarithm decrement, respectively. The correlation between the estimated modeshape $\tilde{\boldsymbol{\varphi}}_i$ $(i = 1, ..., n$) and theoretical modeshape $\boldsymbol{\varphi}_i$ is evaluated by the MAC (Eq. (2.24)). In underdetermined cases, the MAC indicates the accuracy of the clustering algorithm in estimating the directions of the partial modeshapes.

3.2.1 Closely-spaced modes

To demonstrate the capability of the SCA method for identification of closely-spaced modes, a model is set up with the following parameters borrowed from Ref. [93] for direct comparison with the existing SOBI and the modified SOBI method,

$$\mathbf{M} = \begin{bmatrix} 1 & 0 & 0 \\ 0 & 2 & 0 \\ 0 & 0 & 1 \end{bmatrix} \quad \mathbf{K} = \begin{bmatrix} 5 & -1 & 0 \\ -1 & 4 & -3 \\ 0 & -3 & 3.5 \end{bmatrix} \quad \mathbf{C} = \begin{bmatrix} 0.0894 & -0.0084 & 0.0003 \\ -0.0084 & 0.1301 & -0.0244 \\ 0.0003 & -0.0244 & 0.0772 \end{bmatrix}$$
$$(3.7)$$

It is seen from Fig. 3.1 that the 2nd and the 3rd modes are very closely-spaced. The SCA method is performed, and the results are shown in Fig. 3.2- 3.4. Fig. 3.2(a)
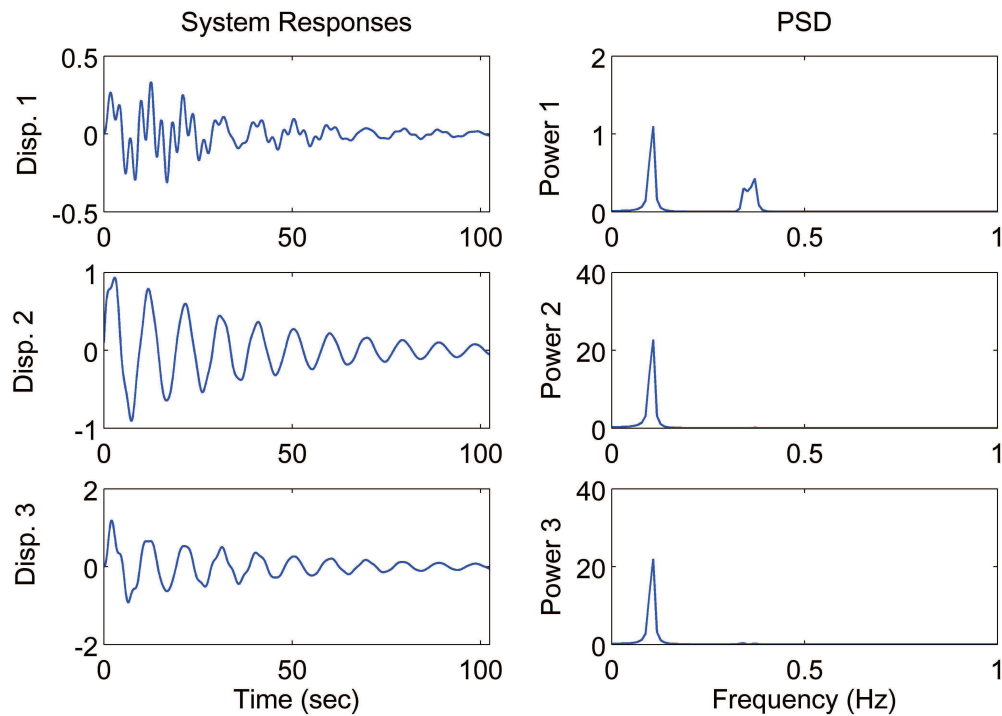
Figure 3.1 : The free-vibration system responses (closely-spaced modes case).

shows that in the underdetermined case, the closely-spaced modeshape directions in the scatter plot of the frequency-domain responses are still significant to distinguish, and the SCA method is capable of accurately recovering even the closely-spaced (2nd and 3rd) modal responses whether in determined (Fig. 3.3) or underdetermined case (Fig. 3.4). Table 3.1 shows that the identified parameters match fairly well those theoretical ones. Note that the SOBI method shows clear degradations for identification of these close modes, as seen in Ref. [93]. Also, with comparable accuracy, the SCA method tends to have simpler implementation than the modified SOBI method with quite a few preprocess steps and parameters to adjust [93]; besides, SCA can additionally handle even the underdetermined situation well.

It is known that traditional methods may meet difficulty in identification of close

modes when noise is present. To see the robustness performance of the SCA method in such a case, 10% RMS (SNR=20 dB) Gaussian white noise is added to the system responses. It is seen that the dominance of the modeshape directions still holds in the scatter plot (Fig. 3.2(b)), and the modal responses are recovered well by the SCA method (Fig. 3.5); similar accuracy is also observed in the determined identification. The SCA method seems to hold well in identification of the close modes in noisy environment.

Another example is shown that the SCA method is also appropriate for identification of closely-spaced modes coupled with high damping, where the damping matrix in Eq. (3.7) is changed to $\mathbf{C} = \alpha\mathbf{M}$, and $\alpha = 0.13$. Fig. 3.6 shows that the 2nd and 3rd modes are completely merged and indistinguishable in the PSD of the system responses. The identification results are presented in Table 3.2 and Fig. 3.7 shows the recovered modal responses in the underdetermined case. Clearly the SCA method has excellent performance in identification of the closely-spaced highly-damped modes.

Table 3.1 : SCA identification of the numerical model (closely-spaced modes)

	Frequency (Hz)			Damping ratio (%)			MAC	
Mode	Exact	Deter-	Under-	Exact	Deter-	Under-	Deter-	Under-
1	0.1039	0.1074	0.1074	4.00	4.00	3.97	1.0000	1.0000
2	0.3425	0.3418	0.3418	2.00	1.88	2.23	0.9998	0.9992
3	0.3713	0.3711	0.3711	2.00	1.84	2.17	0.9991	0.9999

Table 3.2 : SCA identification of closely-spaced highly-damped modes

	Frequency (Hz)			Damping ratio (%)			MAC	
Mode	Exact	Deter-	Under-	Exact	Deter-	Under-	Deter-	Under-
1	0.1039	0.1074	0.1074	9.95	10.00	9.96	1.0000	1.0000
2	0.3425	0.3418	0.3418	3.02	3.14	3.41	0.9999	0.9984
3	0.3713	0.3711	0.3711	2.79	2.81	2.93	0.9996	0.9999

3.2.2 A 6-DOF system example

The SCA modal identification method with the FCM clustering algorithm and ℓ_1-minimization makes no assumption of the dimension (DOFs) of the system; it can be applied to large-scale structures. For demonstration, a 6-DOF system is set up whose parameters are similar with the 3-DOF system in Fig. 2.1, that is, $m_1 = 2, m_2 = m_3 = m_4 = m_5 = 1, m_6 = 3$, $k_1 = k_2 = k_3 = k_4 = k_5 = k_6 = 1$, and $\mathbf{C} = \alpha\mathbf{M}$, $\alpha = 0.08$.

After applying SCA, in determined case, the MAC values for the six modes are 0.9993, 0.9992, 0.9995, 0.9999, 0.9998, and 0.9974, respectively, and the recovered modal responses are monotone with clear exponentially decaying envelops. In underdetermined case, only the first two sensors are used to recover all the six modes. Still, its scatter plot signifies six significant partial modeshape directions (Fig. 3.8), and the recovered modal responses by the SCA method in the underdetermined case are very accurate (Fig. 3.9). It is worth mentioning that the method proposed in Ref. [2] for underdetermined modal identification requires at least four sensors to recover six modes and only two modes are identifiable with two sensors there, whereas SCA recovers all the six modes using only two sensors. This is because as long as

the solution is sparse, ℓ_1-minimization guarantees to find it even from dramatically few observations (sensors)–in fact, larger scale (more DOFs or more active modes present) makes the solution even sparser since the targeted modal response is always monotone at its single active frequency.

It is also found that the FCM clustering algorithm for estimation of the mode-shapes and the ℓ_1-minimization (P_1) for sparse recovery in the underdetermined cases are both very efficient. In this example, ℓ_1-minimization needs to solve 1024 underdetermined linear systems of equations, each of which is of size 2×6; which may appear as heavy computational burden at first sight. However, it converges at a fairly fast rate and conducting for 1024 times costs little computational effort. This is because (P_1) is a well-defined convex optimization problem, which can be solved by the mature linear program technique at little computational expense, even for large-scale underdetermined problem [24]-although the scale in this example (2×6) is not large.

3.3 Experimental verification

The developed SCA modal identification method is also validated by analysis of an experimental model. It is a fixed-base three-story steel frame (Fig. 2.13(a)) with dominant mass on each floor, on top of which the accelerometers are attached to record system responses. Impact excitation is applied to induce free vibration and the system response data are measured by the National Instrument data acquisition system. The sample frequency is originally set at 5128 Hz.

To yield efficient computation without loss of accuracy, the measured data are first down-sampled by a factor of 32, and the procedures of the proposed SCA method is then performed on the data with a Hanning window length of 1024 (Fig. 3.10).

Fig. 3.12 depicts the scatter plots in frequency domain of the system responses in the determined case using all three sensors as well as that using only Sensor 1 (1st floor) and 2 (2nd floor), both revealing three significant clustered (modeshape) directions which are estimated by the FCM clustering algorithm. Fig. 3.13 and 3.14 show that the recovered modal responses in both cases approach quite well the monotone exponentially decaying sinusoids.

Previously the classical peak-picking (PP) method is conducted to identify this model, as already introduced in Section 2.5 of Chapter 2. The detailed identification results are listed in Table 3.3. The identified frequencies by SCA in both determined and underdetermined cases agree well with those by PP, and the MAC values show a high correlation of the identified modeshapes (Fig. 3.11) by these two methods. Note that the damping ratio is not estimated by the PP method since it requires additional processing technique to obtain free vibration for reliable estimation. However, the damping ratio estimated by SCA in the determined and underdetermined cases has reasonable match.

This experimental example validates that the output-only SCA method provides comparable accuracy with the input-output PP method, and yet has advantage of without using input information. Also, the SCA method is automatic, non-parametric, and completely unsupervised, capable of blindly identify modal information directly from system responses. Comparing the underdetermined case to the determined one, the underdetermined SCA gives equally good performance using fewer sensor measurements; this is promising when sensors are limited.

Table 3.3 : Identification results of the experimental model

		Frequency (Hz)		Damping ratio (%)		MAC	
Mode	PP	Determined	Under-	Determined	Under-	Determined	Under-
1	2.55	2.66	2.66	1.12	1.04	0.9997	0.9995
2	7.33	7.51	7.51	1.08	1.03	0.9997	0.9996
3	10.46	10.80	10.80	0.68	0.67	0.9988	1.0000

3.4 Summary

This chapter exploits the sparse nature of the underlying modal responses, proposing an SCA based method to perform output-only modal identification of linear systems, which interprets the modal expansion in a sparse data-clustering perspective. Compared to existing BSS-based modal identification method, the developed SCA algorithm is not only suitable for determined situation, but also capable of identifying modal information when sensors may be highly limited compared to the number of active modes, using the powerful and efficient ℓ_1-minimization technique for sparse recovery.

The SCA method drops the independence assumption used by most BSS techniques; instead, it presumes that sources are sparsely represented in some transformed domain. Based on this principle, the developed SCA method reveals the essence of modal expansion that the monotone modal responses with disjoint sparsest representations in frequency domain naturally cluster to the directions of the modeshapes, which can be readily estimated by a simple automatic clustering algorithm. This surprisingly simple strategy makes the SCA method intuitive and user-friendly for modal identification. Further, ℓ_1-minimization enables SCA to recover all the active

modes even with dramatically few sensors.

The experimental example also show the SCA method provides comparable accuracy with traditional methods (e.g., PP) that use both system input and output information, while it depends only on measured responses, as long as which are dominated by resonant responses. This advantage makes SCA useful when measurement of excitation is impossible or extremely expensive.
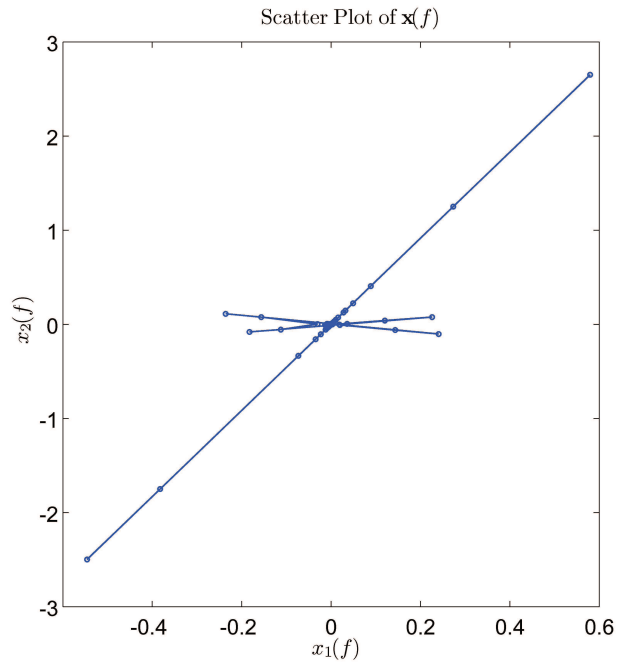
(a)
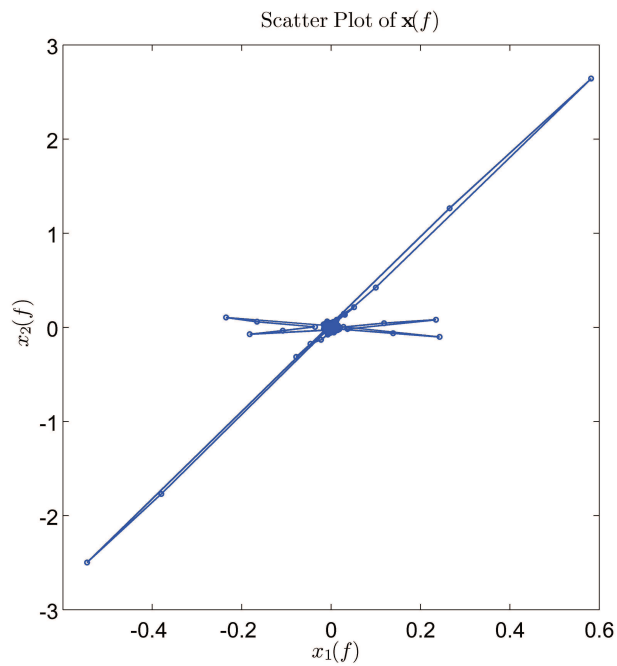
(b)

Figure 3.2 : The scatter plot in frequency domain of the system responses using Sensor 1 and 2 with (a) no noise; (b) 10% RMS noise. (closely-spaced modes case)
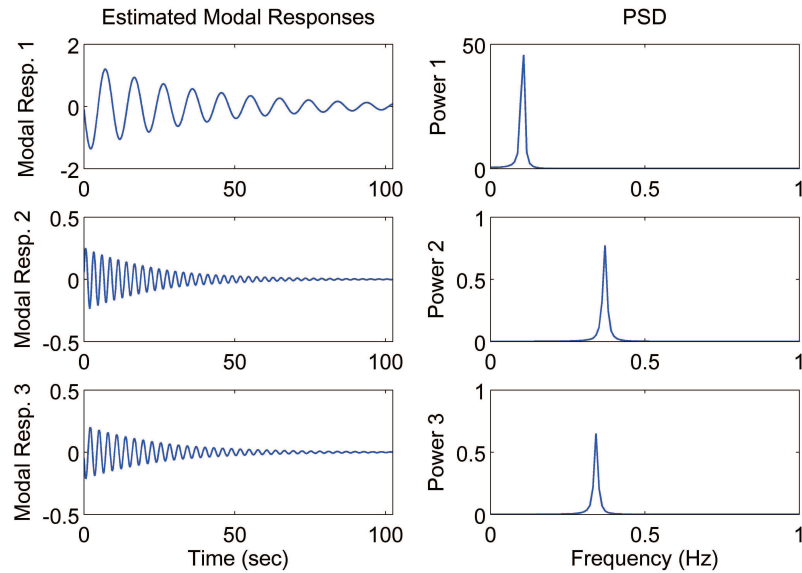
Figure 3.3 : The modal responses recovered by SCA in the determined case using all the three sensors (closely-spaced modes case).
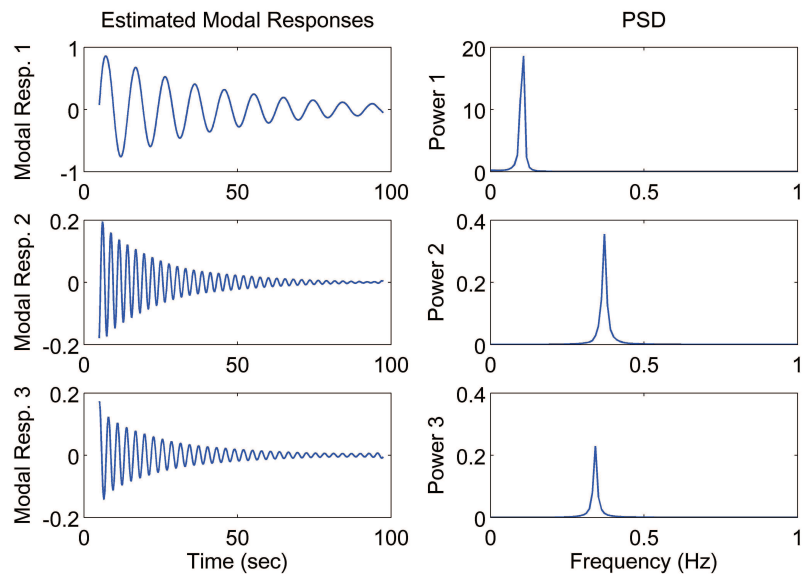
Figure 3.4 : The modal responses recovered by SCA using Sensor 1 and 2 (closely-spaced modes case).
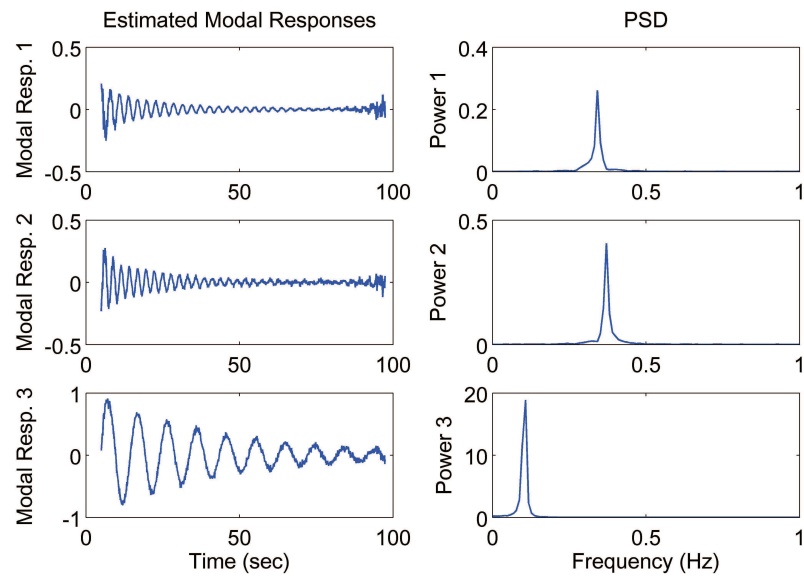
Figure 3.5 : The noisy modal responses recovered by SCA using Sensor 1 and 2 with 10% RMS noise (closely-spaced modes case).
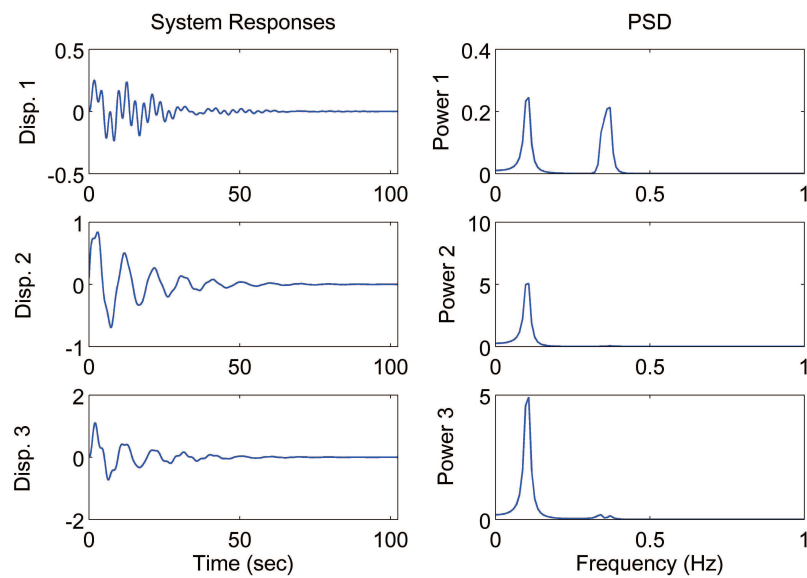
Figure 3.6 : The free-vibration system responses (close modes coupled with high damping case).
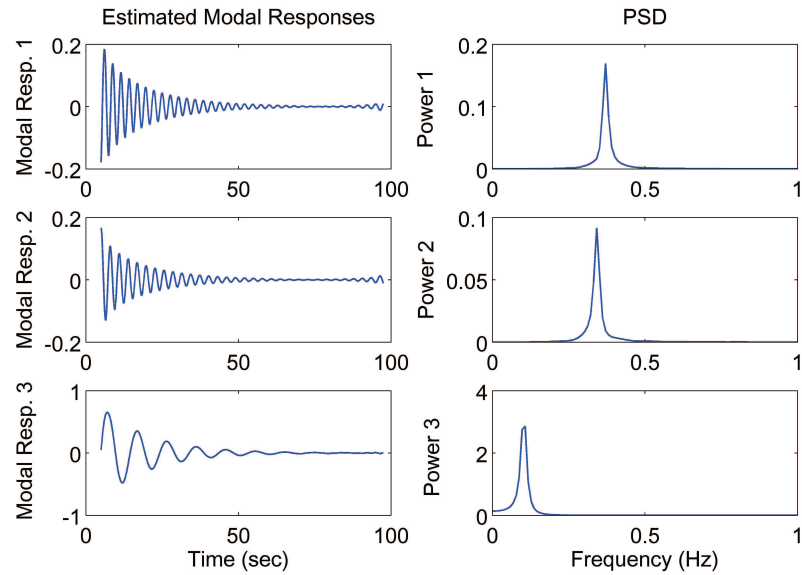
Figure 3.7 : The modal responses recovered by SCA using Sensor 1 and 2 (close modes coupled with high damping case).
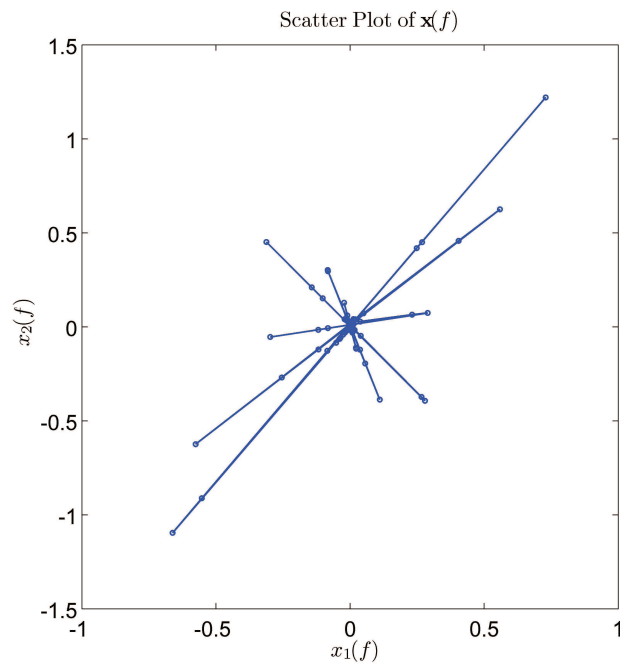
Figure 3.8 : The scatter plot in frequency domain of the system responses using Sensor 1 and 2 of the 6-DOF system.
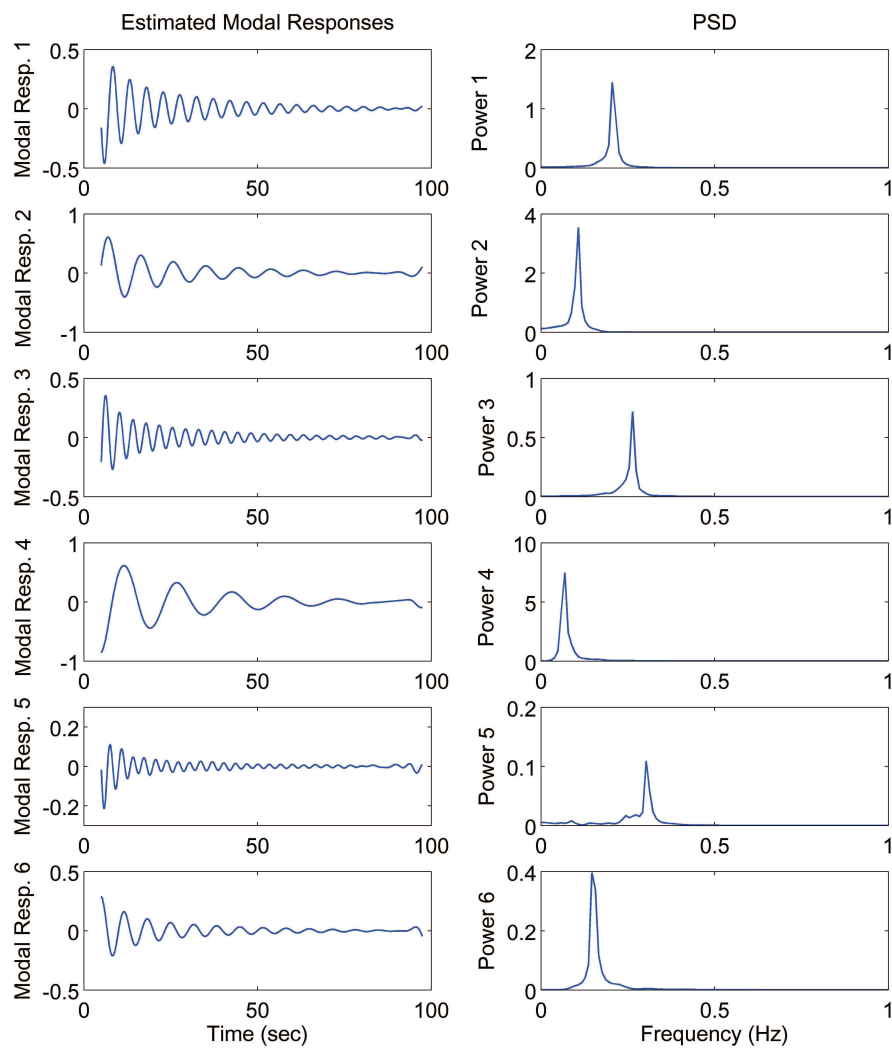
Figure 3.9 : The six modal responses recovered by SCA using Sensor 1 and 2 of the 6-DOF system.
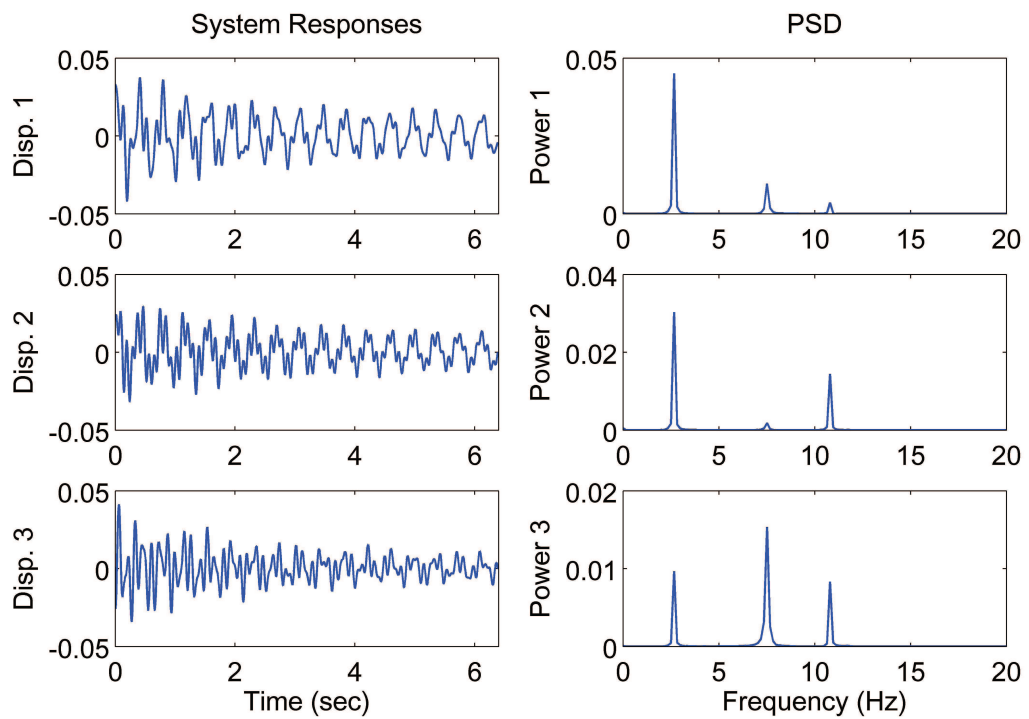
Figure 3.10 : The free-vibration system responses of the experimental model.
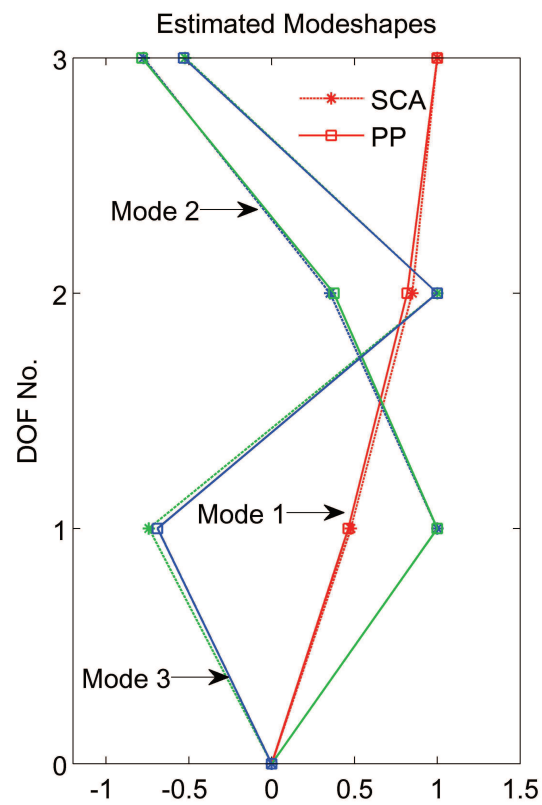
Figure 3.11 : The estimated modeshapes by the FCM clustering algorithm in SCA (dashed line) compared to those by the PP method (solid lines).

(a)

(b)
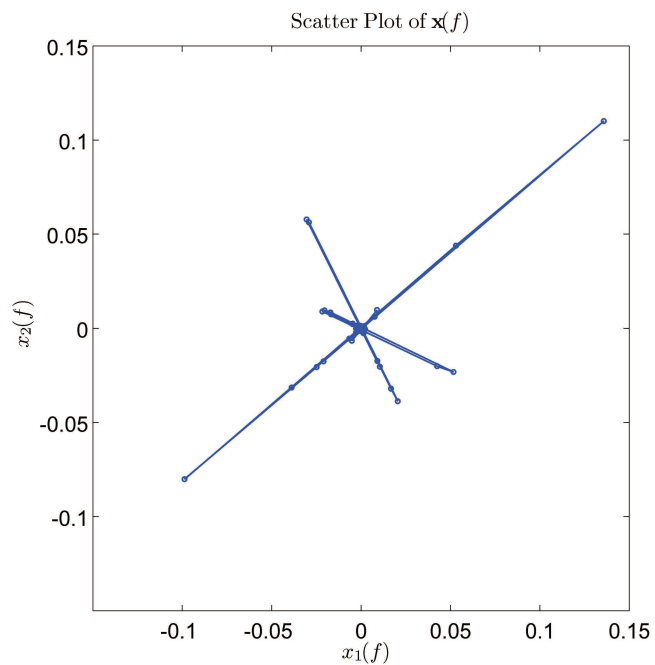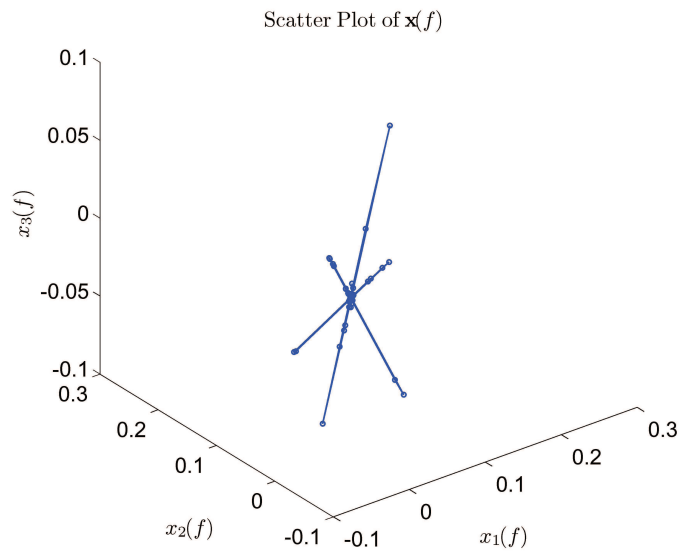
Figure 3.12 : The scatter plot in frequency domain of the system responses of (a) all three sensors; (b) Sensor 1 and 2 in the experimental model.
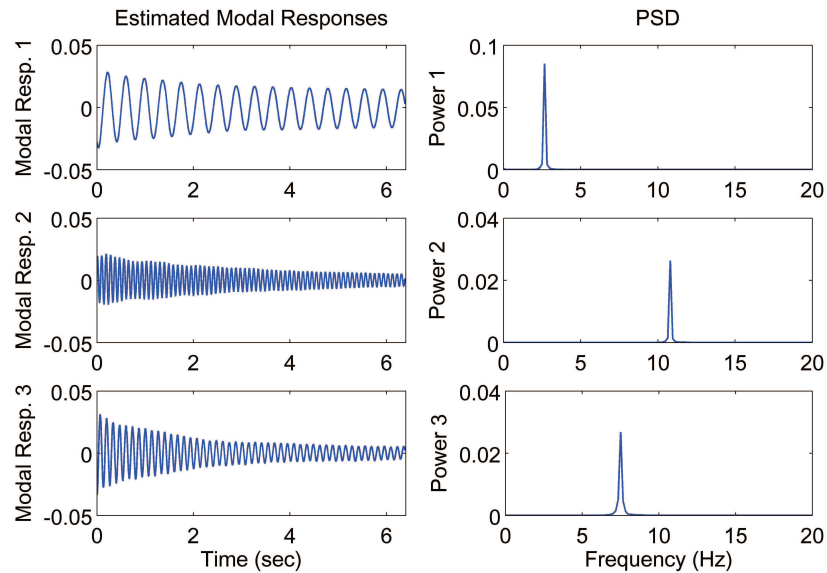
Figure 3.13 : The modal responses recovered by SCA using all the three sensors of the experimental model.
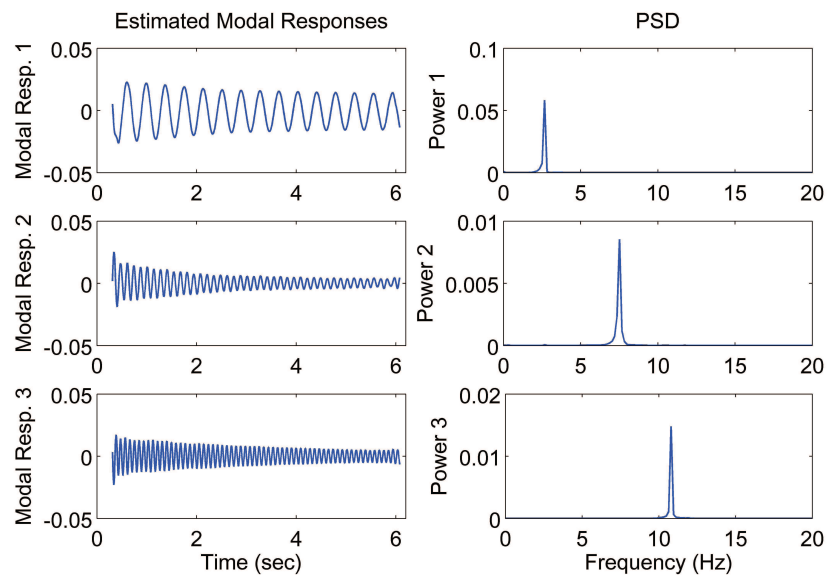
Figure 3.14 : The modal responses recovered by SCA using Sensor 1 and 2 of the experimental model.

Chapter 4

Damage Identification via Sparse Representation

The developed output-only modal identification methods in the previous Chapter 2 and Chapter 3 benefit from the methodology of harnessing the signal property or structure itself of the structural responses and the underlying modal responses. In the data-driven framework, this chapter continues to exploit the signal signature (the sparse pulse-like feature) hidden in the multi-channel structural responses and establishes a new output-only data-driven damage identification method which is able to simultaneously identify both damage instants and damage locations in single or multiple damage events.

4.1 Introduction

As reviewed in Section 1.2.2 of Chapter 1, many existing signal-based techniques have shown significant promise in extracting damage information from measured structural response data; as opposed to structural model (physical or modal) based methods, they feature efficient computation and make no prior assumption with respect to the structural model, which makes them enjoy broader applicability in damage identification. However, reliable damage identification requires careful parameter adjustments by users and shows significant degradations when influenced by measurement noise (e.g., see Fig. 1.2).

Independent component analysis (ICA) [65] is a powerful multivariate data anal-

ysis tool. As an unsupervised (blind) learning algorithm, ICA is able to reveal the characteristic factors hidden in the data using only the observed mixture signals; it has seen various successful applications reported in acoustic [12], communication [87], neural science [89], financial data [8], also in structural dynamics [6], system identification [74][145], and condition monitoring [154][161].

This chapter presents the application of ICA for blind identification of structural damage. It is first justified that ICA's learning rule leads to extract the sparse component, typically indicating damage information (manifesting itself as sparse pulse-like signature), hidden in multi-channel data. Following this finding, structural vibration response data are first transformed into the wavelet domain and then fed as mixtures into the blind source separation (BSS) model, which is analyzed by ICA, realizing accurate and robust identification of both damage instant and location in single or multiple damage events. It is validated by numerical simulations, experimental study, and real-world seismically excited buildings.

4.2 Wavelet transform (WT)

As discussed, the interesting property (e.g., the sparse pulse-like feature which typically indicate damage (Fig. 1.7)) may be revealed on certain wavelet scales (Fig. 1.2(a) and the theoretical background of wavelet transform (WT) has been reviewed in Section 1.3.1 of Chapter 1). However, it is easily destroyed by noise (Fig. 1.2(b)). ICA is capable of extracting the buried pulse-like feature from the noisy wavelet-domain signals, as detailed in the following.

4.3 Independent component analysis (ICA) & damage identification

This section deduces that ICA possesses a learning rule that naturally recovers sparse component, and establishes a new WT-ICA framework for damage identification, revealing both damage instant and location.

4.3.1 The principle of ICA estimation

ICA is popularly used to estimate the blind source separation (BSS) model [65],

$$\mathbf{x}(t) = \mathbf{A}\mathbf{s}(t) = \sum_{i=1}^{n} \mathbf{a}_i s_i(t) \tag{4.1}$$

using only the observed mixture vector $\mathbf{x}(t) = [x_1(t), x_2(t), ..., x_m(t)]^T$; $\mathbf{A}$ and $\mathbf{s}(t) = [s_1(t), s_2(t), ..., s_n(t)]^T$ are the unknown constant $m \times n$ linear mixing matrix and the latent source vector, respectively, to be simultaneously estimated. $\mathbf{a}_i$ is the ith column of $\mathbf{A}$ and associated with the corresponding source $s_i(t)$. The assumption of $m = n$ is imposed herein, i.e., the number of mixtures equals that of the sources and $\mathbf{A}$ is square. With only $\mathbf{x}(t)$ known, Eq. (4.1) may not be mathematically solved by classical method; additional assumption is thus needed to estimate the BSS model.

ICA treats the mixture and source signals as random variables and incorporates the BSS model into a statistical framework. It makes little assumption that the sources are statistically independent at each time instant, and in most applications, this is sufficient to estimate the BSS or ICA model [65].

The principle of ICA estimation is based on the classical central limit theorem (CLT), which states that a sum of independent random variables tends to distribute towards Gaussian, i.e., a mixture of independent random variables is always more Gaussian than any one of the original variables (except that the mixture only contains

one random variable). As seen in Eq. (4.1), mixtures are expressed as a weighted sum of the sources; they are thus always more or equally Gaussian than the sources. This conclusion lays the foundation of the ICA learning rule, which searches for proper de-mixing matrix $\mathbf{W}$ (as the estimation of the inverse of $\mathbf{A}$) such that the recovered independent components (ICs) $\mathbf{y}(t) = [y_1(t), y_2(t), ..., y_n(t)]^T$ obtained by

$$\mathbf{y}(t) = \mathbf{W}\mathbf{x}(t) \tag{4.2}$$

are as non-gausssian as possible and thus approximate the sources $\mathbf{s}(t)$. Each IC $y_i(t)$ is computed by

$$y_i(t) = \mathbf{w}_i\mathbf{x}(t) \tag{4.3}$$

with $\mathbf{w}_i$ the ith row of $\mathbf{W}$. This ICA learning principle can be explained by conducting a variable transformation

$$\mathbf{z}_i = \mathbf{w}_i\mathbf{A} \tag{4.4}$$

and substituting into Eq. (4.3),

$$y_i(t) = \mathbf{w}_i\mathbf{x}(t) = \mathbf{w}_i\mathbf{A}\mathbf{s}(t) = \mathbf{z}_i\mathbf{s}(t) \tag{4.5}$$

Eq. (4.5) shows that the IC $y_i(t)$ is also a weighted sum of the sources. According to CLT, $y_i(t)$ will always be more Gaussian than any of the sources unless it equals one of the sources, in which case $y_i(t)$ becomes least Gaussian. By searching for those ICs which maximize non-gaussianity, the sources (and simultaneously the mixing matrix) can therefore be recovered by ICA.

Non-gaussianity of a random variable v can be measured by some contrast function, e.g., negentropy. A simplified approximation to the negentropy is the classical kurtosis [65], which is defined by

$$\text{kurt}(v) = \text{E}[v^4] - 3(\text{E}[v^2])^2 \tag{4.6}$$

where E[·] denotes the expectation operator. The kurtosis of a Gaussian random variable is zero, and that of a non-gaussian random variable is non-zero. It is easy to estimate and computationally efficient. The more general definition and property of negentropy is described in later section.

The ICA model estimation can therefore be summarized as to find a proper de-mixing matrix such that the recovered ICs maximize the measure of non-gaussianity, e.g., kurtosis. The FastICA is one of the most efficient algorithms implementing ICA estimation, and is adopted in this study. More details can be found in [65].

4.3.2   Damage identification incorporated into ICA model

4.3.2.1   Non-gaussianity and sparsity

The entropy-based negentropy is another measure of non-gaussianity [65] which is more statistically justified. The entropy of a discrete random variable $v = \{v^1, v^2, ..., v^i, ...\}$ is defined by

$$\mathrm{H}(v) = -\sum_i \mathrm{p}(v = v^i) \cdot \log \mathrm{p}(v = v^i) \tag{4.7}$$

or for a continuous random variable u

$$\mathrm{H}(u) = -\int \mathrm{f}(u) \cdot \log \mathrm{f}(u)\mathrm{d}u \tag{4.8}$$

where $\mathrm{p}(\cdot)$ and $\mathrm{f}(\cdot)$ are the probability mass and probability density operators, respectively. Entropy measures the uncertainty or randomness of a random variable. For example, for a random variable with pulse probability density function, its entropy is zero, i.e., it is completely determined.

The Gaussian random variable has the largest entropy among all other random variables with equal variance [36][65], i.e., it is the most random or uncertain one.

On the other hand, a random variable with sparse representation has small entropy as it is less random or easier to be predicted. This conclusion yields the definition of negentropy as a measure of non-gaussianity given by

$$\mathrm{J}(\upsilon) = \mathrm{H}(\upsilon_{gau}) - \mathrm{H}(\upsilon) \tag{4.9}$$

in which υ_{gau} is a standardized Gaussian random variable (zero-mean and unit variance); it quantitatively evaluates the entropy distance of a (standardized) random variable υ from a Gaussian variable. Finding the ICs that maximize the negentropy by ICA thus yields random variables with sparse representation. This finding turns out very useful for damage identification, as subsequently described.

4.3.2.2 Extracting "interesting" sources by ICA for damage instant detection

Damage is typically observed as local phenomenon [41], which may be revealed as pulse-like information hidden in the structural vibration response signals on some sparse domain (Fig. 1.7). As mentioned, the pulse-like feature containing damage information may be buried in the noisy wavelet-domain signals on a certain scale (Fig. 1.2). As ICA biases to extract sparse component from the (possibly very noisy) observations, feed the wavelet-domain responses $\mathbf{x}^l(t)$ at the lth scale as mixtures into the BSS model,

$$\mathbf{x}^l(t) = \mathbf{A}\mathbf{s}(t) \tag{4.10}$$

If there is any pulse-like feature hidden in $\mathbf{x}^l(t)$, ICA will extract it, which is to be revealed in the recovered sparse component $y_j(t)$ with sharp spike indicating damage by

$$\mathbf{y}(t) = \mathbf{W}\mathbf{x}^l(t) \tag{4.11}$$

Such $y_j(t)$ is proposed as the "interesting" source to the damage identification framework. Note that $\mathbf{x}^l(t)$ inherit the time information of the responses; this implies that the recovered "interesting" source $y_j(t)$ retains temporal signature of damage, which is indicated by the instant location of the sharp spike. The simple example in Fig. 1.13(b) in Chapter 1 serves to intuitively explain this conclusion that ICA is able to reveal from the noisy observations the pulse-like feature which contains damage information.

4.3.2.3 Spatial signature in BSS model for damage localization

Expanding the WT-BSS model Eq. (4.1) as

$$
\begin{aligned}
\mathbf{x}^l(t) &= \sum_{i=1}^{n} \mathbf{a}_i s_i(t) \\
x_1^l &= \sum_{i=1}^{n} a_{1i} s_i(t) = a_{11} s_1(t) + a_{12} s_2(t) + ... + a_{1n} s_n(t) \\
x_j^l &= \sum_{i=1}^{n} a_{ji} s_i(t) = a_{j1} s_1(t) + a_{j2} s_2(t) + ... + a_{jn} s_n(t) \\
x_n^l &= \sum_{i=1}^{n} a_{ni} s_i(t) = a_{n1} s_1(t) + a_{n2} s_2(t) + ... + a_{nn} s_n(t)
\end{aligned}
\tag{4.12}
$$

Observe that the mixing coefficient a_{ji} locates the mixture and the source by its indices j and i, respectively, and the column-wise vector $\mathbf{a}_i = [a_{1i}, a_{2i}, ..., a_{ji}, ..., a_{ni}]^T$ contains the spatial signature of the corresponding source $s_i(t)$. Herein, $\mathbf{a}_i$ and its element a_{ji} are proposed as the source distribution vector (SDV) and source distribution factor (SDF), respectively; they describe how source $s_i(t)$ is distributed among n mixtures. Specifically, if a_{ji} has the largest (absolute) value among $\mathbf{a}_i = [a_{1i}, a_{2i}, ..., a_{ji}, ..., a_{ni}]^T$, then $x_j(t)$ contains most $s_i(t)$ component among all the n mixtures.

Take the case in Fig. 1.13(b) for example, the estimated mixing matrix (not normalized) by ICA is $\hat{\mathbf{A}} = \begin{bmatrix} 0.0562 & 1.0186 \\ 0.0246 & 1.0186 \end{bmatrix}$. The first column corresponds to the SDV of IC1 ("interesting" source) which is the recovered pulse-like source of interest. As $\hat{a}_{11}$ is the largest among the SDV, it can be concluded that the mixture at the first location $x_1(t)$ contains most $s_1(t)$ component (the pulse-like feature).

The proposed concepts of SDV and SDF are readily extended to damage localization issue. As the structural response in the vicinity of damage naturally demonstrates most spike-like features, damage can be localized by tracking the spike in the SDV of the recovered pulse-like IC, which is the "interesting" source.

4.4 WT-ICA algorithm for damage identification

Summarizing the aforementioned formulations, the new WT-ICA algorithm is proposed to perform blind identification of structural damage, exploiting the superior properties of WT and ICA, respectively; it includes the following steps.

Step1. Transform the measured structural responses of each sensor location into the wavelet domain, respectively, and select the decomposed signals on a certain WT scale which are observed to contain most damage information (i.e., the pulse-like feature hidden in the noisy wavelet transformed signals).

Step2. Feed the selected wavelet-domain signals on a certain scale at each sensor location as mixtures into the BSS model, which is then solved by the FastICA algorithm, thereby simultaneously obtaining the ICs and their associated SDVs from the mixing matrix.

Step3. The sharp spike in the "interesting" IC (source) identifies damage occurrence instant, while the outstanding spike in the corresponding SDV curve (transformed

into absolute values) of the "interesting" source indicates damage location.

4.5   Numerical simulations

4.5.1   Model description

The 12-DOF numerical model depicted in Fig. 2.9 in Chapter 2 is used to validate the proposed WT-ICA damage identification method. It is considered as a linear system with time-varying stiffness. The parameters are set as follows: the mass is $m_1 = 2, m_2 = m_3 = ... = m_{11} = 1, m_{12} = 3$, the spring stiffness before damage is $k_1 = k_2 = ... = k_{13} = 1$, and proportional damping is considered with respect to the mass matrix as $\mathbf{C} = 0.01\mathbf{M}$.

Damage is simulated by abrupt variation (reduction) of the spring stiffness at certain locations and instants (e.g., Fig. 4.1(a) and 4.1(b)). Free vibration is induced by imposing initial displacement on the DOF. Structural responses are recorded with a sampling frequency of 20 Hz and a time history of 200 seconds. Zero-mean Gaussian white noise (GWN) is added to the system responses to approach the structural operating environment; a signal-to-noise (SNR) level of 50 dB is used herein. The SNR of a signal is defined by

$$\text{SNR} = 20\log_{10}\frac{\text{RMS}(signal)}{\text{RMS}(noise)} \tag{4.13}$$

where RMS denotes the root-mean-square operator of a signal. Various cases are simulated to consider different damage scenarios, with different damage locations, damage occurrence instants, and damage severity; they can be categorized into two patterns: (1) single event; (2) multiple events which simulate a chain of evolutionary damage scenarios.

The developed WT-ICA damage identification algorithm is implemented. The
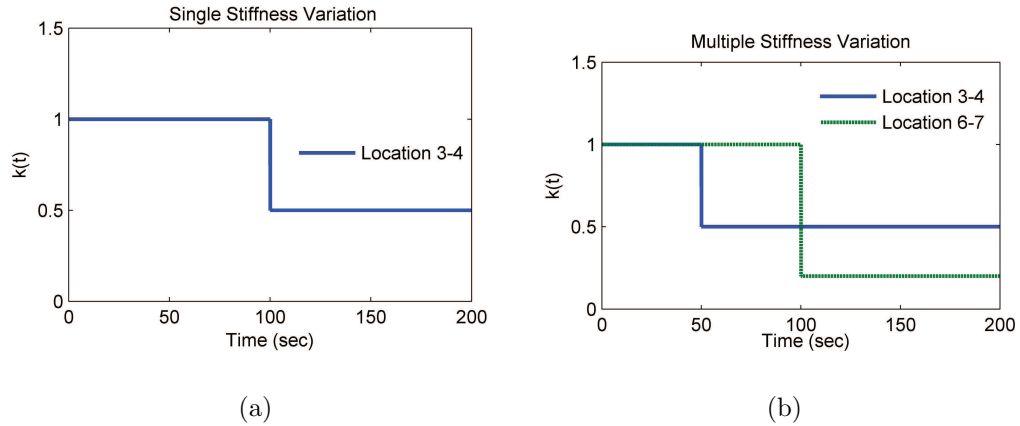
Figure 4.1 : Damage scenarios for system with single and multiple time-varying stiffness.

measured system responses at 12 sensors (DOFs) are preprocessed by the popular db10 wavelet into 4 levels using the Fast DWT [90]. The decomposed signals at the 4th scale (these settings are unchanged throughout all examples in this study)–where most damage information appears (pulse-like features hidden in the noisy wavelet transformed signals) among all the scales–are then selected and fed as mixtures into the BSS model. Subsequently, FastICA is performed on the formulated WT-BSS framework using the kurtosis as the contrast function, thus obtaining the ICs and mixing matrix. The IC with sharp spike is the "interesting" source indicating the damage occurrence instant, and by examining the corresponding SDV, damage is localized by the spike in the SDV curve.

4.5.2   Simulation results

4.5.2.1   Pattern 1: single event

The single damage event considers damage with different severity occurring at the different locations and instants, respectively.

Case 1 with different damage severity: (a) single 80% damage at Location 3-4 at 100th second; (b) single 50% damage at Location 3-4 at 100th second (Fig. 4.1(a)); (c) single 20% damage at Location 3-4 at 100th second.

Case 2 with different damage occurrence instant: (a) single 50% damage at Location 3-4 at 50th second; (b) single 50% damage at Location 3-4 at 150th second.

Case 3 with different damage location: (a) single 50% damage at Location 6-7 at 100th second; (b) single 50% damage at Location 9-10 at 100th second.

Case 1 (b) is used as a reference condition comparing the different damage scenarios. Due to space limitation, only the first four signals of the twelve are presented in the figures. Fig. 4.2 show the damage identification results for Case 1(b) and 1(c).

It is found that WT-ICA is able to accurately identify damage instant and location in all the cases. Specifically, the sharp spike in the wavelet domain gets buried and can barely be observed in the wavelet-domain mixtures (Case 1(c) in Fig. 4.2). However, the hidden pulse-like feature is accurately recovered by ICA, yielding IC1 with an outstanding spike as the "interesting" source which clearly indicates the damage occurrence instant. Further, damage can be accurately localized by examining the spike in the corresponding SDV curves of the "interesting" sources. In addition, Fig. 4.3 shows that the accuracy of WT-ICA holds for different damage instant and location cases, whereas Fig. 4.4(a) presents the comparison of the SDV curves with different damage severity, illustrating that WT-ICA is suitable for both severe and small damage.

4.5.2.2 Pattern 2: multiple events

In extreme events such as earthquakes and impacts, a chain of damage events may occur within a short time. This section investigates the capability of WT-ICA in such
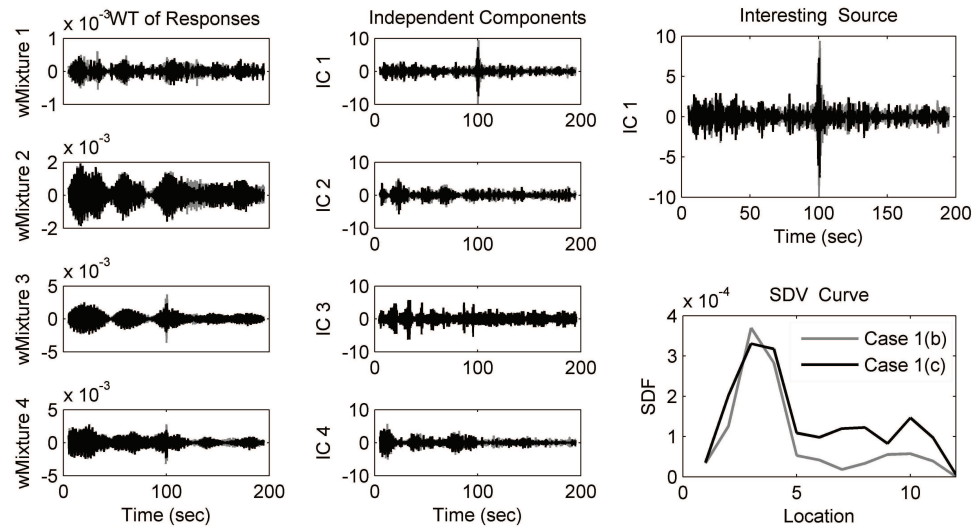
Figure 4.2 : WT-ICA identification results of single damage events: Case 1(b) with 50% damage at Location 3-4 and at 100th second (grey line) and Case 1(c) with 20% damage at Location 3-4 and at 100th second (black line).
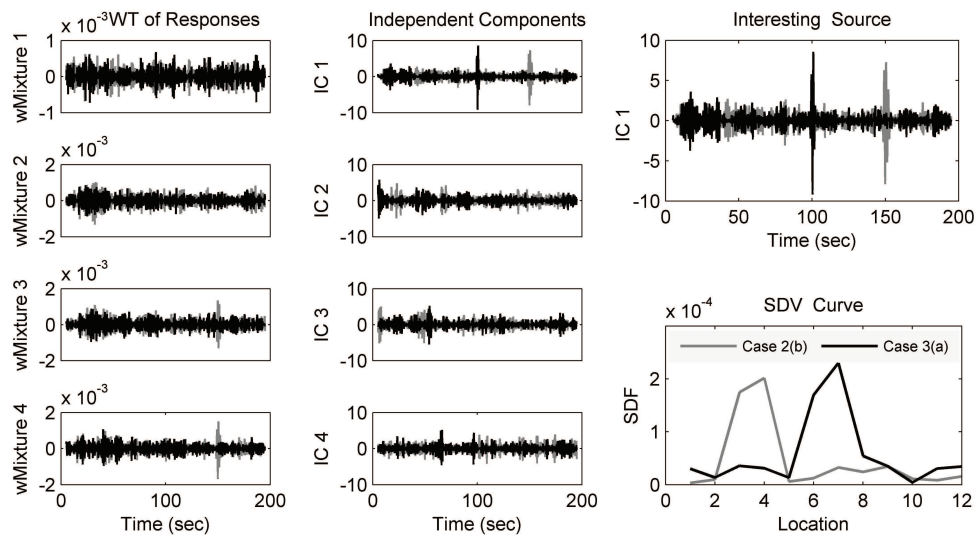
Figure 4.3 : WT-ICA identification results of single damage events: Case 2(b) with 50% damage at Location 3-4 and at 150th second (grey line) and Case 3(a) with 50% damage at Location 6-7 and at 100th second (black line).
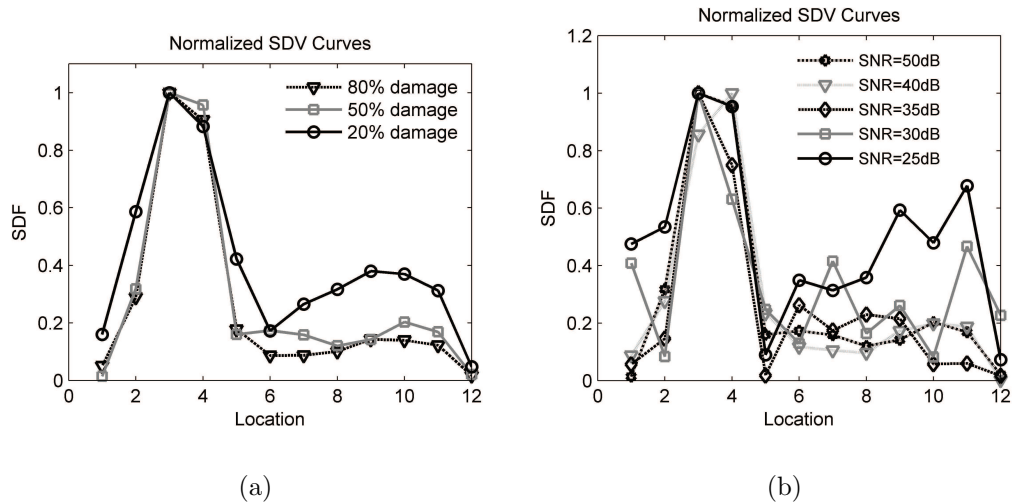
Figure 4.4 : (a) The normalized SDV curves with (a) different damage severity in Case 1, and (b) considering noise effects with different SNRs in Case 1(b).

cases simulated as follows.

Case 4. Multiple damage with different severity at different locations and different instants: first 50% damage at Location 3-4 at 50th second, and then 80% damage at Location 6-7 at 100th second (Fig. 4.1(b)).

Case 5. Single damage developed with different severity at different instants: single 20% damage at Location 3-4 first at 100th second, and then developed to 80% damage at the same Location 3-4 at 150th second.

Case 6. Multiple damage at different location at the same occurrence instant: first 50% damage at Location 5-6 and then 50% damage at Location 9-10 both at 100th second.

Fig. 4.5-4.7 show that WT-ICA is effective to detect and locate damage events which subsequently happen within a short time. While the multiple singularities are deeply buried in the wavelet-domain mixtures, ICA successfully reveals the damage information by the recovered ICs with sharp spike (i.e., the "interesting" sources). Take

Case 4 for example where multiple damage occurs at different locations and different instants, ICA extracts two "interesting" sources with two sharp spikes in recovered IC1 and IC2 (Fig. 4.5), respectively, accurately detecting two damage occurrence instants. Besides, both of the corresponding SDV curves of the two "interesting" sources show clear spikes which accurately localize damage. The identification results in Fig. 4.6 and 4.7 for Case 5 and 6 also well match the predesigned multiple damage scenarios.

4.5.2.3   Noise effects

To account for heavier measurement noise in practice, the system responses with decreasing SNR of 40dB, 35dB, 30dB, and 25dB are used to investigate the robustness of WT-ICA damage identification method. The damage scenarios are also set the same with Case 1(b). Although higher noise level brings disturbance to the "interesting" source, as well as its SDV curve (Fig. 4.4(b)), especially when the SNR drops to 25dB, it appears that the spikes in the "interesting" source and its SDV curve (Fig. 4.4(b)) are still distinguished to realize damage identification. As the SNR decreases under 25dB, the fluctuation of the SDV curve in the undamaged location may become comparable to the spike in the damaged location, thus making WT-ICA less effective.

4.6   Experimental verification

Experimental study is also carried out to validate the method. The three-story scaled steel structure (Fig. 4.8(a)) with dominant mass on each floor is subjected to band-limited white noise excitation at the base. Four accelerometers are embedded to record structural responses; three (#1,3,4) on the right on each floor and one (#2) on
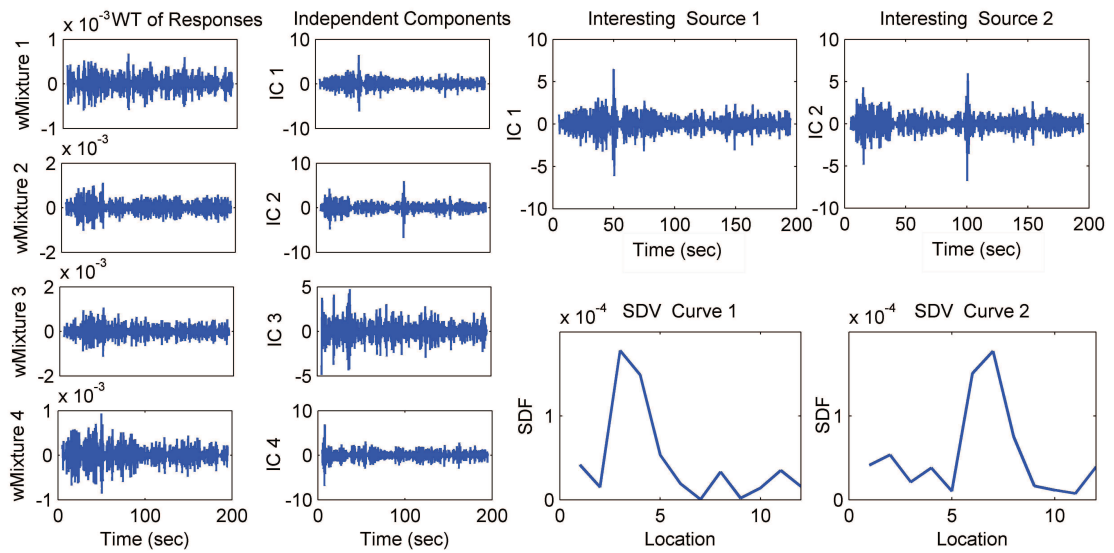
Figure 4.5 : WT-ICA identification results of multiple damage events: Case 4 with 50% damage first at Location 3-4 and 50th second and then 80% damage at Location 6-7 and 100th second.
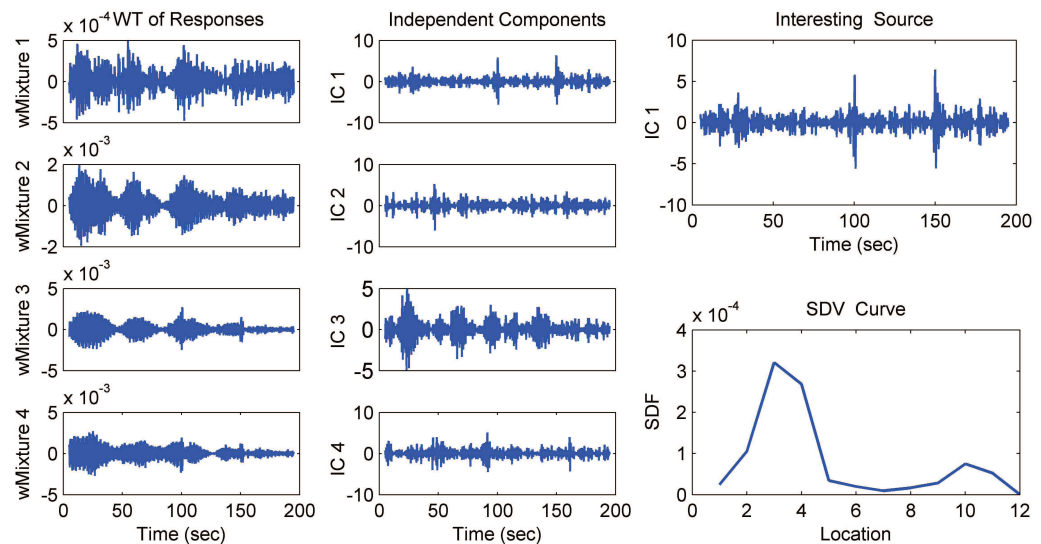
Figure 4.6 : WT-ICA identification results of multiple damage events: Case 5 with damage originated at Location 3-4 first 50% damage at the 50th second and then 80% damage at 100th second.
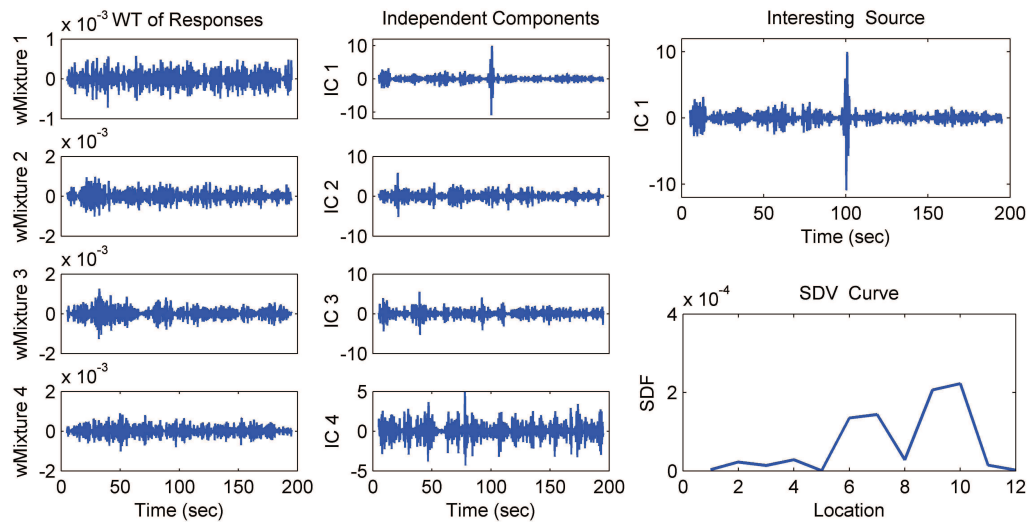
Figure 4.7 : WT-ICA identification results of multiple damage events: Case 6 with 50% damage occurs at the 100th second and simultaneously at both Location 6-7 and Location 9-10.

the left. During the test, the left column suddenly fractured due to damage at the weld (near sensor #2) below the front beam of the 1st floor. The WT-ICA is performed on the measured response data. A segment of 20-second recorded time history containing the damage occurrence instant is shown in Fig. 4.8(b) and the identification results are presented in Fig. 4.9. Obviously, damage information (spikes) is not evident in the structural response time history or in wavelet domain. After conducting ICA, the sharp spikes on the "interesting" source (IC1) and the corresponding SDV curve clearly reveals the damage occurrence instant (at 10th second) and damage location (#2 sensor), respectively, which agree well with the observed damage event.

4.7 Seismic-excited structure example

The WT-ICA method is applied to analyze the real-measured seismic responses of the Los Angeles Fire Command and Control (FCC) building (Fig. 4.10(a)) from the

1994 Northridge earthquake. The FCC building is a two-story base-isolated steel frame structure [101][99], whose responses during the earthquake were recorded by the instrumented sensors (Fig. 4.10(a)). Previous study [101] has shown that multiple one-side impacts against the entry bridge (Fig. 4.10(c)) are observed from 12 second to 16 second in the East-West (EW) direction during the earthquake. Nonlinear behavior occurred due to the time-varying gap (Fig. 4.12(a)) and the entry bridge which behaved as an impact element with time-varying stiffness. After about 16 second, the gap was completely open and the structure underwent vibration without impacts.

The accelerations with 60-second time history from the nine channels (Sensor # 6 for Channel 1, # 7 for 2, etc) in the EW direction are used and transformed into the wavelet domain (five channels with 0-30 second are depicted in Fig. 4.11). There seems to be several sharp spikes in the original time histories and wavelet-domain responses, which are quite noisy and may not lead to clear judgment. After conducting the ICA on the wavelet-domain responses (detail signals on the 4th scale), multiple spikes are clearly revealed and distinguished in the "interesting" ICs (Fig. 4.12(c)), in response to multiple impact events. The first three ICs are selected as the "interesting" sources with sharp spikes indicating multiple impact occurrence instants (Fig. 4.12(c)), which agree well with the previous results in [101] with the most three dominant impacts (Fig. 4.12(a)4.12(b)). The corresponding SDV curves are also presented, showing the locations where the structure suffered from the impacts. It is seen that the peaks are mostly distributed near the base and the roof on the SDV curves, which are quite reasonable, as the impacts occurred directly at the base, and that the roof generally suffered most abrupt drift (as shown in Fig. 4.10(b)) when the impact occurred and is thus more prone to damage.
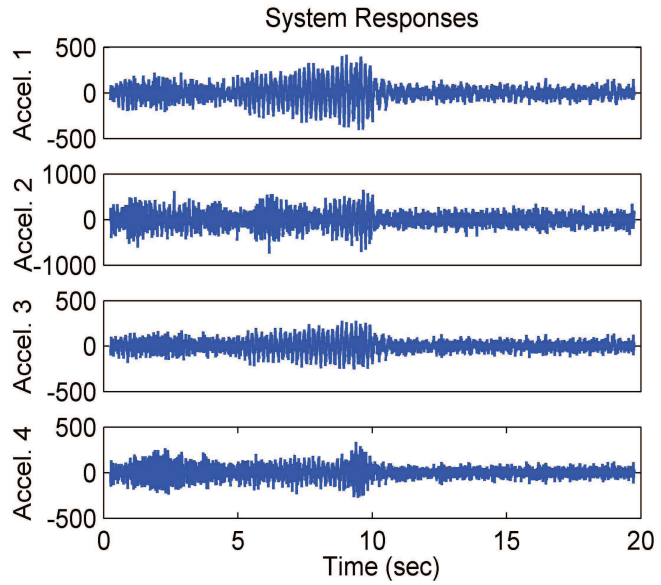
Figure 4.8 : (a) The experimental three-story frame and (b) recorded acceleration responses.
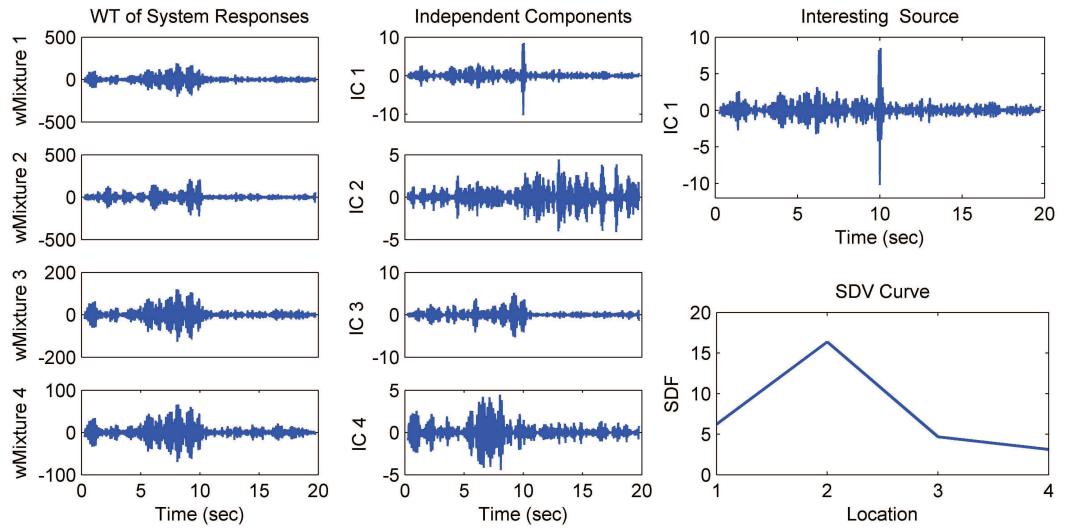
Figure 4.9 : WT-ICA identification results of damage in the experimental system excited by white noise.
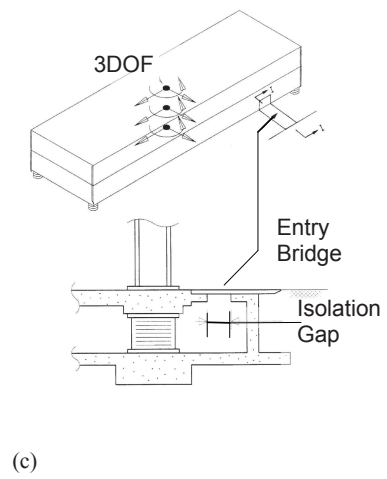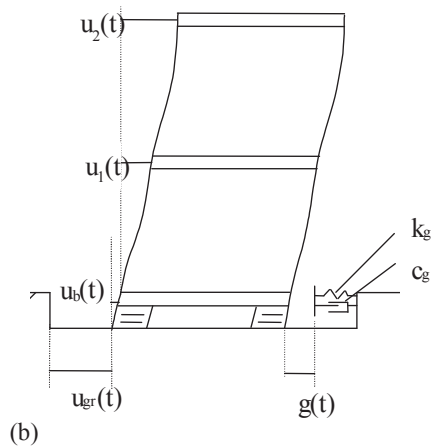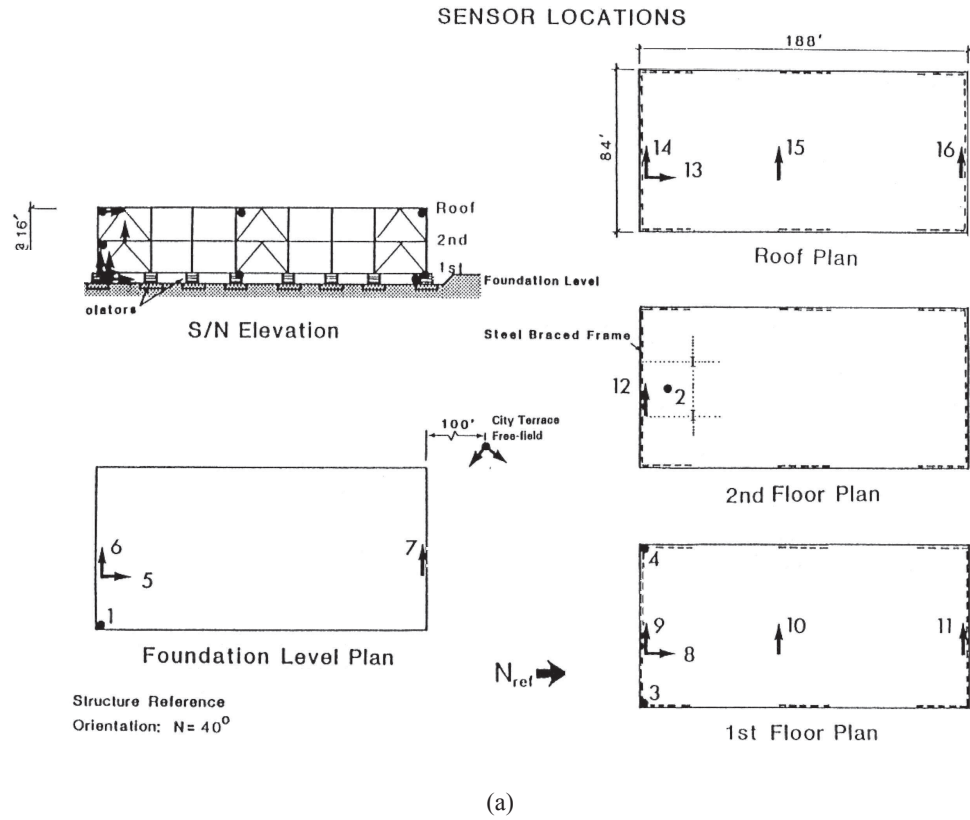
Figure 4.10 : FCC Building (a) Elevation, Plan, and Sensor Locations, (b) Analytical Model, and (c) Entry Bridge and Isolation Gap.
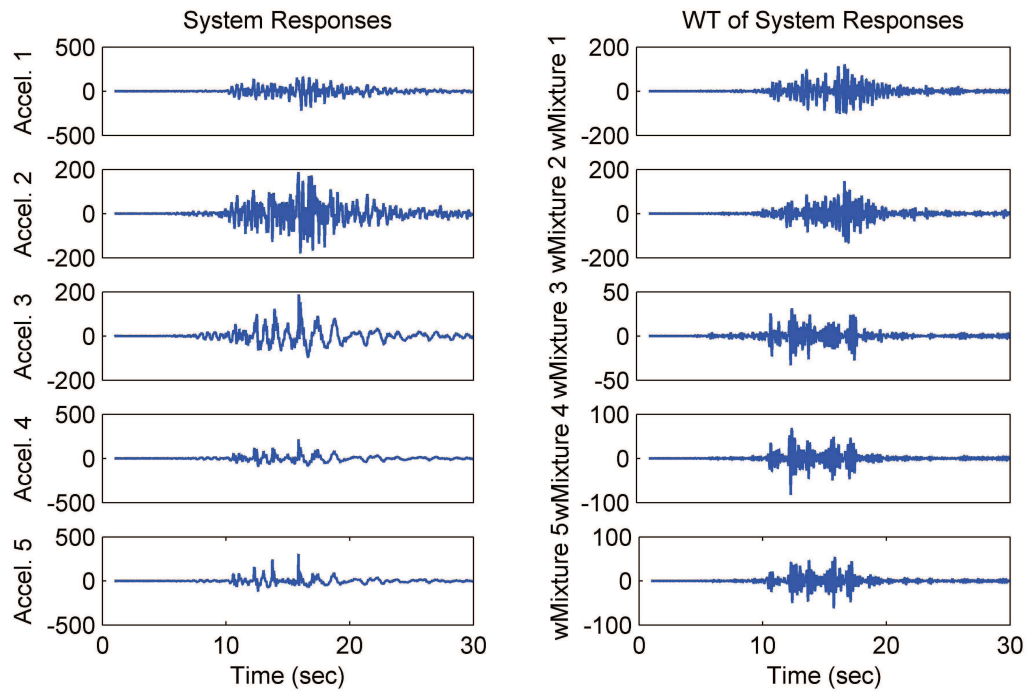
Figure 4.11 : The recorded structural seismic responses (five channels) and their WT.

4.8   Summary

By explicitly targeting the implicit sparse pulse-like damage feature in the multi-channel structural responses, the chapter develops a novel data-driven output-only damage identification method based on WT and ICA. It is found that ICA biases towards sparse representation, which is proposed as the "interesting" source containing targeted damage information hidden in the WT-domain structural responses mixtures which have been fed into the BSS model. The spatial signature contained in the mixing matrix of the established WT-ICA framework is revisited in a novel perspective to admit the damage localization issue. Numerical, experimental, and real-world seismically excited structures examples are presented to illustrate the method. The proposed data-driven WT-ICA algorithm with efficient implementation and little user

(a)

(b)

(c)
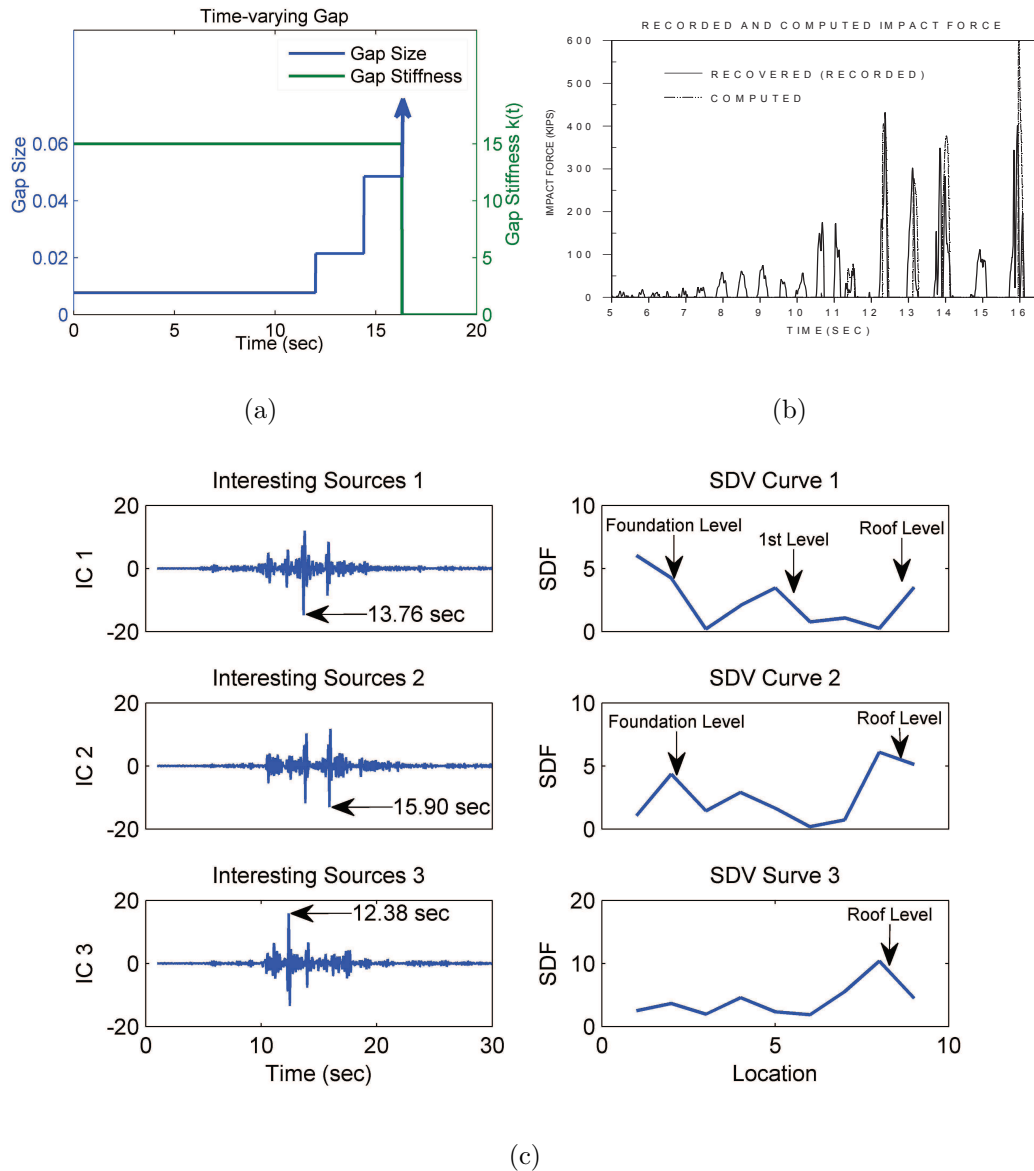
Figure 4.12 : (a) The time-varying gap size and gap stiffness in the FCC building during the earthquake, (b) the recovered and computed impact force time history from Ref. [90], and (c) selected "interesting" sources from ICA and the identification results of the impact occurrence instants and potential damaged locations.

involvement has the potential for application in real-time structural health monitoring and damage detection.

Chapter 5

Sparse Representation Classification

The previous Chapter 4 exploits the sparse pulse-like damage feature hidden in the multi-channel structural responses and develops a new output-only damage identification method in the data-driven framework which is able to simultaneously identify both damage instants and damage locations. This chapter addresses the problems of both locating damage and further assessing damage severity within the classification framework. The classification problem is revisited and the sparsity nature implied in the classification problem itself is exploited, establishing a sparse representation classification framework–an intuitive non-parametric data-driven empirical classification formulation–for damage identification, without a parametric classifier model or the computationally-intensive training process.

5.1 Introduction

The damage identification problem in structural health monitoring (SHM) commonly includes four levels [115]: (1) detecting the presence of damage; (2) locating damage; (3) assessing damage severity; (4) predicting the structural remaining service life. Vibration-based damage identification techniques have been extensively studied in the literatures [41]. In the earlier years, much attention was focused on those methods based on the change of structural modal parameters as damage signature; however, it has been pointed out that modal information alone is not sensitive to lo-

cal damage and that its capability as direct damage indicators is easily influenced by noise. Nevertheless, researches do converge to support the conclusion that structural damage information is hidden in modal features, which need to be further processed for successful damage identification. Also, signal processing damage detection techniques are mostly limited up to the level 2.

With a structural model (e.g., a finite element model) available as reference information, it is possible to develop damage identification methods that can address even the problem of level 3 [41], that is, the quantification of damage severity. Some researchers used the model updating method [50] to address this problem, by comparing the undamaged (reference) and candidate (test) model (physical or modal) matrices [41]. These methods are essentially parametric model based; as such, they are prone to model error.

More recently, the damage identification problem including that of level 3 has been treated as a pattern recognition issue [16][21]. The classification-based methods involve three steps: feature extraction, training, and classification. For damage identification, the extracted features from various predefined or reference damage classes, including different damage locations and damage extents, are used as inputs to train the classifiers, which can then identify the damage class of the test feature representing the current state of the structure. Successful examples include those based on artificial neural networks (ANN) [154][124], support vector machines (SVMs) [137][135][136], nearest neighbor [134], and Markov observers [40]. However, their effectiveness suffers from the training process for the parameteric classifier model (as reviewed in Section 1.2.2 of Chapter 1), which could be computationally intensive and needs the skill of an experienced practitioner.

This chapter proposes a new algorithm in the classification framework for both

locating and assessing structural damage, using the recent theory from blind source separation (BSS) [34] and sparse representation (SR) [20] along with compressed sensing (CS) [26][43]. The proposed damage identification method consists of two steps: feature extraction and classification.

Specifically, in the feature extraction step, the BSS method complexity pursuit (CP) [129] is used to extract the modal features of the structure. As introduced in Chapter 2, CP has been found to be a useful alternative to efficiently perform output-only system identification of many structures with highly-damped, closely-spaced, and non-proportionally damped modes requiring limited parameter adjustments. In the first step of the proposed method, CP serves to blindly extract the structural modal features, which are subsequently used by the classification framework for damage identification.

In the following classification step for both locating damage and identifying damage extent, the sparsity nature of the classification itself is exploited. An SR framework is developed based on the theory of SR and CS [20][26][43], inspired by their recent success on sparse MRI [84], robust SR face recognition [138], and more lately on SHM [9][148][91][109]. The key idea is that the damage class of the test structure naturally belongs to only one unique class of the predefined reference feature space: (1) an over-complete reference feature dictionary is built by concatenating all the modal features of all candidate damage classes; (2) the test modal feature is most sparsely represented as a linear combination of the bases of this reference dictionary, activating only the relevant feature in the same damage class. This establishes a highly underdetermined linear system of equations with an underlying sparse representation that directly dictates the damage class of the test structure. The theory of SR and CS enables one to find the correct sparse solution of such a highly under-

determined linear system of equations using the efficient ℓ_1-minimization technique, leading to the test structure's class of damage location and damage severity.

Numerical simulations and experimental study are conducted to validate the proposed CP-SR method. Results show that it can accurately and efficiently identify the damage locations and damage extents. In addition, several problems of identifying multiple damage, using limited sensors and partial features, and in the presence of heavy noise and random excitation are also presented.

5.2 Blind extraction of modal features

The first step of the proposed method is to blindly extract the structural modal features that carry the damage information. A BSS technique CP that has been presented in Chapter 2 and [147] is used to accomplish this task. The modal features $\boldsymbol{\Phi} \in \mathbb{R}^{n \times n}$ containing the state of the structure are subsequently used by the classification framework for damage identification, as detailed in the ensuing section.

5.3 Sparse representation classification for damage identification

With extracting modal features by CP being the first step, the second step of the proposed method is classification. In this section, a classification framework based on sparse representation for damage identification is developed by exploiting the sparsity nature implied in the classification problem itself.

5.3.1 Classification for damage identification

Given a test feature, the objective of classification is to identify which class it pertains to, within a predefined reference feature space containing a large set of candidate classes. For the damage identification issue, this is equivalent to determining which damage pattern the feature of the test structure belongs to, from a predefined feature class space with various damage classes (i.e., cases with different damage locations or damage severity). This predefined reference feature space comprises those features of various labelled damage classes (e.g., simulated by a structural FEM model). In the proposed method, the test feature and the reference feature space are obtained by the CP method in the first step, blindly extracting the modal features from the structural responses of the test structure and the reference FEM model, respectively.

5.3.2 Classification with SR

Suppose there are N distinct predefined candidate damage classes of an n-DOF structure (simulated by its FEM model), then for the jth class ($j = 1, ..., N$), its structural mode matrix $\mathbf{\Phi}_j \in \mathbb{R}^{n \times n}$ consists of n modal feature columns $\mathbf{\Phi}_j = [\boldsymbol{\varphi}_{j,1}, ..., \boldsymbol{\varphi}_{j,i}, ..., \boldsymbol{\varphi}_{j,n}]$ ($i = 1, ..., n$), where $\boldsymbol{\varphi}_{j,i} \in \mathbb{R}^n$ is its ith column. For N reference damage classes (simulated from the structural FEM model), the predefined reference feature space is the reference modal feature matrix (dictionary) $\mathbf{\Psi} \in \mathbb{R}^{n \times w}$ consists of $w = n \times N$ concatenated modal feature columns,

$$\mathbf{\Psi} = [\mathbf{\Phi}_1, ..., \mathbf{\Phi}_j, ..., \mathbf{\Phi}_N] = [\boldsymbol{\varphi}_{1,1}, ..., \boldsymbol{\varphi}_{j,i}, ..., \boldsymbol{\varphi}_{N,n}] \tag{5.1}$$

The key idea of sparse representation classification is that the damage class of the test structure (represented by the test modal feature columns) can only belong to *one* of the predefined reference damage classes (represented by the reference modal

feature matrix or dictionary); as such, it can be formulated as a sparse representation classification problem.

Specifically, the test structure with a (test) modal feature matrix $\hat{\boldsymbol{\Phi}} = [\hat{\boldsymbol{\varphi}}_1, ..., \hat{\boldsymbol{\varphi}}_n] \in \mathbb{R}^{n \times n}$ (representing its current state) coincides with one of the N predefined candidate damage classes, say, the jth class; then any column of $\hat{\boldsymbol{\Phi}}$, say, the ith column $\hat{\boldsymbol{\varphi}}_i \in \mathbb{R}^n$ ($i = 1, ..., n$), if not normalized, will approximately have only a scale difference $\alpha_{j,i}$ from $\boldsymbol{\varphi}_{j,i} \in \mathbb{R}^n$, which is the ith column of $\boldsymbol{\Phi}_j$ representing the predefined jth damage class, i.e.,

$$\hat{\boldsymbol{\varphi}}_i = \alpha_{j,i} \boldsymbol{\varphi}_{j,i} \tag{5.2}$$

Then expressing $\hat{\boldsymbol{\varphi}}_i \in \mathbb{R}^n$ in terms of the whole reference feature space $\boldsymbol{\Psi} \in \mathbb{R}^{n \times w}$, it can be sparsely represented as a linear combination of the bases (the feature columns) of $\boldsymbol{\Psi} \in \mathbb{R}^{n \times w}$,

$$\hat{\boldsymbol{\varphi}}_i = \boldsymbol{\Psi} \boldsymbol{\alpha}_i = \sum_{k=1}^{N} \sum_{l=1}^{n} \alpha_{k,l} \boldsymbol{\varphi}_{k,l} \tag{5.3}$$

where $\boldsymbol{\alpha}_i = [0, ..., 0, \alpha_{j,i}, 0, ..., 0]^T \in \mathbb{R}^w$ is an underlying sparse vector, in which the location of the non-zero entry $\alpha_{j,i}$ naturally assigns the damage class the given test feature $\hat{\boldsymbol{\varphi}}_i$ falls into within the N predefined reference damage classes (also see Fig. 5.1 for illustrations).

The formulated classification problem for damage identification with a sparse representation therefore centers around the issue of recovering the underlying sparse $\boldsymbol{\alpha}_i \in \mathbb{R}^w$ from the knowledge of the predefined reference matrix $\boldsymbol{\Psi} \in \mathbb{R}^{n \times w}$ and the test feature $\hat{\boldsymbol{\varphi}}_i \in \mathbb{R}^n$.

5.3.3 Sparse solution via ℓ_1-minimization

The reference feature matrix $\boldsymbol{\Psi} \in \mathbb{R}^{n \times w}$ typically consists of a large amount of modal feature columns that correspond to vast candidate damage classes that the structure
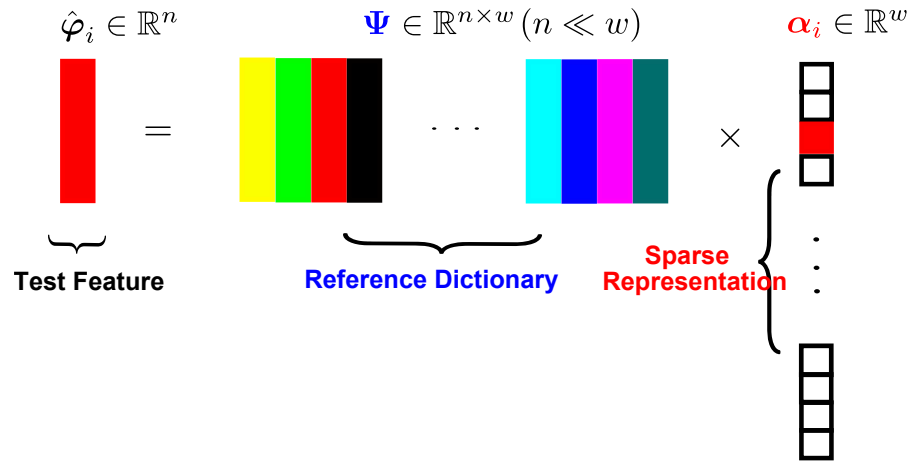
Figure 5.1 : Sparse representation classification paradigm for damage identification. The feature column (red) from the test structure only activates itself in the predefined reference feature dictionary, yielding a sparse representation with only one non-zero entry (red).

may possibly incur; consequently, $n \ll w$ and $\mathbf{\Psi} \in \mathbb{R}^{n \times w}$ is an over-complete reference modal feature dictionary such that the sparse representation classification problem Eq. (5.3) is an (highly) underdetermined linear system of equations, which is ill-posed: there exist *infinite* feasible solutions.

Implied in the nature of the sparse representation classification problem, the sparsest solution to Eq. (5.3), $\boldsymbol{\alpha}_i^\star \in \mathbb{R}^w$ $(i = 1, ..., n)$ with only one non-zero entry $\alpha_{j,i}$, is needed to determine the identity of the test feature, and can be exactly found by the well-known sparsity optimization ℓ_0-minimization program (P_0) [20],

$$(P_0): \quad \boldsymbol{\alpha}_i^\star = \arg \min \|\boldsymbol{\alpha}_i\|_{\ell_0} \quad \text{subject to} \quad \mathbf{\Psi} \boldsymbol{\alpha}_i = \hat{\boldsymbol{\varphi}}_i \qquad (5.4)$$

where $\|\boldsymbol{\alpha}_i\|_{\ell_0} = \#\{r : \alpha_{i,r} \neq 0\}$ is the ℓ_0-norm, simply counting the number of non-zero entries of $\boldsymbol{\alpha}_i$. (P_0) finds a vector $\boldsymbol{\alpha}_i^\star$ with smallest ℓ_0-norm that explains the observation $\hat{\boldsymbol{\varphi}}_i$. This ℓ_0-norm is a very intuitive measure of sparsity, naturally (P_0) seeking the sparsest $\boldsymbol{\alpha}_i^\star$ with fewest non-zero entries that is the correct solution to the

SR classification framework (in Eq. (5.3)), rejecting all other feasible, but less sparse, solutions.

It has been proven, however, that solving (P_0) is in general NP-hard [20]. Fortunately, the theory of SR and CS [20][26][43] establishes that if the solution $\boldsymbol{\alpha}_i$ is sufficiently sparse, then (P_0) can safely be replaced by a convex optimization program ℓ_1-minimization (P_1), known as basis pursuit [31],

$$(P_1): \quad \boldsymbol{\alpha}_i^\star = \arg \min \|\boldsymbol{\alpha}_i\|_{\ell_1} \quad \text{subject to} \quad \boldsymbol{\Psi}\boldsymbol{\alpha}_i = \hat{\boldsymbol{\varphi}}_i \tag{5.5}$$

or a stable version to account for possible noise or errors

$$(P_1^\delta): \quad \boldsymbol{\alpha}_i^\star = \arg \min \|\boldsymbol{\alpha}_i\|_{\ell_1} \quad \text{subject to} \quad \|\boldsymbol{\Psi}\boldsymbol{\alpha}_i - \hat{\boldsymbol{\varphi}}_i\|_{\ell_2} \leq \delta \tag{5.6}$$

in which the ℓ_1-norm is defined by $\|\boldsymbol{\alpha}_i\|_{\ell_1} = \sum_{r=1}^{w} |\alpha_{i,r}|$ and the ℓ_2-norm is defined by $\|\boldsymbol{\alpha}_i\|_{\ell_2} = \sqrt{\sum_{r=1}^{w} |\alpha_{i,r}|^2}$; δ is associated with the noise level. (P_1) and (P_1^δ) can be solved very efficiently via linear programming and convex quadratic programming techniques [24][76], respectively.

Since the underlying $\boldsymbol{\alpha}_i \in \mathbb{R}^w$ is very sparse with only one (or few) non-zero entries, it is guaranteed to be correctly recovered by (P_1) (or (P_1^δ)) from the knowledge of the test feature $\hat{\boldsymbol{\varphi}}_i \in \mathbb{R}^n$ and the predefined reference matrix $\boldsymbol{\Psi} \in \mathbb{R}^{n \times w}$.

5.3.4 Robust damage identification index based on SR classification

Theoretically, only one column (say, the ith column $\hat{\boldsymbol{\varphi}}_i \in \mathbb{R}^n$) of the test structure's modal feature matrix $\hat{\boldsymbol{\Phi}} \in \mathbb{R}^{n \times n}$ is needed to set up the underdetermined sparse representation classification problem in Eq. (5.3), $\hat{\boldsymbol{\varphi}}_i = \boldsymbol{\Psi}\boldsymbol{\alpha}_i$; whose, sparse solution sought by ℓ_1-minimization $\boldsymbol{\alpha}_i^\star \in \mathbb{R}^w$ has only one non-zero entry, say, $\alpha_{j,i}$, indicating the test structure belongs to the jth predefined damage class. Nevertheless, in practice, noise and other factors can affect $\boldsymbol{\alpha}_i^\star$ $(i = 1, ..., n)$, wherein other entries may

only be approximately zero. Also, because damage information may be distributed among all test modal feature columns, it would be more robust to combine more sparse solutions using different test modal feature columns.

With n modal feature columns accompanying each test n-DOF structure and constructing n underdetermined linear systems of equations, there are n recovered sparse solutions $\boldsymbol{\alpha}_i^\star$'s $(i = 1, ..., n)$. Alternatively a simpler and robust damage identification index can be used,

$$\epsilon_j = \sum_{i=1}^{n} \|\hat{\boldsymbol{\varphi}}_i - \boldsymbol{\Phi}_j(\boldsymbol{\alpha}_i^\star)_j\|_{\ell_2} \tag{5.7}$$

where $(\boldsymbol{\alpha}_i^\star)_j \in \mathbb{R}^n$ $(j = 1, ..., N)$ is the jth segment of $\boldsymbol{\alpha}_i^\star \in \mathbb{R}^w$, only consisting of n entries associated with the predesigned jth class; ϵ_j is the recovery error associated with the jth class, summating over the whole n test modal features. This index evaluates how well the partial solution $(\boldsymbol{\alpha}_i^\star)_j$ associated with the jth class reconstructs the test feature $\hat{\boldsymbol{\varphi}}_i \in \mathbb{R}^n$ $(i = 1, ..., n)$; obviously the smallest ϵ among $j = 1, ..., N$ determines which predefined class the test features belong to (i.e., if the test features indeed belongs to, say, the jth class, then its associated recovery error ϵ_j would naturally be smallest), such that the damage class of the test structure can be accordingly assigned.

5.3.5 Robustness of the SR classification

In practice, the test feature column may not exactly correspond to any one of the predefined reference feature columns; this may be due to model errors or simply because the reference dictionary contains no such damage class with a particular feature column. However, within this reference feature dictionary, ℓ_1-minimization can still recover the sparsest solution to the classification problem, picking the most relevant damage class and rejecting all other possible but less relevant damage classes.

In case the damage class of the test structure reside outside the N individual predefined candidate damage classes, yet correspond to some *combination* of these individual candidate classes, $\boldsymbol{\alpha}_i$ will also be a sparse vector with few non-zero entries, each of which also locates the identity of the individual damage class in the combination within the reference feature dictionary. In the proposed damage identification framework, this situation arises in identifying multiple damage.

5.3.6   Limited modal feature columns and limited sensors

For the n-DOF structure (with n modes), in practice, many modes may not be excited and thus may be absent in the structural responses; as a result, CP may not extract these mode feature columns. However, as mentioned in Section 5.3.4, not all modal feature columns are needed for the sparse representation classification method; if only p (it can be $p \ll n$) mode feature columns are available, then in Eq. (5.7), ϵ will only summate over the p modes.

Another common situation is that only limited m sensors are available. If $m < n$ or m is less than the active mode number, the modal identification problem in Eq. (2.13) becomes underdetermined; where, CP will "blindly" extract m mode feature columns $\hat{\boldsymbol{\varphi}}_i \in \mathbb{R}^m$ ($i = 1, ..., m$) that do not correspond to the theoretical structural modeshapes–CP still functions as a dimensionality reduction tool. In this situation, the sparse classification framework still holds provided that the reference matrix is also set up along the same lines (applying CP on m sensors' structural responses from the FEM model), i.e., $\boldsymbol{\Psi} \in \mathbb{R}^{m \times w}$, $w = m \times N$, since $\hat{\boldsymbol{\varphi}}_i \in \mathbb{R}^m$ will still correspond to one of the $\boldsymbol{\Psi} \in \mathbb{R}^{m \times w}$'s columns. However, if m is too small then the spatial resolution would be very poor for locating damage; for example, one may not expect to identify the damage location of a large-scale structure using only one

or two sensors.

5.4 Damage identification algorithm procedure

The proposed damage identification based on SR in the classification framework consists of two stages: locate damage (Stage 1) and assess damage severity (Stage 2). Each stage undergoes the two-step CP-SR procedure: modal feature extraction by CP (Step 1) and SR classification (Step 2); Fig. 5.2 shows the flowchart of the CP-SR procedure, and the whole task is implemented as follows:

Stage 1. Identification of damage location

(1a) Predefine damage classes of the reference structural FEM model with all possible damage locations (e.g., a damage class is defined as the structure damaged at one location with 50% stiffness reduction). For each damage class, simulate the structural responses from the corresponding FEM model, and then use CP to extract the modal feature columns of this damage class. Concatenate all the modal feature columns of all candidate damage classes for the reference feature matrix or dictionary.

(1b) From the structural responses of the test structure, use CP to extract the test modal feature columns.

(2) For *each* test modal feature column, use ℓ_1-minimization to solve (P_1) and obtain the sparse solution. Calculate the recovery error of each damage class using Eq. (5.7). The damage class with the smallest recovery error is the one that the test structure belongs to.

Stage 2. Identification of damage extent Repeat Stage 1, except that the predefined damage classes only consider the reference structural FEM model damaged at the *identified* location with all possible damage extents.
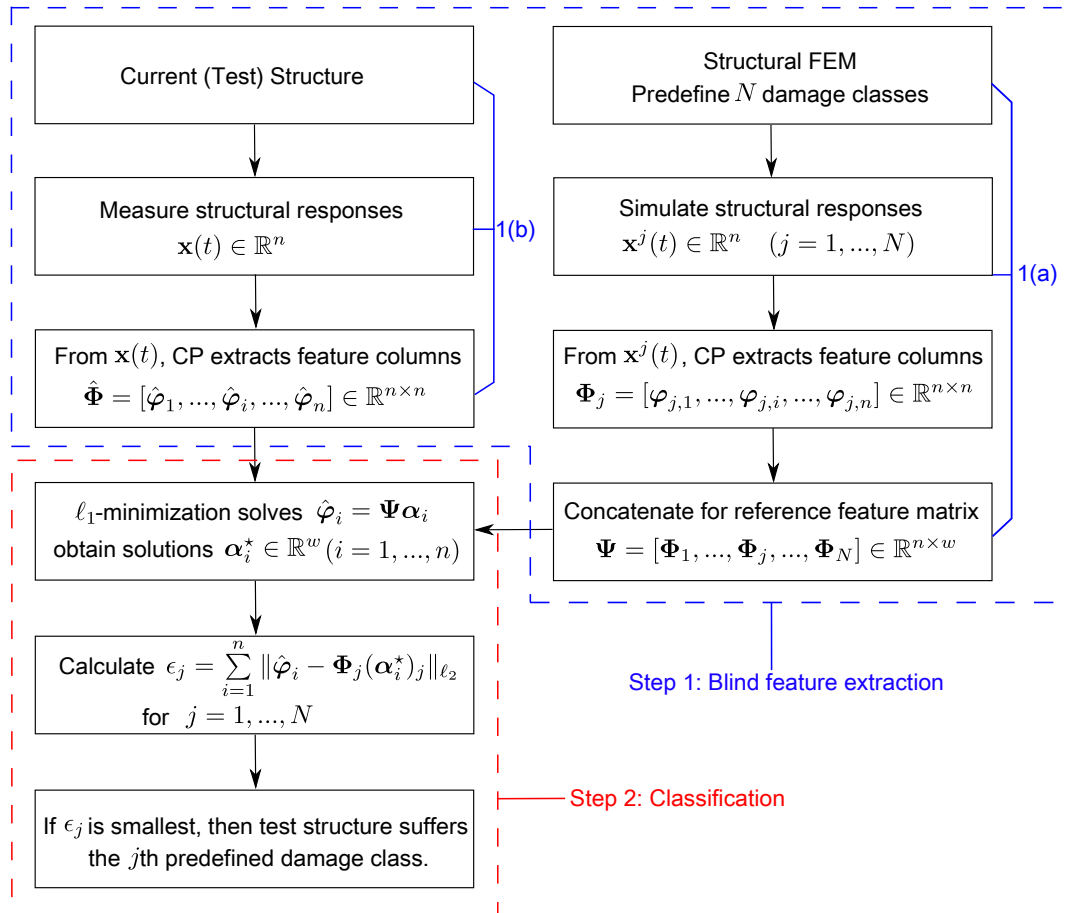
Figure 5.2 : The flowchart of the CP-SR damage identification algorithm. Both Stage 1 locating damage and Stage 2 assessing damage extent undergo this procedure, except the predefined damage classes are different. ($w = n \times N$, and $j = 1, ..., N$ means simulating structural responses for class 1, and then repeat it for class 2, and so on; similarly for $i = 1, ...n.$)

5.5 Numerical simulations

This section presents two numerical structure examples to investigate the ability of the developed CP-SR damage identification method; one is a discrete mass-spring damped model, and the other is a distributed-parameter fixed beam model.

5.5.1 Damage identification of a discrete system

The proposed CP-SR damage identification method is first validated by numerical simulations on an $n = 12$-DOF linear time-invariant spring-mass damped model (Fig. 2.9). The parameters are set as follows: the masses are $m_1 = 2, m_2 = m_3 = ... = m_{11} = 1, m_{12} = 3$, the spring stiffness are $k_1 = k_2 = ... = k_{13} = 1$, and proportional damping is added as $\mathbf{C} = 0.03\mathbf{M}$. The first four natural frequencies of the structure are 0.0378, 0.0716, 0.0990, 0.1250 Hz, respectively. Damage is modeled by stiffness reduction of the spring. Impact or Gaussian white noise excitation is induced at the 6th DOF (mass) and the 200-second structural responses are obtained by Newmark-Beta algorithm with a sampling frequency of 10 Hz. CP extracts structural modal features in the feature extraction step.

5.5.1.1 Noise-free damage identification

Damage localization The first stage is identifying damage location. Since there are 13 candidate damage locations in the structural model, $N = 13$ distinct pre-designed damage classes are simulated, respectively, each has 50% stiffness reduction at single location (e.g., class 1 is defined as 50% stiffness reduction at the Spring 1). The detailed predefined reference damage classes are listed in Table 5.1. For *each* of the $N = 13$ predefined damage classes, $p = n = 12$ modal feature columns are extracted by the CP algorithm from the structural responses measured at the $m = 12$ sensors of the structural FEM model. Concatenating all the modal feature columns of the 13 damage classes, the reference feature matrix $\mathbf{\Psi}_1 \in \mathbb{R}^{n \times w}$ (the subscript here means for Stage 1 of locating damage) is set up with $n = 12$ and $w = 12 \times 13 = 156$ columns and is thus of size 12×156 (Table 5.1); accordingly, for example, the 1st to 12th columns in $\mathbf{\Psi}_1$ is $\mathbf{\Phi}_1 \in \mathbb{R}^{12 \times 12}$ that belongs to damage class 1, and so on. Note

that $\boldsymbol{\Psi}_1$ only needs to be computed once.

Table 5.2 lists the test structure cases with different damage location of different damage extents. For *each* test case, $p = n = 12$ test modal feature columns (e.g., the ith column is $\hat{\boldsymbol{\varphi}}_i \in \mathbb{R}^{12}$) are also extracted by CP from the structural responses; combining with $\boldsymbol{\Psi}_1 \in \mathbb{R}^{12 \times 156}$, 12 underdetermined linear systems of equations $\hat{\boldsymbol{\varphi}}_i = \boldsymbol{\Psi}_1 \boldsymbol{\alpha}_i$ ($i = 1, ..., 12$) are established, each of which is then solved by ℓ_1-minimization to obtain $\boldsymbol{\alpha}_i^\star \in \mathbb{R}^{156}$ ($i = 1, ..., 12$), and the damage index is calculated using Eq. (5.7).

Test Case 1-6 of single damage are considered in this subsection. Fig. 5.3 presents one specific example of the sparse solution to the SR classification framework: the test modal feature is the 12th column $\hat{\boldsymbol{\varphi}}_{12} \in \mathbb{R}^{12}$ of test structure of Test Case 2 (Table 5.2), and the recovered sparse solution $\boldsymbol{\alpha}_{12}^\star \in \mathbb{R}^{156}$ to the underdetermined problem $\hat{\boldsymbol{\varphi}}_{12} = \boldsymbol{\Psi}_1 \boldsymbol{\alpha}_{12}$ has a significant non-zero entry exactly at the 72nd location; as the 61st to 72nd columns of the reference feature dictionary $\boldsymbol{\Psi}_1 \in \mathbb{R}^{12 \times 156}$ is $\boldsymbol{\Phi}_6 \in \mathbb{R}^{12 \times 12}$ which belongs to the predefined damage class 6, then this non-zero $\alpha_{6,12}^\star$ directly indicates the test structure to be damage class 6 (damaged at the 6th spring, see Table 5.1), which exactly agrees with Test Case 2.

As mentioned, it may be more robust to use the recovery error damage index (Eq. (5.7)) involving more test modal features; take the Test Case 2 for example, there are $p = n = 12$ test modal feature columns available, use each of them to obtain 12 sparse solutions along with Eq. (5.7) to calculate the recovery error associated with each predefined damage class. Clearly in Fig. 5.4(a) and Fig. 5.5(a) for Test Case 1-6, damage is accurately located.

It is worth noting that the relaxation of the SR classification framework discussed in Section 5.3.5 is indicated here. Take Test Case 1 (90% damage at the 6th spring) for example, the reference feature dictionary matrix $\boldsymbol{\Psi}_1$ contains no exactly such a

Table 5.1 : Predefined damage classes of the 12-DOF structure for Stage 1.

Class	1	2	$\cdots$	12	13
Damage location	Spring 1	Spring 2	$\cdots$	Spring 12	Spring 13
Damage severity	50%	50%	$\cdots$	50%	50%
Obtained features	$\boldsymbol{\Phi}_1 \in \mathbb{R}^{12\times12}$	$\boldsymbol{\Phi}_2 \in \mathbb{R}^{12\times12}$	$\cdots$	$\boldsymbol{\Phi}_{12} \in \mathbb{R}^{12\times12}$	$\boldsymbol{\Phi}_{13} \in \mathbb{R}^{12\times12}$
Reference matrix	$\boldsymbol{\Psi}_1 = [\boldsymbol{\Phi}_1, ..., \boldsymbol{\Phi}_j, ..., \boldsymbol{\Phi}_{13}] \in \mathbb{R}^{12\times156}$				

Table 5.2 : Test cases of the 12-DOF structure.

	Single damage						Multiple damage	
Test case	1	2	3	4	5	6	7	8
Damage location	Spring 6	6	6	Spring 3	3	3	Spring 3&6	Spring 4&7
Damage severity	90%	50%	20%	90%	50%	20%	50%& 50%	20%& 50%
Extracted features	Each Test Case: $\hat{\boldsymbol{\Phi}} = [\hat{\boldsymbol{\varphi}}_1, ..., \hat{\boldsymbol{\varphi}}_i, ..., \hat{\boldsymbol{\varphi}}_{12}] \in \mathbb{R}^{12\times12}$							

damage class (Table 5.1); however, SR automatically picks the *most relevant* class in the dictionary (50% damage at the 6th spring), rejecting all other possible but less irrelevant classes (damage at other springs). This is sufficient for locating damage while keeping the reference feature dictionary not too large by avoiding vast damage

Table 5.3 : Predefined damage classes of the 12-DOF structure for Stage 2 of Test Case 1-3.

Class	1	2	3	4	5
Damage location	Spring 6	Spring 6	Spring 6	Spring 6	Spring 6
Damage severity	10%	20%	50%	70%	90%
Obtained features	$\mathbf{\Phi}_1 \in \mathbb{R}^{12 \times 12}$	$\mathbf{\Phi}_2 \in \mathbb{R}^{12 \times 12}$	$\mathbf{\Phi}_3 \in \mathbb{R}^{12 \times 12}$	$\mathbf{\Phi}_4 \in \mathbb{R}^{12 \times 12}$	$\mathbf{\Phi}_5 \in \mathbb{R}^{12 \times 12}$
Reference matrix	$\mathbf{\Psi}_2 = [\mathbf{\Phi}_1, ..., \mathbf{\Phi}_j, ..., \mathbf{\Phi}_5] \in \mathbb{R}^{12 \times 60}$				

classes with a combination of different damage locations and extent; such a strategy is further beneficial to a computationally efficient identification. As expected, the recovery error (damage index) at the damage location for Test Case 2 is smallest among Test Case 1-3 (similarly Test Case 5 is smallest among Test Case 4-6), since it has exact corresponding damage class in the reference feature dictionary (Class 6 in Table 5.1).

Identification of damage severity After damage is located, its severity can be conveniently identified as Stage 2 with similar scheme. Take Test Case 1-3 for example, since damage has been already identified at the 6th spring in Stage 1, the predefined damage classes can only consider different damage extents all at this location, as listed in Table 5.3. Here, $N = 5$ candidate damage extents are considered, that is 10%, 20%, 50%, 70%, 90% (arbitrarily finer levels can also be predesigned),
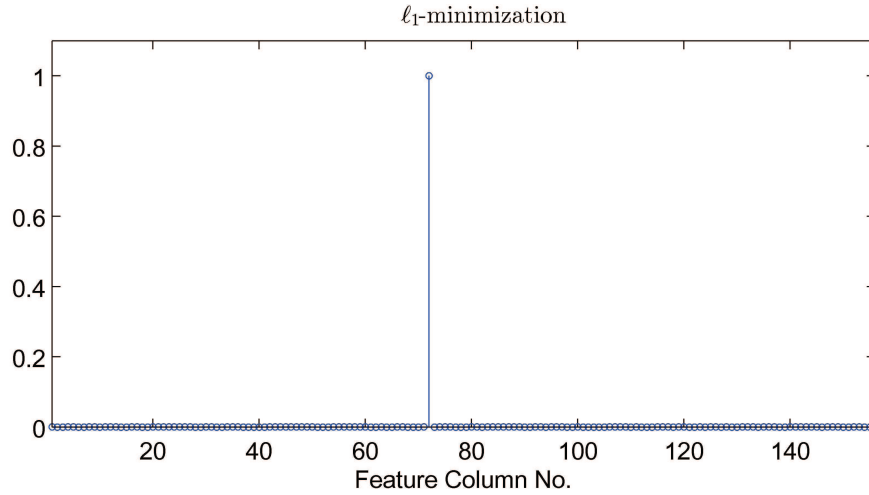
Figure 5.3 : The sparse solution $\boldsymbol{\alpha}_{12}^{\star} \in \mathbb{R}^{156}$ to Eq. (5.3) sought by ℓ_1-minimization. The test feature column $\hat{\boldsymbol{\varphi}}_{12} \in \mathbb{R}^{12}$ is the 12th column (hence the subscript of $\boldsymbol{\alpha}_{12}^{\star}$ and $\hat{\boldsymbol{\varphi}}_{12}$) from Test Case 2 extracted by CP, and the reference feature matrix is $\boldsymbol{\Psi}_1 \in \mathbb{R}^{12 \times 156}$ defined in Table 2. The significant non-zero entry is at the 72nd location, which exactly corresponds to the predefined 6th damage class whose feature columns $\boldsymbol{\Phi}_6 \in \mathbb{R}^{12 \times 12}$ range from the 61st -72nd locations in the reference feature dictionary $\boldsymbol{\Psi}_1 \in \mathbb{R}^{12 \times 156}$.

and the reference feature matrix $\boldsymbol{\Psi}_2$ (Stage 2) therefore comprises $w = 12 \times 5 = 60$ modal feature columns and is of size 12×60. Same procedures are for Test Case 4-6.

CP-SR is applied and the identification results are presented in Fig. 5.4(b) for Test Case 1-3 and Fig. 5.5(b) for Test Case 4-6, which indicate accurate identification of damage extent of the test structure. This example illustrates the convenience of the two-stage identification method: by taking advantage of the identified damage location information, the reference dictionary $\boldsymbol{\Psi}_2$ for identification of damage extent can be dramatically small with few relevant damage classes at the identified damage location, making the procedure more efficient.

Identification of multiple damage In case the test structure suffers damage at multiple locations, it is supposed to set up a new reference feature dictionary compris-

ing all the features of various candidate damage classes, each of which simulates damage at multiple locations. This, unfortunately, will result in an exponential increase of the reference feature matrix size, since there are numerous possible combinations of the damage locations.

In the SR classification method, the multiple-damage class can be approximately treated as a linear combination of the corresponding single-damage classes. Such a strategy, as mentioned in Section 5.3.5, induces the sparse solution to yield multiple non-zero entries, each identifies the individual damage class (location). Following this analysis, with the same reference matrix $\mathbf{\Psi}_1$ consisting of only predefined classes each with single damage location, the proposed method is able to identify multiple damage.

Test Case 7-8 of multiple damage (Table 5.2) are considered. For Stage 1 of locating damage, the above same reference matrix $\mathbf{\Psi}_1 \in \mathbb{R}^{12 \times 156}$ is used. After conducting CP-SR, the calculated recovery errors are presented in Fig. 5.6(a), indicating successful locating multiple damage. Take Test Case 7 (damage at 3rd and 6th springs) for example, there are two significantly smaller recovery errors as a combination of two individual damage locations: one is at the 3rd (pointing to the 3rd class) and the other at the 6th (pointing to the 6th class).

With the identified information of damage locations, a new reference matrix $\mathbf{\Psi}_2$ is accordingly set up for identifying the damage extent. Here, three predefined extents (20%, 50%, and 90%) are used, though finer levels can always be predesigned. Again take Test Case 7 for example, the predefined classes only consist of different damage extents at the identified damage locations at 3rd and 6th spring; this results in $3^2 = 9$ distinct combinations and thus $N = 9$ reference damage classes to simulate. Therefore, $\mathbf{\Psi}_2$ has $w = 12 \times 9 = 108$ modal feature columns and is of size 12×108.

As can be seen in Fig. 5.6(b), the damage extents at the couple of damage locations are also successfully identified, matching the test structure cases.

Random vibration The effectiveness of the proposed method in random vibration is also studied. Test Case 1-3 are considered, where the test structure is subject to zero-mean Gaussian white noise excitation at the 6th DOF, and CP are used to extract the test modal feature columns from the random responses of the test structure. As mentioned, the reference feature matrix Ψ_1 remains unchanged, and Ψ_2 is identical to that in Section 5.5.1.1. The CP-SR identification procedures are conducted. Fig. 5.7 shows that the proposed method shows no degradation in random vibration. This is because the CP algorithm is robust even in random vibration to extract those modal features (modeshapes); see Chapter 2.

Figure 5.4 : Identification results by CP-SR of (a) damage location and (b) damage extent of Test Case 1-3 with single damage.

Figure 5.5 : Identification results by CP-SR of (a) damage location and (b) damage extent of Test Case 4-6 with single damage.
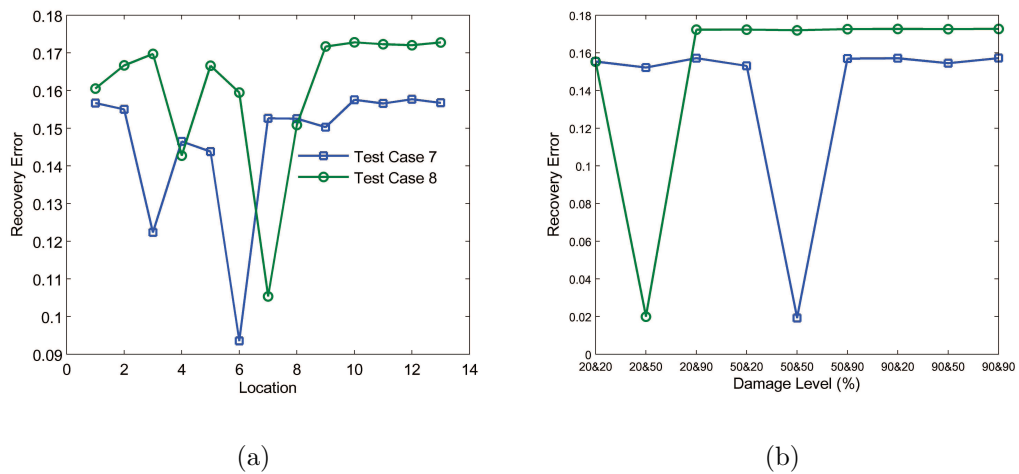
Figure 5.6 : Identification results by CP-SR of (a) damage location and (b) damage extent of Test Case 7-8 with multiple damage.

5.5.1.2 Damage identification with limited features in noisy environment

To be effective for practical applications, the robustness of the proposed CP-SR method against noise must be investigated. This sub-section studies its performance in noisy environment, taking the Test Case 2 for instance. Zero-mean Gaussian white
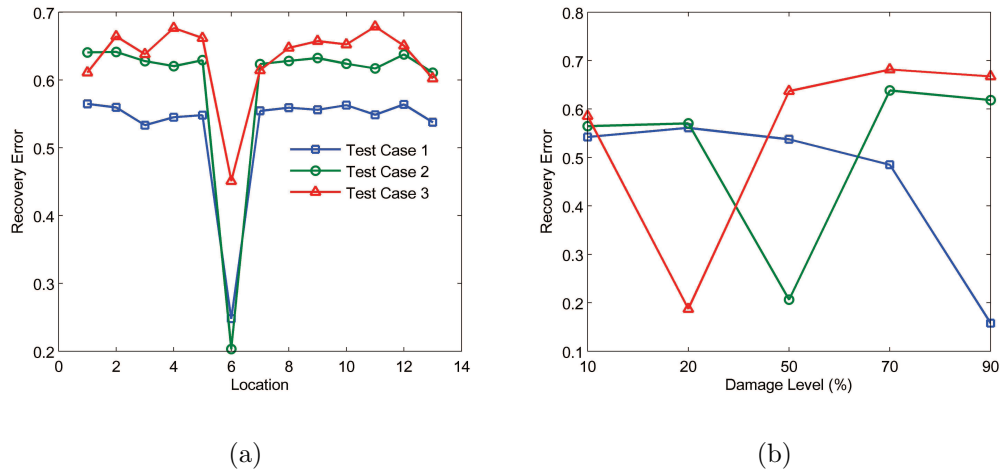
Figure 5.7 : Identification results by CP-SR of (a) damage location and (b) damage extent of Test Case 1-3 with single damage in random vibration.

noise is added to the structural responses measured from the test structure with various signal-to-noise-ratio (SNR) levels, respectively.

The reference feature dictionary for the two stages has already been set up above. Same procedures of CP-SR are performed and the identification results are presented in Fig. 5.8. It is seen that the method accurately locates damage at SNR as low as 15 dB (17.8% RMS noise level), while identification of the damage severity fails at this noise level. This is because with significant noise, the modal feature columns extracted by CP from noisy structural responses can no longer reflect the structural damage features; see for example the lower mode feature columns (Fig. 5.9(a) and the high mode feature (Fig. 5.9(b)), which have been affected by heavy noise.

However, such a problem may be solved by using limited modal feature columns in the CP-SR procedure. As the structural responses are typically dominated by lower-mode components which contain most of the damage information, it is natural to drop those higher-mode components that have been largely contaminated by noise-

these are termed "noise features". This can be implemented automatically since the modal feature columns extracted by the CP algorithm are approximately in frequency sequence; see Chapter 2 and Ref. [147] for more details.

Therefore in the following heavily noisy environment, only the $p = 3$ lower-mode feature columns of the test structure are used and the CP-SR procedures are implemented. The results shown in Fig. 5.10 support such a strategy in noisy environment. There, when the noise is as heavy as comparable to the structural response (SNR=0 dB or 100% RMS noise), CP-SR can still locate damage and assess the damage level.

However, as mentioned in Section 5.3.4, it is usually more robust to include more modal feature columns of the test structure when noise is not heavy; Fig. 5.11 shows the identification results using only $p = 3$ lower-mode feature columns of the test structure in Test Case 1-3 without noise. Clearly Test Case 3 (20% damage) is not accurately identified; contrarily, when using $p = n = 12$ test modal feature columns, this small damage can be accurately identified, as already shown in Fig. 5.4.

This occurs primarily because small damage may cause little variation of test modal features $\hat{\mathbf{\Phi}} \in \mathbb{R}^{12 \times 12}$ that is distributed among all its 12 columns. As such, it is necessary to use all its modal feature columns for the method to identify this little variation (damage)–this is exactly the original strategy of the method: the damage index (recovery error) (Eq. (5.7)) is summated over all modal feature columns-instead of dropping many columns which may cause loss of variation information. Therefore, in heavily noisy environment, this method with partial features ($p < n$) is incapable of identifying *small* damage.

5.5.1.3 Damage identification with limited sensors

This subsection studies the performance of CP-SR when sensors are inadequate compared to the active modes or the DOFs of the structure, i.e., $m < n$. In this situation as mentioned in Section 3.6, the system identification problem Eq. (2.13) becomes underdetermined, where CP extracts $p = m < n$ "blind" feature columns that do not exactly correspond to the modeshapes; most of all, the modal feature columns are degenerate for limited spatial resolution.

For illustrations, Test Case 1-3 are used for example with the same above settings, but using only $m = 6$ sensors. Then CP extracts six modal feature columns for the test structure as well as for each damage class of the structural FEM model, respectively; i.e., $\hat{\boldsymbol{\varphi}}_i \in \mathbb{R}^6$, $w = 6 \times 13 = 78$ for Stage 1 ($w = 6 \times 5 = 30$ for Stage 2), and the reference feature matrix $\boldsymbol{\Psi}_1 \in \mathbb{R}^{6 \times 78}$ in Stage 1 ($\boldsymbol{\Psi}_2 \in \mathbb{R}^{6 \times 30}$ for Stage 2). Fig. 5.12 shows that the CP-SR successfully identified the damage pattern of Test Case 1-2 while failed on the small damage case. This indicates that CP-SR holds as long as the "blind" features reflect the structural variation due to damage as discussed in Section 5.3.6, and its failure on small damage case is mostly because the degenerate feature columns with inherently poor spatial resolution do not contain sufficient structural variation due to *small* damage.

5.5.2 Damage identification of a distributed-parameter beam

This section considers applying CP-SR on a two-dimensional distributed-parameter fixed beam model (Fig. 2.12) shown in Chapter 2. In the feature extraction step, CP extracts $p = m = 6$ modal feature columns from the structural responses. Damage is simulated by reducing the moment of inertia of the cross section. The predefined damage classes are introduced along the same line with those in Section 5.5.1.1: for
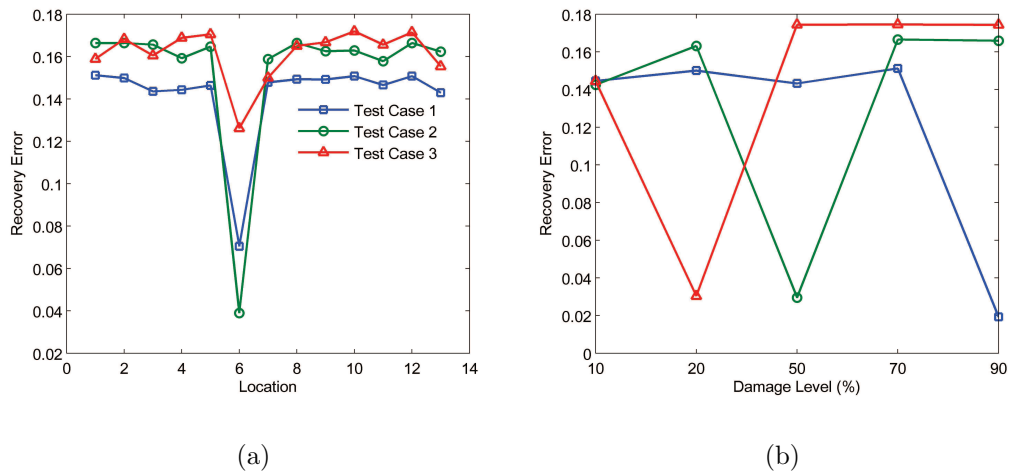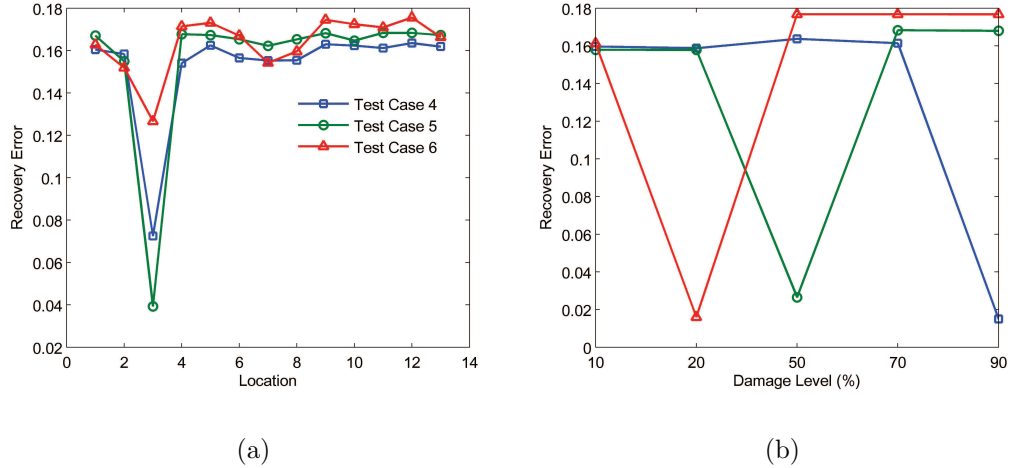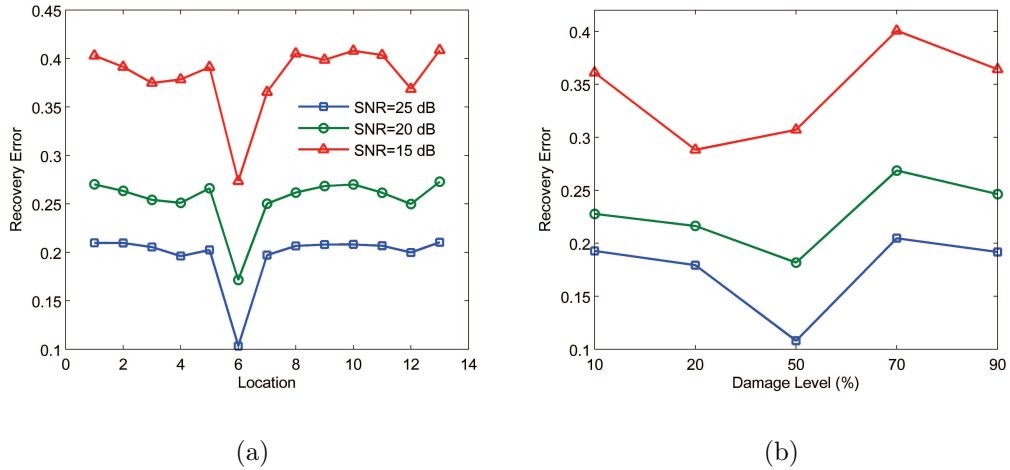
Figure 5.8 : Identification results by CP-SR of (a) damage location and (b) damage extent of Test Case 2 with single damage under different noise levels.

Stage 1, class 1 with 50% damage at element 1, class 2 with 50% damage at element 2, and so on, resulting in $N = 7$ damage classes predefined for Stage 1. For each class, CP extracts six modal feature columns from the structural responses, i.e., $p = 6$, $w = 6 \times 7 = 42$, and $\mathbf{\Psi}_1 \in \mathbb{R}^{6 \times 42}$ for Stage 1.

Three Test Case 1-3 are considered similar with those in Section 5.5.1.1: 90%, 50%, 20% damage at Element 4, respectively. Fig. 5.13(a) presents the identification results of the damage location; clearly CP-SR is accurate for all the test cases. After damage location is identified at the 4th element, Stage 2 for identifying damage extents is conducted. Also $N = 5$ damage extents are considered, that is 10%, 20%, 50%, 70%, and 90%, thus $w = 6 \times 5 = 30$ and the reference feature matrix for Stage 2 is set up $\mathbf{\Psi}_2 \in \mathbb{R}^{6 \times 30}$. As seen in Fig. 5.13(b), CP-SR is also able to identify the damage extents in each test case. This example shows that CP-SR is also applicable on continuous structures. In addition, the method performs well using limited modal feature columns ($p < n$).
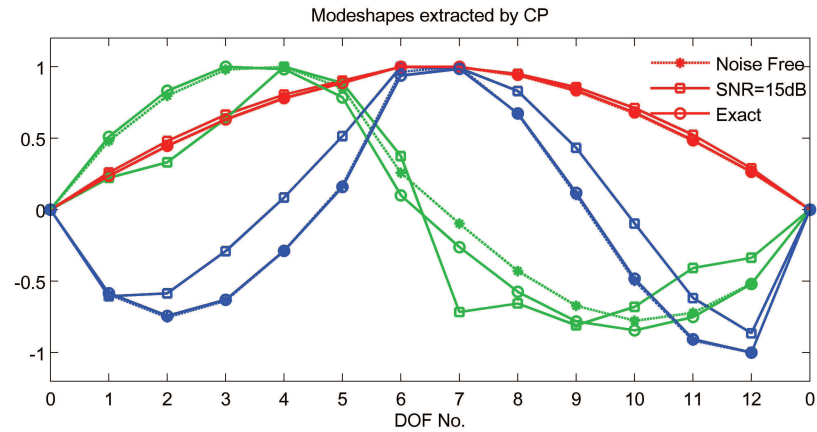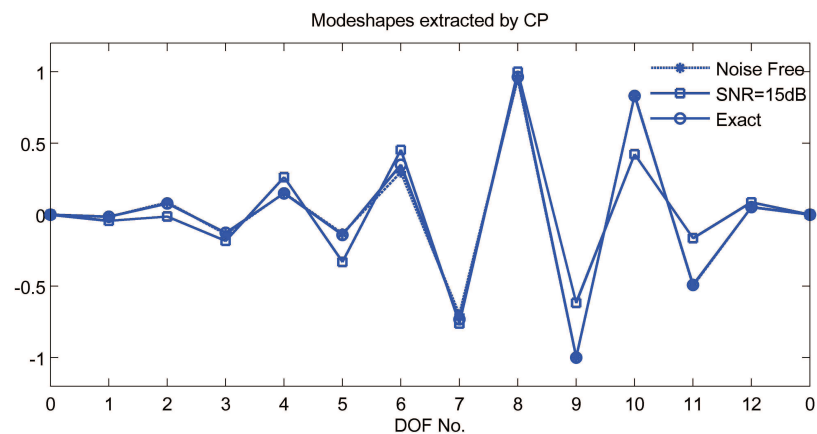
Figure 5.9 : The modeshapes (modal feature columns) from Test Case 2 extracted by CP under noise level of SNR=15dB, compared to those exact modeshapes and those extracted by CP without noise: (a) the 1st-3rd modes and (b) the 12th mode.

5.6   Experimental study

The proposed CP-SR damage identification method is applied on an experimental building structure (Fig. 4.8(a)) (also described in Chapter 4). It is a three-story structure with dominant mass on each floor. Originally four accelerometers are attached to record the structural responses while it was subject to band-limited white
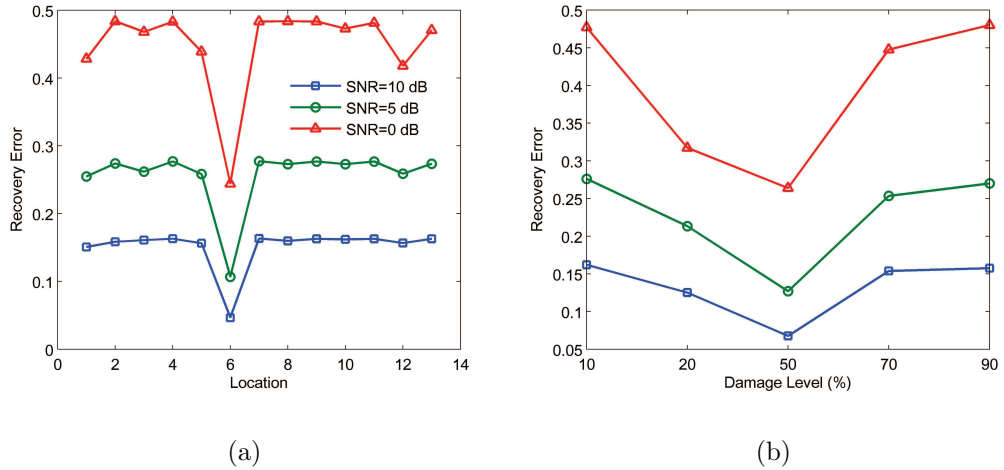
Figure 5.10 : Identification results by CP-SR using only three lower-mode feature columns of (a) damage location and (b) damage extent of Test Case 2 with single damage under different noise levels.
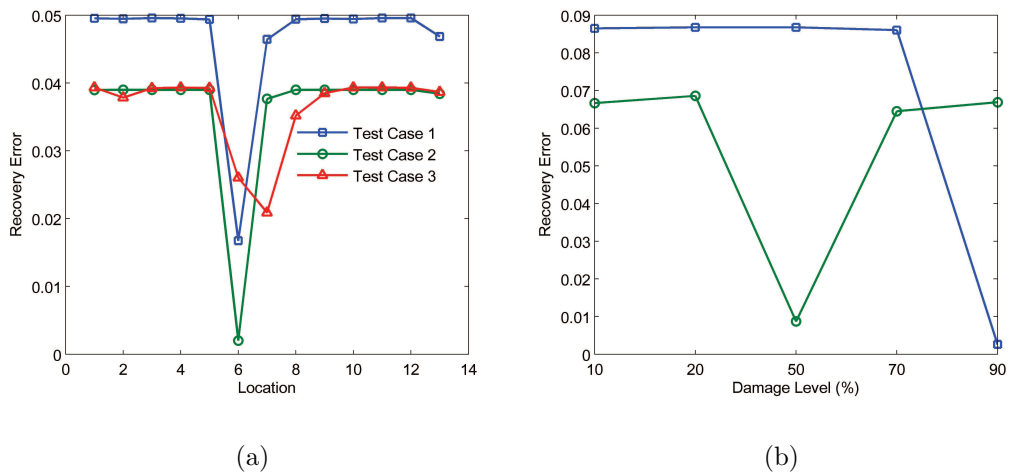
Figure 5.11 : Identification results by CP-SR using only three lower-mode feature columns of (a) damage location and (b) damage extent of Test Case 1-3 with single damage without noise.

noise excitation at the base: three were on the right side of each floor and one on the left side of the 1st floor. The sampling frequency was set at 200 Hz. During the test, the left column between the base and the 1st floor suddenly fractured due to damage
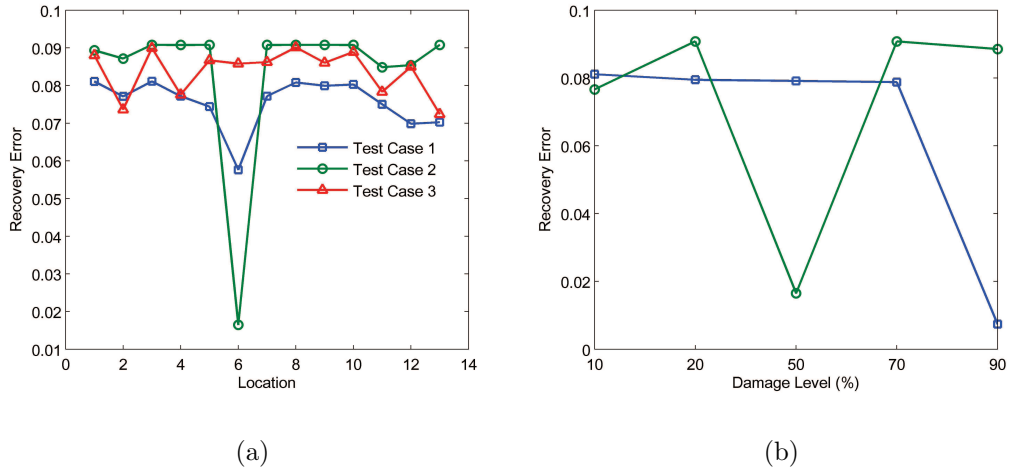
Figure 5.12 : Identification results by CP-SR using only six sensors of (a) damage location and (b) damage extent of Test Case 1-3 with single damage.
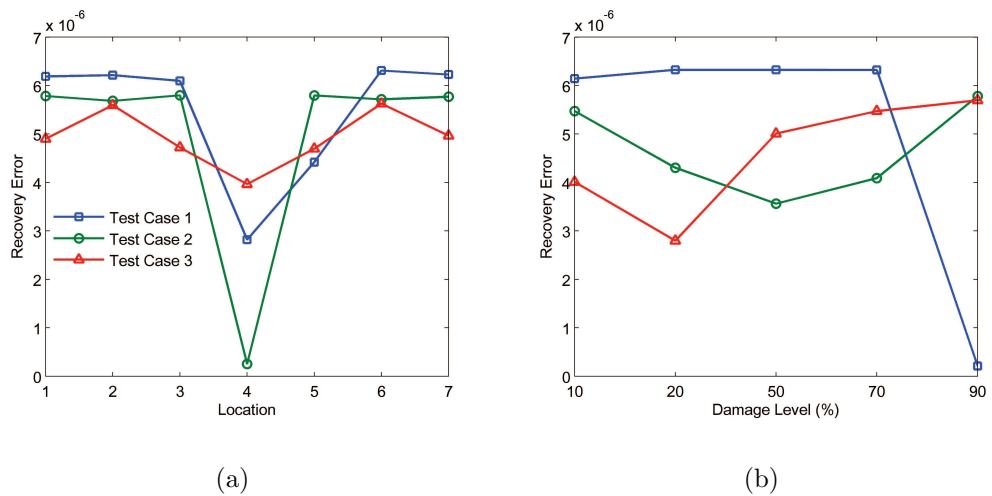
Figure 5.13 : Identification results by CP-SR of the distributed-parameter beam of (a) damage location and (b) damage extent.

at the weld right below the front beam of the 1st floor. However, an FEM model of the healthy structure has already been set up before the test.

A segment of 20-second recorded structural responses (damage occurred at the 10th second) from $m = 3$ accelerometers on the right side and their (normalized)

power spectra density (PSD) before (0-10 second) and after damage (10-20 second) are presented in Fig. 5.14. CP and SOBI are applied to extract three mode feature columns from the structural responses before and after damage, respectively. These "blind" feature columns contain the structural damage information and can be used for the following step of the proposed method.

In building the reference feature matrix using the FEM model, damage is simulated by reducing the lateral stiffness of each floor. For Stage 1 of locating damage, $N = 3$ candidate damage locations are thus considered: class 1 with 50% lateral stiffness reduction of the columns between the base and the 1st floor, and so on for class 2 and 3. Therefore, $w = 3 \times 3 = 9$ and $\mathbf{\Psi}_1 \in \mathbb{R}^{3 \times 9}$. The test feature columns $\hat{\boldsymbol{\varphi}}_i \in \mathbb{R}^3$ ($i = 1, 2, 3$, shown in Fig. 5.15(b)) extracted by CP from the real-recorded post-damage (10-20 second) are used. The identification results using $p = 3$ (including the "blind" features) or $p = 1$ (only the 1st mode) feature columns are shown in Fig. 5.16(a), which indicates that damage is accurately located by CP-SR on the first floor (the column between the base and the 1st floor).

After damage is located, the reference feature matrix in Stage 2 is set up, simulating $N = 5$ damage classes with different damage extents at the identified damage location (i.e., class 1 to 5 are defined by lateral stiffness reduction 10%, 30%, 50%, 70%, and 90%, respectively, all between the base and the 1st floor). $w = 3 \times 5 = 15$ and $\mathbf{\Psi}_2 \in \mathbb{R}^{3 \times 15}$. As seen in Fig. 5.16(b), with both $p = 3$ and limited $p = 1$ feature columns, the CP-SR method identifies the structure to belong to the most serious damage class (the 5th damage class), which quite matches the actual situation-the damaged column was seriously fractured.
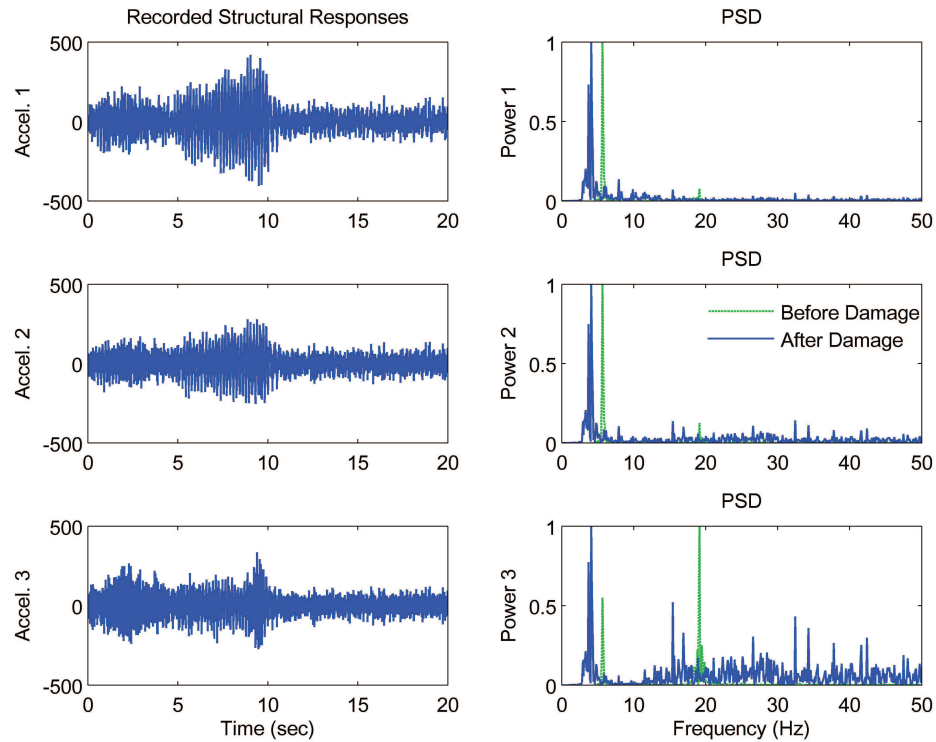
Figure 5.14 : The recorded accelerations (damage at the 10th second) and their normalized power spectra density (PSD) before and after damage.

5.7 Summary

Exploiting the sparsity nature implied in the classification problem itself, this chapter develops a new two-step damage identification method via a combination of blind feature extraction and sparse representation classification framework–an data-driven non-parametric formulation–for identification of both structural damage location and severity, without an parametric classifier model or the computationally-intensive training process. In the feature extraction step, the modal features are blindly extracted by the unsupervised CP system identification algorithm. Then in the classification step, the sparsity nature implied in the classification problem itself is exploited:
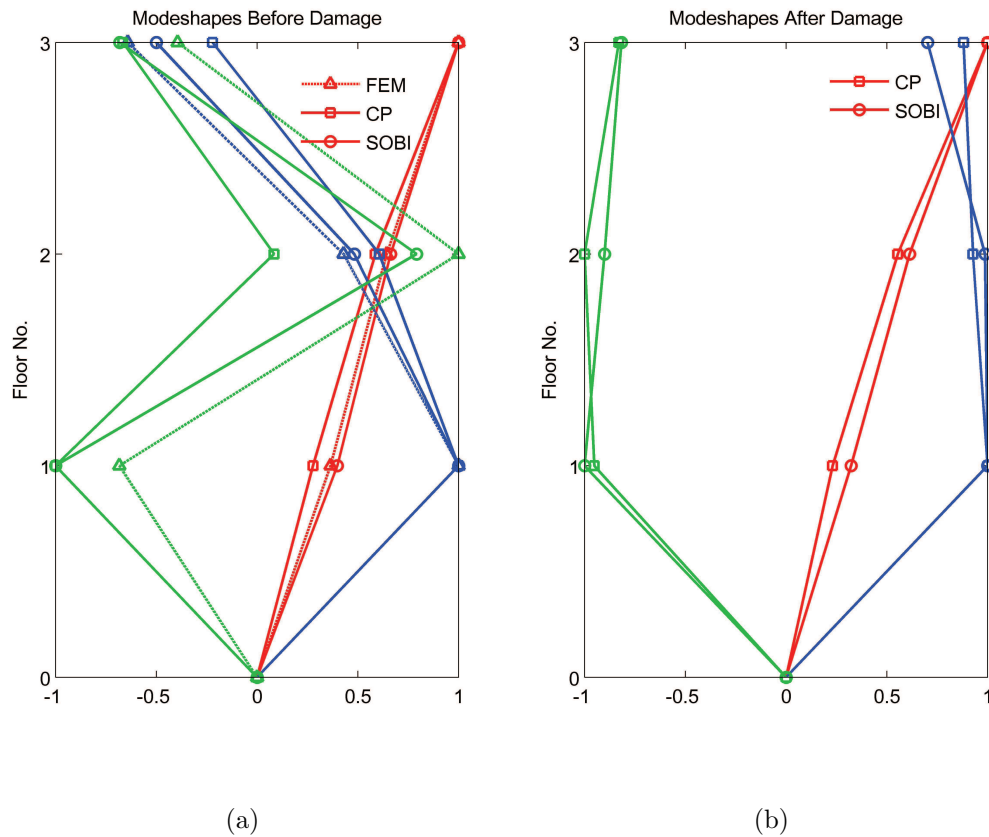
Figure 5.15 : The modeshapes (modal feature columns) extracted by CP compared with those by SOBI and eigenvectors of FEM: (a) before damage and (b) after damage.

expressing the modal feature column of the test structure as a linear combination of the bases of the over-complete reference feature dictionary builds an underdetermined linear system of equations, whose underlying sparse representation is correctly recovered by ℓ_1-minimization, directly assigning the most relevant damage class of the test feature (and rejecting all other possible but less relevant damage classes) so as to realize damage identification.

The capability of CP-SR is first validated by numerical simulations. Results illustrate that CP-SR is suitable for identification of small and severe single or multiple damage. Attribute to the capability of the CP algorithm, the method is also ro-
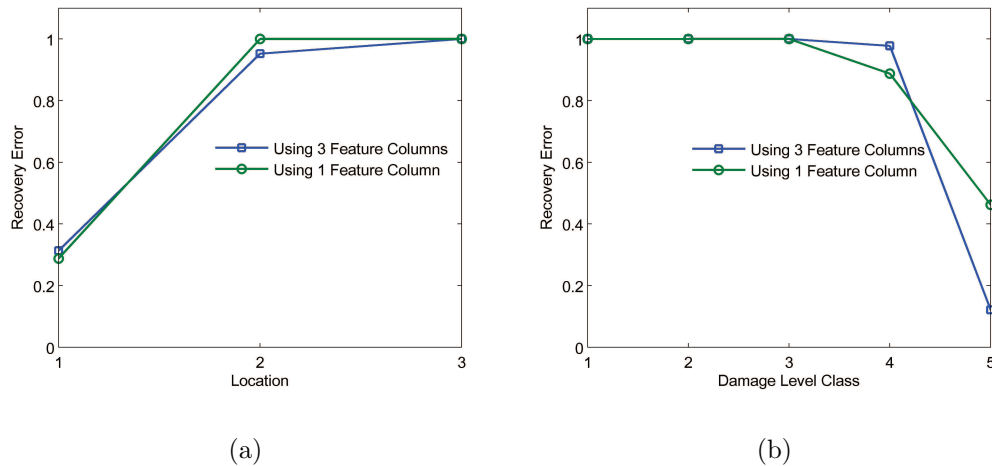
Figure 5.16 : Identification results by CP-SR using three mode feature columns and using only the 1st modeshape (modal feature column) of the experimental structure of (a) damage location and (b) damage extent. (The recovery errors are normalized.)

bust to random excitation. Its effectiveness in noisy environment is also studied. It is found that using only few lower-mode features enhances the robustness of the method against heavy noise, which, in turn, is compromised in identification of very small damage. It is also found that CP-SR is incapable of identifying small damage with very limited sensors or poor spatial resolution. CP-SR is successfully applied on an experimental building structure in both identifying damage location and estimating damage extent. The method is shown to have straightforward implementation and efficient computation as well as robustness in identification of structural damage.

Chapter 6

Dynamic Imaging

This chapter complements the previous Chapter 4 and Chapter 5 for the objective of a multi-scale structural damage detection in a data-driven framework by developing a new local structural assessment method: dynamic imaging (close-up "filming") of structures. The data structure of the multiple images is exploited, which are decomposed into a superposition of a low-rank background component and a sparse innovation (dynamic) component. The low-rank component represents the irrelevant temporally correlated background of the multiple frames, whereas the sparse innovation component indicates the damage-induced information. It is a data-driven and unsupervised (blind) approach that requires no parametric model or prior structural information for calibration, with the potential to benefit real-time automated local damage surveillance and diagnosis of structures where experts' visual inspection is not needed or not possible.

6.1 Introduction

Global SHM with a network of sensors on structures aims to immediately provide global signs of damage information such as damage instants, damage location, and damage severity, which depends on the resolution and dimension of the sensor network and is most effective in real-time implementation. Local structural assessment, on the other hand, conducts a close-up inspection of structural health status and

may more accurately quantify structural damage (e.g., types and severity). Current practice of local structural assessment includes on-site visual inspection of experts and nondestructive testing (e.g., acoustic and ultrasonic) [120]. Although effective in many applications, they can be time-consuming and costly, and limited to areas that are assessable to experts, making them mostly suitable for offline practice.

Recently, digital video cameras have emerged as an alternative tool to facilitate local structural assessment, with the advantages of being low-cost, non-contact, and easy installation, without the need of suspending structural operation during the inspections. Automated video surveillance has been successful in security application [33], traffic and vehicle tracking [60], and license plate recognition [5]. If permanently mounted on appropriate positions, the video cameras are able to continuously perform high-rate close imaging ("filming") of critical structural components such as bridge joints and anchored stay cables, providing local structural information for real-time local SHM. The challenge remains efficiently extracting damage features from the high-rate video stream; especially, an effective automated algorithm without the interference from experts would be highly desirable for online SHM during extreme hazards and for rapid post-disaster assessment of structures.

Quite a few research in the civil structural engineering community have been devoted to processing the images to perform damage identification, among which methods based on edge detection and morphological techniques have been widely studied (see a comprehensive review [69] and many others [3][30][62][51][155][70]). The idea is straightforward: structural damage such as cracks exhibits certain geometric features (e.g., edge-like discontinuity) in the image, which can be segmented by the edge detection or morphological techniques. Although validated by many examples, their success relies on careful mathematical modeling (mostly parametric and user-

dependent) of the geometric features of specific structural damage and the boundary information within the images can affect their effectiveness.

This chapter aims to develop a data-driven framework to automate real-time detection of structural damage by exploiting the fundamental data structure of the high-rate multiple images (video stream). The key idea is that multiple temporal images of structures are slowly changing and highly-coherent among frames and hence have a low-rank structure, unless damage occurs and induce sparse elements in the corresponding temporal frames, corrupting such a low-rank structure. On this basis, the multiple frames are decomposed into a superposition of a low-rank background component and a sparse innovation (dynamic) component by a technique called principal component pursuit (PCP, or robust principal component analysis) [23]. The low-rank component represents the irrelevant temporally correlated background of the multiple frames, whereas the sparse innovation component indicates the damage-induced information, which can be used as an autonomous trigger for damage warning in real time.

The proposed dynamic imaging approach for automated real-time damage detection is significantly different from previous work: it is a purely data-driven and unsupervised method that requires no parametric model of the geometric features or prior structural information for calibration or reference. In addition, PCP has an overwhelming probability of success under broad conditions and can be implemented by an efficient convex optimization program without tuning parameters. Therefore, it can be implemented blindly and automatically, which could benefit real-time automated local damage surveillance and diagnosis of structures without experts' involvement.

Laboratory experiments on concrete structures are conducted to validate the proposed dynamic imaging method. Results demonstrate that this method can efficiently

and effectively track the evolutionary small or severe damage by the recovered outstanding sparse innovation component with the low-rank background subtracted from the original images.

6.2 Principal component pursuit

The principal component pursuit (PCP) or robust principal component analysis (PCA) has been widely studied in high-dimensional data analysis and applications [23][111][150][113]; it is able to decompose a matrix $\mathbf{X} \in \mathbb{R}^{m \times n}$ into a superposition of a low-rank matrix $\mathbf{L} \in \mathbb{R}^{m \times n}$ and a sparse matrix $\mathbf{S} \in \mathbb{R}^{m \times n}$ as

$$\mathbf{X} = \mathbf{L} + \mathbf{S} \tag{6.1}$$

$\mathbf{S} \in \mathbb{R}^{m \times n}$ is said to be sparse if it has only few non-zero entries, and $\mathbf{L} \in \mathbb{R}^{m \times n}$ is low-rank in the sense that its singular value decomposition (SVD)

$$\mathbf{L} = \mathbf{U}\mathbf{\Sigma}\mathbf{V}^T = \sum_{i=1}^{r} \sigma_i \mathbf{u}_i \mathbf{v}_i^T \tag{6.2}$$

has few active (non-zero) singular values ($r \ll \min(m, n)$) where $\mathbf{\Sigma} \in \mathbb{R}^{r \times r}$ has r diagonal elements σ_i as the ith singular value ($\sigma_1 > ... > \sigma_i > ... > \sigma_r$), $\mathbf{U} = [\mathbf{u}_1, ..., \mathbf{u}_r] \in \mathbb{R}^{m \times r}$ and $\mathbf{V} = [\mathbf{v}_1, ..., \mathbf{v}_r] \in \mathbb{R}^{n \times r}$ are called the left- and right- singular vector matrices, respectively.

The $\mathbf{L} + \mathbf{S}$ decomposition of $\mathbf{X}$ is implemented by solving the following convex program

$$(P_*): \quad \text{minimize} \quad \|\mathbf{L}\|_* + \lambda \|\mathbf{S}\|_{\ell_1} \quad \text{subject to} \quad \mathbf{X} = \mathbf{L} + \mathbf{S} \tag{6.3}$$

where $\|\mathbf{L}\|_* := \sum_i \sigma_i(\mathbf{L})$ is termed the nuclear norm of the matrix $\mathbf{X}$, which summates its singular values; $\|\mathbf{S}\|_{\ell_1} := \sum_{ij} |s_{ij}|$ denotes the ℓ_1-norm of the matrix $\mathbf{S}$, which is

thought of as a long vector; $\lambda = 1/\sqrt{\max(m,n)}$ is an universal trading parameter [23]. The nuclear norm is the convex approximation to the rank of a matrix, and the ℓ_1-norm is the tightest convex relaxation to the well-known sparsity measure ℓ_0-norm that simply counting the non-zero entries of a matrix. (P_*) can be interpreted as to find an $\mathbf{L}^\star$ with the smallest rank plus an $\mathbf{S}^\star$ with sparsest representation that explain the observation $\mathbf{X} = \mathbf{L}^\star + \mathbf{S}^\star$.

Candes et al. [23] rigorously proves that with overwhelmingly high probability, (P_*) exactly recovers the true low-rank $\mathbf{L}$ and sparse $\mathbf{S}$, provided that $\mathbf{L}$ is reasonably low-rank but not sparse, and $\mathbf{S}$ is sparse but not low-rank. Note that (P_*) assumes no any *a priori* knowledge of $\mathbf{L}$'s rank nor the distribution of the singular values, nor the magnitudes and locations of the non-zero entries of $\mathbf{S}$; a completely blind decomposition without any tuning parameter can be implemented. The detailed proof is referred to [23].

The convex (P_*) program can be solved using an augmented Lagrange multiplier (ALM) algorithm [81], which efficiently recovers $\mathbf{L}$ and $\mathbf{S}$ from the observation $\mathbf{X}$. Inheriting from the virtue of convex program, the solution to (P_1) found by ALM is always globally optimal.

PCP is significantly different from the traditional principal component analysis (PCA), which is closely related to SVD: PCP explicitly considers the outliers (with arbitrary magnitude and distribution) in $\mathbf{X}$ by decomposing it into a superposition of a low-rank component $\mathbf{L}$ and a sparse component $\mathbf{S}$; on contrary, PCA takes no account of such outliers and a single outlier can render it fail to find the principal components (low-rank structure).

In the proposed method, the recovered sparse matrix $\mathbf{S}$ is of primary interest because it captures the innovation contained in $\mathbf{X}$, which indicates the evolution-

ary damage information and is significantly enhanced by implicitly subtracting the low-rank matrix $\mathbf{L}$ representing the static or slowing changing background from the original observation $\mathbf{X}$. The interpretation of the $\mathbf{L} + \mathbf{S}$ representation in continuous imaging of structures is described as follows.

6.3 $\mathbf{L} + \mathbf{S}$ representation of structural films

The $\mathbf{L} + \mathbf{S}$ decomposition can naturally represent the multiply frames of structures as a superposition of a background component and an innovation component: $\mathbf{L}$ represents the static or slowly changing correlated background component among the temporal frames, which hence is low-rank; $\mathbf{S}$ captures the innovation information in each frame induced by the evolutionary damage, which is inherently sparse standing out from the background.

Specifically, suppose there are N temporal frames, each of which is of resolution $M_1 \times M_2$ where the image height has M_1 pixels and the image width has M_2 pixels. Restacking each temporal frame as a long column vector$\in \mathbb{R}^M$ with $M = M_1 \times M_2$, then the multi-frame data matrix is $\mathbf{X} \in \mathbb{R}^{M \times N}$, whose ith $(i = 1, ..., N)$ column represent the temporal frame at time T_i . PCP decomposes $\mathbf{X} \in \mathbb{R}^{M \times N}$ into a superposition of a low-rank $\mathbf{L} \in \mathbb{R}^{M \times N}$ and a sparse $\mathbf{S} \in \mathbb{R}^{M \times N}$ by solving the convex optimization program (P_*) using the ALM algorithm. Then each column of $\mathbf{L} \in \mathbb{R}^{M \times N}$ and $\mathbf{S} \in \mathbb{R}^{M \times N}$ is restacked back to the original image dimension of $M_1 \times M_2$.

Therefore, each temporal frame is represented by a background component plus an innovation component; the background component represents the static or slowly varying correlated information among different frames, whereas the sparse component presents the dynamic innovation induced by damage. Note that the sparse dynamic

innovation indicating the damage is dramatically enhanced by subtracting the background component from the original image, as seen in

$$S = X - L \qquad (6.4)$$

The paradigm already illustrated in Fig. 1.11 is also presented here (Fig. 6.1) for completeness.

6.4 Experimental validation

6.4.1 Experimental setup

To validate the proposed PCP de-noising algorithm, laboratory experiments are conducted separately on two concrete structural components: a simply-supported beam component and an exterior beam-column joint (T-shape component). The concrete beam is under four-point load, and the beam of the T-shape joint is subjected to vertical cyclic loading and the column is constrained appropriately. The sawtooth loads are applied with increasing amplitudes until failure.

A video camera (Nikon COOLPLIX L18) supported by a tripod is used to videotape a portion of the component during the experiment. The films have a resolution of 240×320 (height $\times$ width) pixels and a rate of 30 images per second. Originally, the film of the beam has a length of 1 hour, 3 minutes, and 11 seconds, and that of the T-shape structure has a length of 28 minutes and 17 seconds. Because this study aims to conduct real-time or near real-time damage detection, sliding segments of the multiply frames each with few-second data (e.g., 7 seconds) are used for analysis; but only several segments are demonstrated here.

The images are truncated into a dimension of 180×240 and a downsampled rate of 10 images per second for the beam, and of 150×240 and 1 image per second

for the T-shape structure. Each segment consists of 7-second data for the beam, and 23-second data for the T-shape structure. Therefore, one segment data is $\mathbf{X} \in \mathbb{R}^{43200 \times 22}$ ($M = 180 \times 240 = 43200$ and $N = 22$) for the beam and $\mathbf{X} \in \mathbb{R}^{36000 \times 23}$ ($M = 150 \times 240 = 36000$ and $N = 23$) for the T-shape structure. Without any preprocessing, they are "blindly" decomposed into a superposition of $\mathbf{L} \in \mathbb{R}^{43200 \times 22}$ and $\mathbf{S} \in \mathbb{R}^{43200 \times 22}$ for the beam, and $\mathbf{L} \in \mathbb{R}^{36000 \times 23}$ and $\mathbf{S} \in \mathbb{R}^{36000 \times 23}$ for the T-shape structure, respectively, by PCP with the ALM algorithm. Without any post-processing, each column of $\mathbf{L}$ and $\mathbf{S}$ is restacked back to the original image dimension; therefore, each temporal original frame is represented as a background component (image) plus an innovation component (image).

6.4.2 Results

Fig. 6.2(a) shows the $\mathbf{L} + \mathbf{S}$ representation of an imaging of the beam at the beginning of the loading, when a small piece of the component fell off from the middle-right side on the top surface. While this damage information is subtle in the original time-evolutionary frames $\mathbf{X}$, it is pronounced in the $\mathbf{S}$ component with the sparse white pixels on top of the falling-off temporal frames. This is because the irrelevant background $\mathbf{L}$, which is seen to change very little among frames, has been (implicitly) suppressed.

Fig. 6.3(a) and Fig. 6.4(a) show the $\mathbf{L} + \mathbf{S}$ representation of imaging of the beam subjected to more severe damage as the loading continues. In both cases, the crack on the top surface developed and finally fell off, whose evolutionary development are captured by the sparse dynamic component $\mathbf{S}$, while the background $\mathbf{L}$ remains slowly varying among the temporal frames. It is also observed that sparse white pixels on top of $\mathbf{S}$ tend to increase with the severity of the damage: small damage

induces few sparse elements (Fig. 6.2(a)) while large damage induces more sparse elements (Fig. 6.3(a) and Fig. 6.4(a)); hence, the sparisty degree of **S** could also serve to indicate damage extents.

Fig. 6.5(a) and Fig. 6.6(a) shows the **L** + **S** representation of imaging of the T-shape structure also under increasing loading. Similarly, the opening process of the crack is captured by the dynamic component **S**, promoting the sparse innovative crack information among the temporally evolutionary frames (Fig. 6.5(a)). In Fig. 6.6(a), it is seen that damage generated multiple cracks simultaneously, which also stand out in the recovered **S** from the background **L**.

6.4.3 Discussions

The broad conditions for the success of PCP in performing the **L** + **S** decomposition of **X** are also validated. The subplots (b) and (c) in Fig. 6.3-6.6 show the singular values of **X**, **L**, and **S**. Obviously, the recovered background **L** is indeed low-rank; take Fig. 6.2(b) for example, only the first two singular values are active with the rest of its singular values rapidly decaying to zero. The fast decaying of the singular values also happens in other cases. This is because **L** represents the highly-correlated background information, which is static or slowly varying among the frames, and hence possesses a low-rank structure. Fig. 6.2(c)- 6.6(c) also show that the recovered sparse **S** is not low-rank whose singular values do not vanish, and it is also easily seen from Fig. 6.2(a)-6.6(a) that the low-rank **L** is not sparse but very dense. Therefore, the **L** + **S** decomposition is well-posed in the framework of dynamic imaging of structures: the background **L** is low-rank but not sparse, and the innovation **S** is sparse but not low-rank.

It is also seen that **X**'s singular values do not vanish whatsoever, which is some-

what expected, because $\mathbf{X}$ is a superposition of a low-rank $\mathbf{L}$ and a sparse outliers $\mathbf{S}$. Moreover, this also implies that additional outliers $\mathbf{S}$ to a low-rank $\mathbf{L}$, which results in $\mathbf{X} = \mathbf{L} + \mathbf{S}$, would corrupt its low-rank structure, which can't be recovered by classic PCA or SVD.

The efficiency of the proposed PCP based dynamic imaging method. For these five cases, the computational time is 3.40 sec, 3.40 sec, and 3.44 sec for the beam structure (a 7-sec segment of data, 22 frames), and 3.32 sec and 2.83 sec for the L-shape structure (a 20-sec segment of data, 20 frames) on a desktop PC with a 3.20 GHz Intel Core i5 650 processor and 6 GB RAM. Also, there is no tuning parameter in the implementation of PCP: the universal trading parameters are set $\lambda = 1/\sqrt{\max(m,n)}$ with $\lambda = 1/\sqrt{43200}$ for the beam and $\lambda = 1/\sqrt{36000}$ for the T-shape structure, and PCP with the ALM algorithm always globally converges to the well-posed solutions.

6.5 Summary

Harnessing the data structure and damage signature intrinsic in the multiple close-up images of structural components, this chapter presents a new data-driven framework of high-rate dynamic imaging (close-up "filming") of structures to automate real-time local damage detection; it adopts the innovative principal component pursuit (PCP) technique, which is able to "blindly" decompose the high-rate multiple frames of structures into a superposition of a low-rank component and a sparse component. In the proposed method, the low-rank component represents the irrelevant highly-correlated background among the temporal frames, whereas the sparse component captures the dynamic innovation information induced by damage.

Laboratory experiments are conducted on two concrete structures and results shows that PCP based dynamic imaging method can effectively track the evolu-

tionary damage information by the recovered sparse innovation component, which is enhanced with the low-rank background suppressed from the frames. Its efficiency and implementation are also demonstrated to be fast and straightforward.

The proposed dynamic imaging method does not require a parametric model or prior structural information (e.g., geometry) for calibrations or reference; it holds the potential for automated online damage surveillance and diagnosis of critical structural components which might be inaccessible to experts (especially during or post-hazards) or as an alternative to experts' visual inspection when they are not available or not possible in real-time local structural health monitoring practice.
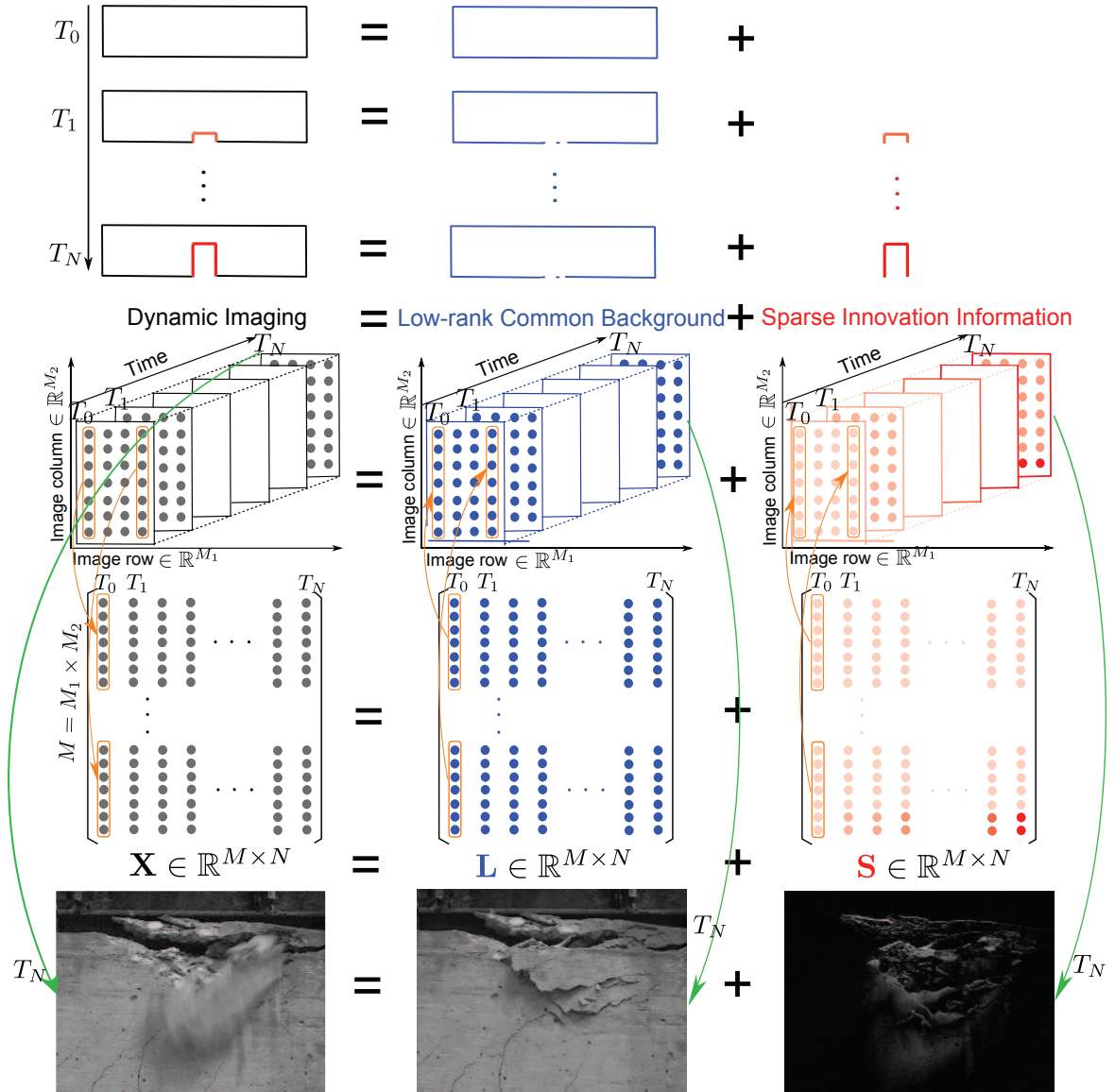
Figure 6.1 : The dynamic imaging of structures paradigm for real-time automated damage detection. The upper plot shows that the multiple frames (black) of the crack developing in the structure (from time T_0 to T_N) can be thought of as a static background (blue) plus the sparse innovation (red) induced by the cracking. The middle plot shows that each temporal frame of resolution $M_1 \times M_2$ is stacked into one column of the data matrix $\mathbf{X} \in \mathbb{R}^{M \times N}$ (each column is of dimension $M = M_1 \times M_2$ rows representing one temporal frame and there are N columns), which is decomposed into a superposition of a low-rank coherent background component $\mathbf{L} \in \mathbb{R}^{M \times N}$ and a sparse innovation component $\mathbf{S} \in \mathbb{R}^{M \times N}$ that indicates the time-evolutionary damage development. Each column of $\mathbf{L} \in \mathbb{R}^{M \times N}$ and $\mathbf{S} \in \mathbb{R}^{M \times N}$ is finally restacked back to the original image dimension, and the bottom plot shows the recovered background component and sparse component at time T_N.

(a)

(b)

(c)

Figure 6.2 : (a) The $\mathbf{L}+\mathbf{S}$ representation of the concrete structure with small damage at the beginning of loading. The original multi-frame data matrix $\mathbf{X} \in \mathbb{R}^{43200 \times 22}$ (a segment of 7-second data consisting of 22 frames, each is of 180×240) is decomposed into $\mathbf{L} \in \mathbb{R}^{43200 \times 22}$ plus $\mathbf{S} \in \mathbb{R}^{43200 \times 22}$ by PCP and then each column is restacked back to its original image dimension. Three temporal frames $\mathbf{X} \in \mathbb{R}^{43200 \times 22}$ (left column) are shown, where $\mathbf{L} \in \mathbb{R}^{43200 \times 22}$ (middle column) represents the slowly changing background, and $\mathbf{S} \in \mathbb{R}^{43200 \times 22}$ (with outstanding white pixels) captures the subtle damage with a small piece fell off from the middle top surface. (b) The singular values of the recovered background component $\mathbf{L} \in \mathbb{R}^{43200 \times 22}$. (c) The singular values of the recovered sparse innovation component $\mathbf{S} \in \mathbb{R}^{43200 \times 22}$.
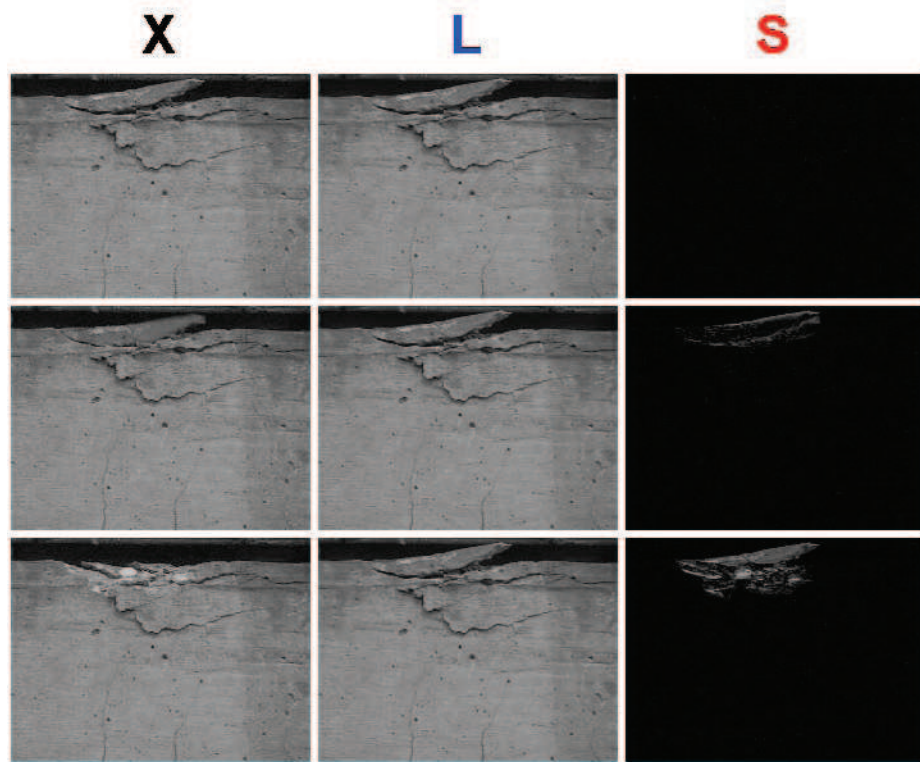
(a)
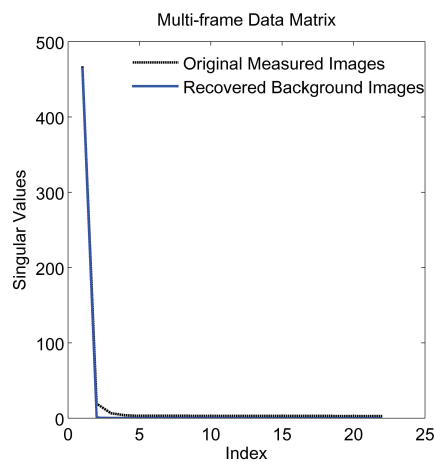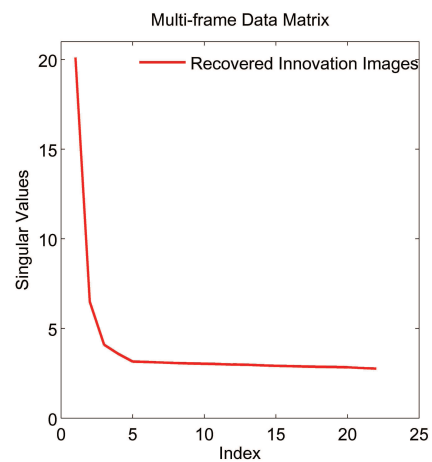
(b)   (c)

Figure 6.3 : (a) The $\mathbf{L} + \mathbf{S}$ representation of the concrete beam with medium damage at the middle of loading. Three temporal frames $\mathbf{X} \in \mathbb{R}^{43200 \times 22}$ (left column) (a segment of 7-second data consisting of 22 frames, each is of 180×240) are shown, with $\mathbf{S} \in \mathbb{R}^{43200 \times 22}$ (with outstanding white pixels) captures the process where a piece structure fell off from the left top surface. (b) The singular values of the recovered background component $\mathbf{L} \in \mathbb{R}^{43200 \times 22}$. (c) The singular values of the recovered sparse innovation component $\mathbf{S} \in \mathbb{R}^{43200 \times 22}$.
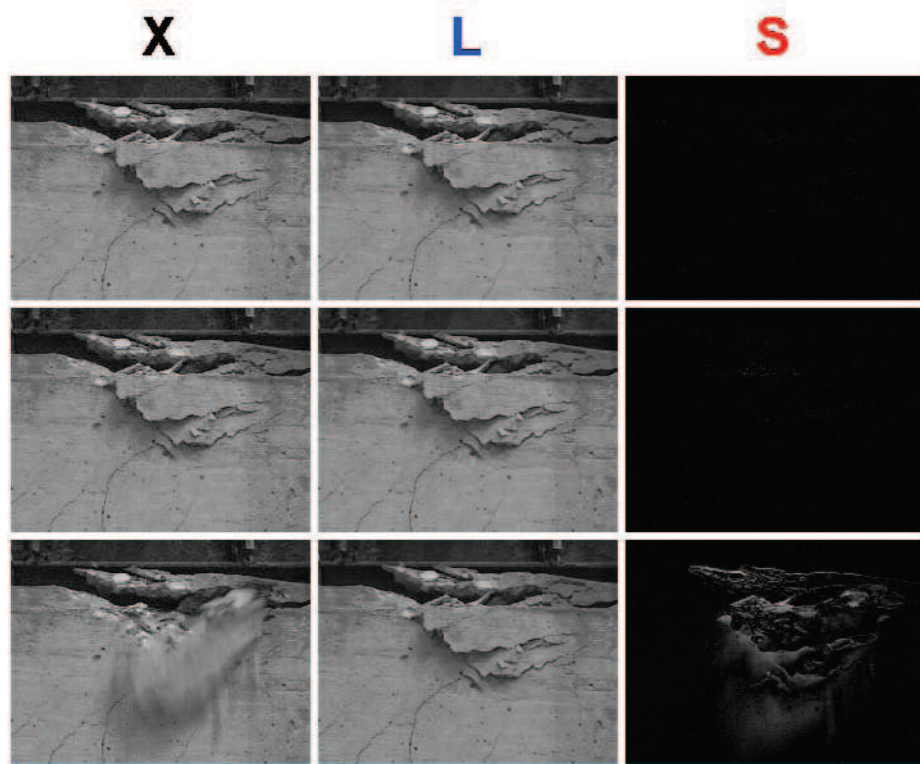
(a)
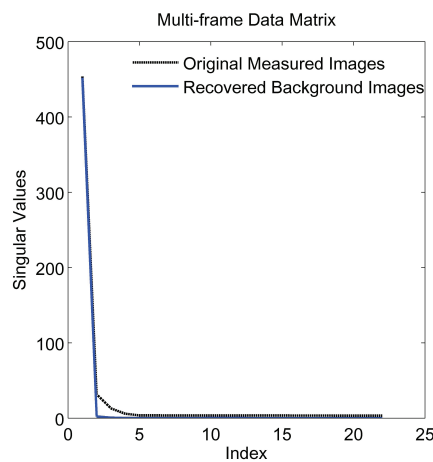
(b)
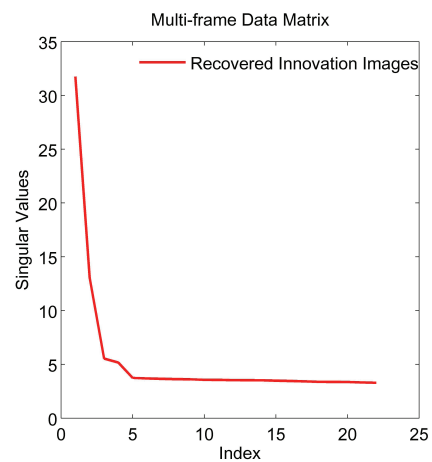
(c)

Figure 6.4 : (a) The $\mathbf{L} + \mathbf{S}$ representation of the concrete beam with larger damage at the middle of loading. Three temporal frames $\mathbf{X} \in \mathbb{R}^{43200 \times 22}$ (left column) (a segment of 7-second data consisting of 22 frames, each is of 180×240) are shown, with $\mathbf{S} \in \mathbb{R}^{43200 \times 22}$ (with outstanding white pixels) captures the process where a large piece structure fell off from the right top surface. (b) The singular values of the recovered background component $\mathbf{L} \in \mathbb{R}^{43200 \times 22}$. (c) The singular values of the recovered sparse innovation component $\mathbf{S} \in \mathbb{R}^{43200 \times 22}$.
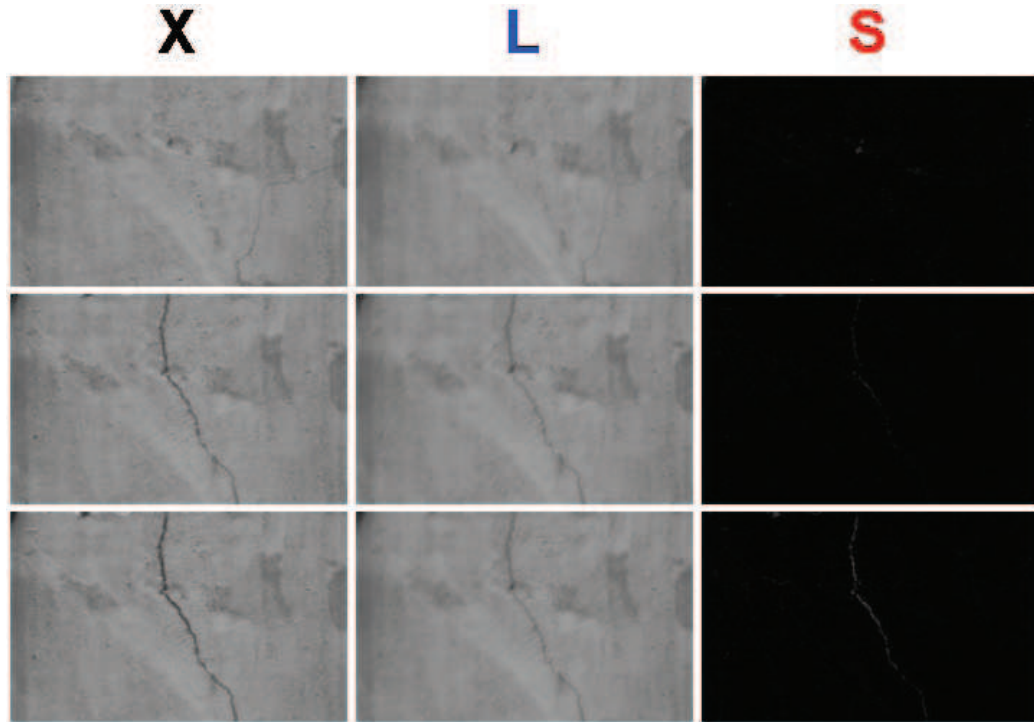
(a)
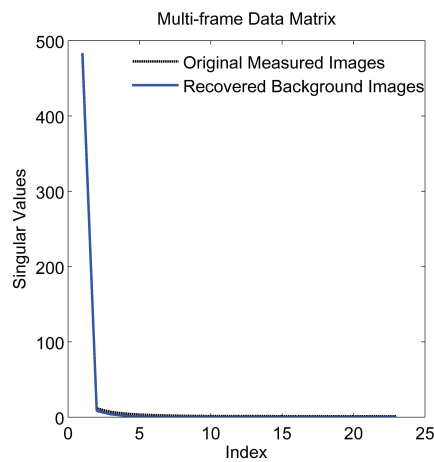
(b)
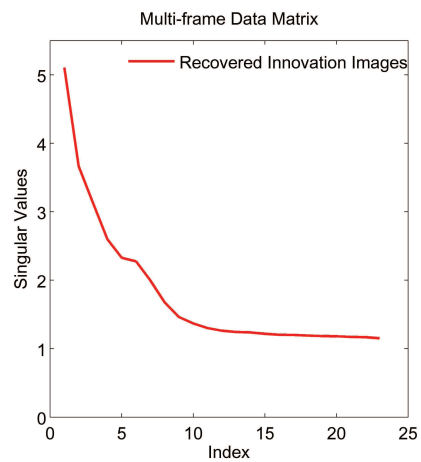
(c)

Figure 6.5 : (a) The $\mathbf{L} + \mathbf{S}$ representation of the T-shape concrete structure with crack opening at the beginning of loading. Three temporal frames $\mathbf{X} \in \mathbb{R}^{36000 \times 23}$ (left column) (a segment of 23-second data consisting of 23 frames, each is of 150×240) are shown, with $\mathbf{S} \in \mathbb{R}^{36000 \times 23}$ (with outstanding white pixels) captures the process where a crack was opening in the middle. (b) The singular values of the recovered background component $\mathbf{L} \in \mathbb{R}^{36000 \times 23}$. (c) The singular values of the recovered sparse innovation component $\mathbf{S} \in \mathbb{R}^{36000 \times 23}$.
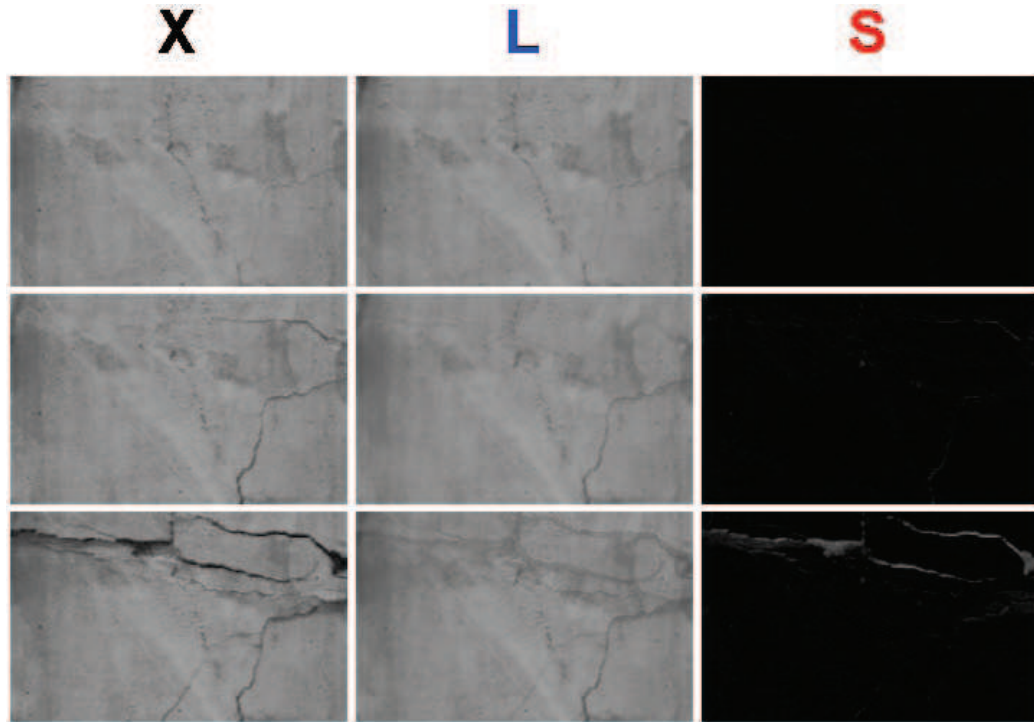
(a)
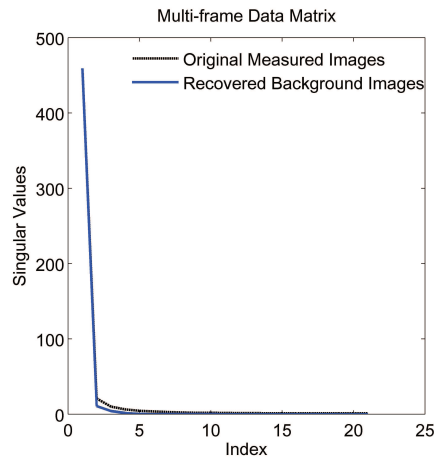
(b)
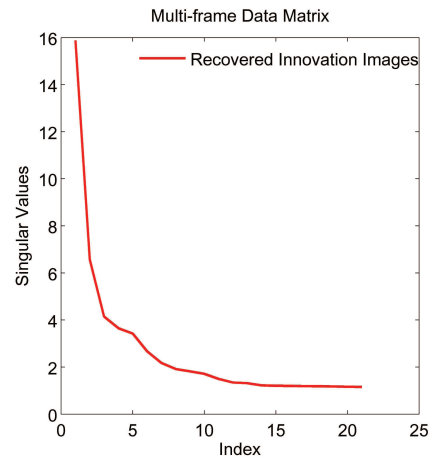
(c)

Figure 6.6 : (a) The $\mathbf{L}+\mathbf{S}$ representation of the T-shape concrete structure with multiple cracks opening at the middle of loading. Three temporal frames $\mathbf{X} \in \mathbb{R}^{36000 \times 21}$ (left column) (a segment of 21-second data consisting of 21 frames, each is of 150×240) are shown, with $\mathbf{S} \in \mathbb{R}^{36000 \times 21}$ (with outstanding white pixels) captures the process where multiple cracks occurred. (b) The singular values of the recovered background component $\mathbf{L} \in \mathbb{R}^{36000 \times 21}$. (c) The singular values of the recovered sparse innovation component $\mathbf{S} \in \mathbb{R}^{36000 \times 21}$.

Chapter 7

Multivariate Data Compression

Addressing the data-intensive issue in modern SHM systems of civil structures with large-scale networked sensors, this chapter develops a new multi-channel data compression scheme based on the low-rank structure of the multi-channel structural responses and the unsupervised multivariate learning technique independent component analysis (ICA), which is able to transform a multivariate data set into a sparse representation space where is optimal for coding and compression, such that both the inner- and inter- dependencies (i.e., redundant information) between the multichannel data are removed for efficient data compression. It is potential for rapid and reliable data transfer, communication (e.g., multi-hop wireless sensor network), storage, and retrieval in online or post-disaster (e.g., earthquake) monitoring and assessment applications of civil infrastructure.

7.1   Introduction

Dense sensor networks are becoming common in the monitoring systems of these large-scale civil infrastructure, grasping comprehensive information of the structural operating performance; as such, the acquired data may be on order of magnitude high in volume, whose transfer, storage, retrieval (especially accessed by remote users), and management remain challenging. Such also tends to impede wider applications of wireless sensor network in infrastructures with limited communication bandwidth

and battery power supply, which especially calls for efficient data transfer and retrieval [123][85].

Data compression technique is therefore of particular importance to manage such large data sets; it reduces the size of the original data from the acquisition station for transfer, and then reconstructs them at the data analysis station. An effective compression scheme contributes to efficient data transfer and fast access to measured data for real-time analysis and evaluation of the structure, which is critical for online monitoring and control. For offline applications, data of smaller size are stored for further retrieval and access. This superiority also stands out in wireless sensor network by taking up smaller communication bandwidth and saving more energy.

The underlying wisdom of the effectiveness of such an application lies in that the raw measured structural vibration data are typically dependent and possess redundancy, which leaves space for data compression before transmission and storage. Transform coding is perhaps the most widely-used compression technique, whose idea is to transform the measured data to a domain where they are more advantageous for compression. Stearns and co-workers ([126][122][127]) examined a series of existing transform coding algorithms for seismic waveform data, including discrete Fourier transform (DFT), discrete cosine transform (DCT), Walsh-Hadamard transform (WHT), linear predictor compression (LPC), and Karhunen-Loeve transform (KLT). However, their effectiveness in compression of structural vibration responses, whose characteristics are distinct from seismic waveform (excitation), is not studied.

Quite a few researchers in civil engineering communities have recently explored the data compression methods of the measured structural vibration response data. Lynch et al. [86] combined wavelet transform and Huffman coding for lossless data compression and transfer to alleviate the power demand on wireless SHM systems.

Zhang and Li [156][157] studied the wavelet-based and LPC methods, respectively, for compression of structural vibration sensor data. Bao et al. [9], Mascarenas et al. [92], Sadhu et al. [116], and O'Connor et al. [109] studied a new compression technique called compressive sampling for structural responses. Whereas encouraging results are seen, high compression ratio is not available in lossless compression application nor accurate reconstruction achieved in lossy compression algorithm. Considering the voluminous data are measured from the dense sensor network in infrastructures, it would be desired to seek more effective methods realizing high compression ratio as well as accurate reconstruction for efficient data transfer and further applications.

One significant drawback with the existing methods-DFT, DCT, WHT, and wavelet, is that they are non-adaptive, i.e., they use fixed transform basis prior to data compression process. This may cause serious problem in practice, e.g., an unfortunate choice of transform basis (cosine, wavelet, etc.), which may not be suitable to a given data set, will provide poor compression performance. Also, these non-adaptive methods can only be applied to single-channel data separately.

On the other hand, it is most useful to find the natural transform basis from the given data sets. Enhanced with a suitable learning rule, an appropriate transform adaptive to the multi-channel data set itself is guaranteed to provide optimal compression performance. The aforementioned KLT is an adaptive transform technique; it decomposes the data set into an uncorrelated space where the redundancy of the inter-correlation within the data set is removed. It is noticed in Spanias et al. [122] that KLT outperformed LPC and gave better performance than other (non-adaptive) transform coding algorithms. However, it only exploits the second-order statistics of the data set.

This chapter proposes a new adaptive transform compression method for struc-

tural response data based on independent component analysis (ICA) [64]. Compared to KLT, ICA transforms the multivariate data set into a new statistically independent representation space such that not only the second-order redundancy, but also the high-order dependency within the data set can be removed for optimal compression performance. To our knowledge, applications of ICA have not yet been explored in data compression in the literatures in any other field.

The proposed method particularly exploits the ICA learning rule, which is found to naturally yield optimal transform for data compression. Besides, it takes advantage of the observation that multi-channel structural dynamic responses are typically low-rank, such that a considerable number of ICA-transformed components are principled (truncated) to achieve higher compression efficiency with fairly little data distortion. The compression performance in two sets of real-measured structural seismic response data from the Northridge Earthquake 1994 [118] shows that the proposed PICA method achieves dramatically high compression ratio with excellent reconstruction accuracy, as compared to the popular wavelet compression method. It is also shown that (principled) ICA slightly outperforms the (principled) PCA method-that used to be considered optimal multivariate data compression scheme-with respect to both CR and reconstruction accuracy, and the advantages of ICA over PCA are expected to be significant if the data set processes stronger high-order dependency.

7.2 Information and entropy

For a random experiment (variable) v including all possible outcomes $\left\{v^1, v^2, ..., v^N\right\}$ with an occurrence probability distribution $\left\{\mathrm{p}(v^1), \mathrm{p}(v^2), ..., \mathrm{p}(v^N)\right\}$ $(\sum_j \mathrm{p}(v^j) = 1)$, the self-information [119] within each event v^j $(j = 1, ..., N)$ is quantitatively mea-

sured by

$$i(v^j) = -\log \mathrm{p}(v^j) \tag{7.1}$$

The most widely used logarithm is $\log_2$, in which case the information unit is bit. For example, a binary-distributed ($N = 2$) variable with $\mathrm{p}(v^j) = 1/2(j = 1, 2)$ contains one-bit information.

Eq. (7.1) shows that an event with smaller probability contains more information amount. Intuitively speaking, the occurrence of a rare event reveals a lot of information. If all the outcomes are independent, the average information associated with v is termed entropy, given by

$$\mathrm{H}(v) = -\sum_{j=1}^{N} \mathrm{p}(v^j) \log \mathrm{p}(v^j) \tag{7.2}$$

A random variable v with small entropy generally possesses sparse distribution, e.g., the entropy of v with a pulse (sparsest) distribution ($\mathrm{p}(v^j) = 1, \mathrm{p}(v^i) = 0, i \neq j$) is zero. In such a case, there is no information (randomness) contained in v, for it is completely determined (i.e., the outcome is always v^j).

Concerning lossless data compression, Shannon's theory [119] states that the average (binary) codeword length needed by the optimal encoding scheme for v at best equals its entropy. On the other hand, if the outcomes of v are statistically dependent, its entropy will always be smaller than that of an independent v; that is,

$$\mathrm{H}(v \left| v^{-1}, v^{-2}, ..., v^{-M} \right.) \leq \mathrm{H}(v) \tag{7.3}$$

where $\left\{ v^{-1}, v^{-2}, ..., v^{-M} \right\}$ is a set of M past histories.

A clever compression strategy becomes clear that by exploiting the inherent dependency within the data, the original data can be transformed into a new representation that has smaller entropy and thus possibly consumes less average codeword length.

This refers to the fundamental idea of transform coding scheme. The next section introduces the ICA transform that yields optimal representation for compression of data.

As per Eq. (7.1) to Eq. (7.3), the formulations can be generalized to the vector space, which deals with multivariate random variable vector $\boldsymbol{v} = [v_1, v_2, ..., v_n]^T$ instead of a single variable v. In the chapter, superscript generally denotes time index while subscript locates spatial index of a signal or a random variable; bold lower-case and bold upper-case letters are understood as vectors and matrices, respectively.

7.3 Independent component analysis

7.3.1 The learning rule of ICA

Given n-dimensional data set (variable vector) $\mathbf{x} = [x_1, x_2, ..., x_n]^T$, ICA is able to linearly transform the multivariate data into a statistically independent space, i.e.,

$$\mathbf{y} = \mathbf{W}\mathbf{x} \tag{7.4}$$

such that the resultant random variable vector $\mathbf{y} = [y_1, y_2, ..., y_n]^T$, termed independent component (IC), is most mutually independent. $\mathbf{W}$ is an $n \times n$ time-invariant transform matrix, each row of which $\mathbf{w}_i$ is found by imposing the transformed component (random variable) y_i as independent as possible among all possible directions,

$$y_i = \mathbf{w}_i\mathbf{x} \tag{7.5}$$

The above equations incorporate ICA into a statistical framework by dropping the time index which is commonly associated with the ICA model [64]

$$\mathbf{x} = \mathbf{A}\mathbf{y} \tag{7.6}$$

where $\mathbf{A}$ is the mixing matrix and $\mathbf{A} = \mathbf{W}^{-1}$. Eq. (7.6) is usually referred to as blind source separation (BSS) problem [34], where $\mathbf{x}$ and $\mathbf{y}$ are mixtures and sources, respectively. Here it is termed as recovery transformation, meaning recovery of $\mathbf{x}$ from the transformed $\mathbf{y}$.

The principle of the ICA learning rule which maximizes independence of y_i is based on the Central Limit Theorem, which states that a sum of independent random variables tends towards Gaussian distribution. This implies that a (linear) mixture of independent variables is more Gaussian than a single variable. Using the theorem, ICA seeks components which are as non-Gaussian as possible, as the estimation of the IC's. In statistics, non-Gaussianity is rigorously measured by negentropy as

$$\text{J}(y_i) = \text{H}(y_{gau}) - \text{H}(y_i) \tag{7.7}$$

where y_i and the Gaussian variable y_{gau} are both standardized to zero-mean and unit-variance. Negentropy evaluates the entropy distance of y_i from y_{gau}, which has the largest entropy among all random variables with equal variance [36][64]; this implies that the obtained y_i that has largest negentropy must have smallest entropy (thus tends to be sparse, also see [146]) among all possible transforms. Therefore, the ICA learning rule naturally yields such optimal component y_i as will consume fewest codeword.

An exact estimation of negentropy of a random variable is difficult in practice. However, it can be approximated by

$$\text{J}(y_i) = [\text{E}\{\text{G}(y_i)\} - \text{E}\{\text{G}(y_{gau})\}]^2 \tag{7.8}$$

in which $\text{E}\{\cdot\}$ is the expectation operator, and $\text{G}(\cdot)$ represents some non-quadratic function. The Gaussian function

$$\text{G}(y_i) = -\exp(-y_i^2/2) \tag{7.9}$$

has the attractive property that it is insensitive to outliers and is adopted in this study.

7.3.2 ICA & mutual information

The learning rule of ICA can also be incorporated into the mutual information framework [64]; it theoretically justifies that ICA provides optimal transform for data compression, as described in the following.

The mutual information among the ICA-transformed components $\mathbf{y} = [y_1, y_2, ..., y_n]^T$ is defined by

$$I(\mathbf{y}) = \sum_{i=1}^{n} H(y_i) - H(\mathbf{y}) \tag{7.10}$$

which is the entropy difference between the sum of n individual random variables and the "joint" random variable vector $\mathbf{y}$. Mutual information naturally measures the statistical dependency between the random variables. For example, if the random variables are statistically independent, the mutual information of $\mathbf{y}$ is minimized to zero, indicating that one variable gives no information on any other one; otherwise it is positive.

According to the property of mutual information [36], if there exists an invertible linear transform $\mathbf{y} = \mathbf{W}\mathbf{x}$, then

$$I(\mathbf{y}) = \sum_{i=1}^{n} H(y_i) - H(\mathbf{x}) - \log |\det \mathbf{W}| \tag{7.11}$$

Since $\mathbf{y}$ is standardized and uncorrelated after preprocessing (described in later section),

$$E[\mathbf{y}\mathbf{y}^T] = E[(\mathbf{W}\mathbf{x})(\mathbf{W}\mathbf{x})^T] = \mathbf{W}E[\mathbf{x}\mathbf{x}^T]\mathbf{W}^T = \mathbf{I} \tag{7.12}$$

Take determinant operator of both sides,

$$\det \mathbf{W} \det \mathrm{E}[\mathbf{x}\mathbf{x}^T] \det \mathbf{W}^T = \det \mathbf{I} = \mathbf{1} \tag{7.13}$$

For a given data set $\mathbf{x}$, $\det \mathrm{E}[\mathbf{x}\mathbf{x}^T]$ is determined; this implies that $\det \mathbf{W}$ must be a constant. Substituting Eq. (7.7) into Eq. (7.11) gives

$$\begin{aligned} \mathrm{I}(\mathbf{y}) &= -\sum_{i=1}^{n} \mathrm{J}(y_i) + (\sum_{i=1}^{n} \mathrm{H}(y_{gau,i}) - \mathrm{H}(\mathbf{x}) - \log|\det \mathbf{W}|) \\ &= -\sum_{i=1}^{n} \mathrm{J}(y_i) + Constant \end{aligned} \tag{7.14}$$

This equation justifies that ICA's learning rule of maximizing negentropy $\mathrm{J}(y_i)$ leads to a minimization of the mutual information between $\mathbf{y}$. Therefore, the statistical dependency within $\mathbf{x}$ is removed and the ICA-transformed components $\mathbf{y}$ are most mutually independent, i.e., no further dependency can be exploited in $\mathbf{y}$. ICA thus naturally yields the optimal (linear) transformation adaptive to data itself for compression in statistical framework.

It should be mentioned that KLT used to be considered as the optimal transform coding [4] restricted to the second-order dependency structure of the data, by transforming data into an uncorrelated space. On the other hand, ICA additionally exploits high-order dependency of the data such that the transformed representation is not only uncorrelated but also most statistically independent. This distinction lies in their different learning rules: ICA imposes independence which is a much stronger condition than uncorrelation used by KLT. In this sense, ICA transform is superior over KLT for data compression.

7.3.3 Implementation of FastICA

Although ICA can be implemented in different frameworks (e.g., infomax [12], joint approximate diagonalization of eigenmatrices (JADE) [27], etc.), this study uses the

FastICA algorithm [64] with a cubic convergence rate, which is computationally efficient and robust. During the implementing FastICA, it is common to conduct preprocessing procedures on the data such like centering and whitening, which serve to simplify the ICA implementation. Especially in the whitening step, one simple yet useful step is adopted by the proposed compression scheme, as detailed in the following.

7.3.3.1 Preprocessing of FastICA

The first preprocessing step embedded in the FastICA algorithm is centering the data $\mathbf{x}$ to zero-mean; this also makes the transformed components $\mathbf{y}$ zero-mean. The following step is to whiten $\mathbf{x}$ using principal component analysis (PCA, a special case of KLT) or eigenvalue decomposition (EVD) operated on the covariance matrix $\mathbf{R}$,

$$\mathbf{R} = \mathrm{E}[\mathbf{x}\mathbf{x}^T] = \mathbf{Q}\mathbf{\Lambda}\mathbf{Q}^T \tag{7.15}$$

where $\mathbf{Q}$ is the orthogonal eigenvector matrix, and $\mathbf{\Lambda}$ is the diagonal eigenvalue matrix $\mathbf{\Lambda} = \mathrm{diag}(\lambda_1, \lambda_2, ..., \lambda_n)$ ($\lambda_1 \geq \lambda_2... \geq \lambda_n$). Whitening then transforms $\mathbf{x}$ into an uncorrelated representation with principal components $\hat{\mathbf{x}} = [\hat{x}_1, \hat{x}_2, ..., \hat{x}_n]^T$ by

$$\hat{\mathbf{x}} = \mathbf{\Lambda}^{-1/2}\mathbf{Q}^T\mathbf{x} = \mathbf{V}\mathbf{x} \tag{7.16}$$

where $\mathbf{V} = \mathbf{\Lambda}^{-1/2}\mathbf{Q}^T$ is the whitening matrix. Similarly there exists a de-whitening matrix $\mathbf{U} = \mathbf{Q}^T\mathbf{\Lambda}^{1/2} = \mathbf{V}^{-1}$ for recovery or inverse transform as

$$\mathbf{x} = \mathbf{Q}^T\mathbf{\Lambda}^{1/2}\hat{\mathbf{x}} = \mathbf{U}\hat{\mathbf{x}} \tag{7.17}$$

Associated with the whitening procedure, one strategy especially appealing to data compression is to drop those principal components with significantly small eigenvalues. This is based on the observation that structural responses are typically low-rank,

since in real world, only a few modes are excited out and present in the structural responses (see Section 1.3.2 of Chapter 1). As small eigenvalue indicates small energy of the corresponding principal component, it would cause little data loss by retaining those dominant components with larger eigenvalues. Meanwhile, it achieves higher compression by only encoding the retained components.

A stable truncation criterion would be according to the ratios between each λ_i and λ_1. Assume m principal components are trivial and discarded (principled), the remaining components becomes $\underline{\hat{\mathbf{x}}} = [\hat{x}_1, \hat{x}_2, ..., \hat{x}_{n-m}]^T$ and the recovery is conducted by

$$\tilde{\mathbf{x}} = \underline{\mathbf{U}}\hat{\mathbf{x}} \tag{7.18}$$

where $\tilde{\mathbf{x}} = [\tilde{x}_1, \tilde{x}_2, ..., \tilde{x}_n]^T$ approximates $\mathbf{x}$, and $\underline{\mathbf{U}}$ is an $n \times (n-m)$ matrix obtained by eliminating the last m columns of $\mathbf{U}$. Note that this strategy renders the first cause for data loss in the proposed compression scheme.

7.3.3.2 FastICA algorithm

The FastICA algorithm which is based on a fixed-point iteration scheme is widely used to implement ICA [64]. After preprocessing, FastICA seeks the de-mixing vector $\underline{\mathbf{w}}_i$, one by one (deflation scheme), such that the resultant component

$$y_i = \underline{\mathbf{w}}_i\hat{\mathbf{x}} \tag{7.19}$$

maximizes the contrast function such like Eq. (7.8). Therefore, the ICA transform is implemented as

$$\underline{\mathbf{y}} = \underline{\mathbf{W}}\hat{\mathbf{x}} \tag{7.20}$$

and the recovery transformation is

$$\hat{\mathbf{x}} = \underline{\mathbf{A}}\underline{\mathbf{y}} \tag{7.21}$$

where $\underline{\mathbf{y}} = [y_1, y_2, ..., y_{n-m}]^T$, and $\underline{\mathbf{A}} = \underline{\mathbf{W}}^{-1}$, both of which are $(n-m) \times (n-m)$ matrices.

FastICA is computationally fast, enjoying a cubic convergence. This is especially suitable for an efficient data compression scheme aimed by this study; the detailed algorithm for performing FastICA can be found in [64].

7.4 Quantization and arithmetic coding

7.4.1 Quantization

As mentioned above, the ICA-transformed components y_i (with possibly smallest entropy) tend to be sparse, with most elements approaching to zero. It would be most useful to drop these elements for data compression. On the one hand, the data needed to be encoded are significantly reduced such that higher compression can be achieved. On the other hand, the remaining data retain most information of the original data; as a result, the reconstructed data suffer little distortion.

The general and effective method to realize this purpose in lossy data compression is quantization [117], which is the process of assigning a small data set to represent a large data set. The ICA compression scheme uses the simplest uniform scalar quantizer which rounds a value to its closest integer as

$$\overline{y}_i^j = \left\lceil y_i^j \right\rceil \tag{7.22}$$

As each y_i is very sparse, the quantized component $\overline{y}_i$ will suffer little data loss in the ICA compression scheme. This accounts for another cause for data loss in the proposed compression scheme.

7.4.2 Lossless Arithmetic coding

The quantized components $\overline{y}_i$ are then encoded using the entropy encoding scheme, among which Huffman and Arithmetic algorithm are two most popular ones. It is known that Arithmetic algorithm yields excellent performance in encoding data with skewed distribution (skewness is with respect to the third-order statistics). This makes it especially suitable to encode $\overline{y}_i$, which has a very sparse representation.

The idea of arithmetic coding [114][117] is to identify each element of the data sequence with unique real number between 0 and 1; each real number is then assigned a binary code. During the coding process, only the non-zero elements in $\overline{y}_i$ needs to be encoded to a binary codeword dictionary $\mathcal{Y}_i$ (correspondingly $\overline{\mathbf{y}}$ to $\boldsymbol{\mathcal{Y}}$), while their positions are also recorded, which are only used in the data recovery stage. Decoding $\mathcal{Y}_i$ exactly to $\overline{y}_i$ can be easily carried out using the dictionary and the recorded positions of the non-zero elements.

7.5 ICA data compression scheme

Summarizing the above formulations, the PICA-based method data compression scheme is implemented along the flowchart (Fig. 7.1). Before data transfer in the acquisition station (wired or multi-hop wireless sensor network (Fig. 7.2)), the multi-channel data set is processed by FastICA, including the truncation step and ICA transform step, yielding the sparse IC's, which are then quantized and encoded to a dictionary. After transferring this dictionary to data analysis station, it is decoded and reconstructed to the original data set along the inverse procedures.
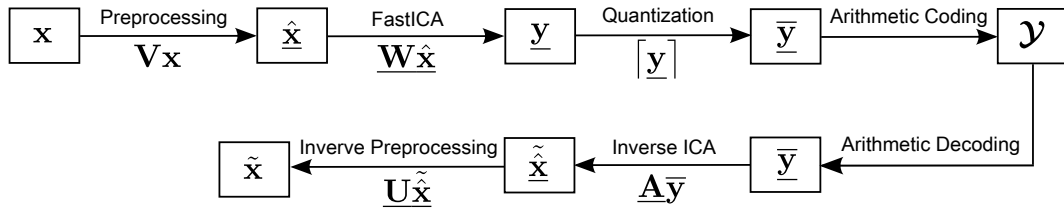
Figure 7.1 : The flowchart implementing ICA data compression scheme (the first line conducts compression and the second one performs recovery).
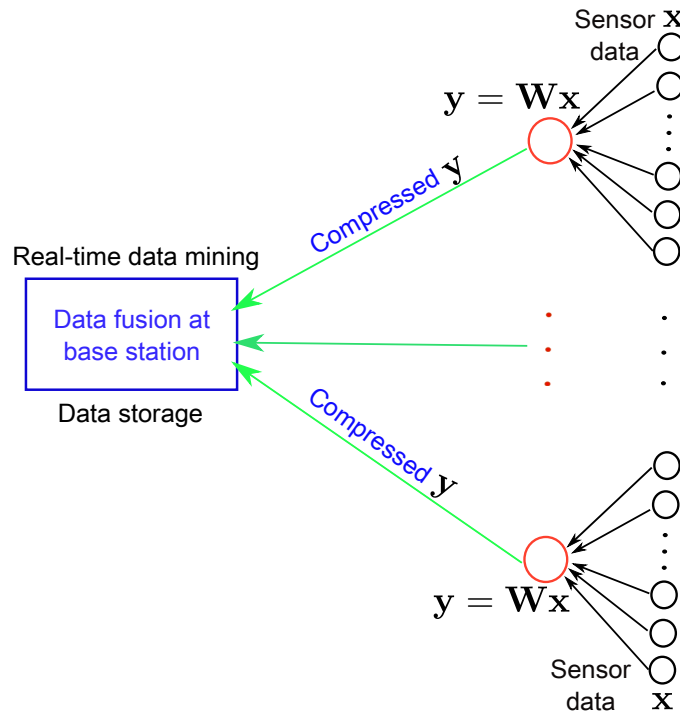
Figure 7.2 : The multivariate ICA data compression scheme for a multi-hop wireless sensor network. The raw sensor data x_i (the ith channel) is first transformed to a larger hop sensor node in the neighborhood, grouping to a multi-channel data set $\mathbf{x}$ which is then compressed by the multivariate ICA scheme to $\mathbf{y}$ with much smaller size. $\mathbf{y}$ is transferred to the base station and recovered to $\mathbf{x}$.

7.6 Structural seismic response examples

7.6.1 Two sets of seismic response data

This section presents two examples to demonstrate the capability of the principled ICA compression method, for the measured structural seismic responses of the Los Angeles Fire Command and Control (FCC) building (Fig. 4.10) and the University of Southern California (USC) hospital building (Fig. 2.16(a)) both from the Northridge Earthquake 1994 [118][100][101]. The FCC building is a two-story base-isolated structure with embedded sensors outlined as shown in Fig. 4.10. The acceleration responses from all the nine channels (Sensor # 6, 7, 9, 10, 11, 12, 14, 15, and 16) in the East-West (EW) direction are used in the example. Each channel data has a time history of 60 seconds sampled at 100 Hz, yielding 6000 samples per channel (e.g., Fig. 7.3 shows the acceleration of CHAN 7). The largest value out of these originally stored samples is $+306.319$ cm/sec^2; therefore, at least a 20-bit digital format (uniform scalar quantizer with data of fixed point type) is consumed by each sample for transmission and storage. The conditions of the acceleration responses of the eight-story base-isolated USC hospital building are similar, except that all the 15 sensors in the EW direction are selected (#6, 7, 8, 10, 11, 12, 14, 15, 16, 18, 19, 20, 22, 23, and 24) on the foundation, lower level, 4th floor, 6th floor, and the roof.

7.6.2 Performance of PICA and comparison to other methods

The proposed method is applied to the 9-channel and 15-channel data sets, respectively. During the whitening of FastICA, the EVD is conducted, yielding the eigenvalue ratios shown in Fig. 7.4. It is seen that in both cases the eigenvalues decay very fast; in this study, the truncation criterion is set at $\lambda_i/\lambda_1 = 3\%$ (the effects of differ-

ent truncated component number are discussed later). Therefore, only six principal components with larger eigenvalues in the FCC case and ten ones in the USC case are retained; simultaneously the remaining three columns of the de-whitening matrix in the FCC case and five columns in the USC case are eliminated for later recovery transform.
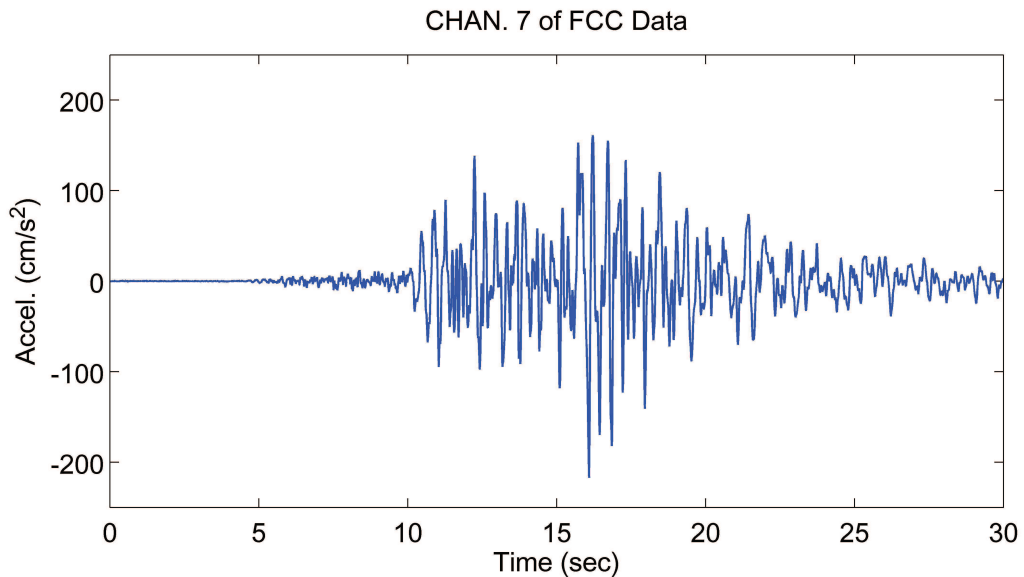
Figure 7.3 : The seismic response data of the FCC building measured at Channel 7 (0-30 second).

FastICA is then performed on the remaining principal components to further remove their high-order dependency, yielding six IC's in the FCC case and ten ones in the USC case, which are then quantized. Fig. 7.5 shows the quantized IC1 of the FCC data, which, compared to the original response data (e.g., Fig. 7.3 at Channel 7), appears to be fairly sparse with only 897 (14.95%) non-zero elements, and its magnitude is much smaller, which would consume much fewer bits. On contrary, if directly quantizing the response data of CHAN 6, for example, it is not sparse with 5217 (86.95%) non-zeros. Subsequently, arithmetic algorithm is applied to encode the
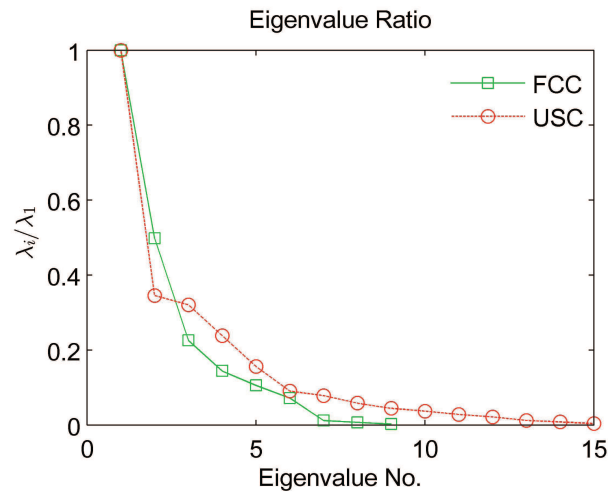
Figure 7.4 : Whitening results of the 9-channel seismic response data of the FCC building and 15-channel data of the USC building.

quantized ICs (the zero-elements are removed and only their positions are recorded) by assigning a binary code dictionary for each of them. The data recovery undergoes the inverse process, using only six components.

For comparisons, the popular wavelet transform (WT) (single-channel) coding scheme is also conducted on the 9-channel and 15-channel data sets, respectively. The db5 wavelet basis is used to decompose the data of each channel into five levels. In the following, the standard Dohono's algorithm [44] is used to shrink the wavelet coefficients on each level, which are then quantized by the same scalar quantizer. Finally, the quantized non-zero coefficients from each channel are, respectively, encoded by the arithmetic coding scheme.

The compression efficiency is evaluated by compression ratio (CR), defined as the ratio between the original data size and the compressed data size (the unit is bits). In addition, the bit rate is also computed as the consumed bits per sample. The

recovery accuracy evaluation at ith channel is calculated by

$$\varepsilon_i = 1 - \frac{\|\tilde{x}_i - x_i\|_{\ell_2}}{\|x_i\|_{\ell_2}} \qquad (7.23)$$

Table 7.1 presents the results which are averaged per channel of the FCC data and USC data, respectively. Take the FCC case for example, the first row shows non-zero sample numbers per channel that have been the transformed and quantized. It is seen that the principled IC, carrying fewest non-zero samples, is sparsest over IC and wavelet. Furthermore, encoding the principled IC consumes much fewer bits (per channel) than the wavelet coefficient and IC, thus yielding higher CR (67.78) and lower bit rate (0.29). Note that PICA only needs to encode six ICs, while standard (non-truncated) ICA and WT have to encode 9 components; this significantly increases the CR of PICA (67.78) over ICA (44.59) and WT (13.33), as well as alleviates the computational costs (for the complete process of encoding and decoding (Fig. 7.1)) of PICA (2.58 sec) over ICA (3.71 sec) and wavelet (6.29 sec), which also indicates the computational efficiency of the multivariate FastICA transform over the univariate wavelet transform in compression of the multiple-channel data sets. Similar results are also seen in the USC example, and not repeatedly detailed. The outcomes live up to the finding of the proposed method that PICA exploits the high-order statistical dependency among the data set and the transformed components have smallest entropy, thus consuming fewest codeword among all possible linear transforms.

It is also worthwhile noting that, though the transformed and quantized (principled) IC and wavelet coefficient (Fig. 7.5) have comparable few non-zero sample numbers (e.g., in the FCC case, 1232 versus 1403), encoding the IC consumes much less bits than the wavelet coefficient. This is because the IC, which is most independent (with respect to even high-order statistics), is favorable to encode by the
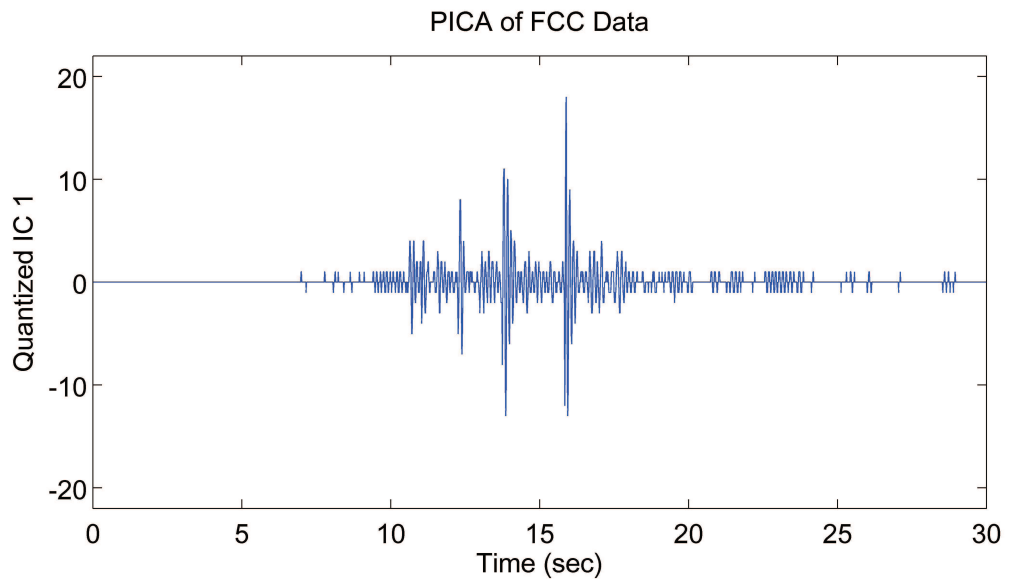
Figure 7.5 : The quantized principled IC1.
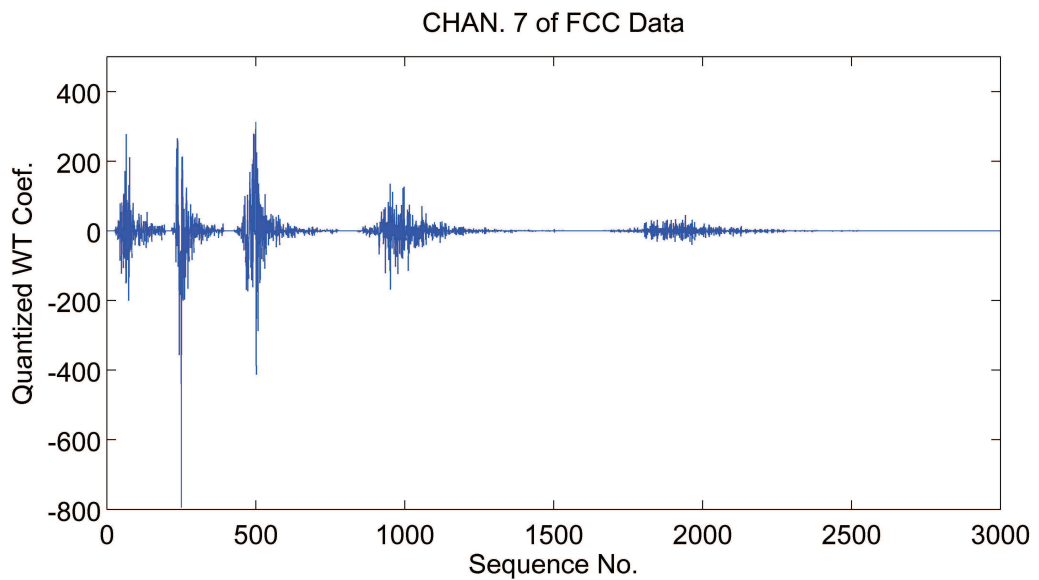
Figure 7.6 : The quantized shrunk wavelet coefficients of channel 7 of the FCC data.

arithmetic algorithm that is especially suitable for the skewed component, as mentioned above.

With respect to the recovery accuracy, WT outperforms PICA and ICA. However, ICA and PICA also yield excellent reconstruction accuracy. For example, in the FCC case, PICA yields 93.32% recovery accuracy while achieving a dramatically higher CR (67.78) than WT (13.33). Fig. 7.7 and 7.8 show the recovery performance for channel #6 of PICA and WT methods of the FCC data in both time and frequency domains. Clearly both WT- and PICA-recovered data yields excellent match with the original data in both cases. On the other hand, PICA achieves a considerably higher CR (67.78) than standard ICA (44.59), at cost of only 1.17% less recovery accuracy. This proves that a simple additional truncation step of PICA pays off by taking advantage of the fact that structural vibration data set from dense sensors are low-rank. Same conclusion can also be drawn in the USC example.

Therefore in practice, if the requirement on the reconstruction accuracy is extremely demanding and the computational time is less important, WT coding method would be a good choice. However, in cases where the data set is considerably large, or in online application where fast transfer is critical, or in multi-hop wireless sensor with inadequate communication bandwidth and power supply, PICA is a reliable and efficient alternative.

7.6.3   Effects of number of retained components comparing to PCA

When applying the truncation step of PICA, the effects of retaining different number of principal components on the CR and recovery accuracy are studied and the results are shown in Fig. 7.9. Obviously, there is a tradeoff between the CR and reconstruction accuracy (in fact, also computational costs). However, it is seen in both FCC and USC cases that the recovery accuracy grows very slowly when retaining more and more components while the CR grows rapidly by dropping more and more
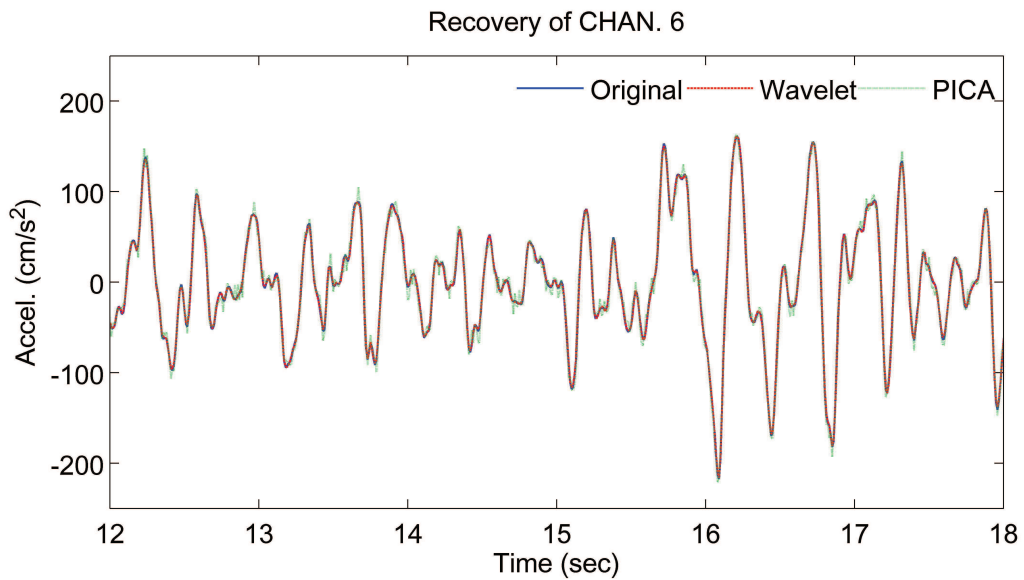
Figure 7.7 : The PICA- and wavelet- recovered response time history data of channel #6 of the FCC building (12-18 sec is shown for visual enhancement).
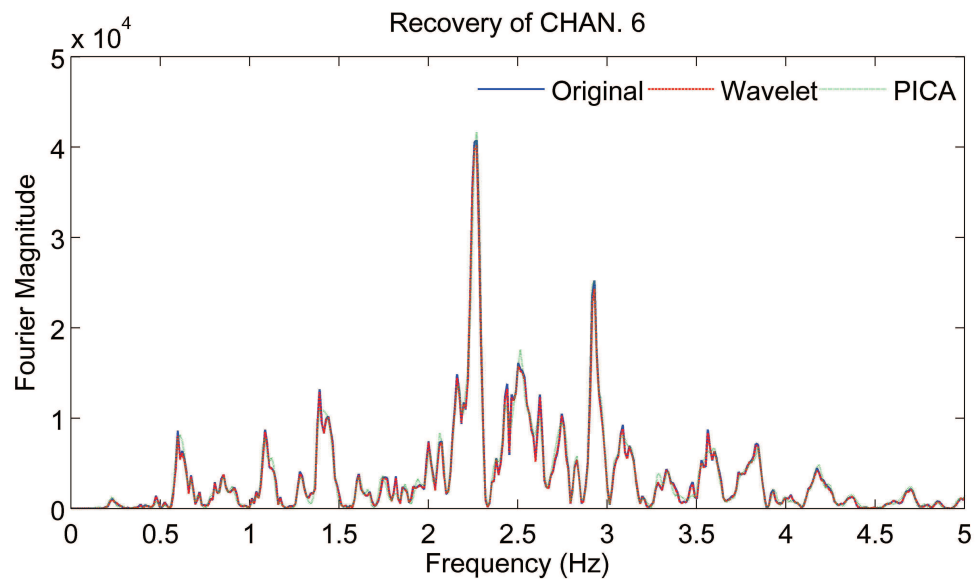
Figure 7.8 : The power spectral density (PSD) of the PICA- and wavelet- recovered response data of channel #6 of the FCC building.

components, and a reasonable tradeoff can be achieved in the neighborhood of retaining 6 and 10 components in the FCC and USC cases, respectively, i.e., setting the

truncation criterion $\lambda_i/\lambda_1 \approx 1\% - 5\%$ is robust and reliable for practical applications.

Also comparing ICA and PCA (only with the whitening step of the FastICA), PPCA and PICA, it is found that the ICA-based methods are slightly better than those only conducting PCA in both CR performance and reconstruction accuracy, while the computational costs of the ICA methods are also slightly higher than PCA methods (thanks to the efficient FastICA algorithm), as shown in Table 7.1 and Fig. 7.9. As mentioned in the theoretical section, the advantages of ICA over PCA depend on the amounts of higher dependency within the data set. The results show that such dependency is small in the FCC and USC data sets, so this advantage is not large but is expected to become more obvious when the structural vibration data possess more high-order dependency. Also it is interesting to note that as the number of the retained components is larger, the advantage is larger, especially for the CR performance of the USC case in Fig. 7.9; this tends to indicate that PICA would stand out from PPCA in handling very large data set (with numerous components or channels).

7.7   Summary

Exploiting the low-rank structure and a novel lossy data compression scheme based on principled ICA is developed in this chapter. It is deduced that the ICA learning rule naturally maps the data set into an independent sparse representation space, where the transformed components have small entropy and can thus be optimally encoded.

The example using two real-measured structural seismic response data sets (i.e., the FCC and USC hospital building from the Northridge Earthquake 1994) is presented to demonstrate the capability of the proposed method. Using the low-rank
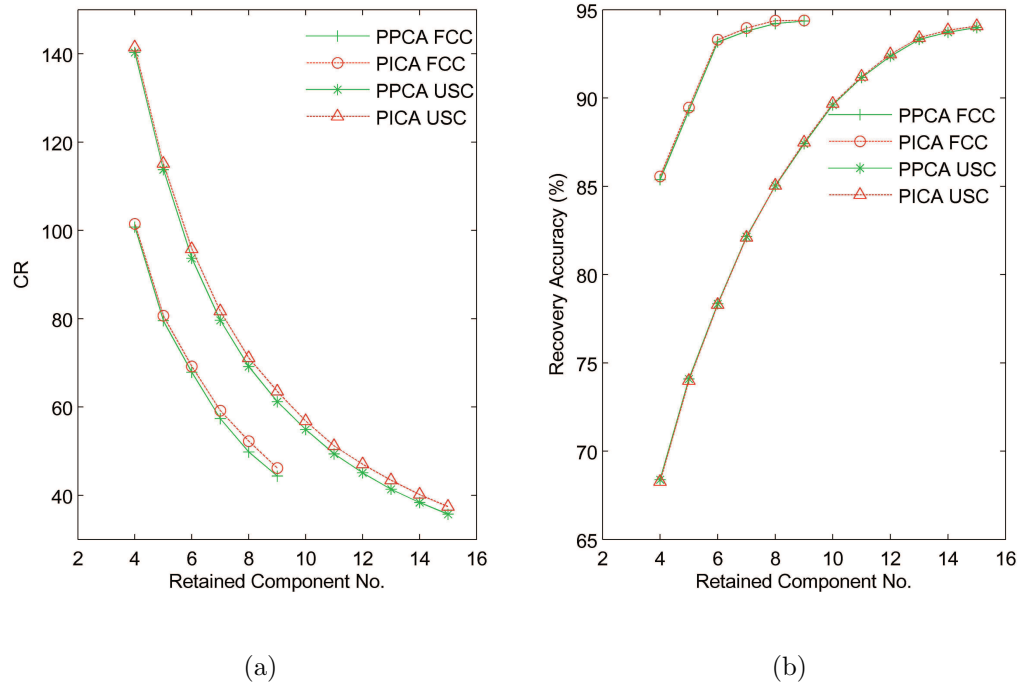
Figure 7.9 : (a) The compression ratio, and (b) recovery accuracy of the PICA compared to PPCA of the FCC data and the USC data, with different retained component numbers.

property of the structural vibrations, the multi-channel data sets are first principled (truncated) in the implementation of FastICA, dropping those principal components with small singular values while retaining excellent reconstruction accuracy. Results show that such a strategy achieves much higher compression efficiency at a little more cost of reconstruction accuracy. Compared with the popular wavelet transform coding scheme, the proposed PICA method achieves a dramatically higher compression ratio (~68) while causing fairly small distortion (~94% recovery accuracy). It is also shown that (principled) ICA slightly outperforms (principled) PCA which used to be considered optimal multivariate transform coding scheme, and the derived formulations of PICA compression method indicate that such an advantage would become

obvious when the structural vibration data set possesses more high-order redundancy or when the data dimension (channel number) is large.

The proposed method uses the FastICA algorithm, which enjoys cubic convergence and is thus computationally efficient. Another advantage of the PICA method resides in its adaptive ability to the data itself, naturally searching for optimal transform basis by the ICA learning rule. Therefore, a "blind" implementation of efficient compression and recovery process may be realized in practice, which is highly desired, especially in real-time wired or multi-hop wireless data transmission, access, and retrieval during extreme events (e.g., earthquakes).

Table 7.1 : Compression performance of the FCC and USC examples.

		Original	Direct	Wavelet	PCA	ICA	PPCA	PICA
FCC	(Trans+Qntz) samples	6000	5256	1403	1250	1232	854	846
	Compressed data (bits)	-	27705	9002	2735	2691	1793	1771
	Compression ratio	-	4.34	13.33	43.89	44.59	66.91	67.78
	Bit rate (bits/sample)	20	3.618	1.500	0.456	0.449	0.299	0.295
	Recovery accuracy (%)	-	99.98	99.85	94.36	94.49	93.16	93.32
	Comp. Time (En- & De-code) (Sec)	-	20.21	6.29	3.47	3.71	2.32	2.58
USC	(Trans+Qntz) samples	6000	5170	1218	1701	1602	1162	1106
	Compressed data (bits)	-	26566	7985	3376	3259	2196	2129
	Compression ratio	-	4.52	15.03	35.55	36.83	54.67	56.39
	Bit rate (bits/sample)	20	4.428	1.331	0.563	0.543	0.366	0.355
	Recovery accuracy (%)	-	99.97	99.81	93.99	94.11	89.61	89.64
	Comp. Time (En- & De-code) (Sec)	-	32.64	9.25	8.05	8.09	5.01	5.31

Chapter 8

Low-rank Structure of Big Data

The multivariate data compression scheme developed in Chapter 7 benefits from the low-rank structure of the multi-channel structural seismic responses. However, it has a premise that the number of the active modes be much less than that of the sensor for a low-rank representation. This chapter further exploits the intrinsic low-dimensional structure of large-scale structural response data, and proposes a matrix-reshape scheme to ensure a low-rank representation of any large-scale structural response data for most effective multi-channel data compression, removing such a common premise as for principal component analysis (PCA) or singular value decomposition (SVD). The key idea of the matrix reshape scheme for guaranteed low-rank representation takes advantage of that mode information (typically few are active, hence the rank of the structural response data matrix is small) remains invariant regardless of the reshaping of the data matrix, which is theoretically justified in this chapter. The effectiveness of the proposed method is demonstrated by significantly compressing the large-scale structural seismic and typhoon response data of the Canton Tower recorded by its SHM system. It is also shown that when using as big data as possible, the low-rank representation becomes more outstanding and hence achieving more effective compression [104].

8.1 Traditional principal component analysis (PCA)

8.1.1 Principal components & vibration modes

In Section 1.3.2 of Chapter 1, the connection between the principal components and vibration modes has been reviewed. Essentially, in structural dynamics, under some assumption, the principal directions would coincide with the mode directions [48] with the corresponding singular values indicating their participating energy in the structural responses $\mathbf{X} \in \mathbb{R}^{m \times N}$, i.e., the structural active modes are captured by r principal components under broadband excitation.

8.1.2 Dimensionality reduction by PCA

With r active principal components, it is possible to reduce the dimension of $\mathbf{X} \in \mathbb{R}^{m \times N}$ by performing a linear transform,

$$\mathbf{Z}_r = \mathbf{U}_r^T \mathbf{X} \tag{8.1}$$

where $\mathbf{Z}_r = [\mathbf{z}_1, ..., \mathbf{z}_r]^T \in \mathbb{R}^{r \times N}$ are the r dominant (uncorrelated) principal components, and $\mathbf{U}_r = [\mathbf{u}_1, ..., \mathbf{u}_r] \in \mathbb{R}^{m \times r}$ is the first r columns of $\mathbf{U} \in \mathbb{R}^{m \times m}$. The recovery of $\mathbf{X} \in \mathbb{R}^{m \times N}$ from the reduced $\mathbf{Z}_r \in \mathbb{R}^{r \times N}$ can be performed by

$$\mathbf{X} = \mathbf{U}_r \mathbf{Z}_r \tag{8.2}$$

For data compression, instead of encoding the original $\mathbf{X} \in \mathbb{R}^{m \times N}$ with m-channel data, one only needs to encode $\mathbf{Z} \in \mathbb{R}^{r \times N}$ with r principal components after the multivariate dimension reduction (the (entropy) encoding step, which can further compress each principal component, is not discussed in this study, however; details can be referred to Ref. [117] or Chapter 7).

Obviously, the dimension reduction for data compression is most effective when $r \ll m$ ($\mathbf{X} \in \mathbb{R}^{m \times N}$ needs to be low-rank), i.e., the channel (sensor) number needs to be (much) larger than that of the involved modes, which is in fact a common assumption where PCA is found effective such as in damage identification and feature extraction [39][49][73]. However, it is not satisfied in many situations: for civil engineering structures, typically large-scale, the sensor number m is not so much more than (often times even less than) the involved r modes; as a result, $r \ll m$ can't be guaranteed for a low-rank representation. A scheme of matrix reshape is proposed to remove this limitation for wider applicability of PCA in multi-channel data compression, as detailed in the following.

8.2 Data compression by low-rank representation with matrix reshape

Originally, $\mathbf{X} \in \mathbb{R}^{m \times N}$ is hardly low-rank; however, applying a simple matrix reshape scheme "generates" a low-rank representation. First, divide the time history of each channel, say, $\mathbf{x}_i \in \mathbb{R}^N$ (ith channel), into l segments, yielding $(\mathbf{x}_i)_j \in \mathbb{R}^v$ as the jth segment of $\mathbf{x}_i$, where $v = N/l$. Then re-stack them into a new structural response matrix $\bar{\mathbf{X}} \in \mathbb{R}^{w \times v}$, where $w = m \times l$ and its ith row $\bar{\mathbf{x}}_i \in \mathbb{R}^v$ as a v-point segment of $\mathbf{x}_i \in \mathbb{R}^N$. Therefore, the SVD of $\bar{\mathbf{X}} \in \mathbb{R}^{w \times v}$ is

$$\bar{\mathbf{X}} = \bar{\mathbf{U}}\bar{\mathbf{\Sigma}}\bar{\mathbf{V}}^T = \sum_{i=1}^{r'} \sigma_i' \bar{\mathbf{u}}_i \bar{\mathbf{v}}_i^T \tag{8.3}$$

The key idea is that because there are still only r modes involved in the re-stacked matrix $\bar{\mathbf{X}} \in \mathbb{R}^{w \times v}$ ($r \ll \min(v, w)$), then

$$\text{rank}(\bar{\mathbf{X}}) = r' \approx r \ll \min(w, v) \tag{8.4}$$

i.e., $\bar{\mathbf{X}}$ becomes a low-rank matrix. The matrix reshape scheme is graphically demonstrated in Fig. 8.1.

Eq. (8.4) can be theoretically justified as follows. Transform each row of $\bar{\mathbf{X}} \in \mathbb{R}^{w \times v}$ to the frequency domain $f \in \Omega$ by right-multiplying $\bar{\mathbf{X}} \in \mathbb{R}^{w \times v}$ with the orthonormal sinusoid basis matrix $\mathbf{C} = [\mathbf{c}_1, ..., \mathbf{c}_v]^T \in \mathbb{R}^{v \times v}$ where $c_{i,j} = \sqrt{2/v} \cos(\pi(2j+1)i/2v)$,

$$\bar{\mathbf{Y}} = \bar{\mathbf{X}}\mathbf{C} \tag{8.5}$$

in which $\bar{\mathbf{Y}} = [\bar{\mathbf{y}}_1, ..., \bar{\mathbf{y}}_w]^T \in \mathbb{R}^{w \times v}$ with the ith row $\bar{\mathbf{y}}_i(f) \in \mathbb{R}^v$ as the discrete cosine transform (DCT) of $\bar{\mathbf{x}}_i(t) \in \mathbb{R}^v$.

Because there are r modes involved (active) under broadband excitation, then for any row of $\bar{\mathbf{X}} \in \mathbb{R}^{w \times v}$, say, $\bar{\mathbf{x}}_i(t) \in \mathbb{R}^v$, its DCT $\bar{\mathbf{y}}_i(f) \in \mathbb{R}^v$ has at most r active (non-zero) elements $\bar{y}_i(f_1), ..., \bar{y}_i(f_r)$, that is,

$$\bar{\mathbf{Y}} = \begin{bmatrix} \bar{\mathbf{y}}_1(f) \\ \vdots \\ \bar{\mathbf{y}}_w(f) \end{bmatrix} = \begin{bmatrix} 0 & \cdots & \bar{y}_1(f_1) & \cdots & 0 & \cdots & \bar{y}_1(f_r) & \cdots & 0 \\ \vdots & \ddots & \vdots & \ddots & \vdots & \ddots & \vdots & \ddots & \vdots \\ 0 & \cdots & \bar{y}_w(f_1) & \cdots & 0 & \cdots & \bar{y}_w(f_r) & \cdots & 0 \end{bmatrix} \tag{8.6}$$

i.e., there are r active (non-zero) columns and $\text{rank}(\bar{\mathbf{Y}}) \approx r$; in addition, $\mathbf{C} \in \mathbb{R}^{v \times v}$ is orthonormal, therefore, $\text{rank}(\bar{\mathbf{X}}) = \text{rank}(\bar{\mathbf{X}}\mathbf{C})$. In summary,

$$r' = \text{rank}(\bar{\mathbf{X}}) = \text{rank}(\bar{\mathbf{X}}\mathbf{C}) = \text{rank}(\bar{\mathbf{Y}}) \approx r \ll \min(w, v) \tag{8.7}$$

In analogy, effective data dimension reduction is finally realized by

$$\bar{\mathbf{Z}}_{r'} = \bar{\mathbf{U}}_{r'}^T \bar{\mathbf{X}} \tag{8.8}$$

Because $r' \ll \min(w, v)$, a significant compression ratio $\rho = r'/\min(w, v)$ can be achieved. Recovery is performed by

$$\bar{\mathbf{X}} = \bar{\mathbf{U}}_{r'}\bar{\mathbf{Z}}_{r'} \tag{8.9}$$

and restacking $\bar{\mathbf{X}} \in \mathbb{R}^{w \times v}$ back to $\mathbf{X} \in \mathbb{R}^{m \times N}$.

Note that the re-stacking guaranteeing low-rank representation removes the constraint that the channel (sensor) number $m > r$ (to ensure redundancy). Besides, the compression ratio $\rho = r'/\min(w,v)$ suggests re-stacking $\bar{\mathbf{X}} \in \mathbb{R}^{w \times v}$ as square as possible for most effective compression efficiency, as will be illustrated by the examples in the following section. It is also interesting to note that long time history (large dimension N) with r' approximately invariant is advantageous for a "most low-rank" representation for data compression, which will also be shown in the following examples.

8.3   Application on SHM data of the Canton Tower

The proposed data compression scheme is applied on the real-measured SHM data of the Canton Tower in this section. The Canton Tower is a high-rise tall building of 610 meters, located in Guangzhou City, China; more description of this structure is referred to Ref. [108]. An advanced SHM system has been instrumented with more than 800 various types of sensors to continuously monitor its performance during construction and service stages. Twenty uni-axial accelerometers, whose layout is shown in Fig. 8.2, were used to continuously record the structural vibration responses (accelerations) in the X and Y axis, with a sampling frequency of 50 Hz. Three data sets of seismic responses and two data sets of typhoon responses are used for demonstrations in this study: the one-hour Burma Earthquake responses (21:29:49-22:29:49, March 24, 2011) $\mathbf{X} \in \mathbb{R}^{20 \times 180000}$, the one-hour Sumatra Earthquake responses (16:08:04-17:08:04, April 11, 2012) $\mathbf{X} \in \mathbb{R}^{17 \times 180000}$, the one-hour Japan Earthquake responses (13:25:37-14:25:37, March 11, 2011) $\mathbf{X} \in \mathbb{R}^{20 \times 180000}$, the twenty-three-hour Nanmadol Typhoon responses (00:07:45-22:07:45, August 31, 2011)

$\mathbf{X} \in \mathbb{R}^{20 \times 4140000}$, and the eighteen-hour Haima Typhoon responses (00:07:22-17:07:22, June 23, 2011) $\mathbf{X} \in \mathbb{R}^{18 \times 3240000}$.

8.3.1   Structural seismic response data

In original data dimension ($m = 20, N = 180000$), they are not low-rank. Fig. 8.3 shows the distribution of their eigenvalues, indicating a compression ratio of about $\rho = 8/20 = 0.4$ can be achieved, which is not significant. On contrary, using a matrix reshape factor of $l = 100$, the new data matrices become $\bar{\mathbf{X}} \in \mathbb{R}^{2000 \times 1800}$ ($\bar{\mathbf{X}} \in \mathbb{R}^{1700 \times 1800}$ for the Sumatra Earthquake), whose eigenvalues decay very fast (Fig. 8.4): the eigenvalues after about the 40th have been approaching to trivial.

Fig. 8.5 further presents the tradeoff between the dimension reduction and the recovery error (in a root-mean-square measure). It is seen that about $\rho = 45/1800 = 0.025$ can be safely achieved with stabilized recovery error, which is consistent with the distribution of their eigenvalues that those after about 40th have become trivial. It is also seen that the structural seismic responses recovered from the compressed data suffer little distortion in both the time-domain and frequency-domain and tend to approach the denoised (smoothed) data [149] of the original structural responses; see Figure 8.6 for example, of the first channel data from the Burma Earthquake case.

Fig. 8.7 also shows the advantage of using a reshape factor l that makes the new matrix as square as possible. In Fig. 8.7(a), it is shown that the ranks r' of the new matrices with different reshape factor do not have much difference (about 25). However, choosing a suitable reshape factor that maximizes $\min(w, v)$ can make the eigenvalues decay fastest, thus achieving most significant compression ratio $\rho = r'/\min(w, v)$; this is seen in Fig. 8.7(b) that $l = 100$ ($w = 2000, v = 1800$) makes the

eigenvalues of the corresponding matrix decaying fastest ("most low-rank"), although other values in the neighborhood of $l = 100$ also have reasonably significant data compression ratio.

8.3.2 Compressing "big data" of structural typhoon responses

The data dimension of the structural typhoon responses is even more large-scale: $\mathbf{X} \in \mathbb{R}^{20 \times 4140000}$ (82.8 million data points) for the Nanmadol Typhoon and $\mathbf{X} \in \mathbb{R}^{18 \times 3240000}$ (58.32 million data points) for the Haima Typhoon. To demonstrate the advantage of the proposed method in compressing very large (or as large as possible) data set, the eigenvalue distributions (normalized) of the different segments (different hour-lengths) of the reshaped $\mathbf{X} \in \mathbb{R}^{20 \times 4140000}$ and $\mathbf{X} \in \mathbb{R}^{18 \times 3240000}$ are shown in Fig. 8.8 and Fig. 8.9. It is seen that for all the typhoon response data sets, the reshaped matrices have low-rank representation, with the eigenvalues decaying very rapidly. However, the low-rank representation of larger data set stands out with fastest-decaying eigenvalues hence achieving most significant data compression: for the 23-hour data set of the Nanmadol Typhoon responses and the 18-hour data set of the Haima Typhoon responses, a significant compression ratio of about $\rho = 0.01$ can be achieved.

8.4 Conclusions

This chapter presents a new multi-channel data compression algorithm by exploiting the intrinsic low-dimensional structure of large-scale structural seismic and typhoon responses. A matrix reshape scheme is proposed for a low-rank representation (by singular value decomposition (SVD) or principal component analysis (PCA)) of the large-scale data for most effective multi-channel data compression, removing the com-

mon constraint that channel (sensor) number needs to be (much) larger than that of the involved vibration modes. The effectiveness of the proposed method is demonstrated by significantly compressing the large-scale structural seismic and typhoon response data of the Canton Tower recorded by its SHM system. Results also show that when using as large-scale data as possible, the low-rank representation after matrix reshape becomes more outstanding and hence achieving more effective compression.
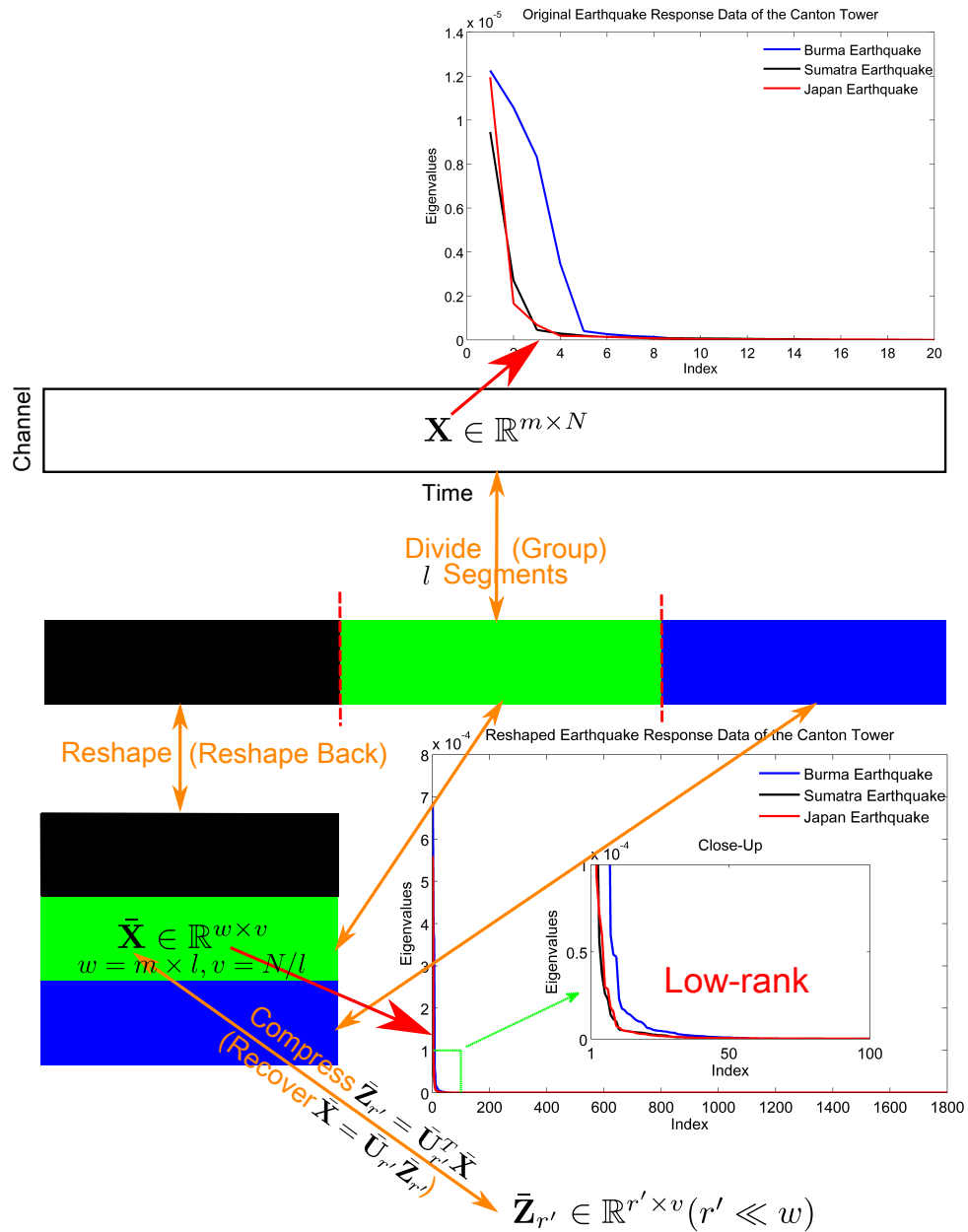
Figure 8.1 : The data compression scheme with the matrix reshaping strategy. The original data matrix $\mathbf{X} \in \mathbb{R}^{m \times N}$ (m channels and each with N time history points) does not have a low-rank structure ($\rho = r/\min(m, N)$ is not low with the active eigenvalue number r and the dimension $\min(m, N)$). Divide the fat $\mathbf{X} \in \mathbb{R}^{m \times N}$ into l segments and reshape it to a new matrix $\bar{\mathbf{X}} \in \mathbb{R}^{w \times v}$ ($w = m \times l, v = N/l$) with each segment as one "row". It turns out that the rank of $\bar{\mathbf{X}} \in \mathbb{R}^{w \times v}$ remains $r' \approx r$ but $\rho' \approx r'/\min(w, v)$ is significantly low hence a low-rank representation. Dimensionality reduction is performed by $\bar{\mathbf{Z}}_{r'} = \bar{\mathbf{U}}_{r'}^T \bar{\mathbf{X}}$ and finally one only needs to encode $\bar{\mathbf{Z}}_{r'} \in \mathbb{R}^{r' \times v}$ with r' components each is of $\mathbb{R}^v$ where $r' \approx r \ll w$. Recovery is performed by the corresponding inverse linear transform $\bar{\mathbf{X}} = \bar{\mathbf{U}}_{r'} \bar{\mathbf{Z}}_{r'}$.
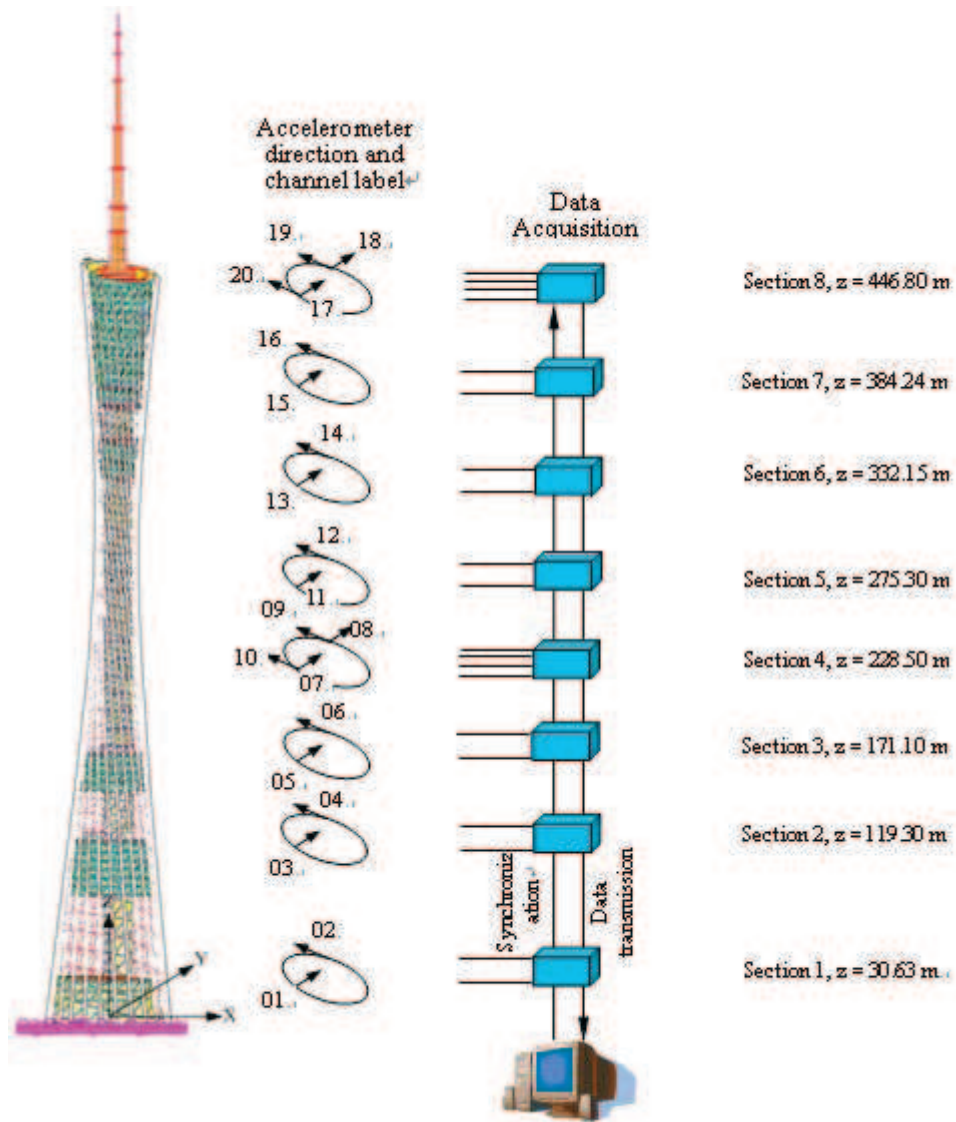
Figure 8.2 : The sensor outline of the ambient vibration testing of the Canton Tower. The number and arrow denote the sensor number and measurement axis, respectively.
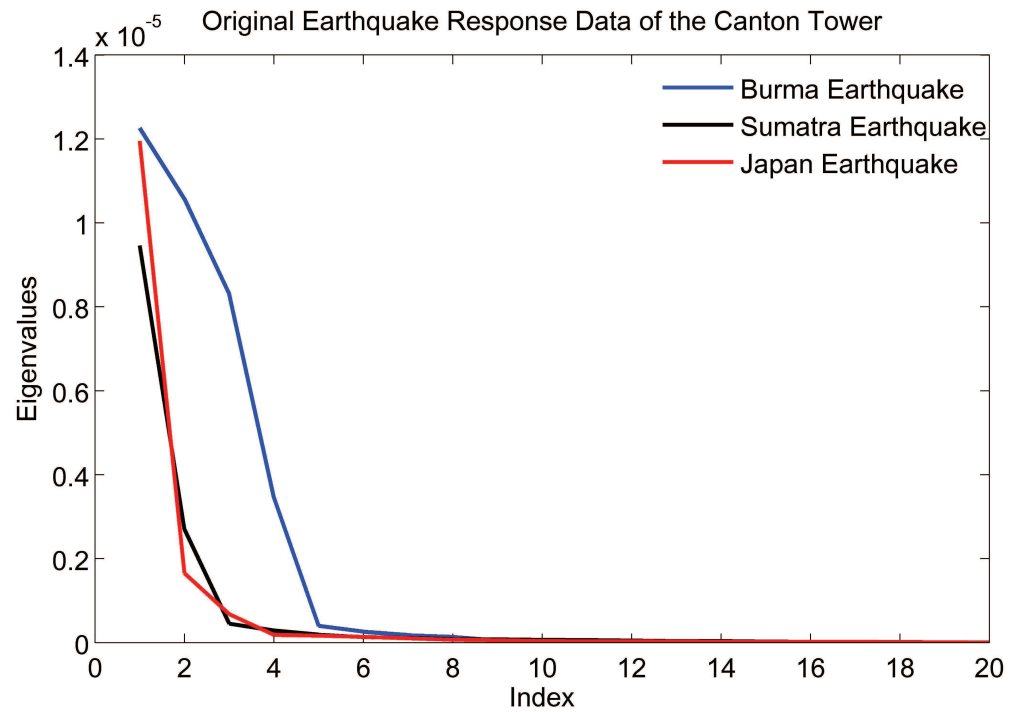
Figure 8.3 : The eigenvalues (square of the singular values) of the earthquake response data matrices of the Canton Tower in their original dimension: $\mathbf{X} \in \mathbb{R}^{20 \times 180000}$ for the Burma Earthquake, $\mathbf{X} \in \mathbb{R}^{17 \times 180000}$ for the Sumatra Earthquake, and $\mathbf{X} \in \mathbb{R}^{20 \times 180000}$ for the Japan Earthquake.
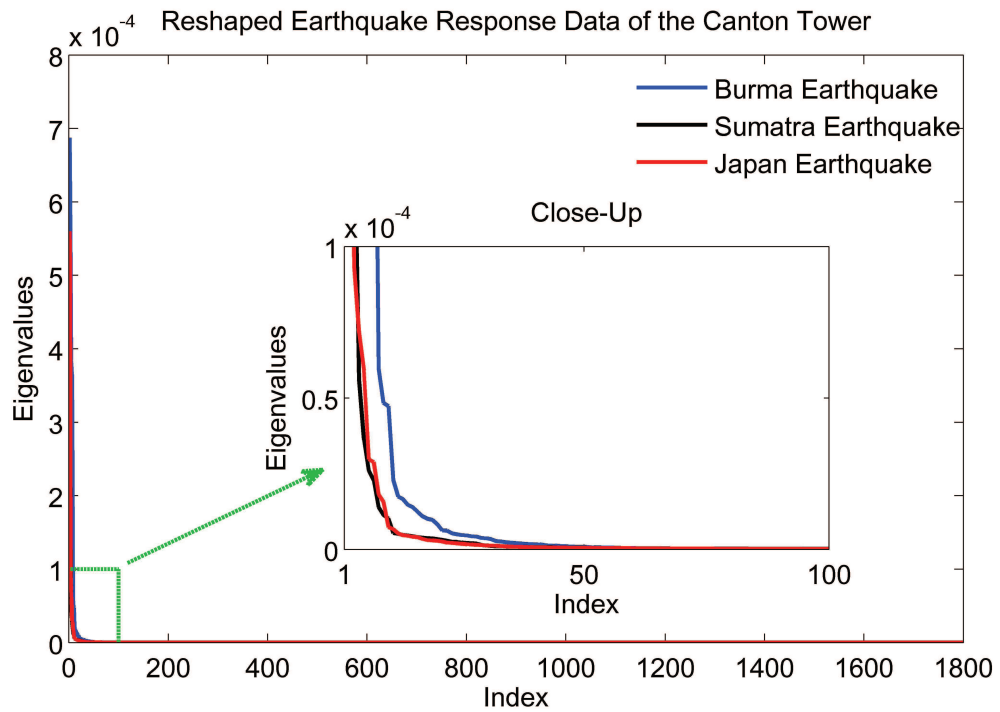
Figure 8.4 : The eigenvalues (square of the singular values) of the earthquake response data matrices of the Canton Tower in reshaped dimension with $l = 100$: $\bar{\mathbf{X}} \in \mathbb{R}^{2000 \times 1800}$ for the Burma Earthquake, $\bar{\mathbf{X}} \in \mathbb{R}^{1700 \times 1800}$ for the Sumatra Earthquake, and $\bar{\mathbf{X}} \in \mathbb{R}^{2000 \times 1800}$ for the Japan Earthquake.
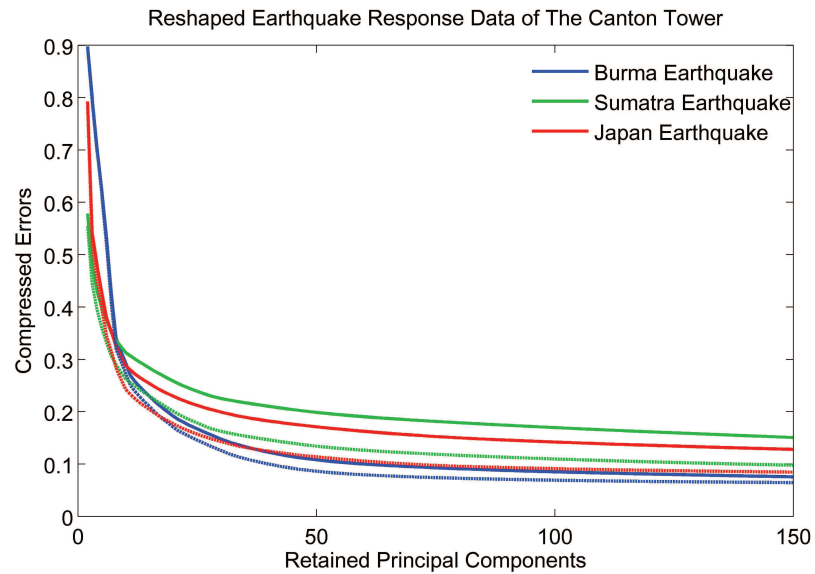
(a)
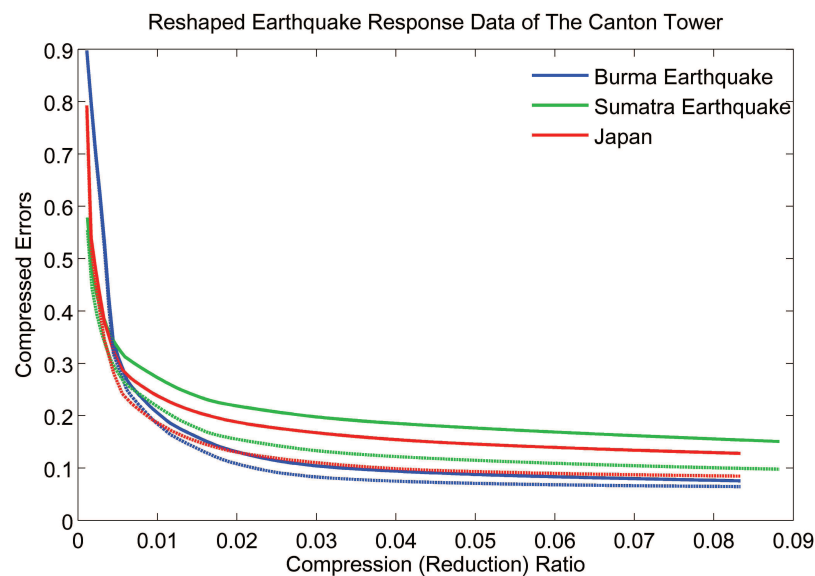
(b)

Figure 8.5 : The recovery errors (averaged per channel) from the compressed data (a) when retaining different numbers of the dominant principal components (b) with the scaled retained number of the dominant principal components normalized by its dimension (compression ratio). The dimensionality reduction are applied on the earthquake response data matrices of the Canton Tower in reshaped dimension with $l = 100$: $\bar{\mathbf{X}} \in \mathbb{R}^{2000 \times 1800}$ for the Burma Earthquake, $\bar{\mathbf{X}} \in \mathbb{R}^{1700 \times 1800}$ for the Sumatra Earthquake, and $\bar{\mathbf{X}} \in \mathbb{R}^{2000 \times 1800}$ for the Japan Earthquake. (The solid lines indicate the errors calculated using the recorded data as correct data and the dashed lines using the PCP-denoised data as correct data.)
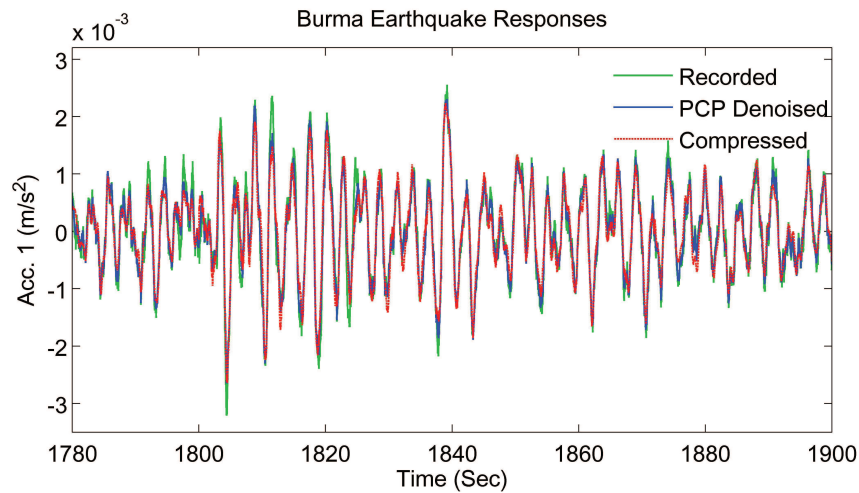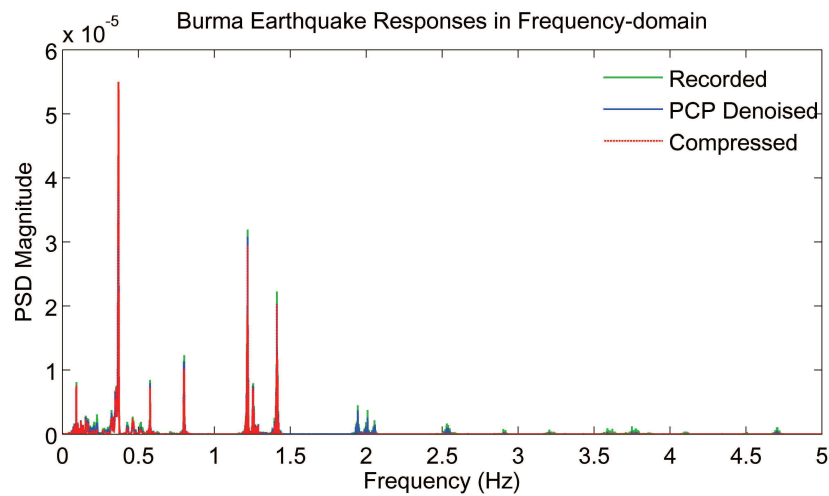
Figure 8.6 : The Burma Earthquake structural responses (accelerations) in Channel 1 of the Canton Tower recovered from the compressed data in (a) time domain and (b) frequency domain, compared to the recorded and PCP-denoised data. The dimensionality reduction are applied on the Burma Earthquake response data matrices in reshaped dimension $\bar{\mathbf{X}} \in \mathbb{R}^{2000 \times 1800}$ with $l = 100$ and only the first 50 principal components with larger singular values are retained (the compression ratio $\rho = 50/1800 = 0.0278$).
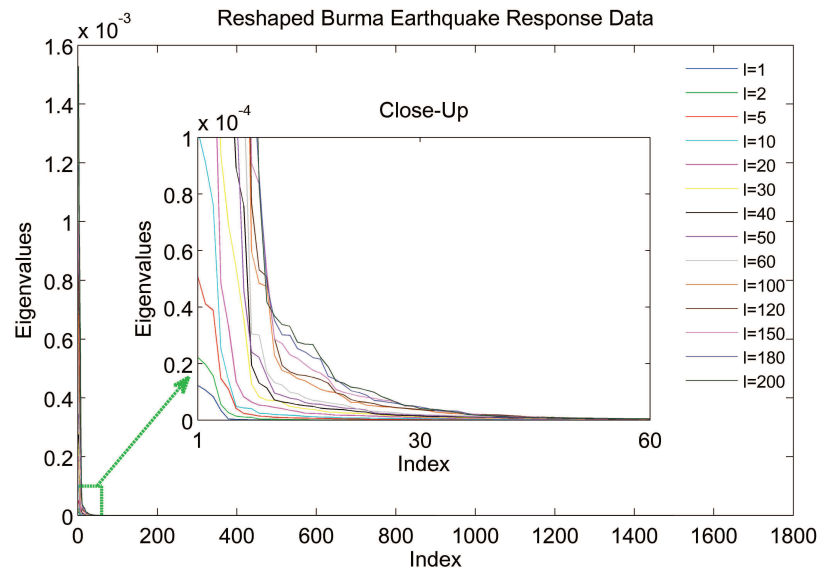
(a)
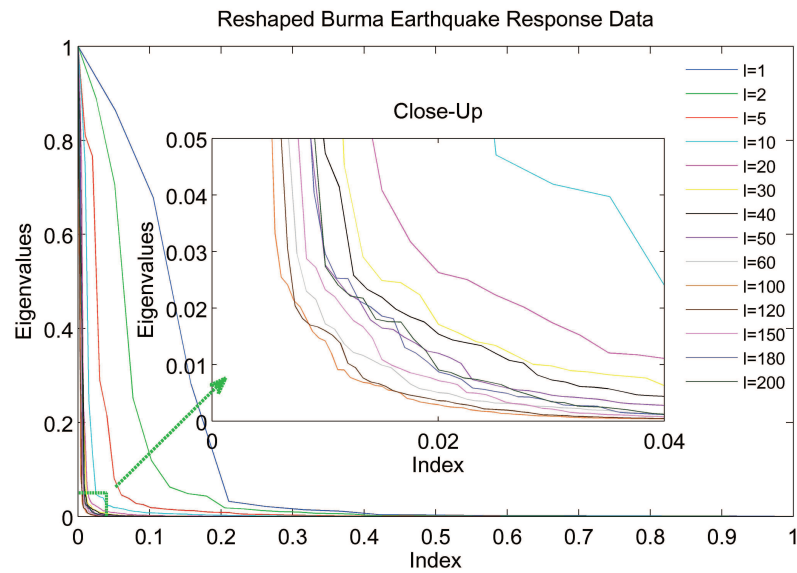
(b)

Figure 8.7 : (a) The eigenvalue of the Burma Earthquake response data matrices $\bar{\mathbf{X}} \in \mathbb{R}^{w \times v}$ of the Canton Tower in reshaped dimension with different reshape factors l (originally $\mathbf{X} \in \mathbb{R}^{20 \times 180000} = \in \mathbb{R}^{m \times N}$, $w = m \times l, v = N/l$). (b) a normalized version of (a), with the eigenvalue index normalized by $\min(w, v)$ and the eigenvalues normalized by the largest one.
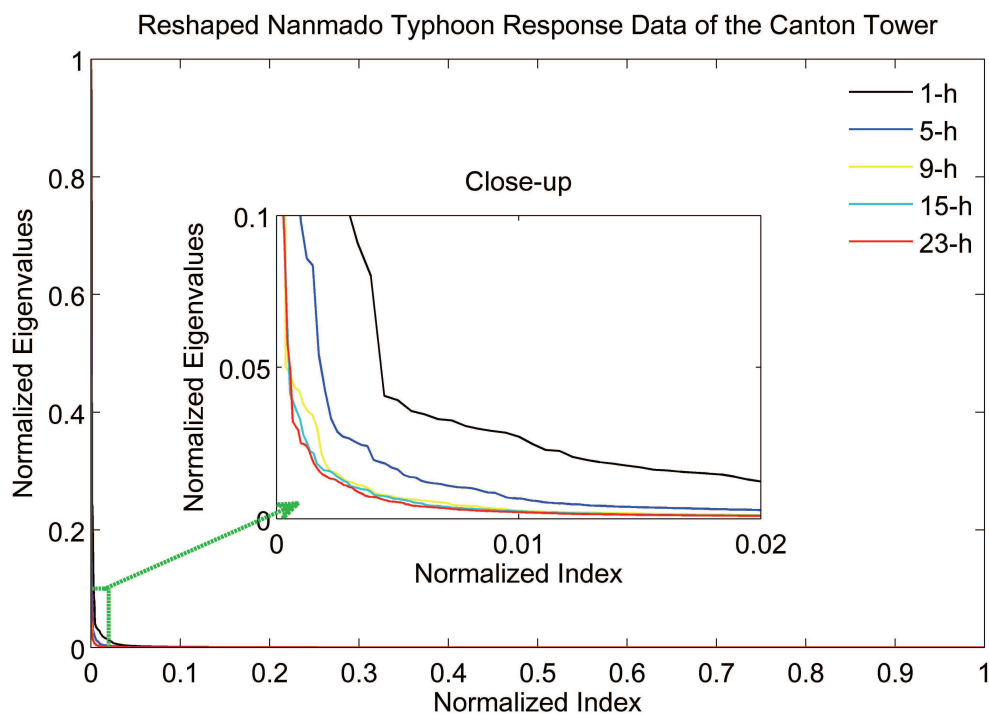
Figure 8.8 : The eigenvalue of the Nanmadol Typhoon response data matrices of the Canton Tower in reshaped dimension: $\bar{\mathbf{X}} \in \mathbb{R}^{2000 \times 1800}$ for the 1-hour data set, $\bar{\mathbf{X}} \in \mathbb{R}^{4000 \times 4500}$ for the 5-hour data set, $\bar{\mathbf{X}} \in \mathbb{R}^{6000 \times 5400}$ for the 9-hour data set, $\bar{\mathbf{X}} \in \mathbb{R}^{7200 \times 7500}$ for the 15-hour data set, and $\bar{\mathbf{X}} \in \mathbb{R}^{9000 \times 9200}$ for the 23-hour data set. The eigenvalue index is normalized by $\min(w, v)$ and the eigenvalues normalized by the largest one of each data set.
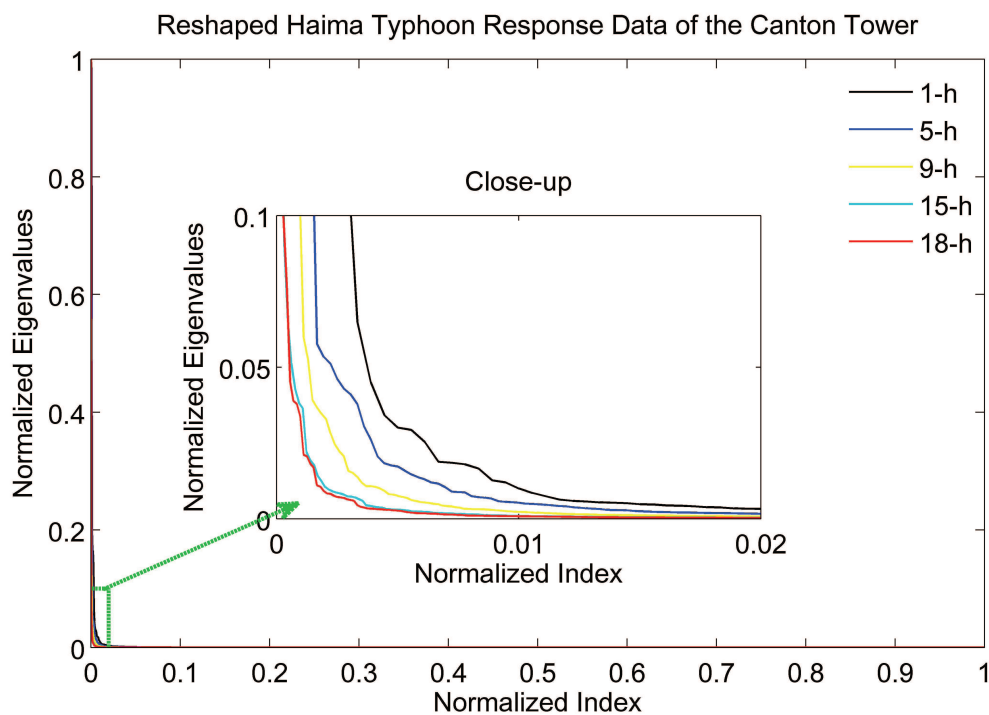
Figure 8.9 : The eigenvalue of the Haima Typhoon response data matrices of the Canton Tower in reshaped dimension: $\bar{\mathbf{X}} \in \mathbb{R}^{1800 \times 1800}$ for the 1-hour data set, $\bar{\mathbf{X}} \in \mathbb{R}^{3600 \times 4500}$ for the 5-hour data set, $\bar{\mathbf{X}} \in \mathbb{R}^{5400 \times 5400}$ for the 9-hour data set, $\bar{\mathbf{X}} \in \mathbb{R}^{6480 \times 7500}$ for the 15-hour data set, and $\bar{\mathbf{X}} \in \mathbb{R}^{8100 \times 7200}$ for the 23-hour data set. The eigenvalue index is normalized by $\min(w, v)$ and the eigenvalues normalized by the largest one of each data set.

Chapter 9

Data Cleansing using Low-rank Representation

Among many data management problems associated with the massive SHM data, a fundamental one would be obtaining truly reliable structural response data for further analysis; such is referred to the data cleaning process [47]. Unfortunately, the real-world measured data typically contains considerable noise or errors that would significantly affect further analysis. For example, Fig. 1.1 shows the ambient vibration response data of the Canton Tower recorded from the structural health monitoring system; it contains remarkable sparse outliers (gross errors), which call for efficient data cleaning or de-noising algorithms before they can be used for structural assessment. This chapter develops a new data denoising method which is able to simultaneously remove both dense noise and gross outliers in SHM data set; it explicitly exploits the structure of the noisy large-scale SHM data: outliers are sparse in nature, and the underlying clean multi-channel structural responses are intrinsically low-rank (with few active modes).

9.1 Introduction

The de-noising problem in structural dynamics and SHM communities have been studied using various techniques. Singular value decomposition (SVD, closely related to the principal component analysis (PCA)) was proposed for noise reduction in vibration signals of rotating machinery [143]. A Bayesian wavelet packet denoising

scheme was developed for system identification; this approach can not only remove the present noise, but also characterize the noise level of the data [71]. Also, an optimal global projection denoising method was proposed to better capture the nonlinear fault features in the vibration signals of the shaft orbits [58]. For removal of the noise in the acoustic emission signals in local SHM damage inspection, particle filter based method was also formulated and found to outperform other filtering methods [158]. Noise suppression method was also reported to facilitate robust damage identification in beam-type structures [11].

These existing methods, however, are mostly devoted to removal of (Gaussian-type) dense small noise in vibration signals; little efforts-if not none-have been made to handle the outliers (sparse spikes with arbitrarily large amplitudes unreasonably present in the signals), which are not uncommon in practical seismic monitoring or SHM systems, such like those shown in Fig. 1.1. Such outliers may arise due to sensor imperfection, instrumentation error, sensor failure, environmental factors, etc, or simply because some measurements are considerably inconsistent.

This chapter develops a new de-noising algorithm in order to simultaneously deal with both dense noise and outliers by exploiting the intrinsic dynamic information contained in the structural responses. The developed method casts the de-noising problem into the framework of low-dimensional matrix recovery in presence of both grossly corrupted errors and small dense noise. First, a simple re-stacking strategy is proposed to guarantee a low-rank representation of the structural response data matrix corrupted by noise, by taking advantage of the observation that mode information (typically few are active, hence the rank of the matrix) remain invariant regardless of the reshaping of the data matrix. The reshaped data matrix is then decomposed into a superposition of a low-rank matrix plus a sparse outlier matrix with small dense

noise via the new technique principal component pursuit (PCP) [23][160], which is also explored in Chapter 6. The denoised low-rank data matrix is finally re-stacked back to its original shape as the estimation of the noise-free data matrix.

9.2 PCA/SVD de-noising

9.2.1 Principal components & vibration modes

In Section 1.3.2 of Chapter 1 and Section 8.1 of Chapter 8, the connection between the principal components and vibration modes has been reviewed. Essentially, in structural dynamics, under some assumption, the principal directions would coincide with the mode directions [48] with the corresponding singular values indicating their participating energy in the structural responses $\mathbf{X} \in \mathbb{R}^{m \times N}$, i.e., the structural active modes are captured by r principal components under broadband excitation. There are typically only few modes are active in the structural responses [149]; in other words, few of its singular values are active: r can be quite small.

9.2.2 PCA de-noising

If $\mathbf{X}$ is contaminated by small dense noise $\mathbf{N}_0$,

$$\hat{\mathbf{X}} = \mathbf{X}_0 + \mathbf{N}_0 \tag{9.1}$$

then de-noising can be achieved by keeping only the r principal components with largest singular values, where the modal components are dominant over the noise, while others dominated by noise are abandoned. Such a strategy is termed PCA de-noising; if $\mathbf{N}_0$ is small and i.i.d. Gaussian, it is optimal in an ℓ_2 sense, and can be realized by the following program

$$(P_2): \quad \text{minimize} \quad \|\hat{\mathbf{X}} - \mathbf{X}\|_{\ell_2} \quad \text{subject to} \quad \text{rank}(\mathbf{X}) \leq r \tag{9.2}$$

where $\|\mathbf{X}\|_{\ell_2} = \sigma_1(\mathbf{X})$. From above, it can be observed that (traditional) PCA de-noising would require $m > r$, i.e., the sensor number needs to be larger than that of the involved modes (such a requirement is in fact a common assumption where PCA is found effective such as in damage identification and feature extraction [39][49][73]), which is not known a priori, however. Empirical thresholding would then be demanded in practice, say, keeping only r' largest principal components. However, even one single outlier in the measurement $\hat{\mathbf{X}}$ would render (P_2) completely fail in finding the true $\mathbf{X}_0$, since the ℓ_2-minimization does not account for such grossly corrupted error, which, unfortunately, is ubiquitous in practice. Robust PCA technique, PCP, explicitly handles both small dense noise and large outliers, detailed as follows.

9.3 PCP de-noising

Robust PCA [23][160], termed PCP, is capable of dealing with the most challenging de-noising problem-when the original data $\mathbf{X} \in \mathbb{R}^{m \times N}$ are addictively corrupted by both gross errors (outliers) and dense noise,

$$\hat{\mathbf{X}} = \mathbf{X}_0 + \mathbf{N}_0 + \mathbf{Z}_0 \tag{9.3}$$

where $\mathbf{Z}_0 \in \mathbb{R}^{m \times N}$ has few (sparse) but gross outlier elements with arbitrarily large and located magnitudes, and $\mathbf{N}_0 \in \mathbb{R}^{m \times N}$ is entry-wise i.i.d. small dense noise. PCP (the stable version) aims to recover $\mathbf{X}_0$ by solving the following convex program

$$(P_*): \quad \text{minimize} \quad \|\mathbf{X}\|_* + \lambda\|\mathbf{Z}\|_{\ell_1} \quad \text{subject to} \quad \|\hat{\mathbf{X}} - \mathbf{X} - \mathbf{Z}\|_{\mathrm{F}} \leq \delta \tag{9.4}$$

where $\|\mathbf{X}\|_* := \sum_i \sigma_i(\mathbf{X})$ is the nuclear norm of the matrix $\mathbf{X}$, which summates its singular values; $\|\mathbf{Z}\|_{\ell_1} := \sum_{ij} |z_{ij}|$ denotes the ℓ_1-norm of the matrix $\mathbf{Z}$, which is thought as a long vector; $\lambda = 1/\sqrt{N}$ is a trading parameter, $\|\mathbf{X}\|_{\mathrm{F}} := \sqrt{\sum_i \sigma_i{}^2}$ is the

Frobenius norm of $\mathbf{X}$, and δ is some bounding parameter related to the small dense noise level.

The nuclear norm is the convex approximation to the rank of a matrix, and the ℓ_1-norm is the tightest convex relaxation to the well-known sparsity measure ℓ_0-norm that simply counting the non-zero entries of a matrix. (P_*) can be interpreted as to find the $\mathbf{X}_0^\star$ with smallest rank and $\mathbf{Z}_0^\star$ with sparsest representation that explain the observation $\hat{\mathbf{X}}$ within a bounded noise level δ.

Candes et al. [23][160] rigorously proves that under surprisingly broad conditions, with overwhelmingly high probability, (P_*) accurately recovers the true low-rank $\mathbf{X}_0$ and sparse $\mathbf{Z}_0$. Note that (P_*) assumes no any a priori knowledge of $\mathbf{X}_0$'s rank nor the distribution of the singular values, nor the magnitudes and locations of the non-zero entries (outliers) of $\mathbf{Z}_0$; all it requires are that $\mathbf{X}_0$ is indeed low-rank and $\mathbf{Z}_0$ sparse. The detailed proof is referred to [23][160]. The convex (P_*) program can be implemented using an Augmented Lagrange multiplier (ALM) method [81]. Inheriting from the virtue of convex program, the solution to (P_*) found by APG is always globally optimal.

9.4 Guaranteed low-rank representation

The PCP technique with (P_1) program is straightforward and tempting for the robust de-noising problem. First, the good news is that the outliers or gross errors $\mathbf{Z}_0 \in \mathbb{R}^{m \times N}$ present in the signals are indeed sparse as indicated by their nature. On the other hand comes the bad news that $\mathbf{X}_0 \in \mathbb{R}^{m \times N}$, which is aimed to be recovered from the noisy measurements $\hat{\mathbf{X}} \in \mathbb{R}^{m \times N}$, is seldom (if ever) low-rank: for civil engineering structures, typically large-scale, the sensor number m is not so much more than (often times even less than) the involved r modes; as a result, $r \ll m$ can't be

guaranteed for a low-rank representation. In fact, this assumption commonly made in previous literatures can seldom be realized in practice that sensor numbers be larger than involved vibration modes. On the one hand, as mentioned, civil engineering structures are typically large-scale and may have numerous active modes; on the other, when subject to complex or varying excitation, the mode number excited out can be time-variant.

The matrix reshape scheme proposed in Section 8.2 of Chapter 8 can be adopted to solve this problem, and the weak assumption for the success of PCP serves as the key to constructing a low-rank representation of the structural response matrix for robust de-noising. Divide the time history of each channel, say, $\mathbf{x}_i \in \mathbb{R}^N$ (ith channel), into l segments, yielding $(\mathbf{x}_i)_j \in \mathbb{R}^v$ as the jth segment of $\mathbf{x}_i$, where $v = N/l$. Then re-stack them into a new structural response matrix $\bar{\mathbf{X}} \in \mathbb{R}^{w \times v}$,

$$\hat{\mathbf{X}} = \mathbf{X}_0 + \mathbf{N}_0 + \mathbf{Z}_0 \tag{9.5}$$

where $w = m \times l$, $\bar{\mathbf{X}}_0, \bar{\mathbf{Z}}_0, \bar{\mathbf{N}}_0 \in \mathbb{R}^{w \times v}$. Such a strategy can be seen as enhancing each original spatial sensors with l "virtual" temporal sensors. Because there are still only r modes involved in the re-stacked matrix $\bar{\mathbf{X}} \in \mathbb{R}^{w \times v}$, then

$$\text{rank}(\bar{\mathbf{X}}) \approx r \ll \min(w, v) \tag{9.6}$$

i.e., $\bar{\mathbf{X}}$ becomes a low-rank matrix (a theoretical justification of Eq. (9.6) is shown in Section 8.2 of Chapter 8). Plus, both the ℓ_1-norm and Frobenius norm of a matrix are summations of its entries and energy, respectively; as such, restacking won't essentially change the property that $\bar{\mathbf{Z}}_0 \in \mathbb{R}^{w \times v}$ remains sparse, and $\bar{\mathbf{N}}_0 \in \mathbb{R}^{w \times v}$ bounded. With these assumptions satisfied, (P_*) accurately estimates the low-rank $\bar{\mathbf{X}}_0 \in \mathbb{R}^{w \times v}$ (and the outliers $\bar{\mathbf{Z}}_0 \in \mathbb{R}^{w \times v}$), which can then be readily re-stacked back to $\mathbf{X}_0^\star \in \mathbb{R}^{m \times N}$.

Note that the re-stacking guaranteeing low-rank representation also benefits the traditional PCA de-nosing when the outliers are absent, as it removes the constraint that the sensor number $m > r$ (to ensure redundancy). Besides, Eq. (9.6) suggests re-stacking $\bar{\mathbf{X}} \in \mathbb{R}^{w \times v}$ as square as possible, but this needs not to be exactly so in practice, as will be illustrated by various examples in the numerical simulation section. It is also interesting to note a somewhat obvious yet strange fact that long time history (large N) is advantageous for a low-rank representation and hence the success of PCP de-noising: large-scale data set is in fact more welcome (this is already seen in Section 8.3.2 of Chapter 8), but the computation burden will of course increase.

9.5 PCP de-noising strategy

The proposed PCP de-noising scheme is able to simultaneously remove both dense noise and gross outliers under broad conditions for success; its implementation is straightforward and efficient, following these steps:

Step 1. According to the matrix dimension, choose a reshape factor l that would make the new structural response data matrix roughly square.

Step 2. Perform PCP on the shaped structural response matrix to recover the low-rank matrix.

Step 3. Re-stack the recovered low-rank matrix back to the structural response matrix in its original shape as the estimation of the clean structural response data.

9.6 Numerical simulation

9.6.1 Model setup

To demonstrate the performance of the proposed PCP de-noising algorithm, numerical simulations are conducted on the 12-DOF linear time-invariant mass-spring damped model (Fig. 2.9) in this section. The parameters are set as follows: the mass is $m_1 = 2, m_2 = m_3 = ... = m_{11} = 1, m_{12} = 3$, the spring stiffness is $k_1 = k_2 = ... = k_{13} = 1$, Proportional damping is considered with respect to the mass matrix as $\mathbf{C} = \alpha\mathbf{M}$ with $\alpha = 0.001$. Newmark-Beta algorithm is used to obtain time histories of the system responses. The sampling frequency is set at 10 Hz, and the time histories 2000 seconds, ending up with $N = 20000$ samples at each of the $m = 12$ channels, i.e., the structural response matrix $\mathbf{X}_0 \in \mathbb{R}^{12 \times 20000}$.

9.6.2 Performance results

9.6.2.1 Reshape & low-rank representations

This section first shows that the strategy of re-stacking the structural response matrix makes low-rank representations that are desired for effective de-noising. Free vibration is induced by initial impact at the 12th DOF Different reshape factors l are applied to re-stack the original clean $\mathbf{X}_0 \in \mathbb{R}^{12 \times 20000}$; for example, if $l = 40$, then $w = 12 \times 40 = 480$, and $v = 20000/40 = 500$, then the re-stacked $\bar{\mathbf{X}}_0 \in \mathbb{R}^{480 \times 500}$, and so on. After conducting SVD on the re-stacked matrix, the singular values are shown from Fig. 9.1 for free vibration case. They indicate that the singular values vanish fast for all the re-stacked matrices, i.e., the rank of $\bar{\mathbf{X}}_0$, r, is small. Take $l = 40$ for example again, $r \ll \min(w, v) = 480$, i.e., $\bar{\mathbf{X}}_0 \in \mathbb{R}^{480 \times 500}$ is indeed a low-rank matrix that may be targeted by the PCP if corrupted by noise in practice, whose performance will be

shown in the following section. Contrarily, for the original $\mathbf{X}_0 \in \mathbb{R}^{12 \times 20000}$ ($l = 1$), although r is small, but $\min(w, v) = 12$, which does not make a low-rank matrix.
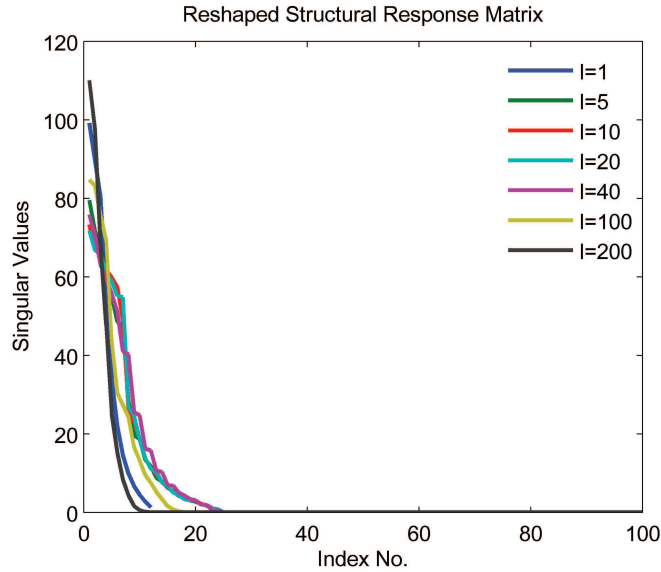
Figure 9.1 : Singular values of the reshaped structural response data matrices of the 12-DOF model with different reshaping factors in free vibration.

9.6.2.2 PCP denoising of outliers

With the re-stacking strategy, the performance of PCP can be applied to simultaneously denoise both dense noise and gross outliers. Dense noise modeled as zero-mean GWN (SNR=20 dB or 10% RMS noise level with respect to the original clean signal) is first added to the structural response $\mathbf{X}_0 \in \mathbb{R}^{12 \times 20000}$ at each channel, and then 1% outliers (i.e., 2400 entries out of the $12 \times 20,000 = 240,000$ ones) are distributed uniformly at random among the matrix with normally-distributed magnitudes (zero-mean and 10-variance) multiplied by the standard deviation of the first displacement $\mathbf{x}_1 \in \mathbb{R}^{20000}$; the measured noisy data matrix is therefore $\hat{\mathbf{X}} \in \mathbb{R}^{12 \times 20000}$ with both dense noise and sparse outliers.

A reshape factor $l = 40$ is used and the PCP is applied to decompose the re-stacked $\bar{\mathbf{X}} \in \mathbb{R}^{480 \times 500}$, and it is shown that the PCP accurately recovers the original clean structural responses from the corrupted measurements. Fig. 9.2 shows that the noisy measurement with both dense noise and gross outliers are smoothly denoised by PCP, and the PCP-denoised signal matches the original clean signal very well.

The PCA-denoising scheme is also conducted for comparisons. PCA fails whenever gross outliers are present, as already shown in Fig. 9.2. To quantitatively measure their performance, the recovery error at the ith channel is measured by

$$\epsilon_i = \frac{\|\mathbf{x}'_i - \mathbf{x}_i\|_{\ell_2}}{\|\mathbf{x}_i\|_{\ell_2}} \tag{9.7}$$

or in an SNR measure

$$\text{SNR} = 20 \log_{10} \frac{\text{RMS}(\mathbf{x}_i)}{\text{RMS}(\mathbf{x}'_i - \mathbf{x}_i)} \tag{9.8}$$

where $\mathbf{x}_i$ and $\mathbf{x}'_i$ are the original clean signal and the de-noised signal at the ith channel. Table 9.1 shows that PCP clearly outperforms PCA in simultaneous denoising both outliers and dense noise.

9.7 Application on Canton Tower SHM data

The proposed PCP de-noising scheme is applied on the real-measured SHM data of the Canton Tower (Fig. 8.2) in this section. The Canton Tower is a high-rise tall building of 610 meters, located in Guangzhou City, China; more description of this structure is referred to Ref. [108]. An advanced SHM system has been instrumented with more than 800 various types of sensors to continuously monitor its performance during construction and service stages. In particular, an SHM benchmark problem was established based on full-scale field measurements; a set of 24-hour ambient vibration data recorded from 18:00 Jan. 19th, 2010 to 18:00 Jan. 20th, 2010 is
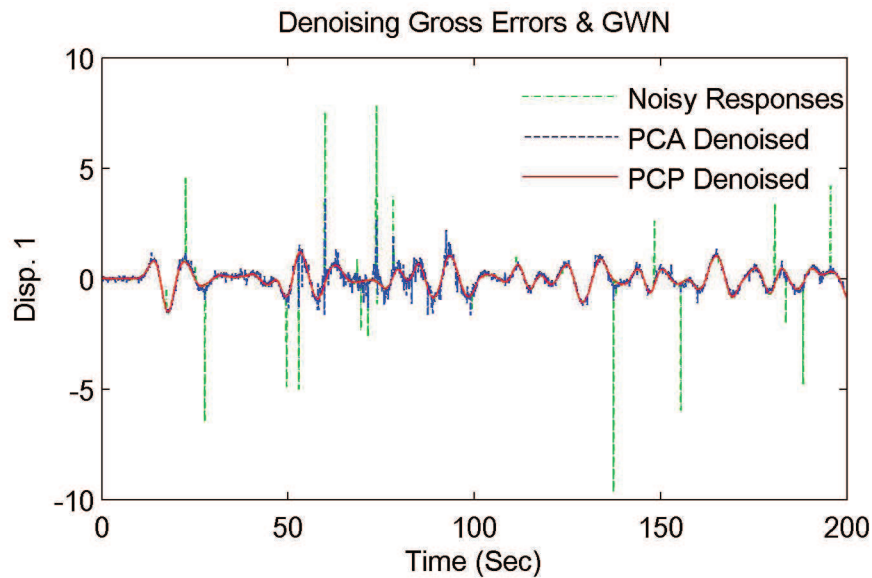
Figure 9.2 : PCP and PCA denoising with re-stacking strategy of the structural responses with both GWN and gross outliers of the 12-DOF model in free vibration (Channel 1), reshaped factor $l = 40$, $\alpha = 0.001$, 0-200 seconds are shown for visual enhancement.

provided on the website [1]. Twenty uni-axial accelerometers, whose layout is shown in Fig. 8.2, were used to record the structural responses in the X and Y axis, with a sampling frequency of 50 Hz.

As shown in Fig. 1.1, remarkable outliers are present in the measured SHM data, which would significantly affect the value of the data for further analysis and identification. The one-hour data from 12:00 Jan. 20th to 13:00 Jan. 20th 2010 is used to show the ability of PCP denoising in this study. The measured structural response data matrix is then $\hat{\mathbf{X}} \in \mathbb{R}^{20 \times 180000}$. The re-stack scheme is applied with $l = 100$ such that the reshaped $\bar{\mathbf{X}} \in \mathbb{R}^{1800 \times 2000}$. The SVD analysis of $\hat{\mathbf{X}}$ shows that the singular values do not vanish whatsoever (Fig. 9.3(a)) and same situation happens for $\bar{\mathbf{X}} \in \mathbb{R}^{1800 \times 2000}$: the PCA de-noising scheme would not work, which is mostly caused by the significant outliers.

Table 9.1 : Denoising performance of PCP and PCA with gross outliers and dense GWN (reshape $l = 40$).

| Channel | Free vibration | | | | Random vibration | | | |
| | SNR (dB) | | Error (%) | | SNR (dB) | | Error (%) | |
	PCP	PCA	PCP	PCA	PCP	PCA	PCP	PCA
1	50.36	12.48	0.30	23.76	48.56	14.24	0.37	19.41
2	50.33	19.52	0.30	10.57	48.74	15.95	0.37	15.94
3	50.09	18.45	0.31	11.95	49.20	17.30	0.35	13.65
4	50.23	16.68	0.31	14.66	49.39	19.93	0.34	10.09
5	49.92	20.64	0.32	9.29	48.93	19.85	0.36	10.18
6	49.89	15.05	0.32	17.69	48.73	13.95	0.37	20.07
7	50.20	19.07	0.31	11.13	48.21	15.50	0.39	16.80
8	50.14	8.76	0.31	36.50	48.73	16.95	0.37	14.20
9	50.12	18.99	0.31	11.23	49.03	22.21	0.35	7.75
10	49.91	18.95	0.32	11.28	48.87	18.61	0.36	11.73
11	49.84	13.47	0.32	21.21	48.37	15.01	0.38	17.77
12	51.50	22.35	0.27	7.63	48.65	19.07	0.37	11.13

PCP is used to denoise $\bar{\mathbf{X}}$, and then re-stack back to $\tilde{\mathbf{X}} \in \mathbb{R}^{20 \times 180000}$ and plotted in Fig. 9.4. Clearly all the outliers are removed by PCP. Looking closely in Fig. 9.5 and 9.6, it is seen that the outliers are picked out and the denoised signals are smooth (such as in Channel 10). Also observing the SVD results (Fig. 9.3(b)), the singular values of the restacked de-noised structural responses decay much faster than the noisy re-stacked one, which means that much less noise are present in the de-noised signals.

For comparisons, the traditional low-pass filter de-noising method with a band-width up to 2 Hz is applied to the measured $\hat{\mathbf{X}} \in \mathbb{R}^{20 \times 180000}$. Results show that the noise is not effectively removed: Fig. 9.5 shows that the outlier is not removed, and there is obvious phase aliasing in the de-noised signal (Fig. 9.6), which does not happen in the PCP-denoised signal.
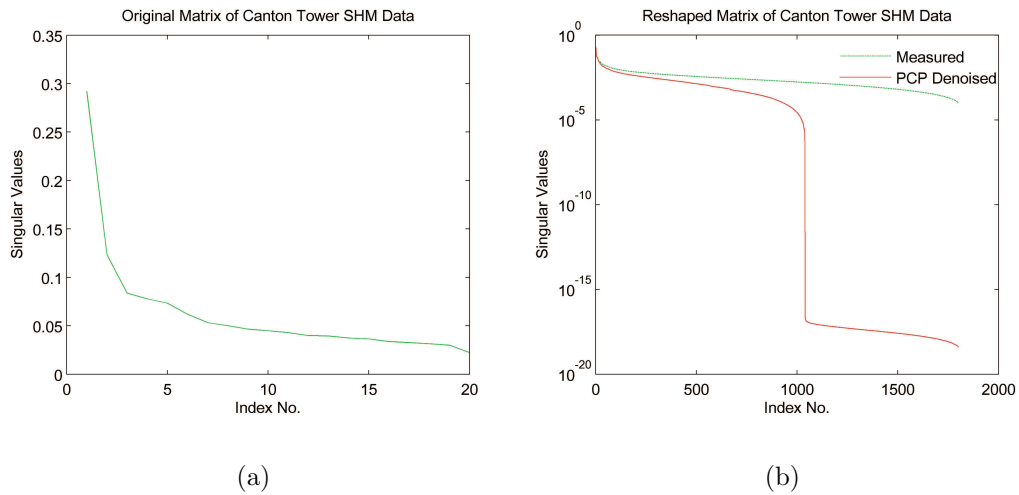
Figure 9.3 : Singular values of the Canton Tower one-hour ambient vibration acceleration matrices: (a) in its original dimension 20×180000 and (b) in reshaped dimension 2000×1800 of the measured data and PCP-denoised data (reshape factor $l = 100$).

9.8 Summary

This chapter presents a new denoising scheme for removal of both dense noise and outliers common in the measured structural vibration responses via principal component pursuit (PCP). It exploits that outliers are sparse in nature, and the underlying clean multi-channel structural responses are intrinsically low-rank (with few active modes). A simple and effective strategy (proposed in Chapter 8) of re-stacking the structural vibration responses, which does not essentially change the contained struc-
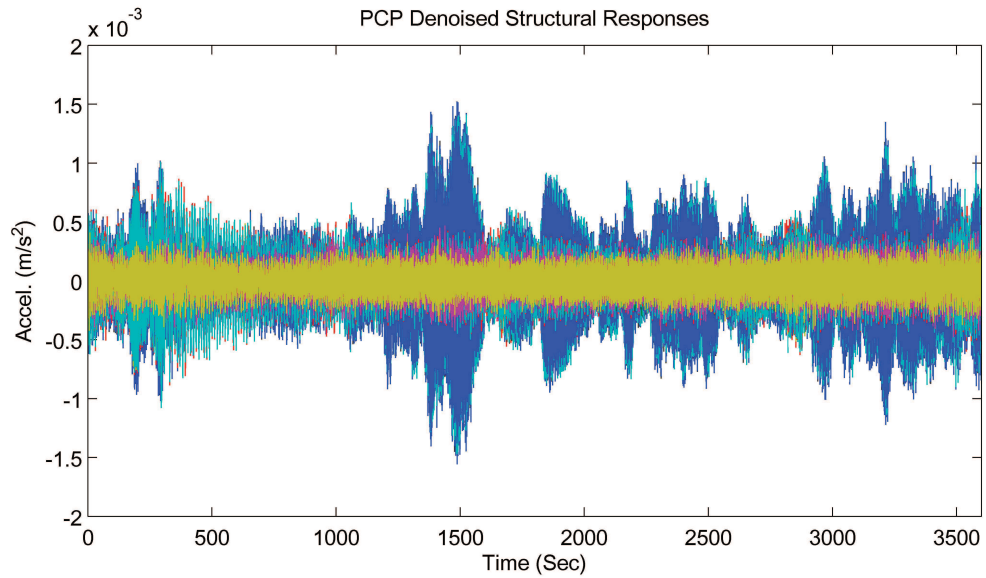
Figure 9.4 : The PCP-denoised (reshape factor $l = 100$) one-hour structural vibration accelerations of the Canton Tower (20 channels' data are shown in different colors).
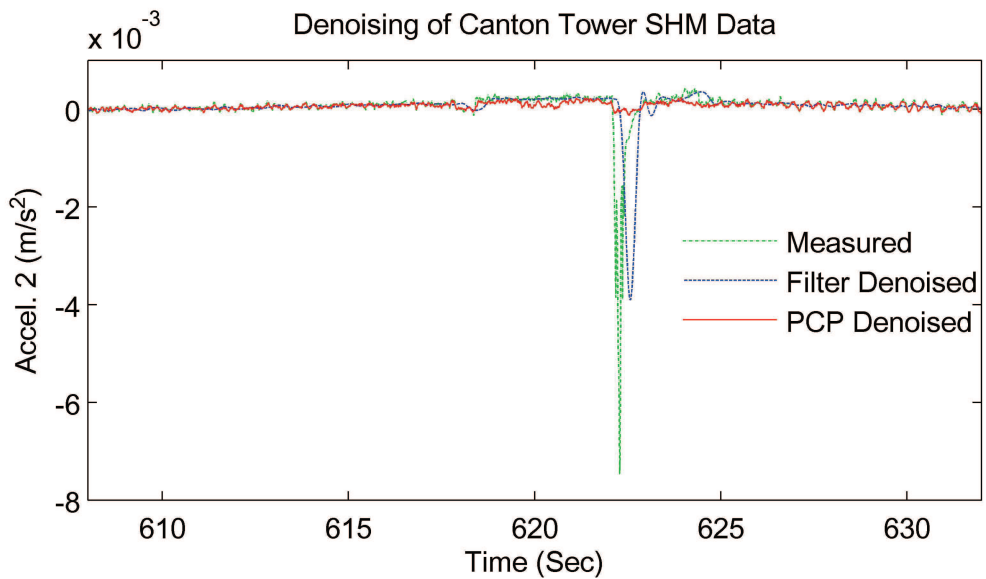
Figure 9.5 : The PCP-denoised and filter-denoised acceleration of Channel 2 of the Canton Tower one-hour SHM data compared to the measured data (shown between 605-635 seconds for visual enhancement).
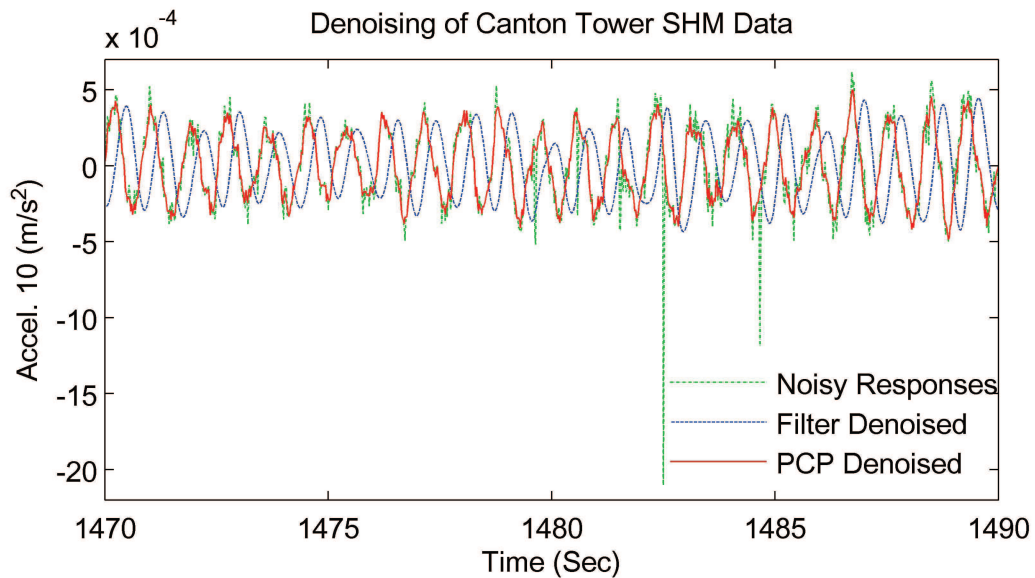
Figure 9.6 : The PCP-denoised and filter-denoised acceleration in Channel 10 of the Canton Tower one-hour SHM data compared to the measured data (shown between 1470-1490 seconds for visual enhancement).

tural dynamic information, is used to guarantee a low-rank representation such that the challenging denoising problem can be cast into the PCP framework.

Detailed numerical simulations are conducted and results shows that PCP works well under various conditions in handling both types of noise altogether; especially, the assumption used to be made in traditional PCA method that sensor number be larger than mode number is avoided thanks to the re-stacking strategy, which also improves the traditional PCA-denoising method when only dense noise is present. Also, compared with PCA with thresholding scheme, the PCP denoising scheme needs no any prior information with respect to the distribution and magnitudes of the data matrix's singular values: it can be implemented "blindly". The ability of PCP for practical applications is also illustrated in denoising the real-measured monitoring data of the Canton Tower. PCP with the re-stacking strategy in denoising the struc-

tural vibration responses would be highly expected for large-scale data management in structural dynamics and SHM applications.

Chapter 10

Conclusions and Future Research

10.1   Conclusions

The dissertation establishes a new paradigm with effective and efficient data processing and management algorithms towards rapid, unsupervised, and automated health monitoring and assessment of civil structures. Different from the traditional model based and parametric methods that are usually computationally intensive and require extensive user-involvement, the proposed methodology is data-driven in nature–by harnessing the data structure itself of the (available) structural response data set. The implications of the sparse representation and low-rank structure of the SHM data set are interpreted as the salient structural dynamic and damage features in output-only modal identification, damage detection and non-destructive assessment, and massive data management of civil structures. Numerical simulations, laboratory experiments, and field measurement data of the super high-rise Canton Tower and seismically excited buildings validates the effectiveness and efficiency of the proposed data-driven paradigm.

- New output-only non-parametric modal identification methods are proposed based on the unsupervised multivariate blind source separation (BSS) techniques. They are data-driven in nature, allowing fairly efficient implementation and imposing little user involvement. Specifically, the signal complexity of the (only available) structural responses and the underlying modal responses are

exploited and a direct connection between the modal expansion and the BSS model with the complexity pursuit (CP) learning rule. CP is found to be suitable for identification of a wide range of linear structures without the need of tuning parameters, as opposed to existing BSS based methods such as ICA (limited to lightly-damped structures) and SOBI (dependent on the lag parameter). Addressing the identification problem with limited sensors in the BSS framework, the proposed SCA based method harnesses the sparsity nature of the underlying modal coordinates; it interprets the modal expansion in a new perspective of sparse clustering, making the output-only modal identification fairly user-friendly and efficient.

- A data-driven multi-scale (global and local) framework is proposed for damage detection of civil structures. The sparse feature is proposed as the salient signature of damage implicit in the (often very noisy) structural data (pulse-like feature in vibration responses or sparse white pixels in the close-up images/videos of structures). This damage indicator–sparse feature–not only has rich implications in mathematical formulation (especially with the explosive development in sparse representation and compressed sensing), but also can serve as a simple and intuitive cue in automated damage alarming systems on civil structures.

In detail, the proposed unsupervised multivariate ICA based damage detection method is capable of extracting the sparse components hidden in the multi-channel noisy structural responses on the (traditional wavelet domain), simultaneously identifying both damage instants and damage locations. In addition, a novel sparse representation classification method is presented for both locating damage and estimating damage severity; it interprets the nature of the classifi-

cation problem in a new perspective of sparse representation and establishes an extremely simple data-driven empirical sparse representation methodology. As opposed to traditional pattern recognition based methods, the proposed method does not require the process of reference training or setting up parametric classifier model that is computationally intensive and user-dependent.

Finally, a new data-driven framework of high-rate dynamic imaging (close-up "filming") of structures is proposed to automate real-time damage detection of local structural components. The data structure of the multiple close-up images is interpreted as a superposition of a low-rank component and a sparse component; the low-rank component represents the irrelevant highly-correlated background among the temporal frames, whereas the sparse component captures the dynamic innovation information induced by damage. As opposed to existing digital image processing techniques for damage detection, the proposed dynamic imaging method does not require a parametric model (without any tuning parameters) or prior structural information (e.g., geometry) for calibrations or reference.

- New data compression and data cleansing algorithms are developed to address the emerging large-scale SHM data management problems. A notable conclusion out of this dissertation work is that low-rank structure exists–intrinsic but implicit–in the multi-channel large-scale structural response data. Such a low-dimensional structure, empirically, stems from that few modes are active in the structural responses. However, originally, limited to the sensor and time-history dimension, the structural response data set generally doesn't have an explicit low-rank representation; a matrix reshape scheme is proposed to guarantee the

low-rank representation of the large-scale data set regardless of the original data dimension. This is theoretically justified that mode information (typically few are active, hence the rank of the structural response data matrix is small) remains invariant regardless of the reshaping of the data matrix.

Specifically, a new unsupervised data compression method is proposed based on low-rank representation and multivariate learning rule ICA. Especially, ICA is found to be the optimal multivariate adaptive learning rule for data compression by transforming the multi-channel structural responses to an most independent space which removes both intra- and inter- redundancy of the multi-channel structural response data. A very high compression ratio is achieved while retaining excellent reconstruction accuracy when compressing two sets of real-recorded structural seismic records.

To guarantee a low-rank representation of any structural response data matrix, a matrix reshape strategy is proposed to achieve most effective compression of very large-scale structural response data. The proposed matrix reshape scheme removes the common premise in existing PCA/SVD based methods that the number of the active modes is much less than that of the sensor for a low-rank representation. Finally, a new and practical data cleansing algorithm is proposed for simultaneously removing both dense noise and gross outliers (naturally as sparse elements) which are ubiquitous in multi-channel SHM data sets (with implicit low-rank structure), while traditional data denoising methods can only deal with (Gaussian-type) white noise.

10.2   Other accomplished research & ongoing research

Within the established data-driven framework for efficient and effective system iden-
tification and health monitoring of civil structures, other accomplished research as
well as several ongoing research, also as part of this thesis work, are briefly mentioned
in the following due to limited space:

- Motivated by the drawback of the original independent component analysis
  (ICA) based output-only modal identification which is only suitable for very
  lightly damped structures, a time-frequency ICA method is proposed to identify
  even highly-damped structures by exploiting the sparse time-frequency (short-
  time-Fourier-transformed (STFT)) representations of the available structural
  responses and the underlying modal responses. Numerical simulations, exper-
  imental study and real-world seismically excited structure examples are pre-
  sented for validation [145]. In addition, complex modes of structures can also
  be very efficiently identified by a straightforward extention of the proposed
  method to a complex-valued representation of the time-frequency ICA method
  [102].

- Existing cable force measurement devices, such as anchor load cells, magnetoe-
  lastic (EM) sensors, and optical fiber Bragg grating (OFBG) sensors, which are
  embedded along with the installing of the newly-built bridge cables, are able to
  directly record the time history of cable tension. It is known, however, that these
  sensors are expensive and the labor of installation these sensors onto cables is
  quite intensive. Moreover, the durability issue of the cable force sensors, which
  may have only few years' service life, significantly hinders their applicability in
  practice [94][131][80]. Considering the costly and challenging effort needed to

replace these cable sensors, it desirable to seek more reliable, economical, and convenient approaches for real-time monitoring of the cable force.

It is proposed in the thesis work [144][106] to exploit the direct formula between time-varying cable tension and its time-varying frequency by the unsupervised real-time learning capability of BSS (Chapter 2) to establish the framework of real-time blind (unsupervised) identification of time-varying system (modal frequency) from only the cable accelerations (output-only) for real-time identification of cable tension time history. The benefit of such a data-driven paradigm is that it uses as little information as the cable accelerations which can be collected from the attached accelerometers that are cost-effective, reliable, and conveniently embedded (or replaced) in any in-situ or new cables. The proposed method has been validated by laboratory experiments of a stay cable and field data of a cable-stayed bridge.

- Modal identification or testing of structures consists of two phases, namely, data acquisition and data analysis. Some structures, such as aircrafts, high-speed machines, and civil structures (e.g., plate-like structures), have active modes in the high-frequency range. In the data acquisition step, the Shannon-Nyquist sampling theorem indicates that capturing the high-frequency modes (signals) requires uniform high-rate sampling to avoid aliasing, which would result in sensing too many samples.

To address this problem, in the thesis work, an alternative *non-traditional* sensing framework–the recently-developed compressed sensing technique with non-uniform low-rate random sampling–is explored. A new method for output-only modal identification of structures in a non-uniform low-rate random sensing

framework is proposed [153] based on a combination of compressed sensing (CS) and blind source separation (BSS). Specifically, the proposed method uses the CP technique (Chapter 2) to directly decouple the non-uniform low-rate random samples of the structural responses, simultaneously yielding the mode shape matrix as well as the low-rate random samples of the modal responses. Then ℓ_1-minimization recovers the underlying uniform high-rate modal response from the CP-decoupled non-uniform low-rate random samples of the modal response, thereby enabling estimation of the frequency and damping ratio. Numerical examples, experimental bench-scale model, and the real-world seismic-excited base-isolated hospital building examples show that it is feasible to use the proposed output-only modal identification method to identify the modes using non-uniform low-rate random sensing, which can be far below what is suggested by the sampling theorem.

Our recent work further extends such a sub-Nyquist non-uniform low-rate random sensing framework to *traditional* uniform low-rate sensing, and proposes a CP based method for output-only modal identification of structures when the uniform sampling rate is far from sufficient or when aliasing has long occurred. More details are covered in Ref. [105].

10.3 Future research

Inspired by the dissertation work, possible future research may be devoted to addressing several major problems in the areas of health monitoring and assessment of civil structures, which are summarized as follows:

- Besides system identification, damage detection, and data compression and

cleansing, the methodology of explicitly harnessing data structure (sparse representation and low-rank structure) of large-scale data sets may be extended to other data problems in civil engineering, such as data sensing and data communication in sensor networks, building information model (BIM), and infrastructure networks.

- The sparse representation classification (Chapter 5) is a general classification framework; it can be easily adaptive to other pattern recognition problems in civil engineering as long as one builds up a reference dictionary (simply lining up all the reference features without training) and represents the test feature as a linear combination of the bases of the reference dictionary. In addition, in the dissertation, although the reference dictionary depends on simulating different classes from a FEM model, it need not necessarily be so; reference features in the dictionary can come from any known prior information, e.g., features learned from historical data and classes if available.

- Currently non-destructive assessment of civil structures are offline. It is possible to embed a digital camera network enhanced with the proposed dynamic imaging method (Chapter 6) to continuously perform close-up monitoring of structures. Such a camera network can be incorporated into the global sensor network for a truly multi-scale SHM system with exchanged and communicated information. For example, normally the cameras take low-rate close-up images to perform long-term assessment of structures such as corrosion and creep, until the global sensor network has detected the damage location area and sends a cue to the cameras in the vicinity of the identified damage location to take high-rate close-up images (especially during extreme events such as earthquakes),

providing finer local damage information.

- The measured massive SHM data are mostly stored in the database without appropriately taken advantage of. The big data technology has presented opportunities of mining these very large-scale data to extract valuable structural information, potentially, due to long-term environmental effects, climate change, and post-disaster effects.

- The developed data-driven paradigm with efficient and effective system identification, damage detection, and data management algorithms has considerable potential to be applied in real-world SHM systems of large-scale civil structures. For example, it may be developed into a software package to be embedded into the computing center in the base station; it can also be modified into decentralized algorithms to be embedded into the wireless sensors with distributed computing capabilities.

Bibliography

[1] http://www.cse.polyu.edu.hk/benchmark/.

[2] Abazarsa, F., Ghahari, S.F., Nateghi, F., and Taciroglu, E. (2013). Response-only modal identification of structures using limited sensors. *Structural Control and Health Monitoring*, 20, 987-1006.

[3] Abdel-Qader, I., Abudayyeh, O., and Kelly, M. (2003). Analysis of Edge-Detection Techniques for Crack Identification in Bridges. *J. Comput. Civ. Eng.*, 17(4), 255-263.

[4] Ahmed, N. and Rao, K.R. (1975). Orthogonal transforms for digital signal processing. Spring-Verlag, New York.

[5] Anagnostopoulos, C., Anagnostopoulos, I., Psoroulas, I., Loumos, V., and Kayafas, E. (2008). License Plate Recognition from still images and video sequences: a survey. *IEEE Transactions on Intelligent Transportation Systems*, 9(3), 377-391.

[6] Antoni, J. (2005). Blind separation of vibration components: principles and demonstrations. *Mechanical Systems and Signal Processing*, 19, 1166-1180.

[7] Antoni, J. and Chuahan S. (2013). A study and extension of second-order blind source separation to operational modal analysis. *Journal of Sound and Vibration*, 332, 1079-1106.

[8] Back, A.D. and Weigend, A.S. (1997). A first application of independent component analysis to extracting structures from stock returns. *International Journal of Neural Systems*, 8, 473-484.

[9] Bao, Y., Beck, J.L., and Li, H. (2010). Compressive sampling for accelerometer signals in structural health monitoring. *International Journal of Structural Health Monitoring*, 10(3), 235-246.

[10] Basu, B., Nagarajaiah, S., and Chakraborty, A. (2008). Online identification of linear time-varying stiffness of structural systems by wavelet analysis. *International Journal of Structural Health Monitoring*, 7, 21-36.

[11] Baneen, U., Kinkaid, N. M., Guivant, J.E., and Herszberg, I. (2012). Vibration based damage detection of a beam-type structure using noise suppression method. *Journal of Sound and Vibration*, 331, 1777-1788.

[12] Bell, A. and Sejnowski, T. (1995). An information-maximization approach to blind separation and blind deconvolution. *Neural Computation*, 7, 1129-1159.

[13] Belouchrani, A., Abed-Meraim, A.K., Cardoso, J.F., and Moulines, E. (1997). A blind source separation technique using second-order statistics. *IEEE Transactions on Signal Processing*, 45, 434-444.

[14] Bernal, D. (2002). Load Vectors for Damage Localization. *ASCE Journal of Engineering Mechanics*, 128(1), 7-14.

[15] Bezdek, J.C. (1981). Pattern recognition with fuzzy objective function algorithms. Plenum Press, New York.

[16] Bishop, C.M. (1995). Neural networks for pattern recognition. Oxford University Press, Oxford.

[17] Borga, M. (1998). Learning multidimensional signal processing. Doctoral dissertation, Linkoping University.

[18] Brincker, R. and Kirkegaard, P.H. (2010). Special issue on operational modal analysis. *Mechanical Systems and Signal Processing*, 24, 1209-1212.

[19] Brincker, R., Zhang, L., and Andersen P. (2001). Modal identification of output-only systems using frequency domain decomposition. *Smart Material and Structures*, 10, 441-445.

[20] Bruckstein, A.M., Donoho, D.L., and Elad, M. (2008). From sparse solutions of systems of equations to sparse modeling of signals and images. *SIAM Review*, 51, 34-81.

[21] Burges, C.J.C. (1998). A tutorial on support vector machines for pattern recognition. *Data Mining and Knowledge Discovery*, 2, 121-167.

[22] Brownjohn, J.M.W. (2003). Ambient vibration studies for system identification of tall buildings. *Earthquake Engineering and Structural Dynamics*, 32, 71-95.

[23] Candes, E., Li, X., Ma, Y., and Wright, J. (2009). Robust principal component analysis. *Journal of ACM*, 58, 1-37.

[24] Candes, E.J. and Romberg, J. (2005). ℓ_1-Magic: recovery of sparse signals via convex programming. http://www.acm.caltech.edu/l1magic.

[25] Candes, E. and Wakin, M. (2008). An introduction to compressive sampling. *IEEE Signal Processing Magazine*, 25, 21-30.

[26] Candes, E., Romberg, J., and Tao, T. (2006). Robust uncertainty principles: exact signal reconstruction from highly incomplete frequency domain. *IEEE Transactions on Information Theory*, 52, 489-509.

[27] Cardoso J. and Souloumiac A. (1993). Blind beamforming for non-Gaussian signals. *IEE Proceedings F*, 140(6), 771-774.

[28] Celebi, M., Sanli, A., Sinclair, M., Gallant, S., and Radulescu, D. (2004). Real-time seismic monitoring needs of a building owner and the solution-A cooperative effort. *Earthquake Spectra*, 19(1), 1-23.

[29] Chen, B. and Nagarajaiah, S. (2008). Structural damage detection using decentralized controller design method. *Smart Structure and Systems*, 4, 779-794.

[30] Chen, L., Shao, Y., Jan, H., Huang, C., and Tien, Y. (2006). Measuring system for cracks in concrete using multitemporal images. *Journal of Surveying Engineering*, 132(2), 77-82.

[31] Chen, S.S., Donoho, D.L., Saunders, M.A. (1999). Atomic decomposition by basis pursuit. *SIAM Journal on Scientific Computing*, 20, 33-61.

[32] Chen, W, Lu, Z., Lin, W., Chen, S, Ni, Y., Xia, Y., and Liao, W. (2011). Theoretical and experimental modal analysis of the Guangzhou New TV Tower. *Engineering Structures*, 33, 3628-3646.

[33] Collin, R., Lipton, A., and Kanade, T. (2000). Introduction to the special section on video surveillance. *IEEE Transactions on Pattern Analysis and Machine Intelligence*, 22(8), 745-746.

[34] Comon, P. and Jutten, C. (2010). Handbook of blind source separation: independent component analysis and applications. Academic Press, New York, NY.

[35] Contreras, M., Nagarajaiah, S., and Narasimhan, S. (2011). Real time detection of stiffness change using a radial basis function augmented observer formulation. *Smart Materials and Structures*, 20, 035013.

[36] Cover, T.M. and Thomas, J.A. (1991). Elements of information theory. Wiley, New York.

[37] CSMIP. (2013). http://www.conservation.ca.gov/cgs/smip/Pages/Station.aspx.

[38] Daubechies, I. (1992). Ten lectures on wavelets. CBMS-NSF conference series in applied mathematics, SIAM.

[39] De Boe, P. and Golinval, J-C. (2003). Principal component analysis of a piezo-sensor array for damage localization. *International Journal of Structural Health Monitoring*, 2, 137-144.

[40] Dharap, P., Koh, B.H., and Nagarajaiah, S. (2006). Structural health monitoring using ARMarkov observers. *Journal of Intelligent Material Systems and Structures*, 17, 469-481.

[41] Doebling, S.W., Farrar, C.R., Prime, M.B., and Shevitz, D.W. (1996). Damage identification and health monitoring of structural and mechanical systems from changes in their vibration characteristics: a literature review, Report LA-13070-MS, UC-900, Los Alamos National Laboratory, New Mexico.

[42] Donoho, D.L. (2006). For most large underdetermined systems of linear equations, the minimal ℓ_1-norm solution is also the sparsest solution. *Communications*

on Pure and Applied Mathematics, 59, 797-829.

[43] Donoho, D.L. (2006). Compressed sensing. *IEEE Transactions on Information Theory*, 52, 1289-1306.

[44] Donoho, D.L. and Johnstone, I.M. (1994). Ideal spatial adaptation by wavelet shrinkage. *Biometrika*, 81, 425-455.

[45] Eglen, S., Bray, A., and Stone J. (1997). Unsupervised discovery of invariances. *Network*, 8, 441-452.

[46] Ewin, D.J. (2000) Modal testing: theory, practice and application, second ed. Research Studies Press, Hertfordshire.

[47] Farrar, C. and Worden, K. (2007). An introduction to structural health monitoring. *Philosophical Transactions of the Royal Society A*, 365, 303-315.

[48] Feeny, B. and Kappagantu, R. (1998). On the physical interpretation of proper orthogonal modes in vibration. *Journal of Sound and Vibration*, 211, 607-616.

[49] Friswell, M.I. and Inman, D.J. (1999). Sensor validation for smart structures. *Journal of Intelligent Material Systems and Structures*, 10, 973-982.

[50] Friswell, M.I. and Mottershead, J.E. (1995). Finite element model updating in structural dynamics. Kluwer Academic Publishers, London.

[51] Fraser, M., Elgamal, A., He, X., and Conte, J. (2009). Sensor Network for structural health monitoring of a highway bridge. *Journal of Computing in Civil Engineering*, 24(1), 11-24.

[52] Gao, Y. and Spencer Jr, B.F. (2006). Online damage diagnosis for civil infrastructure employing a flexibility-based approach. *Smart Materials and Structures*, 15, 9-19.

[53] Georgiev, P., Theis, F. and Cichocki, A. (2005). Sparse component analysis and blind source separation of underdetermined mixtures. *IEEE Transactions on Neural Networks*, 14, 992-996.

[54] Gribonval, R. and Lesage, S. (2006). A survey of sparse component analysis for blind source separation: principles, perspectives, and new challenges, Proceedings of European Symposium on Artificial Neural Networks, Bruges, pp. 323-330.

[55] Hera, A. and Hou, Z. (2004). Application of wavelet approach for ASCE structural health monitoring benchmark studies. *ASCE Journal of Engineering Mechanics*, 130, 96-104.

[56] Hazra, B. and Narasimhan, S. (2010). Wavelet-based blind identification of the UCLA Factor building using ambient and earthquake responses. *Smart Materials and Structures*, 19, 025005.

[57] Hazra, B., Roffel, A.J., Narasimhan, S., and Pandey, M.D. (2010). Modified cross-correlation method for the blind identification of structures. *ASCE Journal of Engineering Mechanics*, 136, 889-897.

[58] Hou, S., Liang, M., and Li, Y. (2011). An optimal global projection denoising algorithm and its application to shaft orbit purification. *International Journal of Structural Health Monitoring*, 10, 603-616.

[59] Hou, Z., Noori, M., and Amand, R.St. (2000). Wavelet-based approach for structural damage detection. *ASCE Journal of Engineering Mechanics*, 126, 677-683.

[60] Hsieh, J., Yu, S., Shen, Y., and Hu, W. (2006). Automatic traffic surveillance system for vehicle tracking and classification. *IEEE Transactions on Intelligent Transportation Systems*, 7(2), 175-187.

[61] Huang, N., Shen, Z., Long, S., Wu, M., Shih, H., Zheng, Q., Yen, N., Tung, C., Liu, H. (1998). The empirical mode decomposition and the Hilbert spectrum for nonlinear and non-stationary time series analysis. *Proceedings of the Royal Society of London, Series A-Mathematical, Physical and Engineering Science*, 454, 903-995.

[62] Hutchinson, T. and Chen, Z. (2006). Improved Image Analysis for Evaluating Concrete Damage. *J. Comput. Civ. Eng.*, 20(3), 210-216.

[63] Hyvarinen, A. (2001). Complexity pursuit: separating interesting components from time series. *Neural Computation*, 13, 883-898.

[64] Hyvarinen, A., Karhunen, J., and Oja, E. (2001). Independent component analysis. Wiley, New York, NY.

[65] Hyvarinen, A., Oja, E. (2000). Independent component analysis: algorithms and applications. *Neural Networks*, 13, 411-430.

[66] Ibrahim, S.R. and Mikulcik, E.C. (1973). A time domain modal vibration test technique. *Shock and Vibration Bulletin*, 43(4), 21-37.

[67] James, G.H., Carne, T.G., and Lauffer, J.P. (1995). The natural excitation technique for modal parameter extraction from operating structures. *Modal Analysis*, 10, 260-277.

[68] Juang, J.N. and Pappa, R.S. (1985). An eigen system realization algorithm for modal parameter identification and model reduction. *Journal of Guidance, Control and Dynamics*, 8, 620-627.

[69] Jahanshahi, M., Kelly, J., Masri, S., and Sukhatme, G. (2009). A survey and evaluation of promising approaches for automatic image-based defect detection of bridge structures. *Structural and infrastructural Engineering*, 5, 455-486.

[70] Jahanshahi, M., Masri, S., and Sukhatme, G. (2011). Multi-image stitching and scene reconstruction for evaluating in structures. *Structural Health Monitoring, An International Journal*, 10(6), 643-657.

[71] Jiang, X. and Mahadevan, S., and Adeli, H. (2007). Bayesian wavelet packet denoising for structural system identification. *Structural Control and Health Monitoring*, 14, 333-356.

[72] Jolliffe, I. (1986). Principal component analysis. Springer-Verlag, New York.

[73] Kerschen, G., De Boe, P., Golinval, J., and Worden, K. (2005). Sensor validation using principal component analysis. *Smart Materials and Structures*, 14, 36-42.

[74] Kerschen, G., Poncelet, F., and Golinval, J-C. (2007). Physical interpretation of independent component analysis in structural dynamics. *Mechanical Systems and Signal Processing*, 21, 1561-1575.

[75] Kijewski, T. and Kareem, A. (2003). Wavelet transforms for system identification in civil engineering. *Computer-aided Civil and Infrastructural Engineering*, 18(5), 339-355.

[76] Kim, S., Koh, K., Lustig, M., Boyd, S., and Gorinevsky, D. (2007). A method for large-scale ℓ_1-regularized least squares. *IEEE Journal on Selected Topics in Signal Processing*, 1, 606-617.

[77] Kisilev, P., Zibulevsky, M. and Zeevi, Y. (2003). A multiscale framework for blind separation of linearly mixed signals. *Journal of Machine Learning Research*, 4, 1339-1364.

[78] Ko, J.M. (2003). Health monitoring and intelligent control of cable-supported bridges. Proceedings of the International Workshop on Advanced Sensors, Structural Health Monitoring, and Smart Structures, Keio University, Japan.

[79] Koh, B.H., Dharap, P., Nagarajaiah, S., Phan, M.Q. (2005). Real-time structural damage monitoring by input error function. *AIAA Journal*, 43, 1808-1814.

[80] Li, H., Ou, J., and Zhou, Z. (2009). Applications of optical fibre Bragg gratings sensing technology-based smart stay cables. *Optics and Lasers in Engineering*, 47, 1077-1084.

[81] Lin, Z., Chen, M., Wu, L., and Ma, Y. (2009). The augmented Lagrange multiplier method for exact recovery of corrupted low-rank matrices. UIUC Technical Report UILU-ENG-09-2215.

[82] Liu, Y., Loh, C., and Ni, Y. (2012). Stochastic subspace identification for output-only modal analysis: application to super high-rise tower under abnormal loading condition. *Earthquake Engineering and Structural Dynamics*, in press, DOI: 10.1002/eqe.2223.

[83] Ljung, L. (1999). System identification: theory for the user, 2nd ed. Prentice Hall, New York.

[84] Lustig, M., Santos, J.M., Donoho, D.L., Pauly, J.M. (2007). Sparse MRI: the application of compressed sensing for rapid MR imaging. *Magnetic Resonance in Medicine*, 58, 1182-1195.

[85] Lynch, J.P., Loh, K.J. (2006). A summary review of wireless sensors and sensor networks for structural health monitoring. *Shock and Vibration Digest*, 38(2), 91-128.

[86] Lynch, J.P., Sundararajan, A., Law, K.H., Kiremidjian, A.S., and Carryer, E. (2003). Power-efficient data management for a wireless structural monitoring system. Proceedings of the 4th International Workshop on Structural Health Monitoring, Stanford, CA.

[87] Madhow, U. (1988). Blind adaptive interference suppression for direct-sequence CDMA. *Proceedings of the IEEE*, 8, 2049-2069.

[88] Maia, N.M.M. (1997). Theoretical and experimental modal analysis. Research Studies Press, Taunton, Somerset, UK.

[89] Makeig, S., Bell, A., Jung, T.P., and Sejnowski, T.J. (1996). Independent component analysis of electroencephalographic data. *Advances in Neural Information Processing System*, 8, 145-151.

[90] Mallat, S. (1999). A wavelet tour of signal processing, 2nd ed.. Academic, San Diego, CA.

[91] Mascarenas, D., Cattaneo, A., Theiler, J., and Farrar, C. (2013). Compressed sensing techniques for detecting damage in structures. *International Journal of Structural Health Monitoring*, in press, DOI: 10.1177/1475921713486184.

[92] Mascarenas, D., Chong, S.Y., Park, G., Lee, J.-R., and Farrar, C. (2012). Application of compressed sensing to 2-D ultrasonic propagation imaging system data. 6th European Workshop on Structural Health Monitoring, Dresden, Germany.

[93] McNeill, S.I. and Zimmerman, D.C. (2008). A framework for blind identification using joint approximate diagonalization. *Mechanical Systems and Signal Processing*, 22, 1526-1548.

[94] Mehrabi, A. (2006). In-service evaluation of cable-stayed bridges, overview of available methods, and findings. *ASCE Journal of Bridge Engineering*, 11(6), 716-724.

[95] Moaveni, B., Hurlebaus, S., and Moon, F. (2013). Special issue on real-world application of structural identification and health monitoring methodologies. *ASCE Journal of Structural Engineering*, 139(10), 1637-1638.

[96] Nagarajaiah, S. and Basu, B. (2009). Output only identification and structural damage detection using time frequency and wavelet techniques. *Earthquake Engineering and Engineering Vibration*, 8, 583-605.

[97] Nagarajaiah, S., Basu, B., and Yang, Y. (2014). Output only modal identification and structural damage detection using time-frequency and wavelet techniques for assessing and monitoring civil infrastructures, Sensor Technologies for Civil Infrastructures: Applications in Structural Health Monitoring (edited by M. Wang, J. Lynch, H. Sohn), Woodhead Publishing.

[98] Nagarajaiah, S. and Dharap, P. (2003). Reduced order observer based identification of base isolated buildings. *Earthquake Engineering and Engineering Vibration*, 2(2), 237-244.

[99] Nagarajaiah, S. and Sun, X. (1996). Response of base isolated building during 1994 Northridge earthquake. Final Report Project No. 1093-556, California Strong Motion Instrumentation Program, Sacramento.

[100] Nagarajaiah, S. and Sun, X. (2000). Response of base-isolated USC hospital building in Northridge earthquake. *ASCE Journal of Structural Engineering*, 126, 1177-1186.

[101] Nagarajaiah, S. and Sun, X. (2001). Base-isolated FCC building: impact response in Northridge earthquake. *ASCE Journal of Structural Engineering*, 127, 1063-1075.

[102] Nagarajaiah, S. and Yang, Y. (2014). Blind modal identification of output-only non-proportionally-damped structures by time-frequency complex independent component analysis. *Smart Structures and Systems*, accepted.

[103] Nagarajaiah, S. and Yang, Y. (2014). Blind identification of output-only systems and structural damage via sparse representation and unsupervised machine learning. Encyclopedia of Earthquake Engineering (edited by Beer, M., Patelli, E., Kougioumtzoglou, I., and Au, I.), Springer-Verlag, in press.

[104] Nagarajaiah, S. and Yang, Y. (2014). Data compression of large-scale structural seismic and typhoon responses by low-rank representation with matrix reshape. *Structural Control and Health Monitoring*, submitted.

[105] Nagarajaiah, S. and Yang, Y. (2014). Output-only modal identification by sub-Nyquist sensing: uniformly down-sampling. In progress.

[106] Nagarajaiah, S. and Yang, Y. (2014). Real-time blind identification of time-varying structures by complexity pursuit. In progress.

[107] Ni, Y., Wong, K., and Xia, Y. (2011). Health checks through landmark bridges to sky-high structures. *Advances in Structural Engineering*, 14, 103-119.

[108] Ni, Y., Xia, Y., Liao, W., and Ko, J. (2009). Technology innovation in developing the structural health monitoring system for Guangzhou New TV Tower. *Structural Control and Health Monitoring*, 16, 73-98.

[109] O'Connor, S.M., Lynch, J.P., and Gilbert, A.C. (2013). Implementation of a compressive sampling scheme for wireless sensors to achieve energy efficiency in a structural health monitoring system. SPIE Smart Structures and Materials + Nondestructive Evaluation and Health Monitoring, San Diego, CA.

[110] Peeters, B., Roeck, G.E. (2001). Stochastic system identification for operational modal analysis: a review. *Journal of Dynamic Systems, Measurement, and Control*, 123, 659-667.

[111] Peng, Y., Ganesh, A., Wright, J., Xu, W., and Ma, Y. (2010). RASL: Robust alignment by sparse and low-rank decomposition for linearly correlated images. IEEE Conf. Computer Vision and Pattern Recognition (CVPR), San Francisco, CA.

[112] Poncelet, F., Kerschen, G., Golinval, J-C., and Verhelst, D. (2007). Output-only modal analysis using blind source separation techniques. *Mechanical Systems and Signal Processing*, 21, 2335-2358.

[113] Ricardo, O., Candes, E., and Sodickson, D. (2013). Low-rank and sparse matrix decomposition for accelerated dynamic MRI with separation of background and dynamic components. *Magnetic Resonance in Medicine*, accepted.

[114] Rissanen, J.J., and Langdon, G.G. (1979). Arithmetic coding. *IBM Journal of Research and Development*, 23(2), 149-162.

[115] Rytter, A. (1993). Vibration based inspection of civil engineering structures. PhD Thesis, Department of Building Technology and Structural Engineering, Aalborg University, Denmark.

[116] Sadhu, A., Hu, B., and Narasimhan, S. (2012). Blind source separation towards decentralized modal identification using compressive sampling. 2012 11th International Conference on Information Science, Signal Processing, and their applications, Montreal, Canada.

[117] Sayood, K. (2000). Introduction to data compression, 2nd ed. Academic, San Diego.

[118] Shakal, A., Huang, M., Darragh, R., et al. (1994). CSMIP strong motion records from the Northridge earthquake of 17 January 1994. Rep. No. OSMS 94-07, Calif. Strong Motion Instrumentation Program, California Department of Conservation, Calif.

[119] Shannon, C.E. (1948). A mathematical theory of communication. *The Bell System Technical Journal*, 27, 379-423, 623-656.

[120] Shull, P. (2002). Nondestructive evaluation theory, techniques, and applications. Marcel Dekker, New York, NY.

[121] Siringoringo, D and Fujino, Y. (2008). System identification of suspension bridge from ambient vibration response. *Engineering Structures*, 30(2), 462-477.

[122] Spanias, A.S., Jonsson, S.B., and Stearns, S.D. (1991). Transform methods for seismic data compression. *IEEE Transactions on Geoscience and Remote Sensing*, 29(3), 407-416.

[123] Spencer Jr, B.F., Ruiz-Sandoval M., and Kurata N. (2004). Smart sensing technology: opportunity and challenge. *Structural Control and Health Monitoring*, 11, 9-19.

[124] Sun, Z. and Chang, C. (2002). Structural damage assessment based on wavelet packet transform. *ASCE Journal of Structural Engineering*, 128, 1354-1361.

[125] Staszewski, W.J. (1997). Identification of damping in MDOF systems using time-scale decomposition. *Journal of Sound and Vibration*, 203, 283-305.

[126] Stearns, S.D. (1987). Seismic data compression using linear predictive coding. Sandia Report SAND87-1384 UC-13, Sandia National Laboratory, Albuquerque.

[127] Stearn, S.D., Tan, L., and Magotra, N. (1993). Lossless compression of waveform data for efficient storage and transmission. *IEEE Transactions on Geoscience and Remote Sensing*, 31(3), 645-654.

[128] Stone, J.V. (1996). Learning perceptually salient visual parameters using spatiotemporal smoothness constraints. *Neural Computation*, 8, 1463-1492.

[129] Stone, J.V. (2001). Blind source separation using temporal predictability. *Neural Computation*, 13, 1559-1574.

[130] Stone, J.V. (2004). Independent component analysis: a tutorial introduction. The MIT Press, Cambridge, MA.

[131] Tabatabai, H. (2005). Inspection and maintenance of bridge stay systems. NCHRP Synthesis 353, National Cooperative Highway Research Program, Transportation Research Board, Washington, DC.

[132] Takhar, D., Bansal, V., Wakin, M., Duarte, M., Baron, D., Kelly, K.F., Baraniuk, R.G. (2006). A compressed sensing camera: new theory and an implementation using digital micromirrors, Proc. Comp. Imaging IV at SPIE Electronic Imaging, San Jose, California.

[133] Taubman, D., and Marcellin, M. (2001). JPEG 2000: image compression fundamentals, standards and practice. Kluwer Academic Press, London.

[134] Trendafilova, I., Cartmell, M.P., and Ostachowicz, W. (2008). Vibration-based damage detection in an aircraft wing scaled model using principal component analysis and pattern recognition. *Journal of Sound and Vibration*, 313, 560-566.

[135] Widodo, A. and Yang, B. (2007). Support vector machine in machine condition monitoring and fault diagnosis. *Mechanical System and Signal Processing*, 21, 2560-2574.

[136] Widodo, A. and Yang, B. (2007). Application of nonlinear feature extraction and support vector machines for fault diagnosis of induction motors. *Expert Systems with Applications*, 33, 241-250.

[137] Worden, K., Lane, A.J. (2001). Damage identification using support vector machines. *Smart Materials and Structures*, 10, 540.

[138] Wright, J., Yang, A.Y., Ganesh, A., Sastry, S.S., and Ma, Y. (2009). Robust face recognition via sparse representation. *IEEE Transactions on Pattern Analysis and Machine Intelligence*, 31, 210-227.

[139] VanOverschee, P. and De Moor, B. (1996). Subspace identification for linear systems: theory, implementation, applications. Kluwer Academic Publishers, Boston, MA.

[140] Xie, S., He, Z., and Fu, Y. (2005). A note on Stone's conjecture of blind source separation. *Neural Computation*, 17, 321-330.

[141] Yang, J.N., Lei, Y., Pan, S., and Huang, N. (2003). System identification of linear structures based on Hilbert-Huang spectral analysis, part 1: normal modes. *Earthquake Engineering and Structural Dynamics*, 32, 1443-1467.

[142] Yang, J.N., Lei, Y., Lin, S., and Huang, N. (2004). Hilbert-Huang based approach for structural damage detection. ASCE Journal of Engineering Mechanics, 130, 85-95.

[143] Yang, W. and Tse, P. (2003). Development of an advanced noise reduction method for vibration analysis based on singular value decomposition. *NDT&E International*, 36, 419-432.

[144] Yang, Y., Li, S., Nagarajaiah, S., Li, H., and Zhou, P. (2014). Real-time output-only identification of time-varying cable tension via complexity pursuit. *ASCE Journal of Structural Engineering*, submitted.

[145] Yang, Y. and Nagarajaiah, S. (2013). Time-frequency blind source separation using independent component analysis for output-only modal identification of highly-damped structures. *ASCE Journal of Structural Engineering*, 139(10), 1780-1793.

[146] Yang, Y. and Nagarajaiah, S. (2014). Blind identification of damage in time-varying systems using independent component analysis with wavelet transform.

Mechanical Systems and Signal Processing, 47(1), 3-20.

[147] Yang, Y. and Nagarajaiah, S. (2013). Blind identification of modal parameters in time domain based on complexity pursuit. *Earthquake Engineering and Structural Dynamics*, 42(13), 1885-1905.

[148] Yang, Y. and Nagarajaiah, S. (2013). Output-only modal identification with limited sensors using sparse component analysis. *Journal of Sound and Vibration*, 332(19), 4741-4765.

[149] Yang, Y. and Nagarajaiah, S. (2013). Data compression of structural seismic responses using principled independent component analysis. *ASCE Journal of Structural Engineering*, 140(7), 04014032.

[150] Yang, Y. and Nagarajaiah, S. (2014). Blind denoising of structural responses with outliers via principal component pursuit. *Structural Control and Health Monitoring*, 21(6), 962-978.

[151] Yang, Y. and Nagarajaiah, S. (2014). Structural damage identification via a combination of blind feature extraction and sparse representation classification. *Mechanical Systems and Signal Processing*, 45(1), 1-23.

[152] Yang, Y. and Nagarajaiah, S. (2014). Structural damage identification via a combination of blind feature extraction and sparse representation classification. *Mechanical Systems and Signal Processing*, 45(1), 1-23.

[153] Yang, Y. and Nagarajaiah, S. (2014). Output-only modal identification by compressed sensing: low-rate random sampling. *Mechanical Systems and Signal Processing*, under review.

[154] Zang, C., Friswell, M.I., and Imregun, M. (2004). Structural damage detection using independent component analysis. *International Journal of Structural Health Monitoring*, 3, 69-83.

[155] Zaurin, R. and Catbas, F. (2010). Integration of computer imaging and sensor data for structural health monitoring of bridges. *Smart Materials and Structures*, 19, 015019.

[156] Zhang, Y., and Li, J. (2006). Wavelet-based vibration sensor data compression technique for civil infrastructure condition monitoring. *ASCE Journal of Computing in Civil Engineering*, 20(6), 390-399.

[157] Zhang, Y., and Li, J. (2007). Linear predictor-based lossless compression of vibration sensor data: system approach. *ASCE Journal of Engineering Mechanics*, 133(4), 431-441.

[158] Zhou, C. and Zhang, Y. (2012). Particle filter based noise removal method for acoustic emission signals. *Mechanical Systems and Signal Processing*, 28, 63-77.

[159] Zhou, W. and Chelidze, D. (2007). Blind source separation based vibration mode identification. *Mechanical Systems and Signal Processing*, 21, 3072-3087.

[160] Zhou, Z., Li, X., Wright, J., Candes, E., and Ma, Y. (2010). Stable principal component pursuit, preprint.

[161] Zuo, M.J., Lin, J., and Fan, X. (2005). Feature separation using ICA for a one-dimensional time series and its application in fault detection. *Journal of Sound and Vibration*, 287, 614-624.